The evolution of supraglacial ponds and ice cliffs on Himalayan debris-covered glaciers

Cameron Scott Watson

Submitted in accordance with the requirements for the degree of
Doctor of Philosophy

The University of Leeds
School of Geography

September 2017

The candidate confirms that the work submitted is his/her own, except where work which has formed part of jointly-authored publications has been included. The contribution of the candidate and the other authors to this work has been explicitly indicated below. The candidate confirms that appropriate credit has been given within the thesis where reference has been made to the work of others.

The work in Chapter three of the thesis has appeared in publication as follows:

> Watson, C.S. Quincey, D.J. Carrivick, J.L. and Smith, M.W. 2016. The dynamics of supraglacial ponds in the Everest region, central Himalaya. *Global and Planetary Change.* **142**, 14-27.
>
> DOI: 10.1016/j.gloplacha.2016.04.008
>
> CSW was responsible for the study design, data analysis, preparation of figures, and writing the manuscript. All other authors contributed to the study design, and commented on draft manuscripts.

The work in Chapter four of the thesis has appeared in publication as follows:

> Watson, C.S. Quincey, D.J. Carrivick, J.L. and Smith, M.W. Rowan, A.V, and Richardson, R. 2017. Heterogeneous water storage and thermal regime of supraglacial ponds on debris-covered glaciers. *Earth Surface Processes and Landforms*.
>
> DOI: 10.1002/esp.4236
>
> CSW was responsible for the study design, data analysis, preparation of figures, and writing the manuscript. All other authors contributed to the study design, and commented on draft manuscripts. The unmanned surface vessel used in this study was designed under the supervision of RR and Shaun Whitehead by a team of Masters students at the University of Leeds.

The work in Chapter five of the thesis has appeared in publication as follows:

> Watson, C.S. Quincey, D.J. Carrivick, J.L. and Smith, M.W. 2017. Ice cliff dynamics in the Everest region of the Central Himalaya. *Geomorphology.* **278**, 238-251.
>
> DOI: 10.1016/j.geomorph.2016.11.017
>
> CSW was responsible for the study design, data analysis, preparation of figures, and writing the manuscript. All other authors contributed to the study design, and commented on draft manuscripts. DQ derived the glacier velocity data.

The work in Chapter six of the thesis has appeared in publication as follows

> Watson, C.S. Quincey, D.J. Smith, M.W. Carrivick, J.L. Rowan, A.V. and James, M. 2017. Quantifying ice cliff evolution with multi-temporal point clouds on the debris-covered Khumbu Glacier, Nepal. *Journal of Glaciology*.
>
> DOI: 10.1017/jog.2017.47
>
> CSW was responsible for the study design, data analysis and interpretation, and writing the manuscript. All other authors contributed to the study design, and commented on draft manuscripts.

Acknowledgements

I am hugely grateful to Duncan Quincey, Jonathan Carrivick, Mark Smith, and Ann Rowan for being the best supervision team I could ever have hoped for. Continued support, regular meetings, great friendship, and your huge range of expertise allowed this project to run seamlessly and be so productive. Thank you also to Ann for inviting me along to several outreach events relating to our work, including a brilliant week at the Royal Society Summer Science Exhibition.

Thanks to my all fellow PhD students for great company, friendship, and our drinking copious amounts of tea. Having a fellow Himalayan Glaciologist (Owen) in the office helped this project along in so many ways. Thanks also to Dave Rounce for the opportunity to work on other collaborative GLOF projects during my PhD. Thanks to Steve Carver, Andy Evans, and colleagues in the River Basin Processes and Management research cluster for feedback on this project as it developed and the loan of equipment.

Dhananjay Regmi and the team at Himalayan Research Expeditions are greatly thanked for enabling fieldwork in Nepal with research permit acquisition, logistical support in the field, and friendly company in Kathmandu. Mahesh Magar is especially thanked for his expert guidance and invaluable field assistance during four trips to Nepal, and hopefully many more to come. The friendliness and hospitality of everyone I met in Nepal during this journey was warming and greatly appreciated.

I am hugely grateful to all the funding organisations that made this work possible including: the University of Leeds, the River Basin Process and Management cluster within the School of Geography, the Mount Everest Foundation, the Royal Geographical Society with IBG, the British Society for Geomorphology, the Petzl Foundation, water@leeds, and Leeds For Life.

Wojciech Marcinek, Daniel Hicks, Adil Tahir, and Charles Howard are thanked for designing and building the unmanned surface vessel (‘BathyBot’) within the School of Mechanical Engineering at the University of Leeds, and Robert Richardson and Shaun Whitehead for their guidance on the USV project.

A final and enormous thankyou to my family and friends for continued support.

Abstract

The widespread negative mass balance of debris-covered glaciers in the central Himalaya is expressed through, and influenced by, glacier surface morphology, including the spatio-temporal dynamics of supraglacial ponds and ice cliffs. These features form a relatively unknown component of the overall melt budget but are thought to be key contributors to a debris-cover anomaly, whereby the insulating effect of debris is offset by enhanced melt at supraglacial ponds and ice cliffs. In this thesis we revealed the role of ice cliff evolution and supraglacial pond dynamics at seasonal to annual timescales using extensive fieldwork and assessments of remotely sensed satellite imagery from the Everest region of Nepal.

Supraglacial pond dynamics were assessed over the last decade using multi-temporal fine-resolution satellite imagery (~0.5−2 m), revealing a net increase in pond area but large inter-annual and seasonal variability. Coalescing and persistent ponds on Khumbu Glacier suggested that a trajectory towards large lake development was underway. Additionally, we revealed that the size distribution of ponds on debris-covered glaciers potentially leads to large classification omissions in studies using medium-resolution (e.g. 30 m) satellite imagery, on the order of 15–88% of ponded area. Instrumentation of ponds on Khumbu Glacier revealed seasonal expansion and drainage, and water temperatures conducive to englacial ablation. We surveyed 24 ponds with an unmanned surface vessel to derive their bathymetry and an empirical area-volume relationship, which can now be used to predict glacier-scale water storage fluxes.

A remote sensing assessment of ice cliffs revealed that on average 49% of cliffs were associated with a supraglacial pond, and that cliff density was positively correlated with glacier mass loss. We presented the first application of 3D point cloud differencing to multi-temporal ice cliff point clouds to quantify the magnitude and spatio-temporal variation in cliff retreat, and revealed the role of ponds and local topography on controlling cliff persistence. We observed mean retreat rates of 0.30–1.49 cm d^{-1} during the winter interval (November 2015–May 2016) and 0.74–5.18 cm d^{-1} during the summer (May 2016–October 2016). Overall, by coupling remote sensing and field-based observations we produced a holistic assessment of ice cliffs and supraglacial ponds. This assessment has improved our process-based understanding of debris-covered glacier evolution and has provided the foundations for better consideration of surface processes in studies modelling glacier evolution.

Table of Contents

List of Tables

List of Figures

List of Abbreviations

ASTER	-	Advanced Spaceborne Thermal Emission and Reflection Radiometer
AVNIR	-	Advanced Visible and Near Infrared Radiometer
DEM	-	Digital elevation model
dGPS	-	Differential global positioning system
GIS	-	Geographic Information System
GLOF	-	Glacial lake outburst flood
GLONASS	-	GLObal NAvigation Satellite System
GNSS	-	Global navigation satellite system
GPS	-	Global positioning system
M3C2	-	Multiscale Model to Model Cloud Comparison
NDWI	-	Normalised Difference Water Index
OBIA	-	Object based image analysis
SfM-MVS	-	Structure from Motion with Multi-View Stereo
SPOT	-	Satellites Pour l'Observation de la Terre
SRTM	-	Shuttle Radar Topography Mission
UAV	-	Unmanned aerial vehicle
USV	-	Unmanned surface vessel

Chapter 1
Introduction

1.1 Introduction

Contemporary deglaciation is a global trend (Zemp et al., 2015; Solomina et al., 2016), which is causing sea level rise (Meier et al., 2007; Radic and Hock, 2011; Gardner et al., 2013; Radić et al., 2014), changing hydrological cycles (Immerzeel et al., 2010; Bliss et al., 2014; Lutz et al., 2014; Pritchard, 2017), and raising socio-economic concerns over water availability and the development of potentially hazardous glacial lakes (Richardson and Reynolds, 2000; Carrivick and Tweed, 2013; Emmer and Vilímek, 2013; Carrivick and Tweed, 2016; Schwanghart et al., 2016). These concerns are particularly pertinent for debris-covered glaciers in the central and eastern Himalaya, which are undergoing rapid mass loss (Bolch et al., 2011; Bolch et al., 2012; Kääb et al., 2012; Nuimura et al., 2012; Kääb et al., 2015).

Regional mass balance trends in the Himalaya broadly reflect the dominance of two contrasting precipitation regimes. The Indian Monsoon brings summer precipitation to the central and eastern Himalaya, whereas a westerly circulation brings winter precipitation in the west (Armstrong, 2010). These climates create a distinct contrast between thinning glaciers in the central and eastern Himalaya, compared to stability and instances of glacier advance observed in the Karakoram over the last decade (Gardelle et al., 2012; Kääb et al., 2012; Gardelle et al., 2013; Vincent et al., 2013). Additionally, observations of comparable thinning rates between clean-ice and debris-covered glaciers (referred to as the 'debris-covered glacier anomaly'), suggests mass loss at ice cliffs and supraglacial ponds on stagnating glacier tongues may offset the insulating effect of a thick debris-layer (Kääb et al., 2012; Nuimura et al., 2012; Gardelle et al., 2013). However, other studies have shown that this is not always the case, since the extent of ponds and cliffs is variable (Ragettli et al., 2016; Vincent et al., 2016). Nonetheless, the role of glacier surface morphology in driving glacier mass loss is still poorly understood, especially surrounding the presence of ice cliffs and supraglacial ponds, which appear as 'hot-spots' of mass loss in assessments of glacier surface elevation change using fine spatio-temporal resolution data (Immerzeel et al., 2014; Pellicciotti et al., 2015; Thompson et al., 2016). The spatio-temporal dynamics and associated feedbacks of these surface features are not explicitly accounted for in models projecting glacier mass loss over the coming decades (e.g. Shea et al., 2015, Rowan et al., 2015). However, it is apparent that coalescing ponds on debris-covered glaciers can promote large lake development and rapid glacier terminus retreat under

a calving regime (e.g. Thakuri et al., 2016). In this thesis I refer to water bodies on the surface of a glacier ≤20,000 m^2 as supraglacial ponds, and those >20,000 m^2 as supraglacial lakes, although there is no clear distinction in the literature. Glacial lakes are referred to by names where available and may be supraglacial or proglacial.

The ablative role of ice cliffs and supraglacial ponds on debris-covered glaciers has long been investigated on a local-scale (e.g. Inoue and Yoshida, 1980; Sakai et al., 1998; Sakai et al., 2000; Benn et al., 2001; Sakai et al., 2002; Thompson et al., 2012). However, multi-glacier, fine spatio-temporal resolution observations are now becoming possible with recent advances in the technology and datasets available to the scientific community. These advances include access to fine-resolution satellite imagery, and the emergence of Structure from Motion with Multi-View Stereo (SfM-MVS) as a technique to develop centimetre resolution digital elevation models (DEMs) and orthomosaics (James and Robson, 2012; Westoby et al., 2012; Smith et al., 2015). Satellite imagery and field-based topographic surveys can be coupled to investigate glacier dynamics at a range of spatio-temporal scales (e.g. Vincent et al., 2016), which is essential if the roles of debris-cover, ice cliffs, and supraglacial ponds for glacier mass loss are to be parameterised in glaciological models.

This thesis focuses on the recent advances in the understanding the surface dynamics of debris-covered glaciers including assessments of supraglacial ponds and ice cliffs. Specifically, it focuses on the utility of fine spatio-temporal resolution satellite imagery and field–based techniques to improve our process-based understanding of how debris-covered glaciers are evolving in the Everest region of Nepal.

1.2 Debris covered glacier evolution

Debris is typically sourced from rock fall avalanches linked to steep accumulation areas (Scherler et al., 2011; Hambrey et al., 2008) or from moraine ridge collapses, and is typically transported englacially before emerging in the ablation zone. Therefore, debris thickness typically increases towards glacier termini (Nakawo et al., 1986; Rounce and McKinney, 2014; Rowan et al., 2015). In the Everest region, glaciers descend some of the highest peaks on earth, and ~32 % of the glacierised area is debris-covered (Thakuri et al., 2014).

Maximum ablation occurs at a critical debris thickness of typically several centimetres; however, above this threshold the ice beneath becomes increasingly insulated and hence ablation is reduced (Östrem, 1959; Mattson et al., 1993; Nakawo and Young, 1982; Nicholson and Benn, 2006). Therefore, the highest rates of surface lowering are found in the mid-ablation zone of debris-covered glaciers where debris cover is thinner. A positive feedback between spatially variable mass loss, glacier stagnation,

and surface ponding of meltwater, can be initiated in response to an initial climatic signal of warming and precipitation decrease, which is described by Benn et al. (2012) and summarised here. Increased mass loss and reduced ice flux in the mid-ablation zone, where debris is thinner, reduces the glacier gradient and promotes stagnation (e.g. Quincey et al., 2009). Surface water can increasingly pond on the low-gradient and low-velocity surface, which absorbs solar radiation and further enhances mass loss. Finally, a trajectory towards lake development starts where ponds at the hydrological base-level are bound by a terminal moraine and drainage is restricted. Ponds then coalesce and expand up-glacier (Reynolds, 2000; Hambrey et al., 2008).

1.3 Supraglacial ponds

Supraglacial ponds are variable in shape, size, temperature, turbidity, and hydrological connectivity (Takeuchi and Kohshima, 2000; Wessels et al., 2002) (Figure 1.1). Before reaching the hydrological base level, ponds are often ephemeral and drain upon interception with an englacial conduit (Benn et al., 2012), transferring their thermal energy englacially (Sakai et al., 2000; Miles et al., 2016a). The enlargement and collapse of englacial conduits is thought to drive the formation of new depressions and ice cliff exposures (Kirkbride, 1993). Fine-resolution DEMs of difference have revealed an association between supraglacial ponds and ice cliffs and high rates of surface lowering on debris-covered glaciers (Immerzeel et al., 2014; Ragettli et al., 2016; Thompson et al., 2016). However, pond instrumentation with temperature and water level sensors, and bathymetric surveys are rare, which has previously limited studies aimed at quantifying their potential ablative role to point-based and single-period assessments (e.g. Sakai et al., 2000; Xin et al., 2012; Horodyskyj, 2015; Miles et al., 2016a; Narama et al., 2017).

Supraglacial ponds can coalesce into larger moraine-dammed lakes (e.g. Rohl, 2008; Basnett et al., 2013; Qiao et al., 2015), associated with low glacier surface gradients of typically less than 2°, and terminus stagnation (Reynolds, 2000; Quincey et al., 2007; Salerno et al., 2012). Monitoring their areal extent, and how it changes seasonally, is therefore important, as it may provide an early indication of an evolutionary trajectory towards large glacial lake development. Currently little is known about the spatio-temporal distribution of ponds; however, recent studies have revealed their seasonal expansion during the Indian Summer Monsoon (Miles et al., 2016b; Narama et al., 2017), which is also the ablation season for these glaciers. Similarly, their volumetric capacity remains unknown, since published bathymetry data are generally only collected for larger (often proglacial) glacial lakes (e.g. Benn et al., 2001; Thompson et al., 2012; Cook and Quincey, 2015). Therefore, seasonal

meltwater fluxes and surface water storage remains to be quantified, yet these are key indicators and drivers of future glacier evolution.

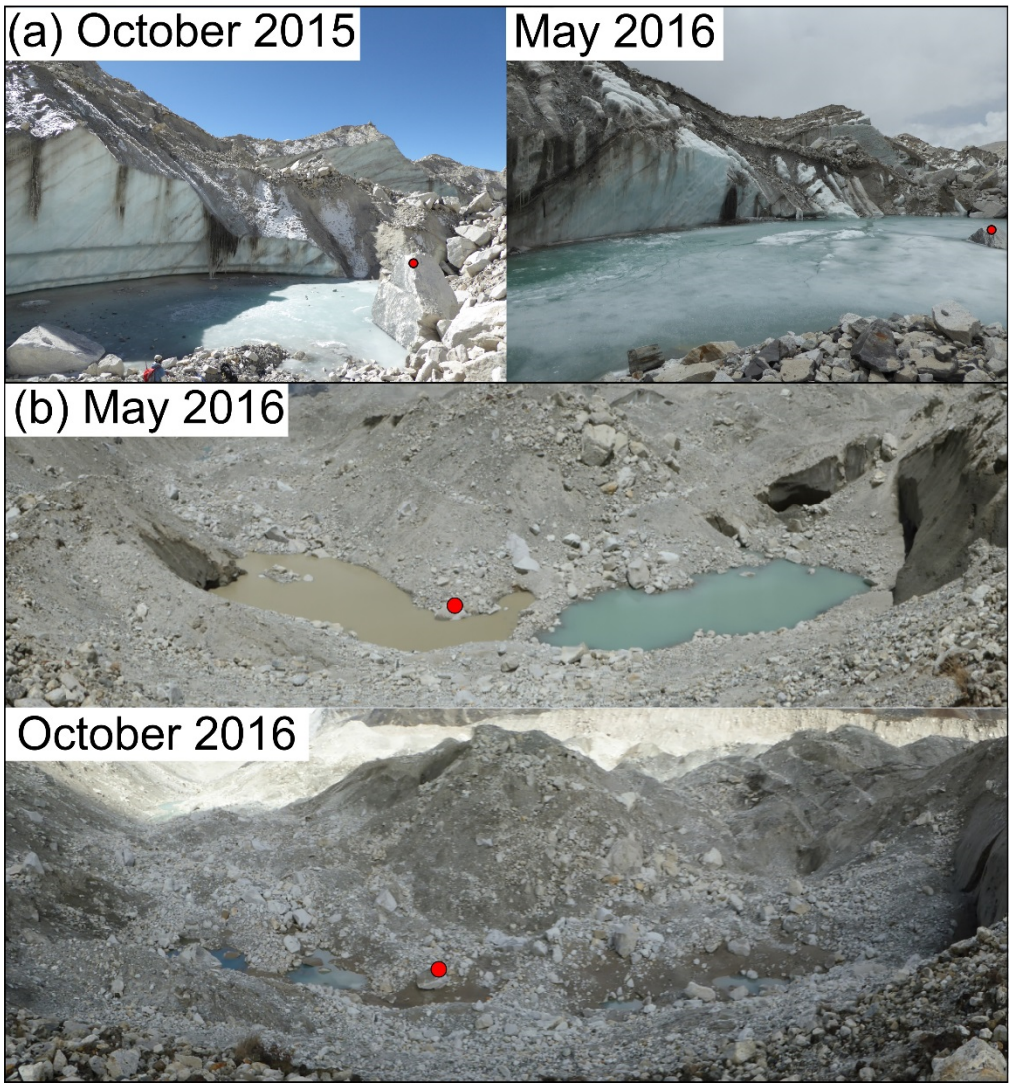

Figure 1.1. Short-term supraglacial pond growth and drainage on Khumbu Glacier. (a) Water level increase Oct−May to the level of a previous undercut notch. (b) Contrasting pond turbidity and pond drainage May−Oct. Red markers indicate coincident features.

1.3.1 Remote sensing of supraglacial ponds

Supraglacial ponds and glacial lakes can be delineated using remotely sensed imagery, either manually (e.g. Salerno et al., 2012; Zhang et al., 2015), or semi-automatically. Semi-automatic approaches include application of the Normalised Difference Water Index (NDWI) to multi-spectral imagery such as Landsat, Advanced Spaceborne Thermal Emission and Reflection Radiometer (ASTER), or Satellites

Pour l'Observation de la Terre (SPOT) (e.g. Huggel et al., 2002; Gardelle et al., 2011; Nie et al., 2013), or the use of object based image analysis (OBIA).

The NDWI requires the determination of an imagery-dependant threshold, which is applied to a band ratio calculation exploiting low water reflectance in the near- or shortwave-infrared spectral region and maximum reflectance in the blue or green spectral region (Huggel et al., 2002; Ji, 2009) (e.g. Equation 1.1).

$$NDWI = \frac{(Band_{NIR} - Band_{Blue})}{(Band_{NIR} + Band_{Blue})} \quad (1.1)$$

Using a NDWI, water can be distinguished from surrounding snow and ice or debris cover on a regional scale. Misclassifications arising from topographic shadows can be reduced by using shadow and slope masks derived from a digital elevation model (DEM) (Chen et al., 2013). However, classification accuracy is also dependent upon sensor resolution and the inclusion of mixed pixels, which may comprise reflectance from water as well as surrounding debris-cover along the pond boundary. Selecting a broad NDWI threshold, which incorporates mixed pixels (e.g. Gardelle et al., 2011) is necessary to classify smaller supraglacial ponds using medium-resolution imagery and to account for the transition between water and debris-cover (Figure 1.2). At the scale of an individual pond, this is likely to lead to over- or under-estimation of the true pond area, or the omission of ponds smaller than the sensor's resolution (i.e. one pixel). Additionally, pixel-based analyses often exhibit high local variability in spectral reflectance due to the presence of mixed pixels, which creates high-frequency (salt and pepper) noise. In contrast, OBIA groups clusters of pixels in remotely sensed imagery into near homogenous objects, and can therefore improve boundary detection of supraglacial ponds on debris-covered glaciers (Nie et al., 2013; Liu et al., 2015; Kraaijenbrink et al., 2016).

When using medium-resolution imagery, greater certainty of water detection can be obtained if the minimum mapping threshold is several pixels in size, such that the water body is sufficiently distinguishable from the surrounding terrain. Therefore, minimum mapping thresholds of 3600 m^2 and 8100 m^2 were used by Gardelle et al. (2011) and Nie et al. (2013) respectively, which represented four and nine 30 m Landsat pixels. Additionally, half or one pixel uncertainty is commonly assumed around the perimeter of each pond or lake (Fujita et al., 2009; Gardelle et al., 2011; Salerno et al., 2012; Liu et al., 2015), therefore larger lakes exhibit lower uncertainty in their areal delineation since their perimeter to area ratio is lower. However, the proportion of supraglacial ponds falling below the minimum mapping threshold on Himalayan debris-covered glaciers was not assessed by previous studies. Hence it is

not known if medium-resolution imagery can adequately delineate the size-distribution of ponds found on debris-covered glaciers.

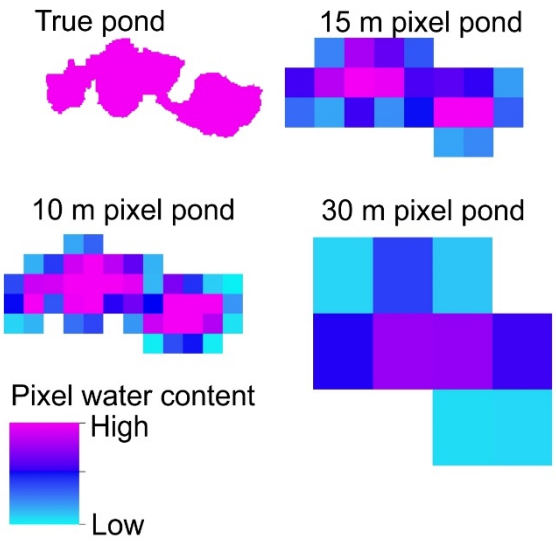

Figure 1.2. Implications of sensor resolution and mixed pixels on the delineation of a supraglacial pond.

1.4 Ice cliffs

Ice cliffs form on debris-covered glaciers through the exposure of glacier ice by localised debris slumping; exposure of ice at the margins of supraglacial lakes; or the collapse of englacial conduit roofs, which also allows supraglacial pond development in the resultant depression (Kirkbride, 1993; Sakai et al., 2000; Benn et al., 2001; Benn et al., 2012). Cliffs range from several to tens of meters high and act as hot-spots of mass loss on debris-covered glaciers (Inoue and Yoshida, 1980; Sakai et al., 1998; Benn et al., 2001; Han et al., 2010; Ragettli et al., 2016; Thompson et al., 2016). Despite the small areal coverage of ice cliffs, estimates of their contribution to glacier-scale mass loss are often substantial, but highly variable (Table 1.1). Similar to supraglacial ponds, ice cliffs are transient features; however, cliff formation and persistence at a glacier-scale has received little attention since field-based access is often difficult.

Table 1.1. Glacier-scale contribution of ice cliffs to Himalayan glacier-scale mass loss

Glacier location and reference	Cliff coverage (%)	Cliff ablation contribution in debris-covered ablation zones
Lirung Glacier, Nepal Buri et al. (2016a)	0.19 (four ice cliffs selected for study)	3.25% of total modelled mass loss
Ngozumpa Glacier, Nepal Thompson et al. (2016)	~5	40% of volume loss over the stagnant zone of the glacier tongue from DEM differencing
Lirung Glacier, Nepal Buri et al. (2016b)	0.09 (two ice cliffs selected for study)	1.23% of total modelled mass loss
Lirung Glacier, Nepal Sakai et al. (2002)	~1.8	20% of total modelled mass loss
Lirung Glacier, Nepal Sakai et al. (1998)	~1.8	69% of total modelled mass loss

Ice cliff retreat rate is primarily governed by shortwave radiation receipt for smaller ice cliffs (Sakai et al., 2002), but calving retreat was observed to dominate on cliffs over ~15 m in height on the Ngozumpa Glacier where cliffs bordered supraglacial ponds (Benn et al., 2001; Thompson et al., 2012). This is similar to a calving front at lake terminating glaciers (e.g. Kirkbride and Warren, 1997). The variable morphology of cliff faces, including slope, aspect, height, debris-cover, and meltwater runnel formation, probably leads to heterogeneous melt across the cliff face. However, spatio-temporal variation in ice cliff melt and the formation and longevity of cliffs is unknown. Fine-resolution multi-temporal satellite imagery and field-surveying techniques such as SfM-MVS offer new opportunities for such research.

The transition of ice cliffs from a melting to calving regime is indicative of rapid lake expansion (Kirkbride, 1993), since ice cliff retreat rates increase from the order of several meters per year to tens of meters per year (Benn et al., 2001). Kirkbride and Warren (1997) described four categories of ice cliff calving: waterline calving, which are frequent but small events occurring close to the waterline and remove several cubic metres of ice; flake calving from the cliff face, removing larger quantities of ice; full-height slab calving, which occurs less frequently than flake calving but involves the detachment of large volumes of ice through the development of crevasses at the cliff top; and subaqueous calving, where a submerged ice foot develops below the zone of greatest undercutting, which may subsequently become detached. On Ngozumpa

Glacier, all full-height slab calving observed by Benn et al. (2001) occurred on cliffs over 15 m high. On the Lirung Glacier, Sakai et al. (2009) observed calving events where ice cliffs were associated with lakes with an ~80 m fetch. However, their dataset was insufficient to determine the precise fetch that initiated calving events. As supraglacial ponds coalesce and persist the conditions for ice cliff retreat by calving become more favourable, therefore studying cliff–pond interactions is becoming increasingly pertinent.

1.4.1 Remote sensing of ice cliffs

Fine-resolution satellite and unmanned aerial vehicle (UAV) imagery offers new opportunities to conduct remotely sensed ice cliff analyses with DEM differencing (Immerzeel et al., 2014; Thompson et al., 2016); by analysing their morphology and spatial distribution (Kraaijenbrink et al., 2016); and quantifying their evolution and role for glacier mass loss (Brun et al., 2016; Buri et al., 2016a). 3D topographic datasets derived from UAV or terrestrial surveys are particularly important to quantify even basic ice cliff characteristics such as area, since cliffs are often near-vertical and include overhanging sections undercut by supraglacial ponds. Traditional DEMs cannot represent overhanging topography and are also poor representations of steep-slope topography (Kolecka, 2012), therefore recent studies have transitioned towards quantifying ice cliff evolution in 3D (e.g. Brun et al., 2016).

1.5 Study region

1.5.1 Everest region

This thesis addresses debris-covered glacier change in the Everest region, but in the context of widespread Himalayan deglaciation. The Everest region encompasses glaciers in the vicinity of Mount Everest including those in both Nepal and China (Tibet) (Figure 1.3). Due to the influence of the Indian Summer Monsoon, which occurs June−September, ~80% of annual precipitation is delivered during these months (Bookhagen and Burbank, 2006; Wagnon et al., 2013). Observations of decreased precipitation due to a weakening of the monsoon (Yao et al., 2012; Salerno et al., 2015) has reduced the replenishment of glacier ice at higher elevations, which would otherwise replace mass loss in the lower ablation zone. Subsequently, glaciers are stagnating and exhibit a spatial trend of mass loss conducive to the development of surface ponds and ultimately large glacial lakes (Reynolds, 2000; Quincey et al., 2009; Benn et al., 2012). The development and potential downstream impacts of these lakes are therefore receiving increased attention (Somos-Valenzuela et al., 2014a; Rounce et al., 2016; Rounce et al., 2017).

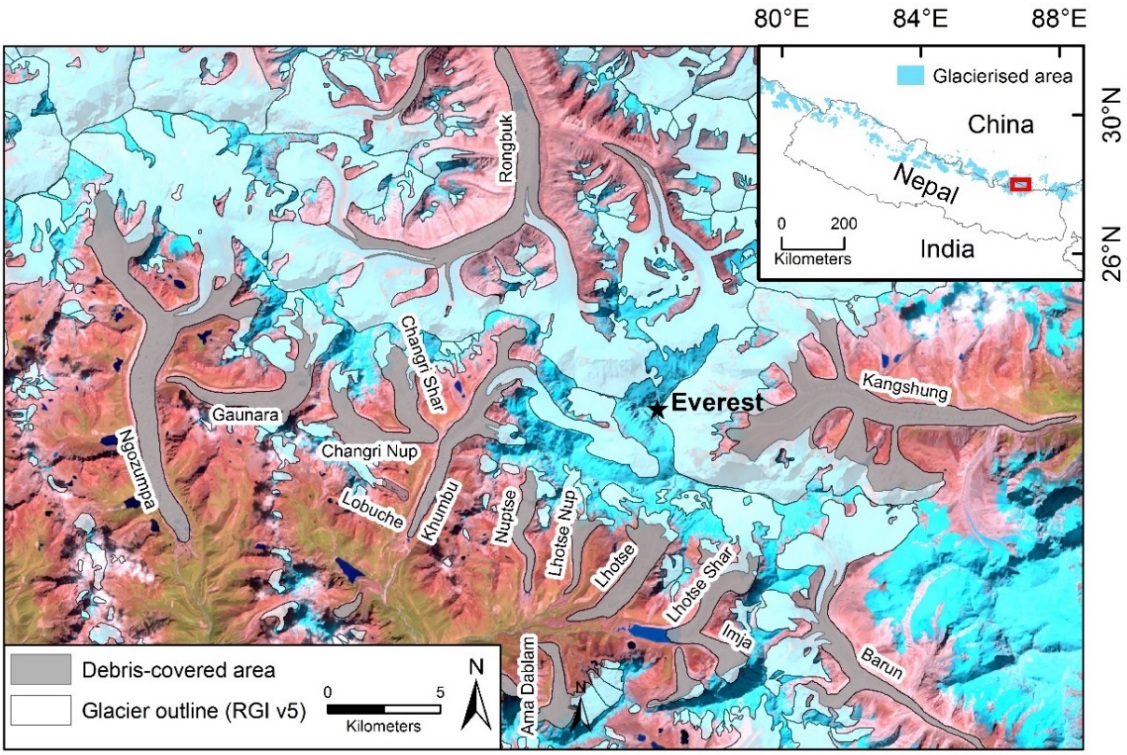

Figure 1.3. Glaciers in the Everest region spanning Nepal and China (Tibet). Backdrop is a Landsat image (band combination of 7, 5, and 4). Glaciers studied in this thesis are labelled.

The glaciers in the Everest region are heavily debris-covered in the lower ablation area, which is sourced from rock fall avalanches and moraine collapse (Hambrey et al., 2008). Debris-thickness typically increases towards the terminus and can exceed several metres in depth (Nakawo et al., 1986; Nicholson and Benn, 2013), which effectively insulates the ice beneath. The surfaces of these glaciers are pitted with supraglacial ponds and ice cliffs, which breaks up the debris continuum (Iwata, 1980) (Figure 1.4).

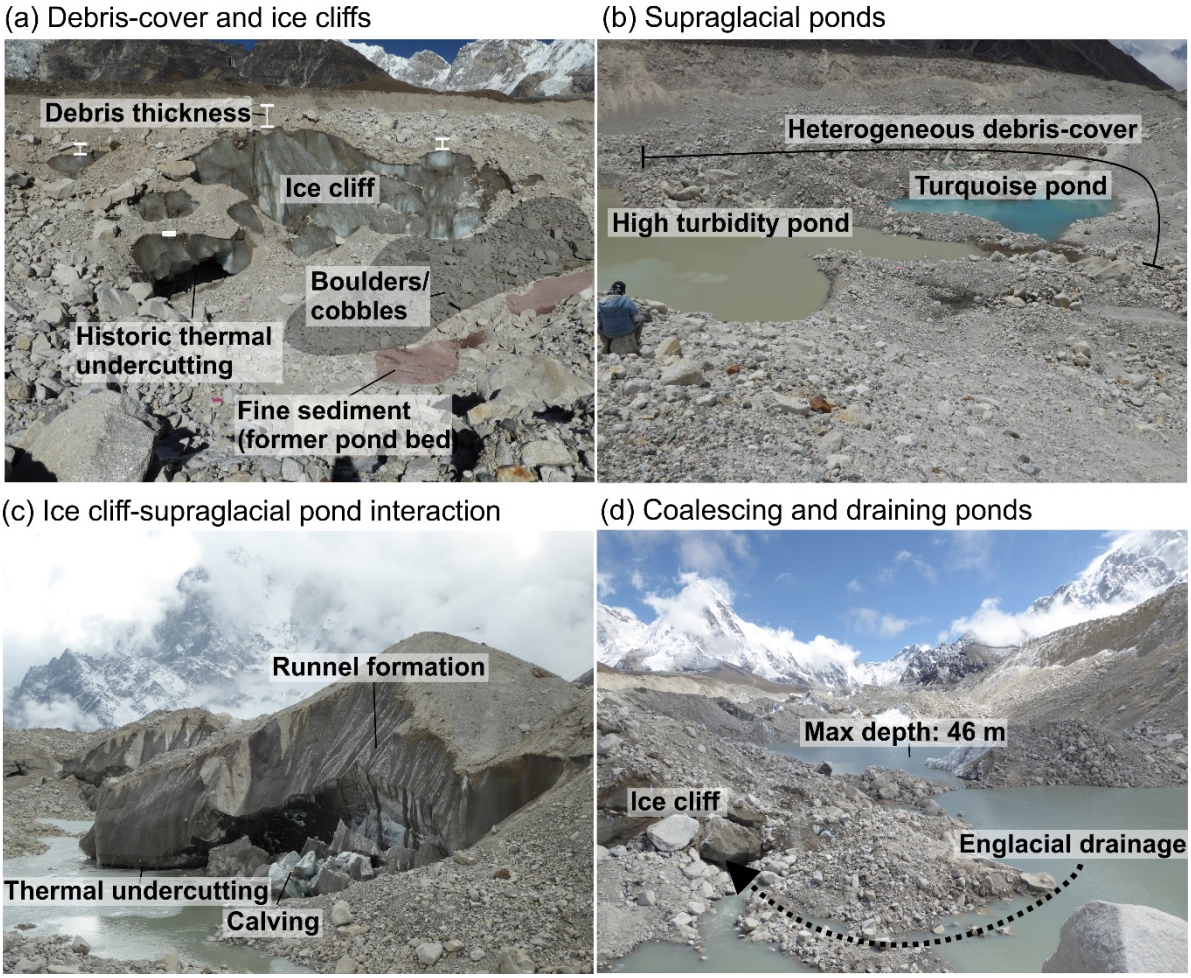

Figure 1.4. Typical surface morphology of Himalayan debris-covered glaciers. Panels (a−d) are from Khumbu Glacier.

In this thesis, I used remotely sensed satellite imagery to study glaciers in the Everest region, and field analyses were undertaken on the Khumbu and Lobuche Glaciers. Khumbu Glacier was the primary field site of interest; however, supraglacial ponds were opportunistically surveyed on Lobuche Glacier in May 2016. Khumbu Glacier is ~17 km long, of which ~10 km is debris-covered, whereas Lobuche Glacier has a debris-covered ablation zone ~1 km in length that is now disconnected from the clean ice at higher elevations. The lower ~4 km of Khumbu Glacier is essentially stagnant (Quincey et al., 2009; Haritashya et al., 2015) and is expected to develop a glacial lake in coming decades (Naito et al., 2000; Bolch et al., 2011). Lake development on Khumbu Glacier would likely follow the pattern observed on Imja Glacier, where supraglacial ponds began to coalesce in the 1950s and had formed a lake by 1975 (Watanabe et al., 1994), which is now over 2.4 km in length. The water level of Imja Lake was reportedly lowered by 3 m in 2016 with the intention of reducing the glacial lake outburst flood (GLOF) risk. Additionally, a large lake is forming on the terminus of Ngozumpa Glacier as ice cliffs retreat and the lake expands, which has the potential to extend ~5−6 km up-glacier (Thompson et al., 2012).

1.5.2 Implications of lake growth

The GLOF risk posed by lake expansion exists on both sides of the Himalayan divide (Nie et al., 2013); however, the greatest exposure is for the more populated south where investment in hydropower developments represent an additional vulnerability (Richardson and Reynolds, 2000; Pritchard, 2017). The nature of GLOF hazard development is dependent on local catchment characteristics, which determine the incidence of triggers and propensity for dam breach, such as ice avalanches or rockfalls in the vicinity of a lake; glacier dynamics, including potential calving activity into the lake; lake characteristics, including the size of lake, expansion rate, existing drainage, dam stability, and dam geometry; and regional influences, such as tectonic activity or extreme precipitation events (Huggel et al., 2002; Westoby et al., 2014; Rounce et al., 2016). Here, the source to impact process chain comprising a GLOF event requires consideration when assessing the likelihood of a breach and the downstream implications (Westoby et al., 2014; Worni et al., 2014).

Within Nepal, 20 potentially dangerous glacial lakes (PDGLs) were identified by Mool et al. (2001), which was revised to 21 following an investigation in 2010 by ICIMOD (2011). Six lakes were classified as high priority, requiring extensive field investigation and monitoring, including Imja Tsho in the Everest Region (ICIMOD, 2011). The Dudh Koshi basin, which incorporates the Everest region of Nepal, includes ~10 PDGLs and the area of moraine-dammed lakes is increasing following glacier recession (Bajracharya and Mool, 2009). Hydraulic and GIS-based modelling studies have revealed notable downstream vulnerability in the region (e.g. Bajracharya et al., 2007; ICIMOD, 2011; Rounce et al., 2016), primarily due to the presence of settlements and agricultural land within close proximity to river channels. The financial capacity to address the GLOF hazard in Nepal is limited, hence external monitoring and mitigation assistance is required (Kattelmann, 2003). However, co-operation and engagement from local communities is essential to reduce social vulnerability (ICIMOD, 2011).

The expansion and potential GLOF risk posed by Imja Lake, located in the Sagmartha National Park, has received significant attention (Bajracharya et al., 2007; Fujita et al., 2009; ICIMOD, 2011; Somos-Valenzuela et al., 2014a), including spatially distributed consideration of water properties (Chikita et al., 2000), and local topography (Chikita, 2007) as drivers of lake expansion. Between 2002 and 2012, the lake volume increased by 25.9 million m^3 and the depth by ~26 m, with most of the expansion attributable to recession of the adjacent glacier terminus (Somos-Valenzuela et al., 2014b).

Hydropower represents a large but underutilised renewable energy resource in Nepal, although the developed capacity is increasing rapidly (Surendra et al., 2011; Sharma

and Awal, 2013; Pritchard, 2017). A similar trend is apparent in Bhutan where future hydropower investments will increase the already notable share of GDP (~22%) derived from hydropower (NEC, 2009). The Dig Tsho outburst of 1985 destroyed a small hydropower plant in Nepal and also damaged agricultural land, which represents a sparse resource in high relief valleys (Vuichard and Zimmermann, 1987). The existence of potentially dangerous glacial lakes in the Everest region and the exposure of downstream communities makes monitoring lake development highly pertinent under climate warming, especially where lake expansion could increase lake susceptibility to mass movement events (Rounce et al., 2016).

1.6 Aim and objectives

Aim:

To quantify supraglacial pond and ice cliff dynamics and to investigate the processes that control them on debris–covered glaciers in the Everest region of Nepal and Tibet.

Objectives:

1. To assess supraglacial pond characteristics and development using remotely sensed imagery, pond bathymetry, and field-based monitoring.
2. To identify glacier-scale ice cliff characteristics in the Everest region and coupling with supraglacial ponds.
3. To quantify spatio-temporal controls on ice cliff retreat and persistence using multi-temporal Structure-from-Motion (SfM) surveys.

The research questions and methods used to address the aims and objectives of this thesis are summarised in Table 1.2.

Table 1.2. Research questions addressed in this thesis

Theme	Research question	Strategy
Long-term supraglacial pond dynamics (Chapter 3)	Is supraglacial water storage increasing on glaciers in the Everest region and what are the implications of using fine-resolution satellite imagery to monitor water storage? Is moderate resolution satellite imagery (e.g. Landsat) suitable for delineating the size range of	Use fine-resolution satellite imagery to delineate supraglacial ponds. Assess the spatio-temporal distribution of ponds.

Theme	Research question	Strategy
	supraglacial ponds that occur on debris-covered glaciers? Do ponds exhibit seasonal expansion and drainage related to the onset and end of the summer ablation season? Does a multi-temporal analysis of fine-resolution satellite imagery suggest that Khumbu Glacier is on a trajectory towards large glacial lake development (e.g. following the trend of Imja Lake)?	
Short-term supraglacial pond dynamics (Chapter 4)	What is the magnitude of seasonal expansion and drainage of ponds and are these changes gradual (e.g. occurring over several months), or abrupt? What is the englacial ablation potential of draining ponds and how does this vary for ponds with and without ice cliffs present? Is there a relationship between pond area and volume, similar to the one identified for larger (typically proglacial) lakes by Cook and Quincey (2015)? Is there a difference between the bathymetry of ponds with and without ice cliffs that would suggest ice cliffs are associated with pond deepening?	Instrument supraglacial ponds with temperature sensors and pressure transducers. Conduct bathymetric surveys of supraglacial ponds with and without ice cliffs.
Spatio-temporal ice cliff	What is the spatial distribution of ice cliffs across debris-covered glaciers and do ice cliffs occur preferentially	Use fine-resolution satellite imagery to delineate ice cliffs

Theme	Research question	Strategy
characteristics (Chapter 5)	in areas of active or inactive glacier flow? Do ice cliffs evolve towards common aspect in response to differential solar radiation receipt and does this depend on glacier flow direction? What is the proportion of ice cliffs associated with supraglacial ponds? Is ice cliff density correlated with glacier surface lowering, since they are hypothesised to be 'hot-spots' of melt?	and supraglacial ponds. Assess their spatio-temporal distribution considering glacier velocity, debris-thickness, and glacier surface lowering.
Ice cliff retreat and persistence (Chapter 6)	How fast do ice cliffs retreat on Khumbu Glacier and how does this compare to previous measurements of retreat on other debris-covered glaciers? Is ice cliff retreat variable across individual cliff faces, which would otherwise be missed by point-based ablation stake measurements? What are the factors controlling ice cliff persistence and hence the considerations for parameterising ice cliff evolution in dynamic glacier models?	Conduct photographic surveys of ice cliffs on Khumbu Glacier to generate topographic point clouds following a Structure-from-Motion workflow. Difference multi-temporal 3D point clouds to quantify ice cliff retreat. Investigate controls on ice cliff evolution.

Chapter 2
Methods summary

2.1 Supraglacial pond analysis

2.1.1 Satellite remote sensing (Chapter 3)

Supraglacial ponds were delineated using object based image analysis (OBIA) applied to the panchromatic band of fine-resolution imagery (Quickbird, GeoEye and WorldView sensors), and manual digitisation in GoogleEarth. OBIA was used to detect pond boundaries through the aggregation of homogenous pond pixels and produce a polygon representing each pond. These polygons were then manually extracted and adjusted where required. For example, floating ice required multiple polygons to be merged, and ponds in the shadow of ice cliffs occasionally required manual correction of the boundary. OBIA does not suffer from the high frequency noise often associated with pixel-based approaches (Nie et al., 2013; Liu et al., 2015), but does require a notably greater time investment. Additionally, it can be used to delineate ponds of variable turbidity, which would otherwise be problematic using a NDWI. High-frequency noise was also apparent when testing a supervised classification approach applied to multi-spectral fine-resolution imagery (Figure 2.1), hence this approach was not pursued.

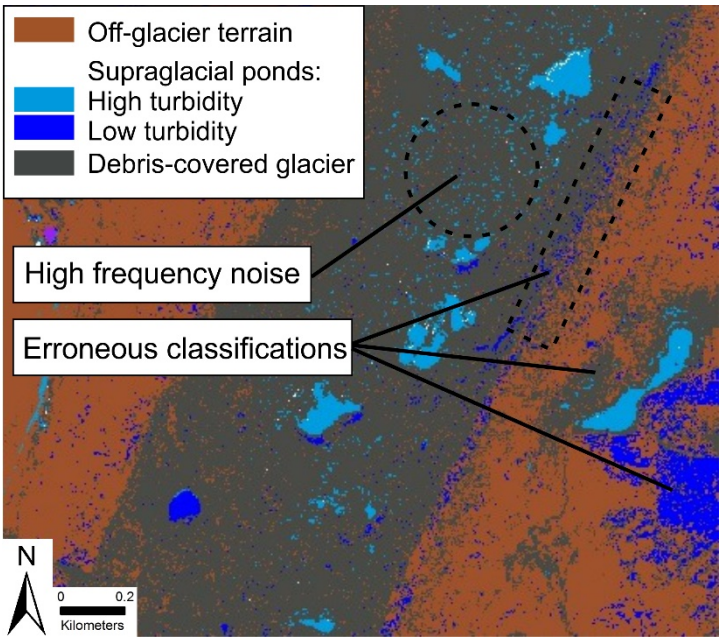

Figure 2.1. A supervised classification of multi-spectral fine-resolution satellite imagery on the lower Khumbu Glacier to delineate supraglacial ponds, debris-cover, and off-glacier terrain.

Spatio-temporal trends in pond presence and area were assessed with distance up-glacier for nine glaciers in the Everest region ~2000−2015 using polygon zones generated at 500 m intervals from the terminus. The frequency of pond occurrence across all images was also derived to reveal areas of pond persistence or drainage. Use of fine-resolution imagery (<2 m) meant that it could be reasonably assumed that the pond datasets represented a near ground-truth of all surface water on the glaciers, and therefore theoretically assess the implications of using medium-resolution imagery (e.g. 30 m Landsat) on pond delineation. The cumulative area of supraglacial ponds at a glacier-scale was therefore assessed with increasing pond size in 300 m^2 bins, to assess potential omissions when using medium-resolution imagery.

2.1.2 Field-based (Chapter 4)

Nine supraglacial ponds were instrumented with temperature sensors (ibutton thermistors DS1922L-F5, number (*n*) = 18) on Khumbu Glacier to monitor their surface and bottom water temperatures for one year (October 2015 to October 2016). Additionally, three were instrumented with Solinst Levelogger Junior Edge pressure transducers to capture water level variation, which were corrected using temperature and air pressure data from a Barologger Edge also deployed on the glacier. All instrumentation was deployed on a rope from an inflatable boat and was weighted with a rock and partially tensioned with a floating buoy. Slack was left in the rope to allow for water level variation, ensuring the sensor was at the surface of each pond.

An unmanned surface vessel (USV) was deployed on 24 supraglacial ponds in May 2016 to derive a bathymetry dataset. The USV was custom-made by a team of MEng students in the School of Mechanical Engineering at the University of Leeds and was equipped to collect georeferenced depth measurements using a single-beam sonar. The USV could safely approach ice cliff faces, which was not possible using a kayak, and was deployed on ponds ranging in size from 39−18744 m^2.

2.2 Ice cliff analysis

2.2.1 Satellite remote sensing (Chapter 5)

Fine-resolution satellite imagery was accessed using GoogleEarth Pro to delineate the top edge of ice cliffs and supraglacial ponds for 14 glaciers in the Everest region, which provided two snap-shots of their distribution during the last decade. I chose to delineate the top edge since the steep slope angle of cliff faces precludes area measurements without corresponding 3D topographic data. The spatial association of a pond with an ice cliff was defined using a 30 m direction buffer from each cliff top edge. This distance was justified considering 30° as the angle of repose for debris and

a cliff height of 15.5 m (a mean observed by Thompson et al. (2016)), which would place a theoretical pond up to 27 m from the top edge of an ice cliff. Additionally, Benn et al. (2001) suggested that a cliff 15 m in height is at the threshold for calving initiation and therefore represents the upper-bound height of a low-gradient cliff face.

Three additional datasets were used to assess spatial trends in ice cliff distribution including glacier velocity, surface lowering (King et al., 2017), and modelled debris-thickness (Rounce and McKinney, 2014). Data availability limited this analysis to a subset of glaciers. Glacier velocity was derived for nine glaciers by feature tracking on a pair of TerraSAR-X images using a cross-correlation algorithm (e.g. Luckman et al., 2007). Glacier surface elevation change data of King et al. (2017) was derived from DEMs of difference between an 8 m DEM generated and distributed by the Polar Geospatial Centre at the University of Minnesota, and the co-registered 30 m resolution 2000 Shuttle Radar Topographic Mission (SRTM) DEM version 3.0. The modelled debris-thickness data of Rounce and McKinney (2014) were derived using an energy balance model and Landsat 7 Enhanced Thematic Mapper Plus (ETM+) satellite imagery (2002 to 2009). Notably this debris-thickness dataset exhibits relative accuracy in thickness values (Rounce and McKinney, 2014); however, the true values of debris over 0.5 m thick were known to be underestimated.

2.2.2 Field-based assessments (Chapter 6)

Nine ice cliffs were surveyed using terrestrial photography during three field campaigns on Khumbu Glacier (October 2015, May 2016, October 2016). High-visibility ground control points (GCPs) (number of GCPs (*n*) = 6–15) were distributed around each cliff and occupied with a Leica GS10 global navigation satellite system (GNSS) for ~5 minutes. Additionally, a GNSS base station was setup on the western lateral moraine of Khumbu Glacier. During each survey 122−564 photographs were taken of each cliff and the surrounding topography, with GCPs in situ.

Following each field campaign the GNSS base station data were post-processed against the Syangboche permanent station (27.8142 N, 86.7125 E) located ~20 km from the field site using Global Positioning System (GPS) and GLObal NAvigation Satellite System (GLONASS) satellites. Field GCPs were then adjusted against this base station data, leading to a mean 3D positional uncertainty of 3.9 mm across all the GCPs. Each photographic survey was processed in Agisoft 1.2.3 with corresponding GCPs following a Structure-from-Motion with Multiview Stereo (SfM-MVS) workflow to generate a dense point cloud of each cliff (e.g. James and Robson, 2012; Westoby et al., 2012; Smith et al., 2015). Glacier displacement between each field campaign was corrected using identifiable features in each model to co-register the later model to the earlier. Co-registered models were analysed in CloudCompare

using the Multiscale Model to Model Cloud Comparison (M3C2) method, which calculates the 3D distance between two point clouds with a 95 % confidence interval (e.g. Barnhart and Crosby, 2013; Lague et al., 2013; Stumpf et al., 2015). I used these 3D difference models to assess ice cliff evolution and the persistence or decay of the cliffs over the study period.

Chapter 3
The dynamics of supraglacial ponds in the Everest region, central Himalaya

C. Scott Watson, Duncan J. Quincey, Jonathan L. Carrivick, and Mark W. Smith

Published in Global and Planetary Change. 2016. 142: 14−27

DOI: 10.1016/j.gloplacha.2016.04.008

3.1 Abstract

The dynamics of supraglacial pond development in the Everest region are not well constrained at a glacier scale, despite their known importance for meltwater storage, promoting ablation, and transmitting thermal energy englacially during drainage events. Here, we use fine-resolution (~0.5–2 m) satellite imagery to reveal the spatiotemporal dynamics of 9340 supraglacial ponds across nine glaciers in the Everest region, ~2000–2015. Six of our nine study glaciers displayed a net increase in ponded area over their observation periods. However, large inter- and intra-annual changes in ponded area were observed of up to 17% (Khumbu Glacier), and 52% (Ama Dablam) respectively. Additionally, two of the fastest expanding lakes (Spillway and Rongbuk) partially drained over our study period. The Khumbu Glacier is developing a chain of connected ponds in the lower ablation area, which is indicative of a trajectory towards large lake development. We show that use of medium-resolution imagery (e.g. 30 m Landsat) is likely to lead to large classification omissions of supraglacial ponds, on the order of 15–88% of ponded area, and 77–99% of the total number of ponds. Fine-resolution imagery is therefore required if the full spectrum of ponds that exist on the surface of debris-covered glaciers are to be analysed.

3.2 Introduction

The increased storage of meltwater in supraglacial, proglacial and ice-marginal settings is symptomatic of deglaciation and is a globally observed trend (Carrivick and Tweed, 2013). Glacial lake development across the central Himalaya (India, Nepal, Bhutan, Tibet (China)) (e.g. Komori, 2008; Gardelle et al., 2011; Nie et al., 2013; Veettil et al., 2015;Wang et al., 2015; Zhang et al., 2015) corresponds with warming temperatures and a trend of negative glacier mass balance (Kääb et al., 2012). The negative mass balance is well known to be modulated by the variable thickness of debris cover that promotes glacier surface lowering in conjunction with a relatively stable terminus position (Bolch et al., 2011). These mass balance trends and glacier characteristics are well documented in the Everest region (e.g. Bolch et al., 2008a, 2011; Benn et al., 2012; Ye et al., 2015), where surface lowering and increasing glacier stagnation has been highlighted to promote increased supraglacial pond formation and their potential coalescence into larger lakes where a low glacier surface gradient exists (Watanabe et al., 1994; Richardson and Reynolds, 2000; Quincey et al., 2007; Rohl, 2008; Thompson et al., 2012).

Glacier-scale observations of the links between areas of high downwasting and the location of ice cliffs and ponds, further reveal their importance for debris-covered glacier ablation (e.g. Immerzeel et al., 2014; Pellicciotti et al., 2015). Local-scale measurements and modelling of ice cliff retreat (e.g. Reid and Brock, 2014; Steiner et al., 2015) and pond energy balance (e.g. Sakai et al., 2000; Miles et al., 2016) have greatly improved process-based understanding in recent years. These ponds also play an important part in the glacier ablation budget, through the transmission of thermal energy to subaqueous ice and to adjacent ice cliffs (Sakai et al., 2000; Benn et al., 2001; Rohl, 2006; Miles et al., 2016). It may be hypothesised that ponds dynamics will be associated with patterns of glacier surface lowering and ice cliff calving. However, this hypothesis remains to be tested because quantitative measurements have hitherto been spatially limited to individual pond basins (e.g. Benn et al., 2001).

Studies focusing specifically on surface water storage in the Everest region have been regionally aggregated (e.g. Gardelle et al., 2011), glacier or lake specific (e.g. Bolch et al., 2008b; Thompson et al., 2012), or covering one point in time (e.g. Salerno et al., 2012) (Table 3.1). Whilst these approaches are merited, they are often limited by data availability, which has historically tended towards medium-resolution imagery, and data suitability, which cannot be determined without ground-truth or fine-resolution imagery. In the Everest region and across the Himalaya previous studies have generally utilised 30 m resolution multi-spectral Landsat imagery, owing to the large temporal archive and simple band ratio application to delineate water bodies (e.g.

Gardelle et al., 2011; Nie et al., 2013; Bhardwaj et al., 2015; Liu et al., 2015; Wang et al., 2015). ASTER (Advanced Spaceborne Thermal Emission and Reflection Radiometer) imagery (15 m resolution) is also popular for glacier scale applications (e.g. Wessels et al., 2002; Bolch et al., 2008b; Thompson et al., 2012), although the archive is shorter (2000–present day). Both sensors are limited by their spatial resolution, meaning associated studies have not been able to focus on detailed changes in ponds through time. This paper aims to present the first fine resolution spatio-temporal analysis of supraglacial pond dynamics to address this shortcoming. We analyse Google Earth, Quickbird, GeoEye and WorldView imagery (0.7–2 m) covering nine glaciers in the Everest region of the central Himalaya. Our objectives are to: (1) characterise the spatial evolution of supraglacial ponds on an individual glacier scale; (2) quantify short-term seasonal and inter-annual change in supraglacial pond area in the region; and (3) evaluate the implications of using medium-resolution satellite imagery (e.g. 15–30 m) to delineate the full spectrum of pond sizes that exist on Himalayan debris-covered glaciers.

Table 3.1. Remote sensing studies of supraglacial water storage in the Everest region

Reference	Date range	Coverage overlap with this study	Imagery (resolution)	Notes
Iwata et al. (2000)	1978 - 1995	Khumbu Glacier	SPOT (not specified)	A sketch map made with SPOT imagery was compared to that of a field survey in 1978
Wessels et al. (2002)	2000	Ngozumpa, Khumbu and Rongbuk glaciers	ASTER (15 m)	Band ratios were used to delineate water for a single time period. Turbid lakes were found in hydrologically connected regions
Bolch et al. (2008)	1962 - 2005	Khumbu, Lhotse and Imja glaciers	Corona, Landsat, topographic maps, Iknos, ASTER (2 – 79 m)	Normalised Difference Water Index (NDWI) and/ or manual delineation was used to classify water bodies.

Gardelle et al. (2011)	1990 - 2009	All glaciers	Landsat (30 m)	A decision tree was used to classify lakes incorporating the NDWI. A minimum lake size of 3,600 m^2 was used. Area change was not reported for individual glaciers, other than a brief comparison with Bolch et al. (2008). An association between negative mass balance and lake expansion is presented
Salerno et al. (2012)	2008	All except Rongbuk Glacier	AVNIR-2 (10 m)	Water bodies were manually digitised for a single time period
Thompson et al. (2012)	1984 - 2010	Ngozumpa Glacier	Aerial photographs (< 1 m), ASTER (15 m)	A multi-temporal analysis of the expansion of Spillway Lake was conducted using satellite imagery and field surveys
Nie et al. (2013)	1990 - 2010	All glaciers	Landsat (30 m)	OBIA was combined with NDWI-based water detection. Ponded area change was not reported for individual glaciers.
Zhang et al. (2015)	1990 - 2010	All glaciers	Landsat (30 m)	Water bodies were manually digitised with a minimum lake size threshold of 2,700 m^2. Ponded area change was not reported for individual glaciers.
Note: studies reporting the expansion of Imja lake are not included				

3.2 Study region

Annual precipitation in the Everest region is dominated by the Indian summer monsoon and the majority of rainfall (~80%) occurs between June–September (Bookhagen and Burbank, 2006; Wagnon et al., 2013). Both the northerly draining Rongbuk catchment and the southerly draining Dudh Koshi catchment display a trend of warming temperatures (Yang et al., 2006; Shrestha and Aryal, 2011), which in conjunction with a potentially delayed (Mölg et al., 2012) and/or weakening monsoon will reduce glacier accumulation (Salerno et al., 2015). Decreasing monsoonal precipitation is likely implicated in reduced glacier driving stresses, causing terminus stagnation and the subsequent development of supraglacial ponds and lakes in the region (Quincey et al., 2009; Salerno et al., 2015). The decadal response of large debris-covered glaciers to climate change suggests negative mass balance conditions will prevail in coming decades, irrespective of any slowdown to contemporary warming (Rowan et al., 2015).

The Everest region is characterised by glaciers that are heavily debris-covered in their lower reach (Figure 3.1). The debris is sourced from rock fall avalanches and from moraine ridge collapses, and typically increases in thickness towards glacier termini (Nakawo et al., 1986). The glaciers are low gradient in the debris-covered area (Quincey et al., 2007), stagnating (Quincey et al., 2009; Dehecq et al., 2015), and are widely losing mass (Bolch et al., 2008a, 2011; Ye et al., 2015). Supraglacial ponds are prevalent features on the low gradient and hummocky topography of debris-covered glacier ablation zones. They vary in size, shape and turbidity (Figure 3.2) as well as situation; some are surrounded by large, calving ice-cliffs whereas others sit in debris-lined hollows. The distinction between what may be described as a pond vs a lake is not well-defined (either theoretically or physically) so herein we refer to all surface water as ponds, unless specifically named otherwise (e.g. Spillway Lake on the Ngozumpa Glacier). Regardless of their size, the upper surface freezes over during the winter period (December–February), although a partially frozen surface may be present up to several months earlier.

Nine debris-covered glaciers in the Everest region spanning Nepal (8) and Tibet (1) were selected for supraglacial pond analysis (Figure 3.1). These nine glaciers drain the Dudh Koshi and Rongbuk catchments respectively. The Rongbuk, Ngozumpa, and Khumbu glaciers are the longest in the study area with debris-covered lengths of ~15 km, ~11 km, and ~11 km, respectively; the shortest is Imja Glacier at ~2 km. The glaciers predominantly flow in a southerly direction with the exceptions of Rongbuk and Ama Dablam Glaciers (northerly flowing), and Imja Glacier (westerly flowing).

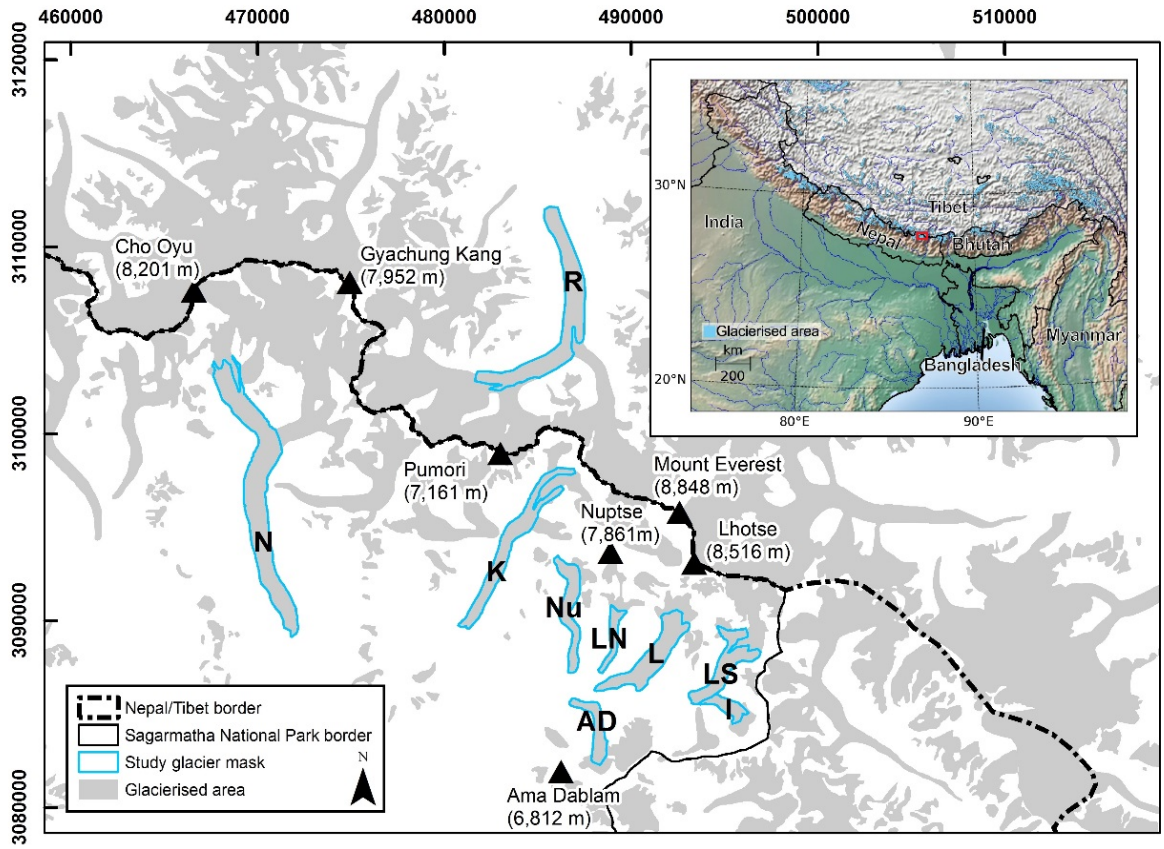

Figure 3.1. Location of the nine study glaciers within the central Himalaya (inset). Selected mountain peaks are shown. K—Khumbu Glacier, N—Ngozumpa Glacier, R—Rongbuk Glacier, Nu— Nuptse Glacier, LN — Lhotse Nup Glacier, L — Lhotse Glacier, LS — Lhotse Shar Glacier, I — Imja Glacier, AD — Ama Dablam Glacier.

3.3 Data sources

This study used 16 time periods of fine-resolution imagery (Table 3.2), comprising nine from Google Earth (<2 m spatial resolution), and seven from WorldView 1 & 2, GeoEye, and QuickBird 2 sensors (0.5–0.6 m spatial resolution). This imagery incorporated post-monsoon/winter periods (termed winter herein) (late September–February), and pre-monsoon/monsoonal periods (termed summer herein) (March–mid September). True-colour orthorectified Google Earth images were accessed using Google Earth Pro. WorldView, GeoEye and Quickbird scenes were orthorectified in ERDAS Imagine using rational polynomial coefficients and the 30 m Shuttle Radar Topography Mission (SRTM) Digital Elevation Model (DEM). Glacier outlines were obtained from the South Asia — East Randolph Glacier Inventory 5.0 (Pfeffer et al., 2014). These outlines were modified manually to reflect the debris-covered area of each study glacier, and only supraglacial ponds falling within this masked area were included in the study.

3.4 Methods

3.4.1 Supraglacial pond classification

A total of 9,340 ponds were classified in this study either semi-automatically using an object-based classification (46%), or manually digitised in Google Earth (54%).

3.4.2 Object based image analysis (OBIA)

For satellite image classifications OBIA offers several advantages over pixel-based approaches. First, it has the ability to detect edges at multiple scales, providing a set of connected curves delineating the boundaries of surface ponds (and other spectrally discontinuous features) regardless of their size. Secondly, in doing this, OBIA also makes use of non-spectral metrics (e.g. image texture) to classify segments, which generally leads to a more refined output than can be achieved using pixel-based approaches. Thirdly, because OBIA leads to the derivation of homogeneous polygons, there is minimal noise in the segmented image, in contrast to often-used ratios such as the Normalised Difference Water Index (Liu et al., 2015). In a Himalayan context, OBIA has previously been applied to Landsat imagery for glacial lake detection (e.g. Nie et al., 2013; Liu et al., 2015) and glacier extent mapping (Nie et al., 2010). We applied it to the panchromatic band of each WorldView, GeoEye, and QuickBird image using ENVI 5.2, to effectively delineate the edges of supraglacial ponds (Figure 3.3). For this analysis the original panchromatic images were resampled to a common resolution of 0.7 m.

Errors in the OBIA approach can arise from under- or over-segmentation of the image, which is sensitive to image-specific scale and merge thresholds. For an under-segmented image, pond boundaries contain adjacent terrain, which cannot be retrospectively removed without manual boundary editing, whereas an over-segmented image represents individual objects with several or more polygons, which can be merged manually (Liu and Xia, 2010). We opted to over-segment each image and then manually inspect each classified pond, editing and merging polygons where required. Segmentation in ENVI involved scale and merge thresholds of ~15 to 25 and ~70 to 80 respectively. Manual merging was generally only necessary where a pond featured partial coverage of floating ice. Pond boundaries were spectrally distinct from the surrounding debris-cover so misclassification was minimal (Figure 3.3). Multi-spectral imagery was available for most time periods (Table 3.2) and was cross-referenced with the panchromatic imagery to check pond boundaries. The final pond boundaries were exported to ArcGIS for analysis. This methodology was chosen to avoid the reliance on user-defined thresholds and hence provide the highest possible

classification accuracies, rather than develop a semiautomatic classification technique.

3.4.3 Manual digitisation

Eight periods of Google Earth imagery (~2 m spatial resolution) increased the temporal resolution and spread of our dataset (Table 3.2). A supplementary ninth image, which did not have full coverage of the Ngozumpa Glacier, was used to quantify the size of Spillway Lake in Jun-15. As we were unable to use the OBIA approach on the Google Earth imagery we digitised the surface ponds by hand in Google Earth Pro and imported the polygons into ArcGIS for further analysis. All digitisation was undertaken by one operator to ensure consistency and ponds in each image were checked for accuracy by revisiting on independent days until no further edits were required.

3.4.4 Uncertainty

Differential GPS (dGPS) points were taken on the boundaries of four stable ponds on the Khumbu Glacier in Oct/Nov 2015 to check against our most recent pond inventory (February 2015). The ponds were clear, on a stagnant and vegetated zone of the glacier (Inoue, 1980; Quincey et al., 2009), and were observed to be stable over our study period. dGPS points showed good agreement with classified pond boundaries and generally fell on or within a one pixel margin of the boundary (Supplementary Figure 3.1).

Uncertainty in classified ponded area was calculated by assuming ±1 pixel in the perimeter of each pond following Gardelle et al. (2011). Although pixel resolution is not explicitly stated in Google Earth imagery, we assumed it to be 1 m for uncertainty estimation based on our field observations compared to the size of features that could be discriminated in the imagery.

In order to assess the uncertainty of the OBIA outputs relative to manual digitisation, one operator manually digitised 50 additional ponds on a panchromatic (0.7 m resolution) image (Supplementary Table 3.1). The areas of digitised polygons were compared to OBIA derived polygons and the area uncertainty when using a ±1 pixel boundary (i.e. the uncertainty assumed in this study). The area difference between OBIA and manual classification methods ranged from 0.3 to 16% with a mean of 6%. The mean area of OBIA derived polygons was 1237 m^2 compared to 1235 m^2 for the manually digitised ponds, suggesting there was no observed digitising bias. In comparison, the assumed uncertainty using a ±1 pixel buffer ranged from 6 to 69% with a mean of 25%. Therefore the uncertainty bounds used in our study are well above the actual uncertainty expected during pond classification.

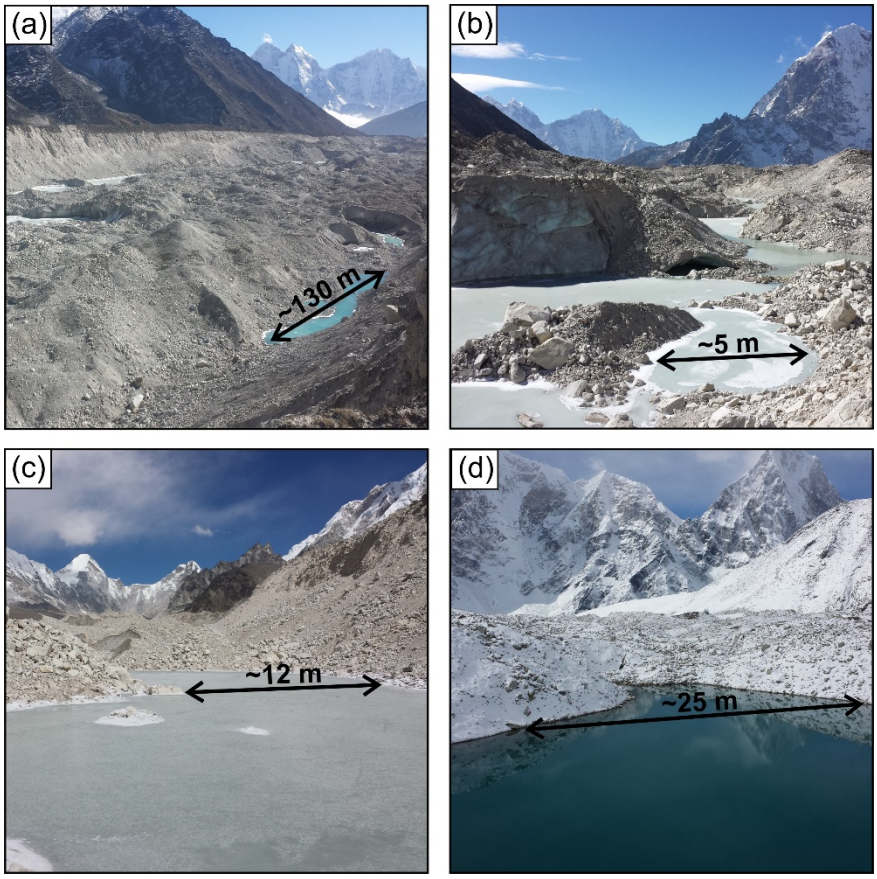

Figure 3.2. Examples of the sizes, shapes, and sediment concentrations of supraglacial ponds on the Khumbu Glacier. Approximate scales are shown for individual ponds. (a) Looking south over across a turbid elongated pond, (b) a turbid and partially frozen irregular shaped pond with adjacent ice cliffs, (c) a completely frozen pond with a more regular shoreline, and (d) a clear and stable pond with a smooth shoreline.

Table 3.2. Spatial and temporal coverage of imagery used in this study.

Image ID/ description and spatial resolution	Image date	K	N	R	Nu	LN	L	LS	I	AD
Google Earth. Supplementary image with Spillway Lake coverage. TCC.	07/06/2015		**							
103001003D7AFE00/ WV02 sensor. PMS. 0.52 – 2.11	02/02/2015	*		*						
Google Earth. TCC	24/01/2015					*	*	*	*	
Google Earth. TCC	13/01/2014	*			*					*

Google Earth. TCC	08/12/2013				*	*	*	*		
ArcGIS Basemap. WV02. MS. 0.50 m	10/07/2013	**								
Google Earth. TCC	23/05/2013				*					
1050410000E0AE00/ GE01. P. 0.50 m	23/12/2012		*							
103001001C5E7600/ WV02. PMS. 0.51 - 2.05 m	11/10/2012			*						
101001000E521A00/ QB02. PMS. 0.67 – 2.67 m	19/10/2011	*		*	*	*	*	*	*	*
102001001745CD00/ WV01. P. 0.52 m	17/10/2011		*							
Google Earth. TCC	09/06/2010		**							
Google Earth. TCC	03/11/2009	*	*							*
Google Earth. TCC	24/05/2009	**								**
10100100013F4E00/ QB02. PMS. 0.62 – 2.49 m	20/09/2002				*	*	*	*		
Google Earth. TCC	18/12/2000									*

WV = WorldView, GE = GeoEye, and QB = QuickBird sensors. TCC = true colour composite, P = panchromatic, PMS = panchromatic and multi spectral. Spatial resolution (panchromatic – multi spectral)

Image date dd/mm/yyyy. '*' & '**' indicate glacier coverage for non-monsoonal (winter), and pre-monsoon/ monsoonal images (summer) respectively

K – Khumbu Glacier, N- Ngozumpa Glacier, R- Rongbuk Glacier, Nu – Nuptse Glacier, LN – Lhotse Nup Glacier, L –Lhotse Glacier, LS- Lhotse Shar Glacier, I – Imja Glacier, AD – Ama Dablam Glacier

3.4.5 Pond and glacier characteristics

Ponded area change with distance up-glacier was calculated using 500 m distance bins from the terminus of each glacier, accounting for curvature along a centreline. Mean pond circularity was calculated using Eq. (1), since some studies have assumed circular ponds when assessing theoretical error (e.g. Salerno et al., 2012).

$$(1)\ \text{Circularity} = \frac{P^2}{4\pi A}$$

where P and A are pond perimeter (m) and area (m^2) respectively. The transition between active and inactive ice was approximated for each glacier using the velocity map outputs of Bolch et al. (2008b); Quincey et al. (2009); Haritashya et al. (2015), and Dehecq et al. (2015), unless this transition occurred up-glacier of the study mask.

3.4.6 Pond area bins

The areas of individual ponds were classified into 300 m^2 bins and used to derive cumulative area distributions for each glacier. 300 m^2 bins were chosen to allow scaling to reflect the Landsat pixel size and were used to estimate potential area uncertainties when using medium-resolution imagery.

3.4.7 Pond frequency

Pond frequency was derived by summing pond area pixels in each image and then normalising the score to derive percentage occurrence over respective images. Pond frequency reveals areas of likely continual pond development, in contrast to areas where ponds were ephemeral. An important distinction exists between ponds that persist over two or more images, those that drain, and those that drain and subsequently refill between time periods. However, the imagery used in this study is of insufficient temporal resolution to report such trends reliably, which would ideally require field-based observations. Additionally, a pond-scale analysis was not the aim of this study. For this reason we take pond frequency to represent a pixel that was classified as water for one or more time periods.

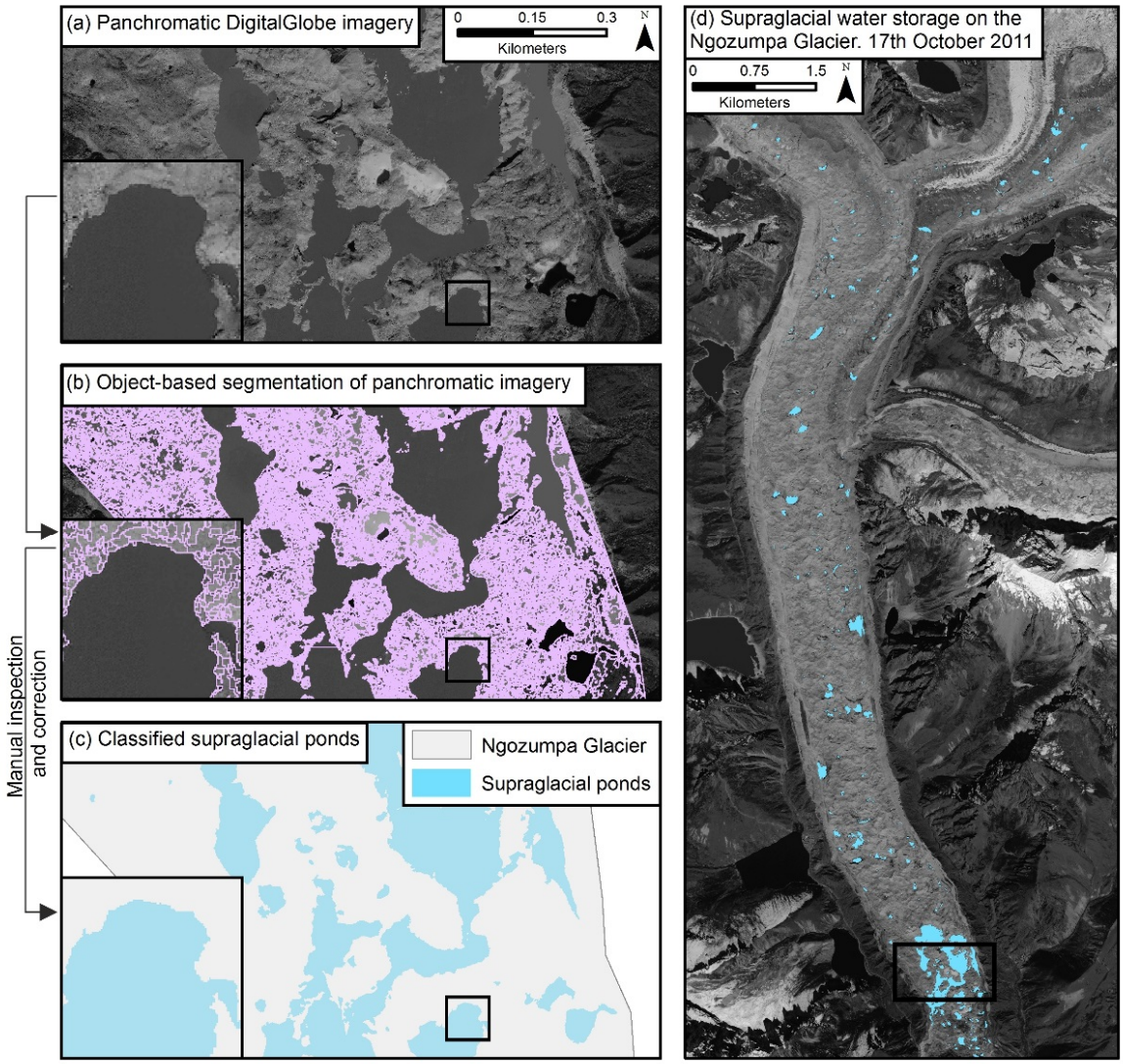

Figure 3.3. The workflow of using panchromatic DigitalGlobe imagery to classify supraglacial ponds. (a) A subset of the original WorldView 1 panchromatic band, (b) object-based edge segmentation on the panchromatic band to delineate surface water, (c) classified supraglacial pond output following manual inspection and correction, and (d) supraglacial ponds on the Ngozumpa glacier (11th Oct 2011). Satellite image courtesy of the DigitalGlobe Foundation.

3.5 Results

3.5.1 Study region ponded area change

Overall change in ponded area across the study glaciers displayed a heterogeneous spatial pattern (Figure 3.4). Considering the largest glaciers (Ngozumpa, Rongbuk, and Khumbu) without their respective terminus lakes, the Ngozumpa Glacier displayed a net loss in ponded area of 29,864 m^2 (Nov-09–Dec-12), the Rongbuk Glacier gained 1,664 m^2 (Oct-11–Feb-15), and the Khumbu Glacier gained 99,889 m^2 (Nov-09–Feb-15). The smaller study glaciers (Nuptse, Lhotse Nup, Lhotse, Lhotse Shar, and Imja)

all featured a ponded area minimum in Oct-11, followed by an increase in surface water storage thereafter. Our analysis showed that without exception there were more ponds evident during summer periods than during the preceding winter (and an according increase in ponded area) (Table 3.3, Figure 3.4). An exceptional increase in ponded area was observed on Khumbu and Ama Dablam glaciers in May-09.

The large supraglacial lakes on the termini of the Ngozumpa and Rongbuk glaciers, termed Spillway Lake and Rongbuk Lake respectively, were both dynamic over the study period (Figure 3.4, Table 3.3) but did not reflect historic trends of expansion (Ye et al., 2009; Thompson et al., 2012). The area of Rongbuk Lake consistently declined (losing 87,451 m^2, Oct-11–Feb-15), whereas Spillway Lake expanded over the period Nov-09 to Jun-10, but displayed an overall net loss 34,566 m^2 (Nov-09–Dec-12). The supplementary Google Earth image from Jun-15 revealed contemporary expansion of Spillway Lake by 26,221 m^2 from Dec-12, reducing the net loss to 8345 m^2 (Nov-09–Jun-15). The size of Spillway Lake and adjacent ponds was 272,982 m^2 in Nov-09. This is in agreement with the value of ~258,000 m^2 (December 2009) reported by Thompson et al. (2012) from a dGPS survey of the lake edge, which also included several additional smaller ponds.

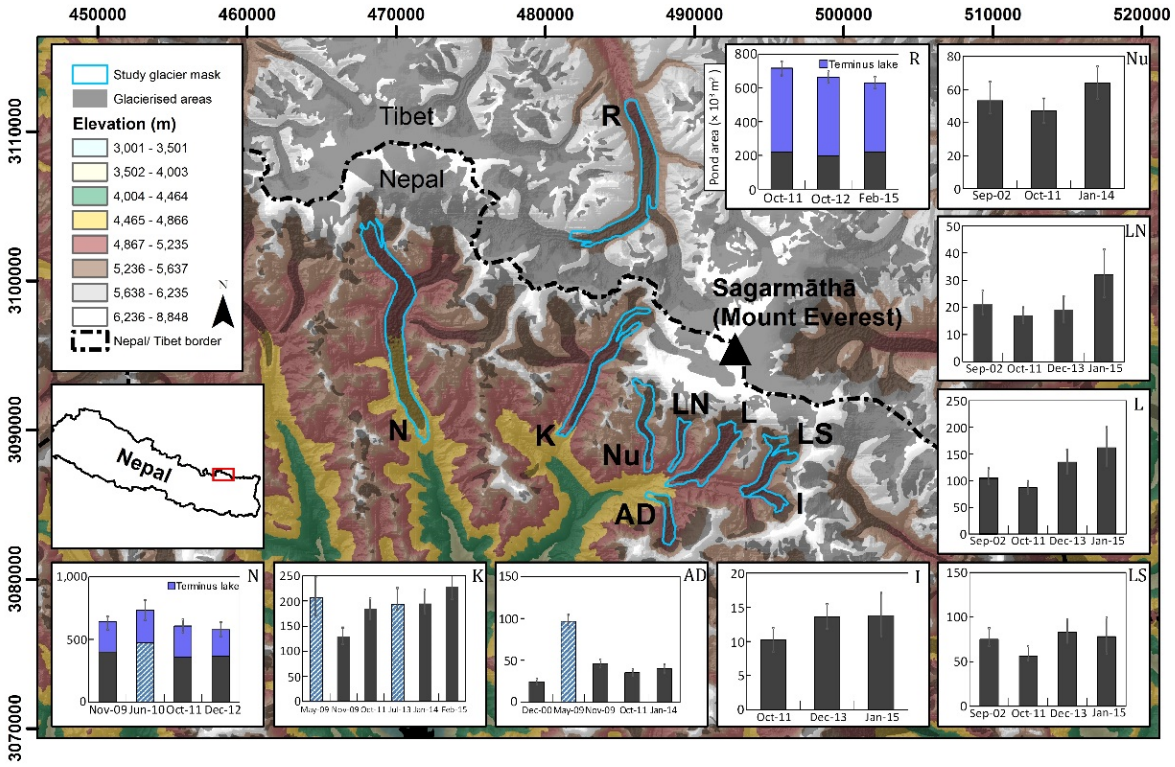

Figure 3.4. Overall supraglacial water storage change within the masked study glacier areas. Error bars are derived from a ±1 pixel uncertainty for classified ponds. Capped purple bars for the Rongbuk and Ngozumpa glaciers represent the area changes of Rongbuk and Spillway lakes respectively. Hashed blue columns represent summer images. K — Khumbu Glacier, N — Ngozumpa Glacier, R — Rongbuk Glacier, Nu — Nuptse Glacier, LN — Lhotse Nup Glacier, L — Lhotse Glacier, LS — Lhotse Shar Glacier, I — Imja Glacier, AD — Ama Dablam Glacier.

3.5.2 Spatial characteristics

3.5.2.1 Glacier-scale pond dynamics

We divided our dataset into the three large glaciers (Figure 3.5a), and the six smaller glaciers (Figure 3.5b) to evaluate ponded area trends up-glacier. Figure 3.5 reveals areas of pond drainage, growth, or stability. As these trends are reported across distance bins they do not reveal individual pond dynamics, but instead highlight areas of dynamic pond activity.

For the large glaciers (Figure 3.5a), areas of greatest pond area often persisted through each image, whilst the magnitude of the total area changed. The relationship between ponded area and distance from the terminus is thus non-monotonic and displays regular variation. This relationship is most pronounced for the Khumbu Glacier, with peaks in ponded area approximately every 2 km moving up-glacier. Ponded area on the Khumbu increased over much of the glacier through time, but especially in the lower 7 km. Relative to winter images (grey scale), summer images

(blue scale) featured increased ponded area through time in the upper 6 km of the Khumbu, in contrast to a decreased area near the terminus (0.5–4 km), although only two summer time periods were available for comparison (Figure 3.5a).

Spillway and Rongbuk lakes migrated up-glacier over the observation period and their overall size diminished (Figure 3.5a, Table 3.3). Up-glacier expansion of Spillway Lake (Figure 3.6b) was coincident with locations of ice cliffs and lake deepening identified by Thompson et al. (2012, cf. their Figure 6c). Pond variability was low immediately up-glacier of both lakes, although this variability extended notably further on the Rongbuk Glacier before reaching an increase in ponded area at ~8.0 km (Figure 3.5a).

Surface water storage on the smaller glaciers in the region (Figure 3.5b) was much more variable. In recent years the greatest expansion in ponded area was in the regions of 2.5 to 4.0 km (Nuptse), 2.5 to 4.0 km (Lhotse Nup), 4.5 to 6.5 (Lhotse), and 1.5 to 2.5 km (Ama Dablam). Imja Glacier showed a small increase in ponded area between 1.0 and 1.5 km up-glacier. The two most recent images for Lhotse Shar (Dec-13, Jan-15) revealed greatest pond expansion 2.0 to 4.5 km up-glacier, although ponded area in Dec-13 was higher than that of Jan-15.

Table 3.3. Supraglacial pond inventory characteristics and area change.

Glacier ID	Debris-covered area (km^2)	Image date (dd/mm/yyyy)	Supraglacial ponds		
			Number	Area (m^2)	Mean circularity[1]
K	7.1	02/02/2015	362	228,391	3.6
		13/01/2014	285	183,723	1.7
		10/07/2013	301	193,562	2.0
		19/10/2011	259	183,980	3.4
		03/11/2009	185	128,502	1.8
		24/05/2009	471	206,590	2.9
N	16.3	07/06/2015		*272,982	
		23/12/2012	770	579,152	3.0
				*246,761	
		17/10/2011	563	607,356	3.5
				*289,671	
		09/06/2010	1022	733,641	1.6

				*300,602	
		03/11/2009	545	643,582	1.7
				*281,327	
R	11.4	02/02/2015	333	632,019	3.4
				*409,659	
		11/10/2012	352	665,805	2.8
				*469,186	
		19/10/2011	420	717,806	3.0
				*497,110	
Nu	3.9	13/01/2014	131	63,788	1.5
		19/10/2011	163	47,080	2.6
		20/09/2002	132	53,332	3.1
LN	1.5	24/01/2015	145	32,392	2.0
		08/12/2013	77	18,812	1.7
		19/10/2011	63	16,760	2.6
		20/09/2002	66	21,271	2.8
L	6.3	24/01/2015	722	161,709	1.8
		08/12/2013	344	134,564	1.6
		19/10/2011	211	86,699	2.7
		20/09/2002	207	105,192	2.7
LS	4.7	24/01/2015	355	78,397	1.8
		08/12/2013	174	82,748	1.8
		19/10/2011	144	56,297	2.5
		20/09/2002	164	74,899	2.7
I	1.5	24/01/2015	52	13,767	1.9
		08/12/2013	25	13,585	1.6
		19/10/2011	39	10,186	2.9
AD	2.6	13/01/2014	52	40,124	1.6
		19/10/2011	53	35,607	2.8
		03/11/2009	39	46,171	1.6
		24/05/2009	76	96,547	1.5
		18/12/2000	38	24,517	1.4

K – Khumbu Glacier, N- Ngozumpa Glacier, R- Rongbuk Glacier, Nu – Nuptse Glacier, LN – Lhotse Nup Glacier, L –Lhotse Glacier, LS- Lhotse Shar Glacier, I – Imja Glacier, AD – Ama Dablam Glacier
1. A circle would have a score of 1. Examples are given in Supplementary Figure 3.1.
*Contributing area of terminal lakes (Ngozumpa Glacier: Spillway Lake; Rongbuk Glacier: Rongbuk Lake)

2.5.2.2 Glacier-scale pond frequency

Increased hydrological connectivity is apparent in the lower 0.5 to 4 km of the Khumbu Glacier, which notably extends up the eastern margin (Figure 3.7b). In this zone of high pond frequency (bounded by the black rectangle in Figure 3.7b), ponded area increased by 33,593 m^2 (66%) (2009–2015). On the Khumbu Glacier, this connectivity between larger ponds was often by narrow inlets not easily identifiable on the imagery (Figure 3.6a), but their existence was confirmed by field observations in Oct/Nov 2015.

The smaller study glaciers (Figure 3.7c) generally featured several distinct areas of high pond frequency (e.g. near the Nuptse terminus) but no evidence of increasing surface connectivity between pond basins. Lhotse Shar and Imja glaciers were an exception, where a large supraglacial lake (Imja Lake) is already established on the lower debris-covered area. Up-glacier of this lake there are discrete areas of high pond persistence along the full length of the debris-covered zone.

Spillway and Rongbuk lakes persisted over our study period (Figure 3.7a, d), although areas of drainage and growth were apparent at both locations (Figure 3.6b, c). Drainage was especially pronounced on the lower terminus of the Rongbuk Glacier where a large pond drained over our study period (Nov-09–Dec-12) (Figure 3.6c). On the Ngozumpa Glacier drainage events were widespread above Spillway Lake (Figure 3.6b).

3.5.3 Cumulative pond area

Cumulative area distributions of supraglacial ponds revealed inter and intra-annual variability across all of our study glaciers. Smaller ponds accounted for a proportionally greater area on summer images, relative to winter images (e.g. Figure 3.8a, b, i). At a glacier scale, evidence of a recent trajectory towards smaller pond distributions was clear on several glaciers including Khumbu, Lhotse Nup, Lhotse, and Lhotse Shar (Figure 3.8a, e–g).

The percentage of ponded area smaller than one (900 m^2) and four (<3600 m^2) Landsat pixels was glacier dependent, reflecting contrasting pond-size distributions (Figure 3.9a). A mean across all glaciers revealed ponds <900 m^2 accounted for 15 to

40% of total ponded area and those <3600m^2 accounted for 43 to 88%. When investigating the numbers of ponds, these statistics are notably higher at 77 to 89%, and 93 to 99% respectively (Figure 3.9b). These statistics revealed potential omissions when using medium-resolution (e.g. 30 m Landsat) imagery for supraglacial pond delineation. For a theoretical four-pixel ASTER imagery threshold (900 m^2), potential pond omissions for the larger glaciers in our study region (Khumbu, Ngozumpa, and Rongbuk) were in range of 17 to 19% of the overall ponded area (Figure 3.9a). However, on smaller glaciers with smaller pond size distributions, this was up to 40% (Lhotse Nup Glacier). The vertical dashed lines on Figure 3.8 provide a visual representation of potential omissions, which are variable by glacier, year, and season. Our analysis revealed a trajectory towards large lake development for the Khumbu Glacier, with smaller ponds becoming more prevalent, in conjunction with an increase in the size of the largest pond observed, excluding Oct-11 (Figure 3.8a). Spillway and Rongbuk lakes featured a stall in growth from historic trends (Ye et al., 2009; Thompson et al., 2012) and a decrease in overall area due to prominent drainage events.

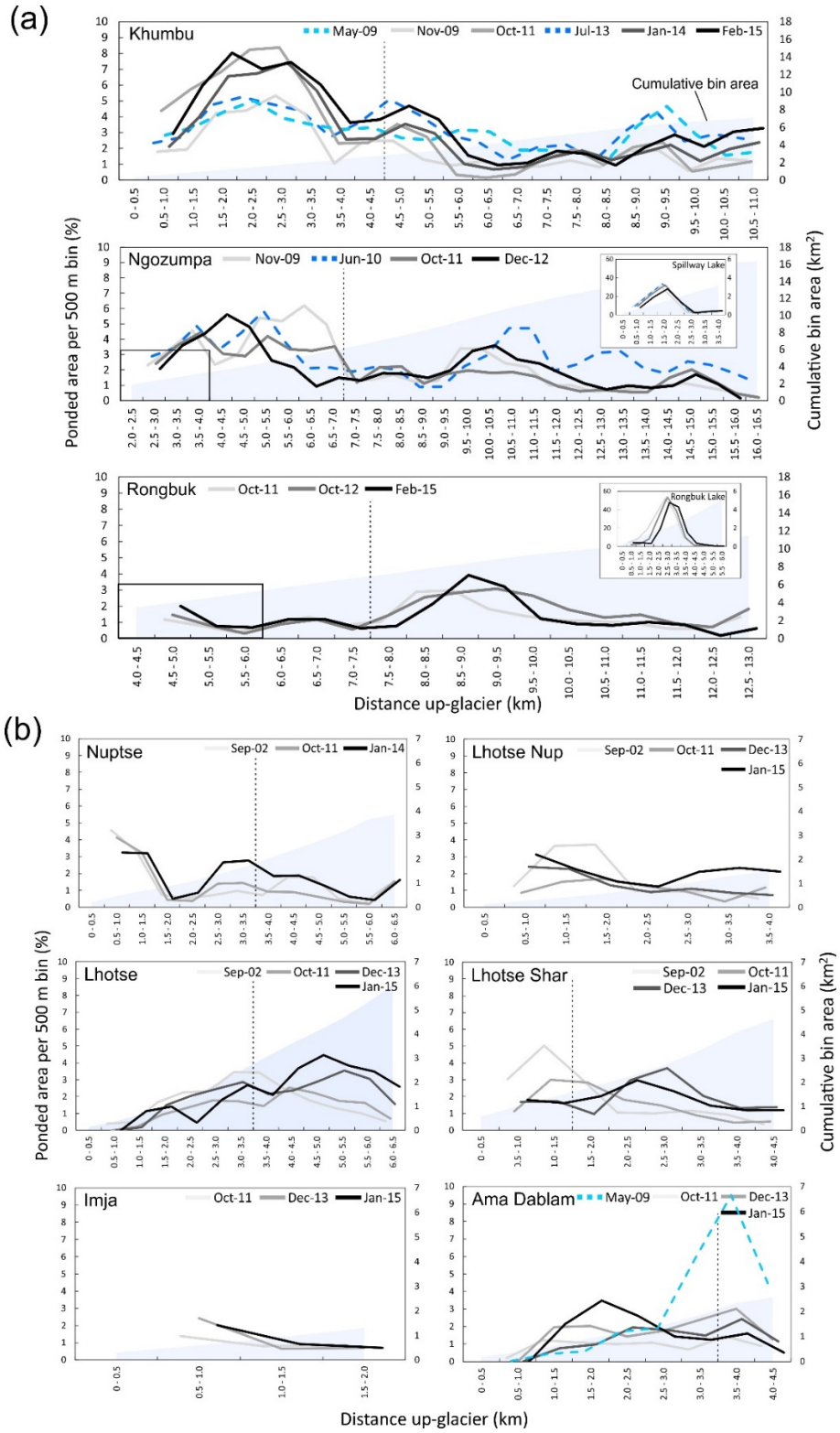

Figure 3.5. Two-period moving average of ponded area with distance up-glacier, aggregated to 500 m bins. (a) The three largest study glaciers with Spillway and Rongbuk lakes shown inset for respective glaciers. (b) The smaller study glaciers. The vertical dashed line indicates the approximate transitions from active to inactive ice, i.e. areas with a velocity lower than ~10 m a^{-1}. This boundary is split on Lhotse Shar Glacier (see Figure 3.7c).

3.6 Discussion

3.6.1 Trends in supraglacial pond development

Utilising an unprecedented spatiotemporal archive of fine-resolution satellite imagery, our results demonstrate a heterogeneous pattern of supraglacial pond and thus of temporary water storage dynamics in the Everest region glaciers.

Inter- and intra-annual pond change revealed in this study likely reflects a combination of meltwater generation (Gardelle et al., 2011), englacial inputs and drainages (Gulley and Benn, 2007), and precipitation inputs (Liu et al., 2015). Our detection of substantial year-to-year variations suggests that caution should be applied in studies using only a few images with a large temporal interval, since it is not known how representative a chosen image is over the respective timescale. Other studies have generally selected autumn and winter images for analysis of Himalayan glacier surfaces since low cloud cover often persists, and lake area changes are expected to be minimal at that time owing to negligible precipitation inputs (Gardelle et al., 2011; Thompson et al., 2012; Wang and Zhang, 2014; Liu et al., 2015). Our results demonstrated the magnitude of changes expected during the summer period for the Khumbu, Ngozumpa and Ama Dablam glaciers (Figure 3.4). These summer dynamics have not previously been reported at a glacier-scale. The substantial summer pond growth we observed reveals the responsiveness of ponds to seasonal controls on precipitation and surface hydrology. The summer season features enhanced precipitation, pond ablation, meltwater generation, and increased pond connectivity with the englacial drainage system (Sakai et al., 2000; Wang et al., 2012; Miles et al., 2016). Pond development therefore proceeds alongside sporadic drainage events.

The area of supraglacial ponds is widely used as a proxy for their potential importance for water storage and glacier ablation (e.g. Gardelle et al., 2011; Liu et al., 2015; Wang et al., 2015; Zhang et al., 2015), however, volumetric estimates are required to assess true water storage dynamics. The compiled area-volume relationship dataset of Cook and Quincey (2015) features only two data points below a pond area of 10,000 m^2, hence pond bathymetry for the size of supraglacial ponds commonly encountered on our study glaciers is urgently required (Figure 3.8).Nevertheless we present a first-order estimate of the volumetric contributions and temporal dynamics of supraglacial ponds for our study glaciers in Supplementary Table 3.2.

3.6.1.1 Glacier-scale ponded area patterns

Of the three largest glaciers, the Rongbuk featured a lower and less pronounced up-glacier ponded area distribution (Figure 3.5a). We attribute this to an extensive supraglacial drainage stream, which extends the full length of the upper glacier before

reaching Rongbuk Lake. The stream is likely able to efficiently drain a large proportion of melt water generated from the extensive surface lowering identified by Ye et al. (2015). The active ice boundary approximated from Quincey et al. (2009) is also expected to have receded further up-glacier reflecting reduced glacier accumulation (Yang et al., 2006), allowing enhanced ponding in the 8 to 10 km zone (Figure 3.5a). The Khumbu Glacier also features a supraglacial drainage network between 6 and 8 km up-glacier, which may explain the lower pond presence here, since repeated hydrofracturing in this area, which has compressional ice flow, allows supraglacial water drainage englacially (Benn et al., 2009). No extensive supraglacial drainage network exists on the Ngozumpa Glacier to explain similar zones of subdued ponded area. However, we note lower ponded area at ~13 km up-glacier, coinciding with the confluence of a tributary glacier (Figures. 3.5a and 3.6b).

Other factors contributing to ponded area dynamics exist: the prevalence of a low surface gradient (<2°) across our study glaciers is well known (e.g. Quincey et al., 2007; Bolch et al., 2008a); similar debris-covered glaciers exhibit a non-linear mass-balance profile with elevation (Pellicciotti et al., 2015); and inactive ice is common across much or all of the debris-covered zones (e.g. Figure 3.5 dashed vertical line), promoting pond expansion and coalescence (Bolch et al., 2008b; Quincey et al., 2009; Haritashya et al., 2015; Dehecq et al., 2015). Velocity fields created with fine-resolution imagery (e.g. Kraaijenbrink et al., 2016) have not yet been derived for glaciers in our study region, but would allow an association between glacier flow dynamics, surface lowering, and pond development, comparable to the imagery resolution used in this study. Internal pond feedbacks also act to enhance growth through the absorption and transmission of solar radiation to the underlying ice (Sakai et al., 2000), and through ice cliff calving events at ponds of sufficient size (Sakai et al., 2009).

Khumbu and Ngozumpa glaciers (in particular the latter) featured repeat pond presence at similar locations through time (Figures 3.5a and 3.7a, b). Glacier flow is expected to cause englacial conduit reorganisation and efficient drainage (Quincey et al., 2007), hence low pond frequencies would be expected in areas of active flow up-glacier, which supports our results. We did not conduct a pond-by-pond analysis in this study or an analysis of potential pond advection down glacier, although we expected this to be minimal over our study period. However, we suggest that the continued development of this fine-resolution dataset could reveal drainage and refill cycles of ponds at discrete locations, determined by glacier flow characteristics, and perhaps also influenced by basal topography of the glacier, similar to the topographic coupling observed on large ice sheets (e.g. Lampkin and VanderBerg, 2011). Within inactive ice zones, drainage events (e.g. Figure 3.6b) reveal ponds are actively melting

down at their base and intercepting englacial conduits or exploiting relic crevasse traces (Gulley and Benn, 2007). This is not apparent at Spillway and Rongbuk lakes, which have generally, although not entirely, displayed stability overall, with small areas of drainage and expansion. Spillway Lake is known to have a variable thickness of sediment on the lake bed, and contemporary expansion is concentrated around ice cliffs and regions of thin basal debris coverage (Thompson et al., 2012). The large drainage event down-glacier of Rongbuk Lake (Figure 3.6c) was likely caused by interception with a supraglacial drainage channel close to the western pond margin.

Smaller glaciers in the region do not show a clear trend in the spatial distribution of ponded area, likely because although surface lowering is prevalent across the debris-covered zones, large ponds have not yet become established (Bolch et al., 2011) (Figure 3.7c). However, a transitional trend towards smaller ponds is apparent (Figure 3.5b), suggesting that smaller basins are becoming created and/or activated, concurrent with ongoing surface lowering. Potential overdeepenings in this region highlighted by Linsbauer et al. (2016) suggest that future glacial lakes could develop if supraglacial ponds begin to coalesce. Our results demonstrate a non-linear trend of ponded area increase in the region and an increasing importance of smaller ponds becoming established. Since our findings are expected to be applicable across Himalayan debris-covered glaciers in negative mass balance regimes, previously unreported smaller ponds will help understand the coupling between ponded area, local-scale topographic change, and a size-dependant influence of ponds on surface lowering.

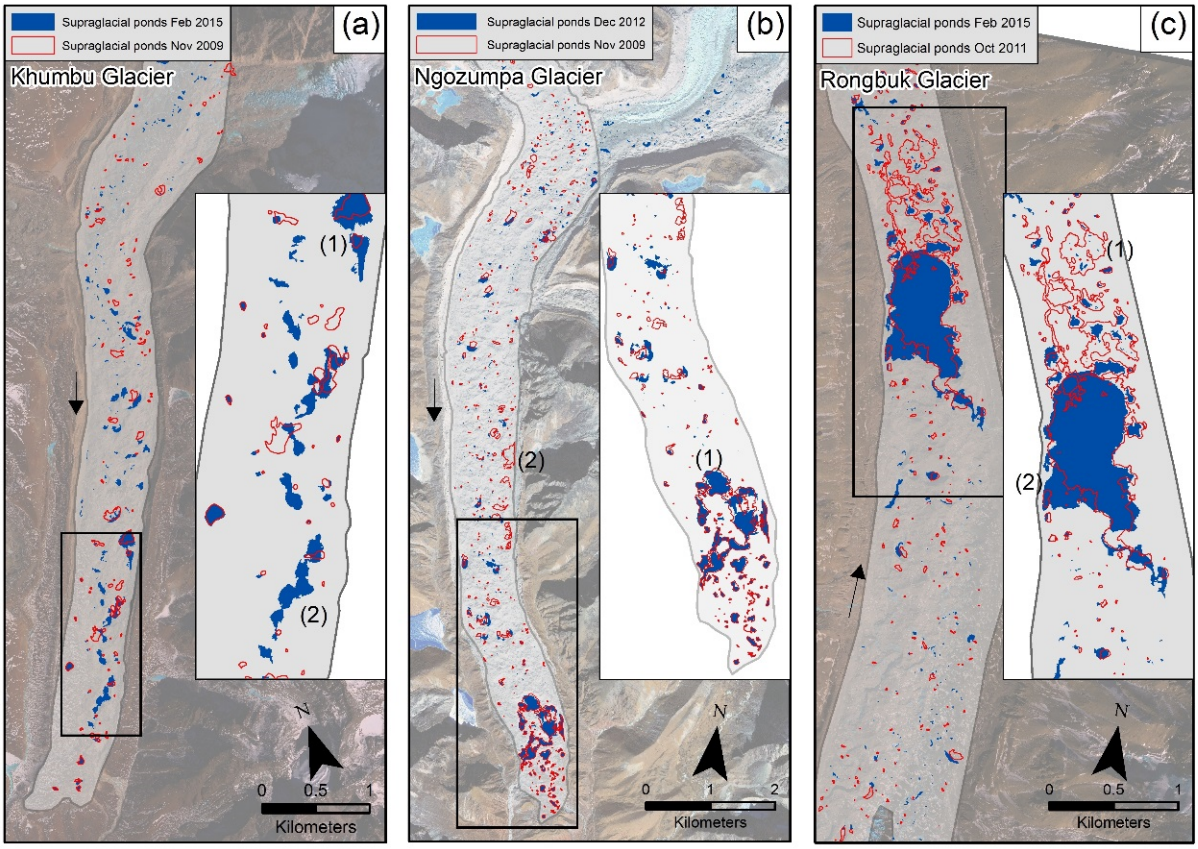

Figure 3.6. Ponded area change for the Khumbu (a), Ngozumpa (b), and Rongbuk (c) glaciers, between the earliest and latest non-summer image. (a-1) Pond expansion, (a-2) pond expansion along the easterly margin, (b-1) up-glacier expansion and partial drainage of Spillway Lake, (b-2) mid-glacier pond drainage, (c-1) extensive drainage below Rongbuk Lake, and (c-2) up-glacier expansion of Rongbuk Lake. Arrows indicate ice flow direction. Satellite images courtesy of the DigitalGlobe Foundation.

3.6.1.2 Seasonal variation in supraglacial pond development

The temporal resolution available for several of our study glaciers revealed higher total ponded area during the summer season compared to preceding and succeeding winters (Figure 3.4), and a transition towards smaller ponds accounting for proportionally greater area (Figure 3.8). Increased thermal energy stored and transmitted by ponds to the underlying ice during the summer season increases meltwater generation and hence pond expansion (Sakai et al., 2000; Wang et al., 2012;Miles et al., 2016), in association with high precipitation during this season (Bookhagen and Burbank, 2006; Wagnon et al., 2013). The seasonal impact of this meltwater generation at a glacier-scale depends predominately on the presence of outlets from ponds restricting expansion, and the role of sporadic drainage events transporting water englacially. Our data suggest that ponds attain their maximum size during the summer period, increasing the likelihood of drainage through hydrofracture and the expansion of englacial conduits by warm pond water (Benn et al., 2009).

Hence total ponded area is reduced approaching the winter period. The transition towards smaller ponds and a higher number of ponds during the summer season (Figure 3.8, Table 3.3) suggests smaller basins become active, but exist as transient features, similarly draining approaching the winter period. Future studies tracking the development of individual ponds at similarly high temporal and spatial resolution, coupled with pond-scale energy balance modelling (e.g. Miles et al., 2016) is required to refine understanding of debris-covered glacier surface hydrology and the importance for ablation at a glacier-scale.

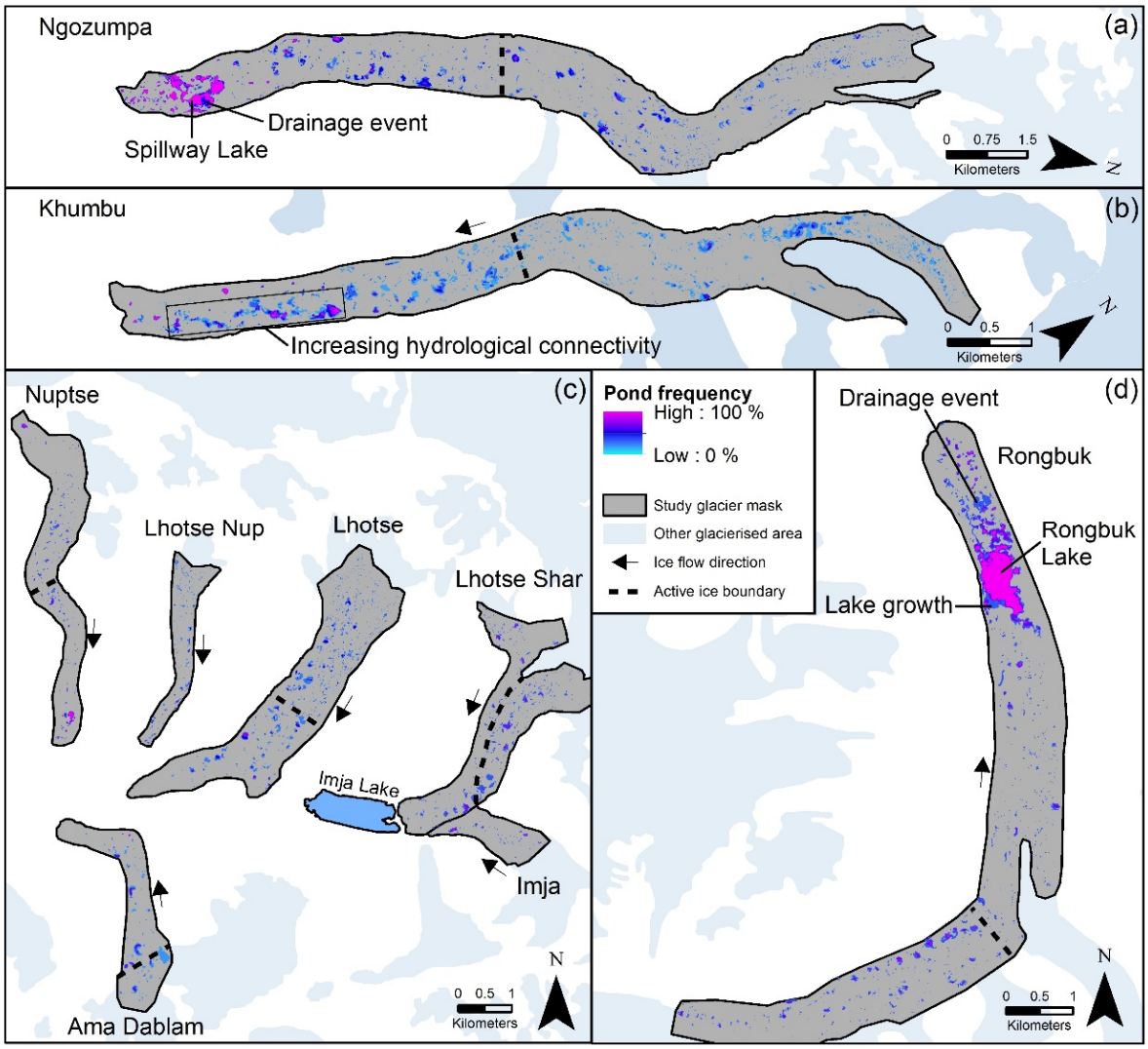

Figure 3.7. Pond frequency normalised to the respective number of images used. Dashed lines indicate the approximate transition between active and inactive ice. A zoomed in view of Spillway and Rongbuk Lakes is shown in Supplementary Figure 3.2 for clarity.

3.6.2 Lake development trajectory

The development of large glacial lakes in the region raises concerns about future GLOF risk (Benn et al., 2012), and rapid glacier mass loss and glacier retreat if a

calving front develops (e.g. Imja Lake) (Somos- Valenzuela et al., 2014). Recent expansion of supraglacial ponds on the eastern margin of the Khumbu Glacier (Figures 3.6a and 3.7b) suggests it may be entering a transitional phase towards large glacial lake development in the lower ablation area. This development was proposed by Naito's et al. (2000) modelling study, and a large overdeepened basin on the lower ablation area was modelled by Linsbauer et al. (2016). We identified a winter image trajectory towards smaller ponds contributing greater total ponded area (Figure 3.5a), larger ponds overall (Figure 3.8a), and an increase in ponded area in the lower ablation zone of the Khumbu Glacier (Figure 3.5a). This pattern suggests firstly that small basins are becoming occupied with meltwater as surface lowering prevails, promoting the development of a reverse glacier surface gradient (Bolch et al., 2011), and secondly that these ponds are now persisting in some cases and coalescing into a connected chain of ponds. The outlet pond on the Khumbu Glacier represents the hydrological base level at the eastern lateral moraine, and was observed in the field and on satellite imagery to have high sediment build up on the bed. This sedimentation and subsequent insulation of any remaining ice below promotes a stable base level, which is conducive to the connection and expansion of ponds up-glacier, following trends of Imja, Spillway, and Rongbuk lakes. However, in the case of the Khumbu Glacier, across-glacier expansion is restricted by a vegetated stable zone to the west.

Thompson et al. (2012) revealed an exponential growth rate of Spillway Lake since 2001, from lake inception in the 1980s. Rongbuk Lake began development in the 1990s but has shown similar rapid expansion (Chen et al., 2014). However, in our study, both lakes decreased in area (Spillway Lake: net loss of 8345 m^2 Nov-09 to Jun-15, Rongbuk lake: net loss of 87,451 m^2 Oct-11 to Feb-15) despite expanding up-glacier (Figure 3.5a insets). We propose that although these lakes are continuing to expand up-glacier through ice cliff retreat and basal melt, they have stalled due to supraglacial drainage channel evolution and a likely lowering of the hydrological base level. Thompson et al. (2012) identified that a connection made between 2001 and 2009 between Spillway Lake and a second smaller lake closer to an easterly draining supraglacial channel, had the potential to re-route the drainage of Spillway Lake and lower the hydrological base level, causing a likely stall in the lake expansion. However, our Dec-2012 image revealed that this channel did not develop and that drainage is still predominantly through the western moraine. If this western channel incised and subsequently lowered the base level, this could explain the lake drainage observed in this study as the lake level adjusts (e.g. Figure 3.6b). Contemporary expansion to Jun-15 (Table 3.3) suggests this channel has now stabilised and up-glacier expansion of Spillway Lake is likely to continue.

3.6.3 Uncertainties in pond detection and delineation

Previous studies reporting supra- and pro-glacial lake dynamics in the Everest region have utilised the long temporal archive of Landsat imagery (e.g. Gardelle et al., 2011; Nie et al., 2013; Bhardwaj et al., 2015; Liu et al., 2015; Wang et al., 2015). Landsat features a relatively short revisit period (16 days), hence cloud free images are usually available outside of the monsoon season. Other multi-temporal studies have used a range of fine- to medium-resolution imagery, often in combination (Table 3.1).

Decadal trends across the Himalaya were presented by Gardelle et al. (2011) and Nie et al. (2013) using Landsat imagery from three and four time periods, using a four and nine 30 m pixel minimum detection threshold, respectively. Whilst our results are broadly in agreement with observed increasing water storage trends in the Everest region, we highlight notable short-term variability and suggest that Landsat imagery is not appropriate for glacier-scale pond monitoring in the Himalaya.

The irregular shape (mean circularity index values of 1.4 to 3.5, Table 3.3) and size distribution of ponds (Figures 3.2 and 3.8) does not lend to alignment with a 30 m pixel (Figure 3.10), since a large proportion of ponded area is accounted for by small ponds. Firstly, this suggests that approximating ponds as circular objects for purposes of uncertainty estimation is not appropriate, since pond circularity is highly variable but rarely approaching the ideal value of one (Table 3.3). Secondly, this study revealed that ponds <900 m^2 accounted for 15 to 40% of total ponded area and those <3600 m^2 accounted for 43 to 88% (Figure 3.9). When quantifying the numbers of ponds present, these statistics were 77 to 89% and 93 to 99% respectively. Although the total number of ponds is less important than overall area, the distribution of smaller ponds indicates where debris-cover is likely to be thin, and so integration with energy balance models and surface lowering maps would be beneficial. These statistics represent potential pond omissions using thresholds of 900 m^2 and 3600 m^2, which represent the area of four ASTER pixels (15 m) or one Landsat pixel (30 m), and four Landsat pixels respectively. Since the application of this imagery usually relies on a variable NDWI threshold, our error estimates

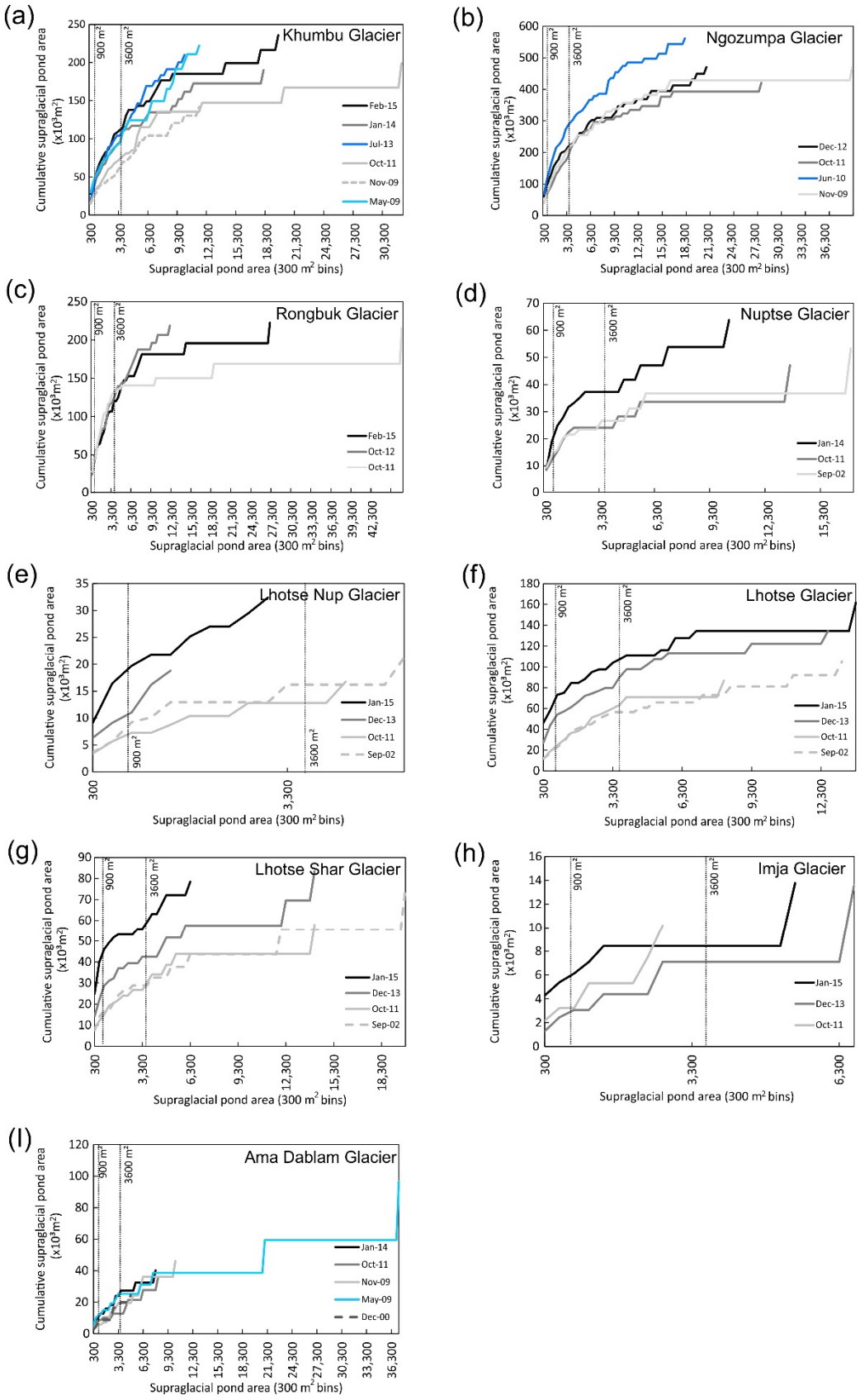

Figure 3.8. Cumulative pond area distribution for post-monsoon/Winter (PMW) images (grey scale) and pre-monsoon/monsoon (PMM) (blue scale) time periods. The terminal lakes on the Ngozumpa and Rongbuk glaciers are not shown here for clarity.

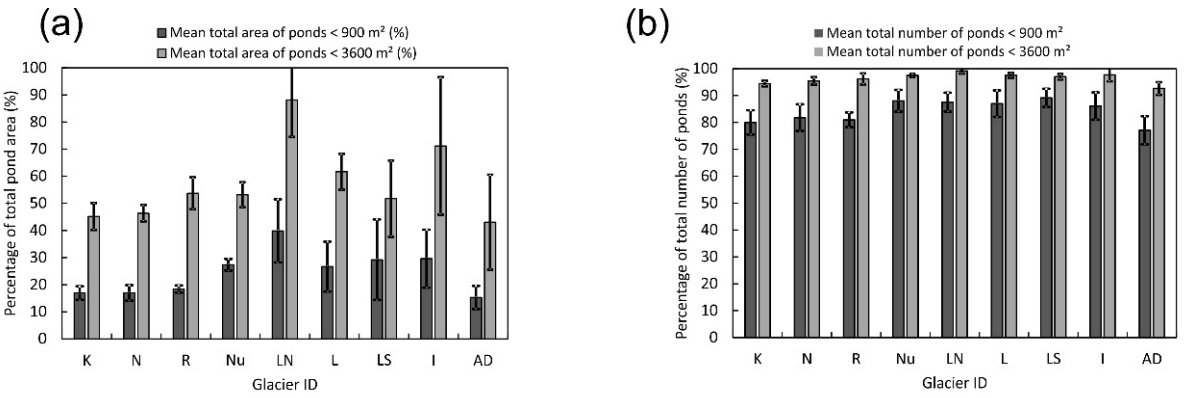

Figure 3.9. Proportion of (a) pond areas and (b) pond frequency, falling below a 900m^2/ 3600m^2 threshold for each study glacier. Values represent a mean across all time periods and error bars show standard deviation.

represent the upper bounds. Nonetheless, a broad threshold is often used to capture mixed pixels containing majority water (e.g. Gardelle et al., 2011), hence ponded area could equally be systematically overestimated if pond distributions tend towards smaller ponds on the order of one 30 m pixel (Figure 3.10c). We show an idealised theoretical variation in ponded area with variable threshold in Supplementary Figure 3.3.

This study has also shown that pond size-area distributions are not static (Figure 3.8), hence revealing the potential for an inter-annual and seasonal bias when using multi-temporal Landsat images for supraglacial pond delineation. The small size and shallow nature of supraglacial ponds (Cook and Quincey, 2015) means area fluctuations can be large, which requires a small pixel size (<10 m) for adequate detection of seasonal trends (Strozzi et al., 2012). Supraglacial pond delineation with medium-resolution imagery is also hindered by pond turbidity and frozen ponds (Bhatt et al., 2007; Racoviteanu et al., 2008). On the Khumbu Glacier we observed a large number of frozen or partially frozen surfaces upon commencement of a field campaign (11th Oct 2015). For this reason, we suggest a transition towards finer-resolution imagery is advantageous for multi-temporal monitoring of supraglacial ponds. However, we acknowledge that Landsat imagery will continue to be a valuable asset when monitoring larger glacial lakes where the edge effects of pixel resolution are substantially lower.

3.7 Conclusion and future work

This study presents the first extensive application of fine-resolution satellite imagery to undertake a multi-temporal, multi-glacier analysis of supraglacial pond dynamics. Inter- and intra-annual changes in glacier-scale ponded area were up to +17% and -52% respectively, reflecting drainage events, pond expansion and coalescence, and

melt season pond expansion. Additionally, despite the prevalence of a negative mass balance regime, a net increase in ponded area was only apparent on six of our nine study glaciers. This short-term variability may sit within decadal scale regional increases (e.g. Gardelle et al., 2011), but nevertheless indicates that stagnating, low gradient, and thinning debris-covered glaciers in the Himalaya do not linearly accrue ponded area through time without notable inter- and intra-annual variability. An evolutionary trajectory towards smaller ponds accounting for larger proportional area was discovered for several glaciers including: Khumbu, Nuptse, Lhotse Nup, Lhotse, and Lhotse Shar. Therefore, pond size distribution may be intrinsically linked to the evolution of debris-covered glaciers under negative mass balance and is likely to have consequent implications for the positive-feedback enhancement of melt, in and around the pond environment (Sakai et al., 2000). However, a longer pond record and analysis of coincident local weather conditions is needed to confirm this.

Spillway and Rongbuk lakes, previously thought to be expanding exponentially, featured a halt in growth during our study period due to notable drainage events. These drainages were likely caused by (i) lowering of the hydrological base level, and (ii) interception with a supraglacial drainage network, respectively. However, both lakes are actively growing up-glacier and so will likely continue to expand once supraglacial drainage channels have stabilised, as evidenced for the Ngozumpa Glacier. The formation and persistence of a chain of ponds on the lower ablation area of the Khumbu Glacier is indicative of a transitional phase towards large lake development in association with a stable hydrological base level, and should be monitored over coming years.

We have shown that fine-resolution imagery is necessary to represent the full spectrum of supraglacial pond sizes that exist on debris-covered glaciers in the Everest region of the central Himalaya. Medium-resolution imagery (e.g. 30 m Landsat) is likely to lead to large omissions of supraglacial water storage on the order of 15 to 88% of total ponded area, and 77 to 99% of the total number of ponds. Nonetheless, medium-resolution Landsat imagery will remain valuable for large glacial lake monitoring, but small changes in water extent (e.g. inter-annual) are likely to be missed (Strozzi et al., 2012). Inter-annual and seasonal biases would also be expected when using medium-resolution satellite imagery, since cumulative pond-size distributions were found to vary inter- and intra-annually, and were glacier specific.

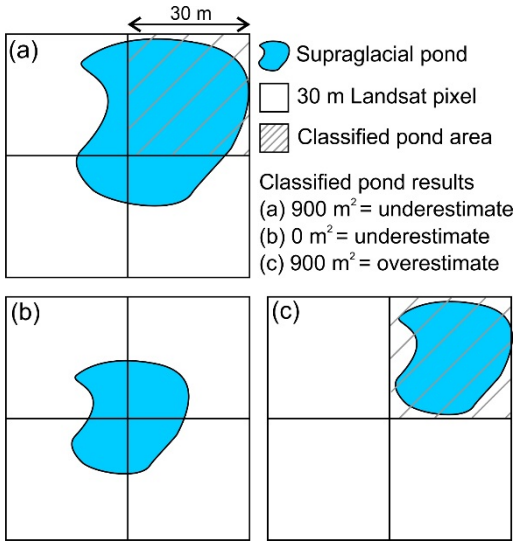

Figure 3.10. Hypothetical pond classification scenarios using Landsat imagery. Classifications are dependent on a user-determined threshold which assigns ponds to a raster grid based on the strength of their spectral signature within each pixel. (a) The pond is larger than one pixel but covers a small proportion of three adjacent pixels, (b) The pond is aligned at the centre of four pixels but does not dominate any, and (c) the pond is smaller than one pixel but dominates the spectral signature and is classified as one pixel in size.

Acknowledgements

The DigitalGlobe Foundation is thanked for access to satellite imagery, which made this study possible. C.S.W acknowledges fieldwork support from the School of Geography at the University of Leeds, the Royal Geographical Society (with IBG), the British Society for Geomorphology, and water@leeds. Dhananjay Regmi and our logistics team from Himalayan Research Expeditions are thanked for invaluable support during fieldwork, Pascal Buri for loan of a boat, and the NERC Geophysical Equipment Facility for loan of a dGPS and technical assistance. We thank the reviewers of an earlier manuscript for constrictive comments.

3.7 References

Benn, D. Gulley, J. Luckman, A. Adamek, A. and Glowacki, P.S. 2009. Englacial drainage systems formed by hydrologically driven crevasse propagation. *Journal of Glaciology.* **55**(191), 513-523.

Benn, D.I. Bolch, T. Hands, K. Gulley, J. Luckman, A. Nicholson, L.I. Quincey, D. Thompson, S. Toumi, R. and Wiseman, S. 2012. Response of debris-covered glaciers in the Mount Everest region to recent warming, and implications for outburst flood hazards. *Earth-Science Reviews.* **114**(1–2), 156-174.

Benn, D.I. Wiseman, S. and Hands, K.A. 2001. Growth and drainage of supraglacial lakes on debris-mantled Ngozumpa Glacier, Khumbu Himal, Nepal. *Journal of Glaciology.* **47**(159), 626-638.

Bhardwaj, A. Singh, M.K. Joshi, P.K. Snehmani Singh, S. Sam, L. Gupta, R.D. and Kumar, R. 2015. A lake detection algorithm (LDA) using Landsat 8 data: A comparative approach in glacial environment. *International Journal of Applied Earth Observation and Geoinformation.* **38**, 150-163.

Bhatt, M.P., Masuzawa, T., Yamamoto, M. and Takeuchi, N. 2007. Chemical Characteristics of Pond Waters within the Debris Area of Lirung Glacier in Nepal Himalaya. *Journal of Limnology.* **66**, 71-80.

Bolch, T. Buchroithner, M. Pieczonka, T. and Kunert, A. 2008a. Planimetric and volumetric glacier changes in the Khumbu Himal, Nepal, since 1962 using Corona, Landsat TM and ASTER data. *Journal of Glaciology.* **54**(187), 592-600.

Bolch, T. Buchroithner, M.F. Peters, J. Baessler, M. and Bajracharya, S. 2008b. Identification of glacier motion and potentially dangerous glacial lakes in the Mt. Everest region/Nepal using spaceborne imagery. *Nat. Hazards Earth Syst. Sci.* **8**(6), 1329-1340.

Bolch, T. Pieczonka, T. and Benn, D.I. 2011. Multi-decadal mass loss of glaciers in the Everest area (Nepal Himalaya) derived from stereo imagery. *The Cryosphere.* **5**(2), 349-358.

Bookhagen, B. and Burbank, D.W. 2006. Topography, relief, and TRMM-derived rainfall variations along the Himalaya. *Geophysical Research Letters.* **33**(8), 1-5.

Carrivick, J.L. and Tweed, F.S. 2013. Proglacial lakes: character, behaviour and geological importance. *Quaternary Science Reviews.* **78**, 34-52.

Chen, W. Doko, T. Liu, C. Ichinose, T. Fukui, H. Feng, Q. and Gou, P. 2014. Changes in Rongbuk lake and Imja lake in the Everest region of Himalaya. *ISPRS - International Archives of the Photogrammetry, Remote Sensing and Spatial Information Sciences.* 259-266.

Cook, S.J. and Quincey, D.J. 2015. Estimating the volume of Alpine glacial lakes. *Earth Surf. Dynam.* **3**, 559-575.

Dehecq, A. Gourmelen, N. and Trouve, E. 2015. Deriving large-scale glacier velocities from a complete satellite archive: Application to the Pamir–Karakoram–Himalaya. *Remote Sensing of Environment.* **162**, 55-66.

Gardelle, J. Arnaud, Y. and Berthier, E. 2011. Contrasted evolution of glacial lakes along the Hindu Kush Himalaya mountain range between 1990 and 2009. *Global and Planetary Change.* **75**(1–2), 47-55.

Gulley, J. and Benn, D.I. 2007. Structural control of englacial drainage systems in Himalayan debris-covered glaciers. *Journal of Glaciology.* **53**(182), 399-412.

Haritashya, U.K. Pleasants, M.S. and Copland, L. 2015. Assessment of the evolution in velocity of two debris-covered glaciers in Nepal and New Zealand. *Geografiska Annaler: Series A, Physical Geography.* **97**(4), 737–751.

Immerzeel, W.W. Kraaijenbrink, P.D.A. Shea, J.M. Shrestha, A.B. Pellicciotti, F. Bierkens, M.F.P. and de Jong, S.M. 2014. High-resolution monitoring of Himalayan glacier dynamics using unmanned aerial vehicles. *Remote Sensing of Environment.* **150**, 93-103.

Inoue, J.a.Y., M. 1980. Ablation and heat exchange over the khumbu glacier. *J. Japan. Soc. Snow Ice (Seppyo).* **39**, 7-14.

Iwata, S. Aoki, T. Kadiota, T. Seko, K. and Yamaguchi, S. 2000. Morphological evolution of the debris cover on Khumbu Glacier, Nepal, between 1978 and 1995. In: Nakawo, M.Raymond, C.F. and Fountain, A., eds. *IAHS Publ. 264 (Symposium at Seattle 2000 – Debris-Covered Glaciers)*, *Seattle, Washington, U.S.A*. IAHS Publication, 3-12.

Kääb, A. Berthier, E. Nuth, C. Gardelle, J. and Arnaud, Y. 2012. Contrasting patterns of early twenty-first-century glacier mass change in the Himalayas. *Nature.* **488**(7412), 495-498.

Komori, J. 2008. Recent expansions of glacial lakes in the Bhutan Himalayas. *Quaternary International.* **184**(1), 177-186.

Kraaijenbrink, P. Meijer, S.W. Shea, J.M. Pellicciotti, F. de Jong, S.M. and Immerzeel, W.W. 2016. Seasonal surface velocities of a Himalayan glacier derived by automated correlation of unmanned aerial vehicle imagery. *Annals of Glaciology.* **57**(71), 103-113.

Lampkin, D.J. and VanderBerg, J. 2011. A preliminary investigation of the influence of basal and surface topography on supraglacial lake distribution near Jakobshavn Isbrae, western Greenland. *Hydrological Processes.* **25**(21), 3347-3355.

Linsbauer, A. Frey, H. Haeberli, W. Machguth, H. Azam, M.F. and S., A. 2016. Modelling glacier-bed overdeepenings and possible future lakes for the glaciers in the Himalaya–Karakoram. *Annals of Glaciology.* **57**(71).

Liu, D. and Xia, F. 2010. Assessing object-based classification: advantages and limitations. *Remote Sensing Letters.* **1**(4), 187-194.

Liu, Q. Christoph, M. and Shiyin, L. 2015. Distribution and interannual variability of supraglacial lakes on debris-covered glaciers in the Khan Tengri-Tumor Mountains, Central Asia. *Environmental Research Letters.* **10**(1), 1-10.

Miles, E.S. Pellicciotti, F. Willis, I.C. Steiner, J.F. Buri, P. and Arnold, N.S. 2016. Refined energy-balance modelling of a supraglacial pond, Langtang Khola, Nepal. *Annals of Glaciology.* **57**(71), 29-40.

Mölg, T. Maussion, F. Yang, W. and Scherer, D. 2012. The footprint of Asian monsoon dynamics in the mass and energy balance of a Tibetan glacier. *The Cryosphere.* **6**(6), 1445-1461.

Naito, N. Nakawo, M. Kadota, T. and Raymond, C.F. 2000. Numerical simulation of recent shrinkage of Khumbu Glacier, Nepal Himalayas. In: Nakawo, M.Raymond, C.F. and Fountain, A., eds. *IAHS Publ. 264 (Symposium at Seattle 2000 – Debris-Covered Glaciers)*, *Seattle, Washington, U.S.A*. IAHS Publication, 245-254.

Nakawo, M. Iwata, S. Watanabe, O. and Yoshida, M. 1986. Processes which distribute supraglacial debris on the Khumbu Glacier, Nepal Himalaya. *Annals of Glaciology.* **8**, 129-131.

Nie, Y. Liu, Q. and Liu, S. 2013. Glacial Lake Expansion in the Central Himalayas by Landsat Images, 1990–2010. *PLoS ONE.* **8**(12), 1-8.

Nie, Y. Zhang, Y.L. Liu, L.S. and Zhang, J.P. 2010. Glacial change in the vicinity of Mt. Qomolangma (Everest), central high Himalayas since 1976. *Journal of Geographical Sciences.* **20**(5), 667-686.

Pellicciotti, F. Stephan, C. Miles, E. Herreid, S. Immerzeel, W.W. and Bolch, T. 2015. Mass-balance changes of the debris-covered glaciers in the Langtang Himal, Nepal, from 1974 to 1999. *Journal of Glaciology.* **61**(226), 373-386.

Pfeffer, W.T. Arendt, A.A. Bliss, A. Bolch, T. Cogley, J.G. Gardner, A.S. Hagen, J.O. Hock, R. Kaser, G. Kienholz, C. Miles, E.S. Moholdt, G. Molg, N. Paul, F. Radic, V. Rastner, P. Raup, B.H. Rich, J. Sharp, M.J. and Randolph, C. 2014. The Randolph Glacier Inventory: a globally complete inventory of glaciers. *Journal of Glaciology.* **60**(221), 537-552.

Quincey, D.J. Luckman, A. and Benn, D. 2009. Quantification of Everest region glacier velocities between 1992 and 2002, using satellite radar interferometry and feature tracking. *Journal of Glaciology.* **55**(192), 596-606.

Quincey, D.J. Richardson, S.D. Luckman, A. Lucas, R.M. Reynolds, J.M. Hambrey, M.J. and Glasser, N.F. 2007. Early recognition of glacial lake hazards in the Himalaya using remote sensing datasets. *Global and Planetary Change.* **56**(1–2), 137-152.

Racoviteanu, A.E. Williams, M.W. and Barry, R.G. 2008. Optical remote sensing of glacier characteristics: A review with focus on the Himalaya. *Sensors.* **8**(5), 3355-3383.

Reid, T.D. and Brock, B.W. 2014. Assessing ice-cliff backwasting and its contribution to total ablation of debris-covered Miage glacier, Mont Blanc massif, Italy. *Journal of Glaciology.* **60**(219), 3-13.

Richardson, S.D. and Reynolds, J.M. 2000. An overview of glacial hazards in the Himalayas. *Quaternary International.* **65–66**, 31-47.

Rohl, K. 2006. Thermo-erosional notch development at fresh-water-calving Tasman Glacier, New Zealand. *Journal of Glaciology.* **52**(177), 203-213.

Rohl, K. 2008. Characteristics and evolution of supraglacial ponds on debris-covered Tasman Glacier, New Zealand. *Journal of Glaciology.* **54**(188), 867-880.

Rowan, A.V. Egholm, D.L. Quincey, D.J. and Glasser, N.F. 2015. Modelling the feedbacks between mass balance, ice flow and debris transport to predict the response to climate change of debris-covered glaciers in the Himalaya. *Earth and Planetary Science Letters.* **430**, 427-438.

Sakai, A. Nishimura, K. Kadota, T. and Takeuchi, N. 2009. Onset of calving at supraglacial lakes on debris-covered glaciers of the Nepal Himalaya. *Journal of Glaciology.* **55**(193), 909-917.

Sakai, A. Takeuchi, N. Fujita, K. and Nakawo, M. 2000. Role of supraglacial ponds in the ablation process of a debris-covered glacier in the Nepal Himalayas. In: Nakawo, M.Raymond, C.F. and Fountain, A., eds. *IAHS Publ. 264 (Symposium at Seattle 2000 – Debris-Covered Glaciers)*, *Seattle, Washington, U.S.A*. IAHS Publishing, 119-130.

Salerno, F. Guyennon, N. Thakuri, S. Viviano, G. Romano, E. Vuillermoz, E. Cristofanelli, P. Stocchi, P. Agrillo, G. Ma, Y. and Tartari, G. 2015. Weak precipitation, warm winters and springs impact glaciers of south slopes of Mt. Everest (central Himalaya) in the last 2 decades (1994–2013). *The Cryosphere.* **9**(3), 1229-1247.

Salerno, F. Thakuri, S. D'Agata, C. Smiraglia, C. Manfredi, E.C. Viviano, G. and Tartari, G. 2012. Glacial lake distribution in the Mount Everest region: Uncertainty of measurement and conditions of formation. *Global and Planetary Change.* **92-93**, 30-39.

Shrestha, A.B. and Aryal, R. 2011. Climate change in Nepal and its impact on Himalayan glaciers. *Regional Environmental Change.* **11**, 65-77.

Somos-Valenzuela, M.A. McKinney, D.C. Rounce, D.R. and Byers, A.C. 2014. Changes in Imja Tsho in the Mount Everest region of Nepal. *The Cryosphere.* **8**(5), 1661-1671.

Steiner, J.F. Pellicciotti, F. Buri, P. Miles, E.S. Immerzeel, W.W. and Reid, T.D. 2015. Modelling ice-cliff backwasting on a debris-covered glacier in the Nepalese Himalaya. *Journal of Glaciology.* **61**(229), 889-907.

Strozzi, T. Wiesmann, A. Kääb, A. Joshi, S. and Mool, P. 2012. Glacial lake mapping with very high resolution satellite SAR data. *Natural Hazards and Earth System Sciences.* **12**(8), 2487-2498.

Thompson, S.S. Benn, D.I. Dennis, K. and Luckman, A. 2012. A rapidly growing moraine-dammed glacial lake on Ngozumpa Glacier, Nepal. *Geomorphology.* **145**, 1-11.

Veettil, B. Bianchini, N. de Andrade, A. Bremer, U. Simões, J. and de Souza Junior, E. 2015. Glacier changes and related glacial lake expansion in the Bhutan Himalaya, 1990–2010. *Regional Environmental Change.* 1-12.

Wagnon, P. Vincent, C. Arnaud, Y. Berthier, E. Vuillermoz, E. Gruber, S. Ménégoz, M. Gilbert, A. Dumont, M. Shea, J.M. Stumm, D. and Pokhrel, B.K. 2013. Seasonal and annual mass balances of Mera and Pokalde glaciers (Nepal Himalaya) since 2007. *The Cryosphere.* **7**(6), 1769-1786.

Wang, S. and Zhang, T. 2014. Spatial change detection of glacial lakes in the Koshi River Basin, the Central Himalayas. *Environmental Earth Sciences.* **72**(11), 4381-4391.

Wang, W.C. Xiang, Y. Gao, Y. Lu, A.X. and Yao, T.D. 2015. Rapid expansion of glacial lakes caused by climate and glacier retreat in the Central Himalayas. *Hydrological Processes.* **29**(6), 859-874.

Wang, X. Liu, S.Y. Han, H.D. Wang, J. and Liu, Q. 2012. Thermal regime of a supraglacial lake on the debris-covered Koxkar Glacier, southwest Tianshan, China. *Environmental Earth Sciences.* **67**(1), 175-183.

Watanabe, T. Ives, J.D. and Hammond, J.E. 1994. Rapid Growth of a Glacial Lake in Khumbu Himal, Himalaya: Prospects for a Catastrophic Flood. *Mountain Research and Development.* **14**(4), 329-340.

Wessels, R.L. Kargel, J.S. and Kieffer, H.H. 2002. ASTER measurement of supraglacial lakes in the Mount Everest region of the Himalaya. *Annals of Glaciology.* **34**, 399-408.

Yang, X. Zhang, Y. Zhang, W. Yan, Y. Wang, Z. Ding, M. and Chu, D. 2006. Climate change in Mt. Qomolangma region since 1971. *Journal of Geographical Sciences.* **16**(3), 326-336.

Ye, Q. Bolch, T. Naruse, R. Wang, Y. Zong, J. Wang, Z. Zhao, R. Yang, D. and Kang, S. 2015. Glacier mass changes in Rongbuk catchment on Mt. Qomolangma from 1974 to 2006 based on topographic maps and ALOS PRISM data. *Journal of Hydrology.* **530**, 273-280.

Ye, Q. Zhong, Z. Kang, S. Stein, A. Wei, Q. and Liu, J. 2009. Monitoring glacier and supra-glacier lakes from space in Mt. Qomolangma region of the Himalayas on the Tibetan Plateau in China. *Journal of Mountain Science.* **6**(3), 211-220.

Zhang, G. Yao, T. Xie, H. Wang, W. and Yang, W. 2015. An inventory of glacial lakes in the Third Pole region and their changes in response to global warming. *Global and Planetary Change.* **131**, 148-157.

Chapter 4
Heterogeneous water storage and thermal regime of supraglacial ponds on debris-covered glaciers

C. Scott Watson, Duncan J. Quincey, Jonathan L. Carrivick, Mark W. Smith, Ann V. Rowan, and Robert Richardson

Earth Surface Processes and Landforms. 2017.

DOI: 10.1002/esp.4236

4.1 Abstract

The water storage and energy transfer roles of supraglacial ponds are poorly constrained, yet they are thought to be important components of debris-covered glacier ablation budgets. We used an unmanned surface vessel (USV) to collect sonar depth measurements for 24 ponds to derive the first empirical relationship between their area and volume applicable to the size distribution of ponds commonly encountered on debris-covered glaciers. Additionally, we instrumented nine ponds with thermistors and three with pressure transducers, characterising their thermal regime and capturing three pond drainage events. The deepest and most irregularly-shaped ponds were those associated with ice cliffs, which were connected to the surface or englacial hydrology network (maximum depth = 45.6 m), whereas hydrologically-isolated ponds without ice cliffs were both more circular and shallower (maximum depth = 9.9 m). The englacial drainage of three ponds had the potential to melt ~100 ± 20 × 10^3 kg to ~470 ± 90 × 10^3 kg of glacier ice owing to the large volumes of stored water. Our observations of seasonal pond growth and drainage with their associated calculations of stored thermal energy have implications for glacier ice flow, the progressive enlargement and sudden collapse of englacial conduits, and the location of glacier ablation hot-spots where ponds and ice cliffs interact. Additionally, the evolutionary trajectory of these ponds controls large proglacial lake formation in deglaciating environments.

4.2 Introduction

Debris-covered glaciers are an increasingly common part of the mountain cryosphere, as glacier mass loss promotes the exhumation of englacial rock debris and the development of supraglacial debris layers (Benn et al., 2012; Thakuri et al., 2014). A combination of low glacier surface gradients, stagnating glacier termini and negative mass balance regimes is initiating increased supraglacial water storage on Himalayan debris-covered glaciers through the positive feedback of solar radiation absorption and transmission to glacier ice (Reynolds, 2000; Sakai et al., 2000; Quincey et al., 2007; Benn et al., 2012; Salerno et al., 2012). Coalescing ponds approaching the hydrological base level can ultimately form large proglacial lakes, which are impounded at the edge of a glacier and can expand rapidly through calving (Kirkbride, 1993; Watanabe et al., 1994; Sakai et al., 2009; Rohl, 2008; Carrivick and Tweed, 2013). In this paper we define supraglacial ponds as water bodies ≤20,000 m2 (e.g. Biggs et al., 2005). The expansion of supraglacial ponds and proglacial lakes is ongoing across the central and eastern Himalaya (Komori, 2008; Gardelle et al., 2011; Nie et al., 2013; Wang et al., 2015; Zhang et al., 2015; Watson et al., 2016; Nie et al., 2017), and is of great concern not least due to the potential glacial lake outburst flood (GLOF) hazards for downstream communities and infrastructure (Kattelmann, 2003; Benn et al., 2012; Carrivick and Tweed, 2016; Rounce et al., 2016; Rounce et al., 2017a), but also for potential effects on glacier flow dynamics and on glacier mass balance (Carrivick and Tweed, 2013).

Glacial lake bathymetry data are predominantly collected for large proglacial lakes in order to parameterise GLOF hazards or to investigate the ice-marginal lake interactions at glacier calving fronts (Fujita et al., 2009; Shrestha and Nakagawa, 2014; Somos-Valenzuela et al., 2014a; Lamsal et al., 2016; Purdie et al., 2016; Sugiyama et al., 2016). Cook and Quincey (2015) compared three commonly-used empirical relationships between glacial lake area and volume, the latter as derived from some knowledge of lake bathymetry, and replotted a compiled dataset of 75 lake measurements, which included several lakes surveyed multiple times. Their analysis revealed that predicted lake volume can vary by an order of magnitude for a given area due to variable lake bathymetry morphologies. A wide spread of predicted volumes is problematic when attempting to characterise an increasing number of lakes developing in deglaciating basins (Carrivick and Tweed, 2013). Additionally, the bathymetry of proglacial lakes or ponds associated with debris-covered glaciers cannot be derived using remotely sensed imagery due to high turbidity, in contrast to

examples of supraglacial lakes from Greenland (e.g. Box and Ski, 2007; Moussavi et al., 2016; Pope et al., 2016). Therefore, there is a clear requirement to better constrain empirical relationships between lake area and volume and to include data from the size distribution of supraglacial ponds typically found on debris-covered glaciers (Cook and Quincey, 2015).

Supraglacial ponds and adjacent ice cliffs appear as hot-spots of melt in multi-temporal digital elevation model (DEM) differencing, in contrast to subdued melt under a thick insulating debris-layer (e.g. Nicholson and Benn, 2013; Immerzeel et al., 2014; Pellicciotti et al., 2015; Ragettli et al., 2016; Thompson et al., 2016). Therefore, quantifying the spatio-temporal dynamics of supraglacial ponds and their interaction with ice cliffs is essential to assess their contribution towards glacier-wide ablation and seasonal water storage (Miles et al., 2016b; Watson et al., 2016); however, little is known about their seasonal expansion and contraction, thermal regime, or bathymetry. Optical satellite images are often obscured by clouds during the Indian Summer Monsoon, which restricts assessments of seasonal pond dynamics. Cloud-penetrating synthetic aperture radar (SAR) data has been used to map and monitor glacial lake dynamics on the Greenland Ice Sheet (e.g. Miles et al., 2017); however, Himalayan applications are limited to large proglacial lakes thus far (Strozzi et al., 2012). Additionally, studies instrumenting ponds with temperature or water level sensors are rare (e.g. Xin et al., 2012; Horodyskyj, 2015; Miles et al., 2016a; Narama et al., 2017). Notably, the modelling of supraglacial pond energy balance by Sakai et al. (2000) and Miles et al. (2016a) revealed that ponds effectively absorb and transmit thermal energy englacially, and therefore are likely to be key contributors to glacier downwasting.

In this study, we aimed to assess the annual variation in supraglacial pond dynamics and characteristics in order to assess their role for water storage, englacial ablation, and interaction with ice cliffs on debris-covered glaciers. Specifically we: (1) derive the bathymetry, thermal regime, and seasonal water level change, of supraglacial ponds on Khumbu and Lobuche Glaciers in the Everest region of Nepal; (2) use the bathymetry of 24 supraglacial ponds to derive an empirical area-volume relationship; (3) quantify the potential englacial ablation of draining ponds; (4) quantify the variation in pond morphology in relation to the presence of ice cliffs.

4.3 Data collection and methods

4.3.1 Study sites

Field data were collected on the debris-covered zones of Khumbu and Lobuche Glaciers in the Everest region of Nepal during three field campaigns (October/ November 2015, May 2016, and October 2016) (Figure 4.1). Khumbu Glacier is ~17

km long with a ~10 km debris-covered ablation area, of which the lower ~4 km is essentially stagnant (Quincey et al., 2009). Within this stagnating part of the glacier, supraglacial ponds are increasingly coalescing to form a connected chain of surface water that is approaching the glacier's hydrological base level (Watson et al., 2016), which is expected to transition into a proglacial lake (Naito et al., 2000; Bolch et al., 2011). By comparison, Lobuche Glacier is smaller, with a relic debris-covered ablation zone ~1 km in length that is now disconnected from clean ice at higher elevations in the accumulation area.

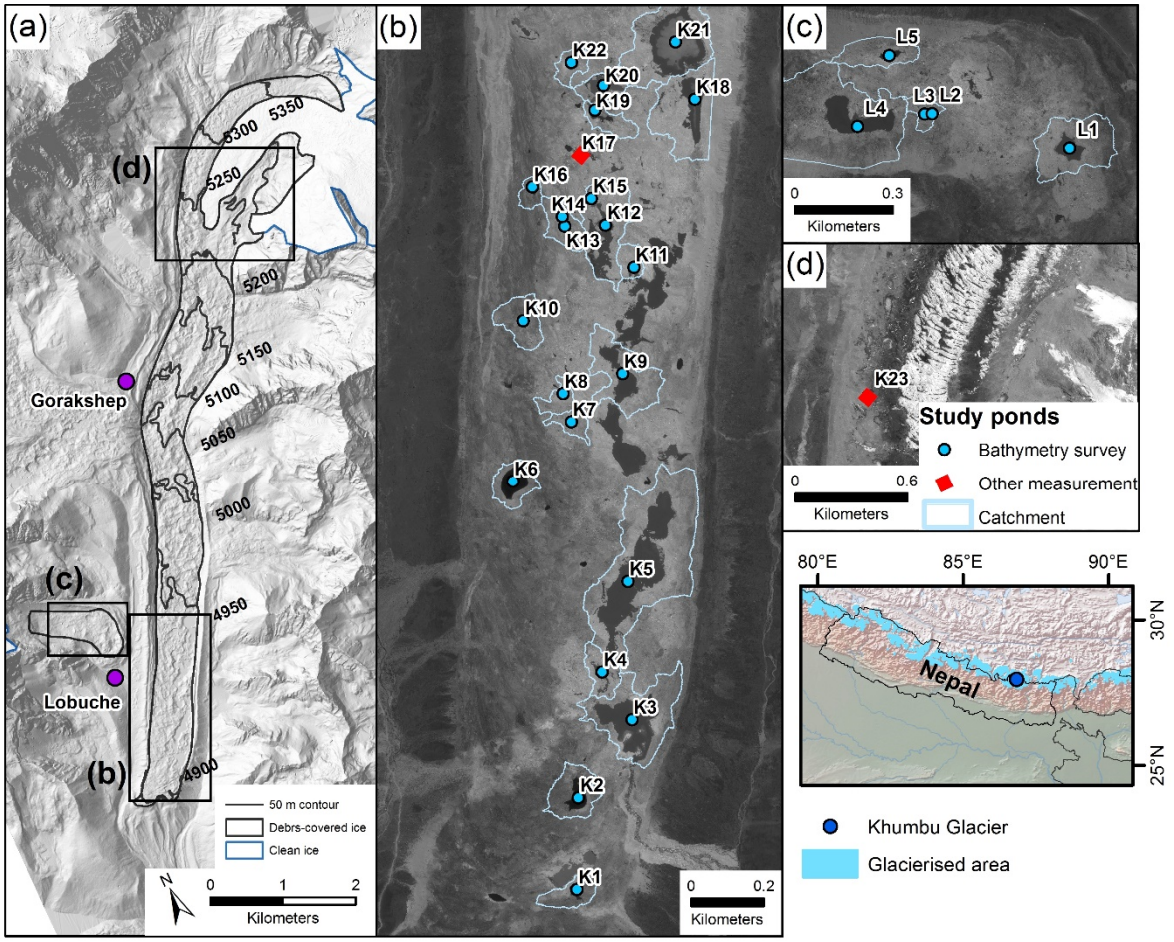

Figure 4.1. (a) The location of the study ponds on Khumbu and Lobuche Glaciers, Nepal with a hillshaded Pleiades DEM background. (b) The lower terminus of Khumbu Glacier (c) The disconnected terminus of Lobuche Glacier. (d) The upper ablation zone of Khumbu Glacier at the transition from debris-covered to clean ice. Pond catchments are shown as light blue polygons (b and c). Inset backdrops are a panchromatic Pleiades satellite image (16th May 2016).

4.3.2 Pond depth surveys

An unmanned surface vessel (USV) was custom-built for the acquisition of global positioning system (GPS)-referenced depth measurements from unfrozen supraglacial ponds (Table 4.1, Figure 4.2). The USV was deployed on 24 supraglacial

ponds during a field campaign in May 2016 and completed a total survey distance of 18 km. Ponds were surveyed along transects (Figure 4.2c), although the track spacing was variable between ponds and was greatest for larger ponds.

Table 4.1. USV specifications

Feature	Specification
Dimensions L × W × H	56 × 45 × 16 cm
Weight	5.5 kg
Power	2 × 5800 mAh 11.1V LiPo batteries
Speed	~3 km/h
Sonar	Furuno 235dt-pse 235 kHz Maximum depth reading: 100 m 1 measurement per second Accuracy: ±3%
Assembly time	15 minutes
Remote control range	150 metres

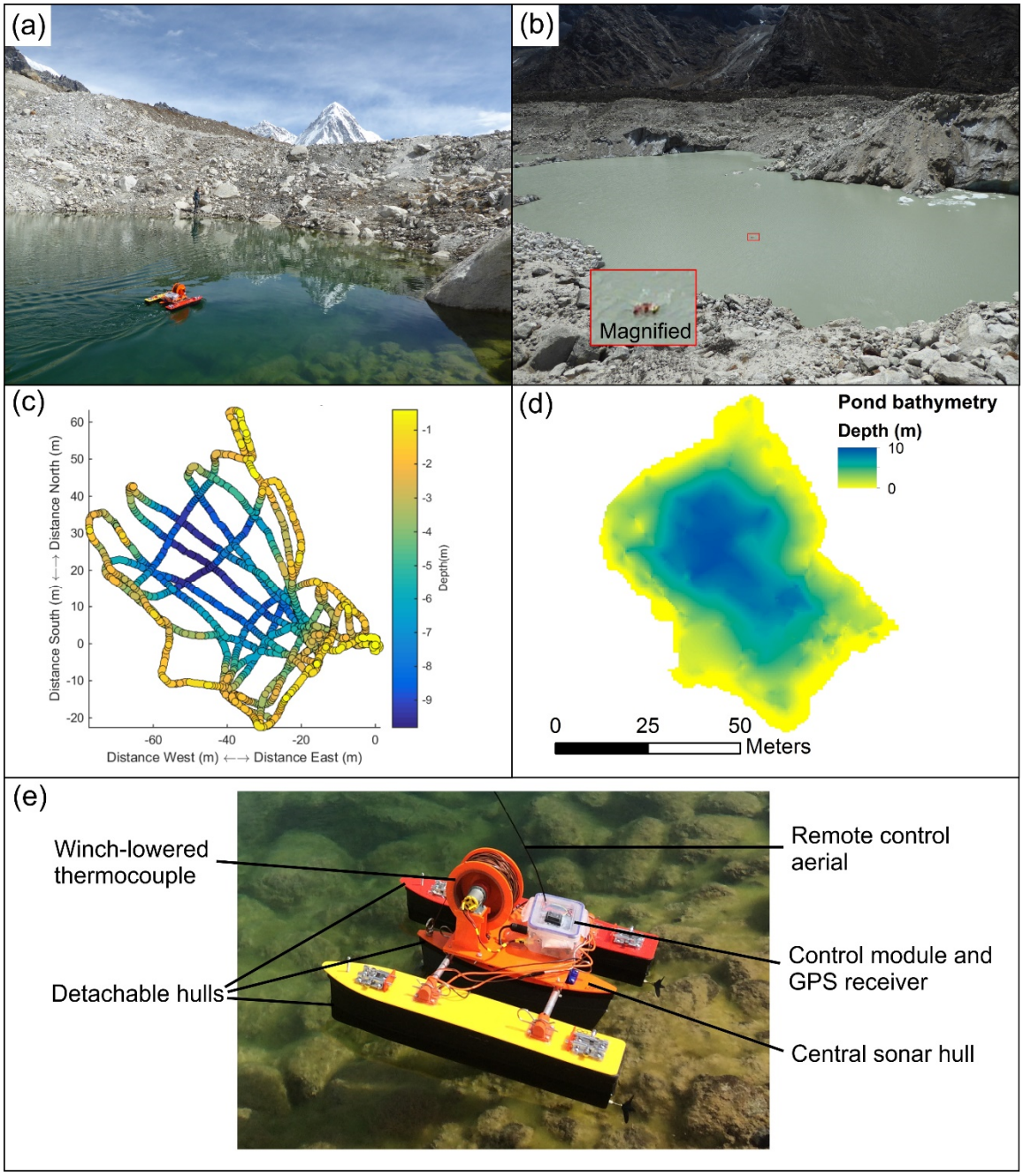

Figure 4.2. (a) The unmanned surface vessel deployed on a small isolated 'green' pond with no ice cliffs present, and (b) a large connected highly-turbid 'grey' pond with ice cliffs. (c) An example of the point depth measurements collected during a survey, and (d) bathymetry derived by interpolation of the data in (c). (e) The unmanned surface vehicle and modular components.

4.3.3 Supraglacial pond characteristics

Ponds were classified into three categories to characterise their hydrological connectivity and turbidity (e.g. Wessels et al., 2002; Takeuchi et al., 2012): 'isolated ponds' (n = 9) did not have inflows/outflows of water or ice cliffs; 'connected ponds without ice cliffs' (n = 6) were of higher turbidity and had inflows or outflows of water; and 'connected ponds with ice cliffs' (n = 9) were of highest turbidity, had inflows or

outflows of water, and exhibited regular debris input due to ice cliff retreat. In this study, all ponds with ice cliffs had hydrological connectivity beyond their individual basins, although we note that this may not always be the case. Similarly, ponds may transition from one classification to another. The pond classification can generally be recognised by characteristic colours: isolated ponds were either green or clear, ponds connected without ice cliffs were turquoise, and ponds connected with ice cliffs were grey.

Hereon, ponds are referred to by their ID number (Figure 4.1), prefixed by 'K' for ponds on Khumbu Glacier or 'L' for ponds on Lobuche Glacier. The area and boundary of ponds was derived following Watson et al. (2016), by applying object-based image analysis (OBIA) classification applied to a panchromatic Pleiades satellite image (16th May 2016) followed by manual inspection and editing using corresponding multi-spectral imagery. All bathymetric surveys were conducted within 14 days of this image, hence we assumed that pond area did not change within this interval. However, pond boundaries buffered by one pixel were used in an uncertainty assessment described in the next section.

4.3.4 Supraglacial pond bathymetry

Sonar depth measurements collected by the USV were interpolated using the Natural Neighbour algorithm in ArcGIS, which preserves the values of measurement points, to derive the bathymetry for each supraglacial pond. Interpolated depths were gridded at 0.5 m resolution and forced to zero at the pond boundary derived from the Pleiades imagery, other than where an ice cliff was present, since cliffs are associated with pond deepening (Miles et al. 2016a; Watson et al. in press). The surface area and volume of each pond were used to derive a power-law area-volume relationship. We performed a leave-one-out analysis to assess the uncertainty when deriving pond volumes using this area-volume relationship. Here, the area and volume of individual ponds were omitted from the dataset and an updated area-volume relationship was derived. We then used this updated relationship to predict the omitted pond's volume and assess the difference compared to the volume predicted using the original relationship (i.e. with the complete pond dataset). Uncertainties in pond area and volume were derived from 1000 Monte Carlo simulations of pond area and volume for each pond. Here, a Gaussian error model with a standard deviation equal to 3 % of the maximum pond depth (based on the sonar sensor uncertainty) was added to interpolated pond bathymetries using pond extents derived from the Pleiades satellite image (500 simulations), and these same pond extents with a one pixel buffer (500 simulations). These buffered pond extents represented potential pond expansion in the 14 day interval between the acquisition of the satellite image, and the final bathymetric surveys. Each simulation produced an estimate of pond area and volume,

and the uncertainties reported in Table 2 represent one standard deviation of the 1000 simulations.

To investigate the spatial relationship between water depth and ice cliff presence, we generated sub samples of pond depth for all ponds with and without ice cliffs present. For ponds without an ice cliff present, polygonal buffers were generated from the pond shorelines at 0−5 m and 5−10 m. For ponds with an ice cliff present, polygonal buffers were also generated from pond shorelines at 0−5 m and 5−10 m, and additional buffers of the same distance were generated from the shoreline bounded by ice cliffs. These buffers were used to extracted depth measurements using both the raw data points and interpolated pond bathymetry. Pair-wise Mann-Whitney U tests were then used to test for differences between each subsample of depth measurements.

4.3.5 Supraglacial pond instrumentation and monitoring

Ibutton thermistors (DS1922L-F5, number (*n*) = 18, with a manufacturer's stated accuracy ±0.5°) were deployed in eight supraglacial ponds in October 2015 to monitor the thermal regime for one year, with a recording frequency of 60 minutes. Thermistors were shielded in a metal casing and deployed on a string, with one sensor floating at the pond surface attached below a floating buoy and one anchored at the bed by a weight. The strings were reset after downloading data in May 2016 where despite a clear water level rise for several ponds, the buoys remained at the surface due to slack left in the system. Therefore, we expect the top sensors were within 20 cm of the surface at all times. Pond K12 had two thermistor strings, one near an inlet to the pond and one near an ice cliff. Water level change was recorded at three ponds which captured different pond characteristics and drainage regimes (K9, K19, K18/21) using Solinst Levelogger Junior Edge pressure transducers.

Thermistors and pressure transducers were calibrated in a controlled temperature environment, revealing a maximum deviation of ±0.22°C, which was within the manufacturer's stated accuracy of ±0.5°C. Individual temperature calibrations were applied to the field data based on the mean deviation from one thermistor used as a reference logger located in pond K9. Pressure transducers were barometrically compensated using data from the Barologger to report the water level change in ponds K9, K19 and K18/21. Here, water level refers to depth of water above the pressure transducer, which was not the point of maximum pond depth for K9 and K18/21, but was for K19.

Ponds K18/21 and K9 were turbid, with ice cliffs present, and had englacial (K18/21) and supraglacial (K9) drainage outlets. Pond K19 appeared less turbid and did not have an ice cliff present but did have a drainage outlet. The pressure transducer in the channel connecting K18/21 was withdrawn in May 2016 following entrapment on the

bed. A Barologger Edge was deployed on Khumbu Glacier, which was shielded from solar radiation and recorded 1 m above-ground temperature and atmospheric pressure, for correction of the pond data.

We used corresponding pond bathymetry and water level data to derive a volumetric time-series for ponds K9 and K19. This was derived by simulating pond drainage at 20 cm increments and calculating the remaining pond area and volume for each iteration. Polynomial trend lines were fitted to area-volume scatter plots and the relationship was used to estimate the pond volume for each water level measurement. This was not possible for K18/21, since the pressure transducer became exposed and was withdrawn before bathymetry was collected in May 2016. Supraglacial pond drainage was simulated for all ponds with bathymetry data to derive individual area-volume relationships. Finally, study pond catchments were derived using ArcHydro Tools in ArcGIS and the circularity of pond boundaries was calculated using:

$$(1)\ \text{Circularity} = \frac{\mathrm{P}^2}{4\pi\mathrm{A}}$$

where *P* and *A* are pond perimeter (m) and area (m^2) respectively. A circle would have a score of one.

4.4 Results

4.4.1 Supraglacial pond bathymetry and volume

The area of supraglacial ponds ranged from 39 m^2 (K14. Maximum depth of 1.3 m) to 18,744 m^2 (K21. Maximum depth of 45.6 m) with interpolated volumes of 24 m^3 and 290,928 m^3 respectively (Table 4.2). K21 was also the deepest pond at 45.6 m. Surveyed ponds had a total volume of 407,214 ± 2908 m^3 and 92,020 ± 680 m^3 on Khumbu and Lobuche Glaciers respectively. The water volume on Lobuche Glacier represents the total visible surface water storage since all supraglacial ponds were surveyed, whereas an estimated 26% of total pond area was surveyed on Khumbu Glacier.

Table 4.2. Supraglacial pond characteristics

Pond ID	Area (m^2)	Volume (m^3)	Maximum depth (m)	Connectivity (I – Isolated, C – connected, CI – connected with ice cliff present)	Circularity	Elevation (m)	Notes
K1	943 ± 36	1443 ± 41	5.5	I	1.90	4892	

K2	2729 ± 63	9049 ± 111	9.9	I	2.37	4906	
K3				C		4905	Data gaps*
K4	958 ± 34	1460 ± 29	3.5	CI	1.83	4910	
K5				CI		4912	Data gaps*
K6	4010 ± 56	19042 ± 119	9.1	I	1.28	4926	
K7	255 ± 10	379 ± 18	4.3	I	1.38	4924	
K8	250 ± 13	445 ± 18	4.4	C	1.14	4922	
K9	5422 ± 54	26959 ± 213	14.6	CI	3.47	4913	
K10	392 ± 11	752 ± 24	4.5	I	1.27	4929	
K11	600 ± 28	882 ± 22	3.4	CI	1.98	4914	
K12	3654 ± 107	5746 ± 158	6	CI	6.63	4913	
K13	231 ± 10	342 ± 13	3.3	I	1.14	4926	
K14	39 ± 6	24 ± 4	1.3	I	1.36	4926	
K15	596 ± 18	1087 ± 28	4	CI	1.73	4914	
K16	625 ± 16	1497 ± 32	5.5	I	1.55	4932	
K18	6482 ± 119	30058 ± 293	13.5	C	3.40	4917	
K19	1193 ± 59	2116 ± 66	6.1	C	4.00	4927	Main drainage event 19-25/07/16
K20	3502 ± 56	13369 ± 163	8.8	CI	2.61	4925	Drainage initiation on 19/07/2016
K21	18744 ± 97	290928 ± 1528	45.6	CI	1.56	4917	
K22	754 ± 24	1634 ± 28	4.5	I	1.27	4932	Drained 27-29/08/16
K23						5211	Drainage initiation on 02/07/16

L1	3789 ± 38	16986 ± 101	9.8	CI	1.63	4965
L2	207 ± 10	235 ± 16	3.1	C	2.05	4971
L3	318 ± 11	496 ± 19	4.3	C	1.53	4971
L4	13101 ± 192	71514 ± 502	17.2	CI	2.71	4970
L5	1530 ± 40	2789 ± 42	4	C	1.84	4977
*Bathymetry not used due to partial pond coverage						

The bathymetric data revealed that ponds rapidly deepen from the shoreline into one or more distinct basins (Figure 4.3). The maximum pond depths for connected ponds with an ice cliff, connected ponds without an ice cliff, and isolated ponds, were 45.6 m (K21), 13.5 m (K18), and 9.9 m (K2) respectively. Hydrologically-isolated ponds tended to be more circular in shape (mean circularity 1.50 ± 0.40) when compared to connected ponds with or without ice cliffs (mean circularity 2.54 ± 0.50) (Table 4.2), which had elongated or multiple basins (e.g. Figure 4.3f, g). Despite being initially classified as an isolated pond, an ice cliff appeared at the southern margin of K6 over the summer monsoon and the water level had dropped ~1 m between May−October 2016. Therefore, the pond classifications used in this study are not exclusive and ponds may transition between classes. Connected ponds with ice cliffs were generally deeper in areas adjacent to the cliff faces and there was no evidence of an ice ramp protruding from any of the faces (e.g. Figure 4.3b, c, d). However, this was less apparent for several smaller ice cliffs (e.g. Figure 4.3a) or those bounded by areas of slumping debris, where pond depth increased more gradually from the shoreline.

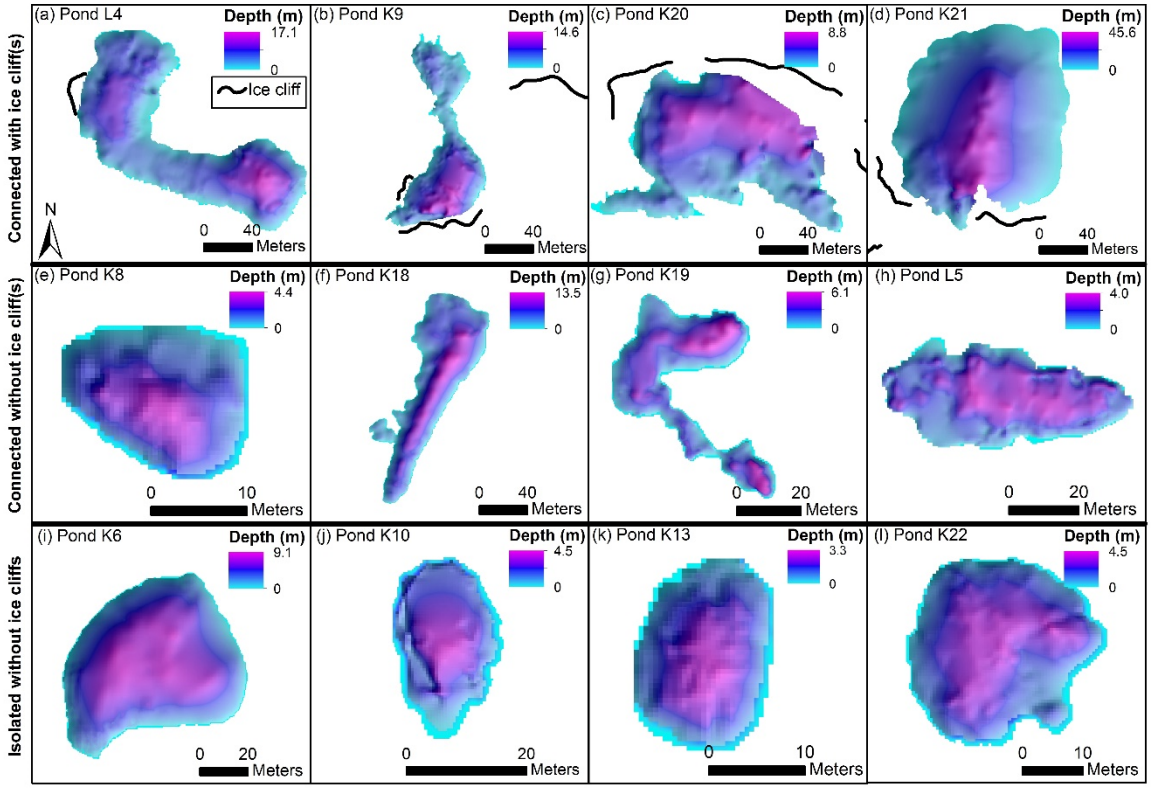

Figure 4.3. Examples of pond bathymetry for connected ponds with ice cliffs (a−d), connected ponds without ice cliffs (e−h), and isolated ponds (i−l). The top edge of adjacent ice cliffs are shown as black lines. Note different scales between panels. A smoothed (low-pass filter) hillshade overlay is shown with transparency.

We analysed the spatial variation in pond bathymetry using two shoreline buffers (0−5 m and 5−10 m) for groups of ponds with and without ice cliffs (Figure 4.4). The buffers for ponds with ice cliffs were split into cliff and non-cliff shoreline zones. Considering pond depth characteristics using the raw data points (e.g. Figure 4.2c), for ponds with ice cliffs, the area of pond 5−10 m from the ice cliff face had the highest median and mean depth (4.70 and 7.62 m respectively) (Figure 4.4). The median depth 0−5 m from ice cliffs (4.00 m) was significantly deeper than the median depth 0−5 m from non-cliff shorelines (1.60 m) (pair-wise Mann-Whitney U test, $p < 0.05$). Considering the non-cliff shoreline of ponds with and without ice cliffs, the 5−10 m zones were statistically different although this difference was small (median depths of 3.40 m and 3.70 m respectively). Pond depth comparisons using the interpolated pond bathymetry were similar to those using the raw data points, but generally of shallower depth (Supplementary Figure 4.1).

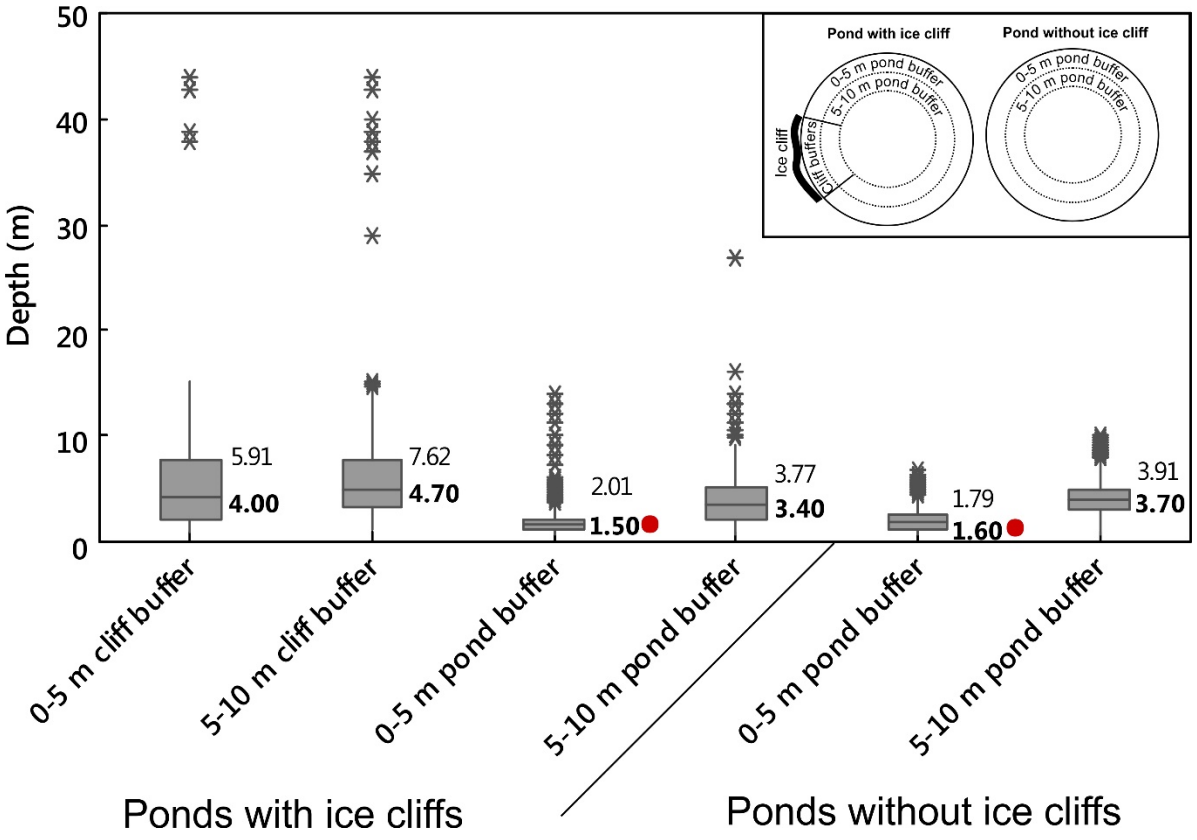

Figure 4.4. Depth characteristics of all ponds with and without cliffs using the raw data points sampled with buffers (illustrated in the inset). All buffers were tested against each other using pair-wise Mann-Whitney U tests. Medians (bold) were statistically significant at $p < 0.05$ unless indicated with a red circle. Mean values are shown above the median. Boxes indicate the interquartile range, whiskers extend to the maximum and minimum data point within 1.5 times the interquartile range from the top and bottom of the boxes respectively, and stars are outliers (greater than 1.5 times the interquartile range from the edge of the box).

4.4.2 Area-volume relationships

The area and volume of surveyed supraglacial ponds in this study followed a power-law trend with a strong positive correlation (R^2 = 0.98) (Figure 4.5a); however, connected ponds with ice cliffs displayed greatest variability. The observed power-law relationship was comparable to that for the compiled dataset of Cook and Quincey (2015) but substantially extends coverage to include much smaller ponds (Figure 4.5b). When comparing the area-volume data points during simulated pond drainage (n = 761), the gradient of the power-law increased and had a slightly lower R^2 of 0.97 (Figure 4.5c). The calculated area-volume relationship for K6 and K20 highlighted the effects of variable pond geometry (Figure 4.5d). K6, which had a regular shoreline and simple geometry draining into a central basin (Figure 4.3i), had a good fit to the power-law (Figure 4.5d). In contrast, K20 (Figure 4.3c) had an irregular shoreline and featured high-depth areas adjacent to an ice cliff, which had greater deviation from the power-law (Figure 4.5d). The ability to predict an individual pond volume V (m^3) using

area A (m^2) using the power law (Equation 2) was not related to pond size (Supplementary Figure 4.2), and instead likely reflects variable pond morphologies. The mean difference between pond volumes calculated using the bathymetry and predicted pond volumes was 22.8%, or 18.5% with an outlier (K21) removed. The mean of the predicted pond volumes (mean pond area of 14609 m^2) underestimated the pond volumes calculated using the bathymetry (mean pond area of 20801 m^2). Based on the addition of the new data from our study, the modified area-volume relationship of Cook and Quincey (2015) becomes:

$$V = 0.1535A^{1.39} \quad (2)$$

from the original:

$$V = 0.2A^{1.37} \quad (3)$$

The percentage differences between volumes predicted using the new versus old equation ranged from 7% (K21) to 19% (K14). We also note that the pond with an ice cliff studied by Miles et al. (2016a) on Lirung Glacier, Nepal, had an area of 650 m^2 and estimated volume of 1250 m^3, which is accurately predicted by Equation (2) as 1245 m^3.

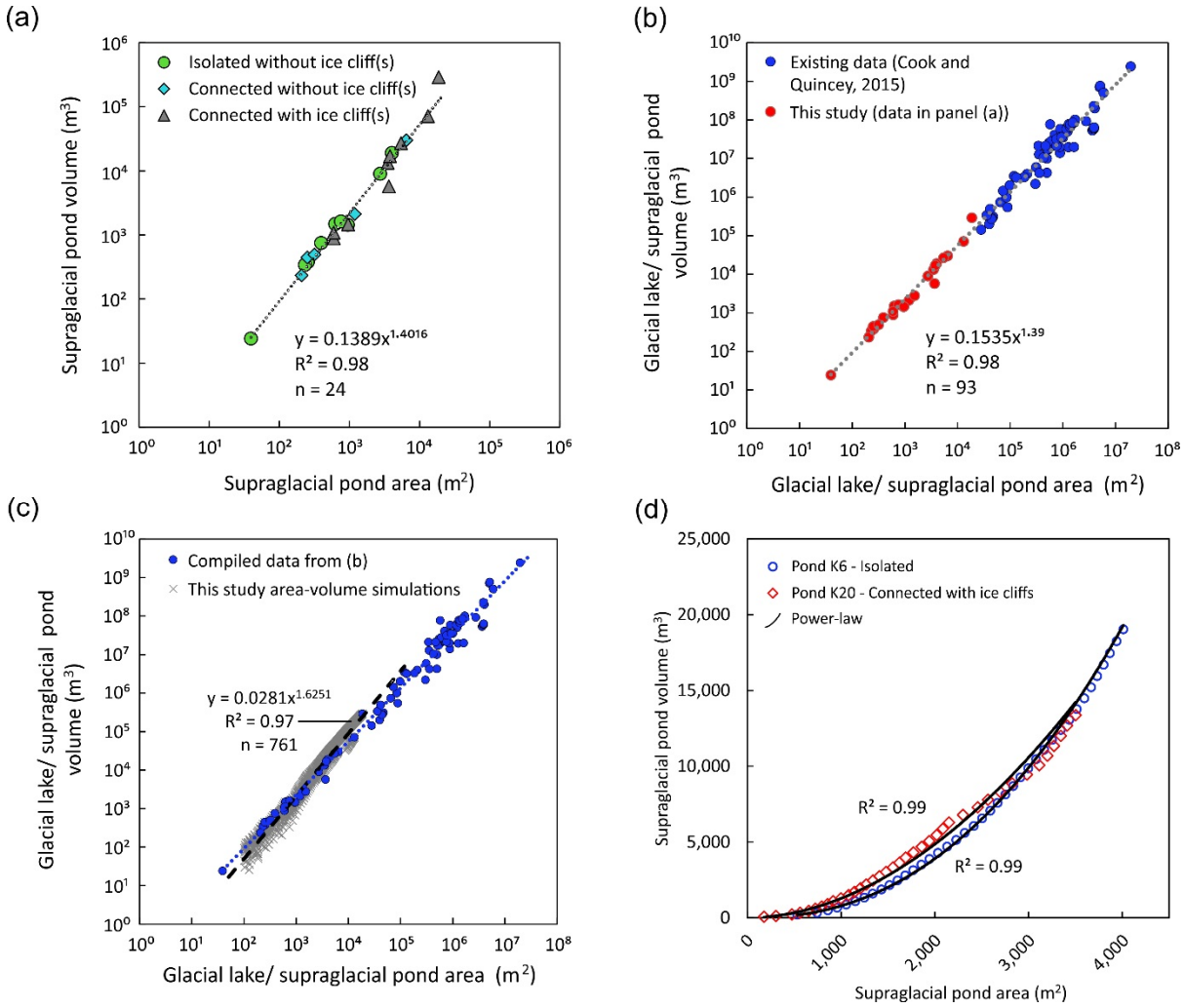

Figure 4.5. (a) Area-volume relationships derived from data in this study. (b) The data of this study combined with the compiled dataset of Cook and Quincey (2015). (c) The data of (b) with additional data points from simulating the drainage of surveyed ponds. A power law is fitted through the simulated drainage data points (n = 761). (d) The area-volume relationship for ponds K6 and K20 during simulated drainage. A power law is fitted for each pond.

4.4.3 Supraglacial pond thermal regime and drainage events

After deployment of the pressure transducer in October 2015, the water level at K19, which was connected without an ice cliff, gradually increased before stabilising December 2015 to March 2016 (Figure 4.6a). The water level started to rise in the first two weeks of April 2016 and the diurnal temperature range increased. The water level reached a peak on the 20th June 2016 at 7.1 m with an estimated volume of 3,145 m^3. The water level then decreased gradually until the 18th July 2016. Subsequent drainage occurred 19th−25th July 2016 from a water level of ~6.4 m to ~3.4 m, which corresponded to an estimated 2,106 m^3 decrease in volume. Diurnal temperature range increased following this drainage (Figure 4.6a). The final drainage event began

10th–11th September 2016 and the water level was zero by 22:00 on the 12th September 2016. Notably, the drainage event initiated on the 19th July 2016 was coincident with a rapid temperature rise in the neighbouring pond K20 (Supplementary Figure 4.3), which we interpret as a coincident drainage event exposing the temperature logger to the atmosphere. K20 was not instrumented with a pressure transducer but field observations confirmed complete drainage by the start of October 2016.

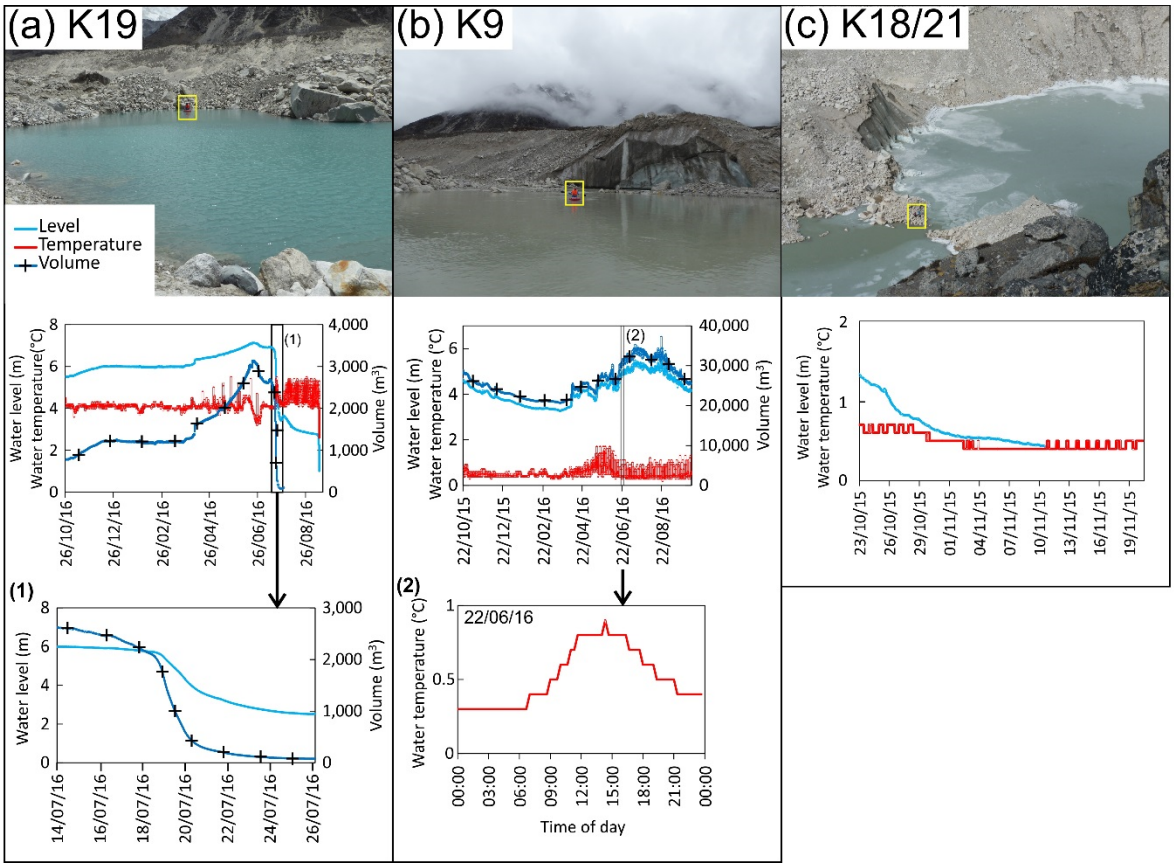

Figure 4.6. Water level and temperature for (a) K19, (b) K9, and (c) K18/21. Slumped ice plates are visible along the shoreline of K21 in November 2015 (c). Pond bathymetry was used to derive a volumetric time series for (a) and (b). Pond temperatures represent the pond bed. Yellow rectangles indicate the author for scale. Dates are dd/mm/yy.

The water level of K9, which was connected and with several ice cliffs, decreased during winter until ~20th March 2016 (Figure 4.6b). The water level then increased during summer reaching peaks on the 12th July 2016 (5.5 m) and 21st August 2016 (5.7 m) before decreasing throughout September 2016. The rising and falling limbs both include a diurnal temperature cycle, but not a diurnal water level fluctuation. The initial and final water level of K9 were comparable (4.6 m on 22nd October 2015 and 4.1 m on 6th October 2016). Notably, the water level of K18/21 also decreased during

the ~1 month of observations in winter, and was also apparent from slumped ice plates around the margin of the pond (Figure 4.6c).

The absolute temperature of K9 was lower than K19; however, the diurnal temperature variation was greatest for K9 with a summer variation of ~0.5°C (Figure 4.7). In contrast, the summer diurnal temperature variation for K19 was ~0.2°C. There was evidence of a subdued winter diurnal temperature cycle in K9 but not in K19; however, the water temperature remained above 4°C in K19 during winter.

Three complete pond drainage events were observed over the study period at K19, K20, and K22. The potential internal glacier ablation resulting from pond drainage through downstream ice *Mi*, assuming a temperature drop to 0°C, can be estimated using Equation (4) (e.g. Thompson et al., 2016):

$$M_i = M_w \Delta T \left(\frac{C}{L}\right) \quad (4)$$

where *Mw* is the water mass, ΔT indicates the difference in temperature between observed and zero, *C* the specific heat capacity of water (4.2 kJ kg^{-1} k^{-1}) and *L* the latent heat of melting (344 kJ kg^{-1} k^{-1}). For ΔT we calculated the mean surface temperature and mean bottom temperature of the day prior to drainage and then used the median of these two values. Measurement uncertainties in pond temperature (± 0.5°C) and volume (Table 4.2) were used to derive a confidence interval when calculating the englacial ablation potential of drained ponds. The drainage of K22 with a water mass of 1634 ± 28 × 10^3 kg and temperature change 10.3 ± 0.5 °C had an englacial ablation potential of 203 ± 14 × 10^3 kg. The drainage of K20 with a water mass of 13369 ± 163 × 10^3 kg and a temperature change of 2.9 ± 0.5 °C had an englacial ablation potential of 473 ± 88 × 10^3 kg. The drainage of K19 with a water mass of 2116 ± 66 × 10^3 kg and temperature change of 4.0 ± 0.5 °C had an englacial ablation potential of 103 ± 17 × 10^3 kg.

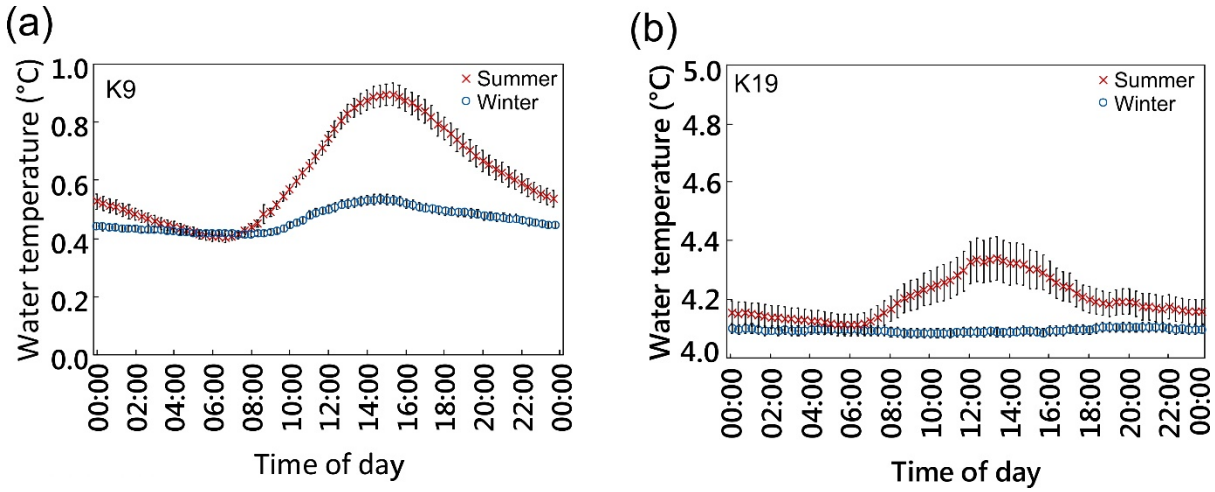

Figure 4.7. Mean and standard deviation of 20 minute daily pond bottom water temperatures for ponds (a) K9 and (b) K19. Note the broken y-axis (b). Winter and summer intervals are 28/10/15−19/03/16 and 20/03/16−01/09/16 respectively.

4.4.4 Ponds temperature

The mean water temperature of isolated ponds and connected ponds without ice cliffs, was greater than connected ponds with ice cliffs (Figure 4.8). Mean bottom water temperatures for connected ponds with ice cliffs ranged from 0.1 to 0.5°C for winter and 0.2 to 2.0°C for summer. In contrast, the mean bottom water temperatures for isolated and connected ponds without ice cliffs ranged from 4.1 to 5.0°C for winter and 4.2 to 9.8°C for summer. Summer surface water temperatures were comparable to summer bottom water temperatures, suggesting that ponds were well mixed. The greatest difference in mean summer surface and bottom water temperature was 1.2°C for K13. Winter surface temperatures were distinctly different from the winter bottom water temperatures for five ponds (K12, K23, K19, K13, K22), suggesting that temperature loggers became frozen in a layer of ice over winter, which was supported by field observations. K9 had an inflow and outflow of water and was largely ice-free on 22nd October 2015, but had developed a surface layer of ice ~10 cm thick by 11th November 2015. Other ponds without hydrological connectivity were observed to be freezing over upon arrival into the field on 20th October 2015.

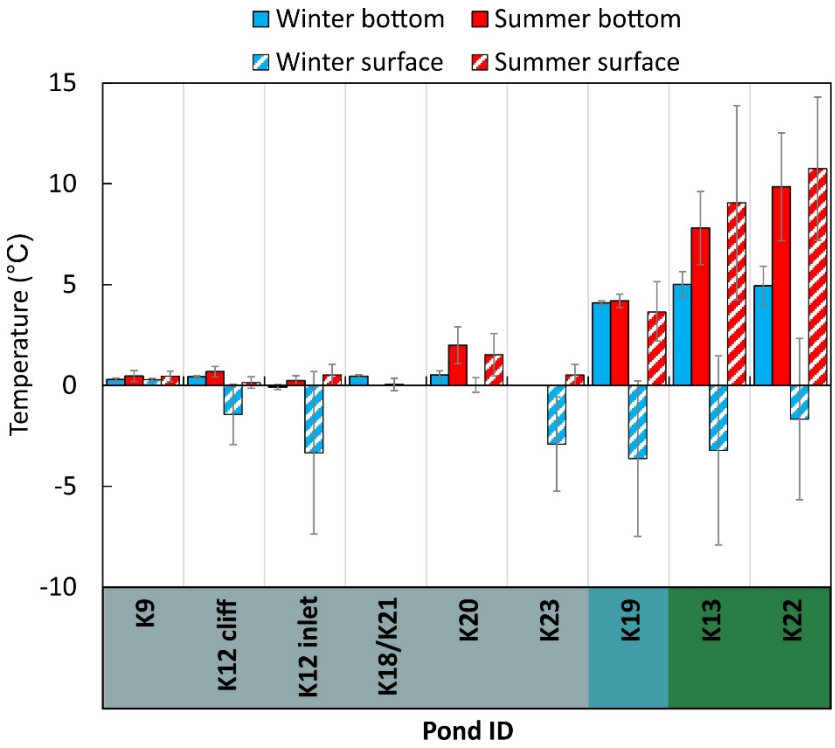

Figure 4.8. Seasonal supraglacial pond bottom and surface water mean temperatures. Error bars indicate one standard deviation. Coloured x-axis represents indicative pond colour for connected ponds with an ice cliff (grey), connected ponds without an ice cliff (turquoise), and isolated ponds without cliffs (green). With the exception of K23 (5211 m), ponds are at similar elevation (4892-4932 m).

4.5 Discussion

4.5.1 Supraglacial pond bathymetry

Our data contribute to a sparse bathymetry dataset of supraglacial ponds on Himalayan debris-covered glaciers, which is due to the significant effort that is required to make distributed depth measurements. Point measurements of pond or lake depths are usually made using a sonar after cutting through the frozen surface (Benn et al., 2001); directly through the frozen surface using sonar (Thompson et al., 2012); from a boat (Rohl, 2008; Somos-Valenzuela et al., 2014b); or more recently using ground-penetrating radar (GPR) (Mertes et al., 2016), which provides additional information on basal sediment. The spatial resolution of surveys can be increased when using an USV (Horodyskyj, 2015), which also allows sampling close to ice cliffs where falling debris would otherwise restrict safe access.

Hydrologically-isolated ponds without ice cliffs were located along the western margin of Khumbu Glacier, which is stagnant and supporting some scrub vegetation in parts (Inoue and Yoshida, 1980); however, the sub-debris ice content is unknown. These isolated ponds often exhibited a green appearance due to algal growth and low

turbidity (Takeuchi et al., 2012), and were generally smaller and shallower than the other ponds surveyed. However, isolated ponds K2 and K6 had depths of 9.9 m and 9.1 m respectively (Table 4.2). Notably, an ice cliff developed along the margin of K6 and the water level dropped by over 1 m during the 2016 summer monsoon. Pond K6 was identified by Iwata et al. (1980) in 1978 and has persisted in a similar shape with little change in areal extent (Watson et al., 2016). It is not clear whether a degrading ice core in this area will lead to further drainage. Nonetheless, it indicates that apparently stable ponds on stagnant parts of the glacier may still be actively deepening towards the hydrological base level.

Connected ponds with ice cliffs had the greatest depths and often elongated or multiple basins (Figure 4.3). The greatest measured depth was 45.6 m at K21, which is located in an area of maximum ice thickness of ~100 m (Gades et al., 2000). The maximum depth was observed adjacent to a large ice cliff (Figure 4.3d), similar to observations by Thompson et al. (2016) and Horodyskyj (2015) on Ngozumpa Glacier, who observed maximum depths of 27 m and 54 m close to ice cliffs. Miles et al. (2016a) observed linearly increasing pond depth approaching an ice cliff on Lirung Glacier, although depth measurements were limited due to rockfall hazard. Whilst pond depth generally increased approaching large ice cliff faces in our observations (Figure 4.3), this was not the case for many smaller ice cliffs or those in areas of slumping debris. This variability led to greatest depth observations in areas 5−10 m from cliff faces (Figure 4.4). Shallower pond depth around small ice cliffs likely reflects newly exposed cliff faces or areas where thick subaqueous debris cover due to slumping restricts basal melt (Mertes et al., 2016). In contrast, larger cliff faces develop and persist where subaqueous thermal erosion matches or exceeds subaerial melt or calving (Benn et al., 2001; Sakai et al., 2009). Here, rapid cliff retreat limits debris accumulation at the cliff base and hence it is likely that subaqueous melt of the cliff and pond bed promotes deepening approaching the cliff face. Therefore, the bathymetry of ponds with ice cliffs indicates whether pond expansion is likely, and hence the evolutionary trajectory of the cliff-pond coupling.

4.5.2 Area-volume relationships

We have derived a new empirical area-volume relationship by extending the dataset of Cook and Quincey (2015), through measuring the bathymetry of 24 supraglacial ponds on two debris-covered glaciers not included in their original analysis. Watson et al. (2016) found that individual ponds <3,600 m^2 made up 48−88% of pond area on nine debris-covered glaciers in the Everest region, which is well represented by the range of ponds in this study (39−18,744 m^2), but was not represented in existing datasets (Cook and Quincey, 2015). All surveyed ponds followed a power-law

relationship between area and volume (Figure 4.5a); however, ponds with ice cliffs displayed greatest deviation from this trend, owing to the prevalence of deep zones adjacent to ice cliffs (e.g. K21 Figure 4.3d), or to elongated irregular shaped basins (e.g. K12). This variable morphology was apparent when using a power law to predict individual pond volumes (Supplementary Figure 4.2), where the mean difference between the pond volume and predicted pond volume was 22.8%, or 18.5% with an outlier (K21) removed. An even larger bathymetric dataset would further refine empirical area-volume relationships and facilitate further analysis of ponds of variable ice cliff presence, different hydrological connectivity, and at different stages of development. However, it is clear that area-volume relationships derived from predominantly proglacial lakes can be extended to smaller ponds.

A mean of ~50% of ice cliffs featured a supraglacial pond in the Everest region (Watson et al., 2017), therefore around half of all pond morphologies are expected to be highly dynamic due to ice cliff retreat. In contrast, subaqueous sub-debris melt rates and therefore geometry changes are expected to be low for those without ice cliffs (Miles et al., 2016a). Multi-temporal supraglacial pond bathymetry data are therefore required to assess pond evolution and the trajectory of proglacial lake development. Simulating pond drainage increased the number of area-volume data points (Figure 4.5C) and was used to reconstruct volume change, which is useful to assess the seasonal water storage of ponds. However, these represent a snapshot of pond bed morphology and do not reveal anything about its genesis.

4.5.3 Supraglacial pond drainage and thermal regime

Supraglacial ponds display considerable inter- and intra-annual variation in their surface area (Miles et al., 2016b; Watson et al., 2016), including evidence of a seasonal peak related to the onset of the ablation season with the Indian Summer Monsoon in June (Liu et al., 2015; Miles et al., 2016b; Narama et al., 2017). The observed hydrological regime of ponds K19 and K9 displayed a seasonal trend and water levels peaked in late June and early July 2016 respectively (Figure 4.6a, b). The water level of K9 dropped slightly before a secondary peak on the 21st August. K9 had both an inflow and outflow of water and formed part of a connected series of ponds on the easterly margin of Khumbu Glacier (Figure 4.1b). Therefore, the seasonal water level peak of this pond reflects a combination of maximum meltwater generation during the monsoon and the state of drainage channel evolution at this time, before the water level began to drop in late August 2016.

The sporadic drainage of K19 was likely due to the interception and enlargement of an englacial conduit, which drained most of the pond and was more rapid than the gradual seasonal expansion and drainage observed at K9. The main drainage event

at K19 occurred 19th−25th July 2016; however, the water level of the pond began to drop gradually several days prior to this. Notably, the adjacent pond K20 also appeared to drain on the 19th July 2016, inferred by the aerial exposure of the temperature logger (Supplementary Figure 4.3). The temperature of K19 rose from 4°C to 5.5°C within 24 hours during this drainage event (Figure 4.6a), which may be due to greater local radiation heating as the pond volume decreased. K20 had a lower temperature (~3°C), although it appears likely that both ponds exploited the same englacial conduit to drain and hence developed a sub-surface connection. It is clear that ponds in close proximity are likely to exhibit or develop sub-surface connections that are not apparent from surface observations. Notably, the timing and connectivity of these ponds is also consistent with the observations of Narama et al. (2017), who also observed englacial drainage for June-July for supraglacial ponds in the Tien Shan Mountains.

Water temperatures of ponds with ice cliffs (n = 6) were generally close to zero degrees Celsius and featured a frozen surface during winter, and summer surface temperatures did not exceed 4.2°C (Figure 4.8). The pond monitored by Xin et al. (2012) also had an ice cliff present but was located at ~1685 m lower elevation and had an average summer surface temperature of 9.0°C. The pond with an ice cliff monitored by Miles et al. (2016a) at an elevation of 4070 m had an average temperature of 1–1.5°C and was more comparable to our study ponds. From surveys of ponds on debris-covered glaciers in Nepal, Sakai et al. (2009) revealed that subaqueous melt exceeds subaerial ice cliff melt at ponds with a water temperature of 2−4°C and a fetch of >20m, and that a fetch >~80 m is required for calving. During our study, full-slab calving was observed at K15 and block calving was apparent prior to K12 being instrumented in October 2015 (Supplementary Figure 4.4). These ice blocks at K12 had melted by May 2016. The ponds had fetches of ~35 m and ~140 m respectively, estimated following Sakai et al. (2009). The temperature at K15 was not recorded but the basin was connected to K12, which had a mean temperature of <1°C, and hence did not meet the expected calving criteria. We note that Sakai et al. (2009) also observed a calving cliff with a pond temperature of less than <1°C on Khumbu Glacier, but with a larger fetch of 94 m. It is likely that the higher turnover of water into K15 via an inlet, promoted thermal undercutting and calving despite the small fetch. The role of water inflows should therefore be considered alongside wind-driven currents in the energy-balance modelling of supraglacial ponds (e.g. Miles et al., 2016a).

The temperature of isolated ponds was notably higher than those with ice cliffs, and all had mean temperatures >4°C at the pond bed over winter, suggesting that their thermal energy was stored over winter, insulated by a layer of snow-covered ice

(Figure 4.8). Ponds K19, K20, and K22 drained over the study period with englacial ablation potentials of 103 ± 17 × 10^3 kg, 473 ± 88 × 10^3 kg, and 203 ± 14 × 10^3 kg respectively. Notably K20 had the greatest englacial ablation potential despite having the lowest temperature (1.8°C), due to its volume. These values only represent englacial ablation due to drainage without considering the turnover of water through each pond during their lifespan. Nonetheless, our observations support the role of seasonal pond dynamics acting as a notable source of glacier ablation (Miles et al., 2016a).

4.5.4 Implications of seasonal pond dynamics

Through revealing short-term supraglacial pond dynamics on two Himalayan debris-covered glaciers, our study adds further evidence to support observations of cyclical pond growth and drainage due to ablation and precipitation input during the summer monsoon, followed by winter freezing of the pond surface, which subdues or inhibits diurnal temperature cycles. However, we observed ponds continuing to drain throughout winter (e.g. K9 and K18/K21), suggesting that the hydrological system and hence englacial ablation remained active at this time. Sporadic drainage events are imposed on the seasonal cycle of pond expansion as ponds intercept englacial conduits and stored thermal energy is transmitted englacially, contributing notably to glacier-scale ablation (Sakai et al., 2000; Miles et al., 2016a). Additionally, meltwater was conveyed through ponds by a network of supraglacial and englacial channels (e.g. K15), which leads to a high overturning rate conducive to the undercutting and calving of adjacent ice cliffs (Sakai et al., 2009; Miles et al., 2016a).

Our observations of glacier surface hydrology in the lower ablation zone suggest that seasonal pond expansion and drainage was linked to meltwater generation from glacier ablation; however, this seasonal trend was occasionally interrupted by sporadic short-term drainage events, where ponds intercepted an englacial conduit. These conduits become enlarged when supporting a drainage event and grade towards the hydrological base level, and may support multiple drainage events in between periods of dormancy (Gulley and Benn, 2007; Gulley et al., 2009; Benn et al., 2009). In this study we investigated the potential englacial ablation from draining ponds; however, the quantity and ablative role of water stored in blocked englacial conduits remains unknown. Englacial water storage likely also responds to seasonal ablation processes driving meltwater generation, which is stored and released during outburst flood events (e.g. Rounce et al., 2017b) or buffered by the internal drainage system for larger low-gradient glaciers. In the upper ablation zone of debris-covered glaciers, observations of increased summer velocities on Lirung and Ngozumpa Glaciers, suggest that basal-sliding is promoted where surface meltwater is routed the glacier

bed (e.g. via crevasses) (Kraaijenbrink et al., 2016; Benn et al., 2017). Seasonal velocity observations are lacking for Khumbu Glacier; however, it is likely that surface-bed hydrological connections play a similar role.

Knowledge of short-term pond dynamics and evolution as presented in this study allows a greater understanding of their potential role for glacier-scale ablation, in addition to developing future links between observed mass loss and the meltwater budget. Several key lines of enquiry should be pursued to better constrain the role of the pond-cliff interaction for glacier-wide ablation, and to quantify seasonal meltwater fluxes, which will become increasingly important as the reservoirs of freshwater locked in glaciers decline over the coming century:

(1) Observations of pond dynamics throughout the summer monsoon with high temporal resolution optical or SAR imagery could be used in association with empirical area-volume relationships to predict water fluxes.

(2) Distributed instrumentation of ponds on other debris-covered glaciers combined with pond energy balance modelling (e.g. Miles et al., 2016a) would allow a spatio-temporal assessment of pond thermal regimes and water level fluctuations, which could be used to model their total contribution to glacier-scale ablation.

(3) Multi-temporal pond bathymetry is required to quantify expansion processes related to ice cliff retreat or debris infilling (e.g. Thompson et al., 2016; Mertes et al., 2016), and to better understand the interface between the thickness of basal sediment and glacier ice, which has a large influence on subaqueous melt rates.

4.6 Conclusions

A spatially distributed bathymetric survey of supraglacial ponds has extended the compiled dataset of Cook and Quincey (2015), to determine an empirical relationship between pond area and volume for the size-distribution of ponds commonly encountered on Himalayan debris-covered glaciers. We revealed evidence of pond deepening in association with the presence of ice cliffs up to a depth of 45.6 m, which supports observations of thermal undercutting and their role as hot-spots of melt on debris-covered glaciers. Downward grading of the pond bed in association with ice cliff retreat is likely to promote ice cliff persistence (Watson et al., in press), and a contrasting evolutionary trajectory compared to ponds without ice cliffs. The water temperatures of ponds with ice cliffs (n = 9) were generally close to zero degrees Celsius, and summer surface temperatures did not exceed 4.2°C. The temperature of hydrologically isolated ponds was notably higher and all had mean temperatures >4°C

at the pond bed over winter, suggesting that their thermal energy is stored over winter, trapped in by an insulating layer of snow-covered ice.

Seasonal expansion and drainage of ponds was observed, which supports satellite remote sensing observations (Liu et al., 2015; Miles et al., 2016b; Watson et al., 2016). Continued pond drainage throughout winter suggests the hydrological system and therefore englacial ablation remains at least partially active throughout the year. Sporadic drainage events were imposed on this seasonal cycle as ponds intercepted englacial conduits and transferred their stored thermal energy englacially. Increased meltwater generation during the summer monsoon is also likely to be expressed through englacial water storage and release (Rounce et al., 2017b), in addition to conduit enlargement and collapse, leading to the formation of new surface depressions and ice cliffs.

Acknowledgements

We thank Wojciech Marcinek, Daniel Hicks, Adil Tahir, and Charles Howard for designing and building the USV ('BathyBot') within the School of Mechanical Engineering at the University of Leeds, and Robert Richardson and Shaun Whitehead for their guidance on the project. C.S.W acknowledges fieldwork support from the School of Geography at the University of Leeds, the Mount Everest Foundation, the British Society for Geomorphology, the Royal Geographical Society (with IBG), the Petzl Foundation, and water@leeds. Advanced Elements Kayaks are thanked for a PackLite kayak and Pascal Buri for an earlier dinghy, which enabled pond access. The Natural Environment Research Council Geophysical Equipment Facility is thanked for loaning Global Navigation Satellite Systems receivers and for technical assistance under loan numbers 1050, 1058, and 1065. The Pleiades satellite images was supplied by the European Space Agency under Category-1 Proposal Id. 32600. Dhananjay Regmi and Himalayan Research Expeditions are thanked for fieldwork support and research permit acquisition. Mahesh Magar is thanked for invaluable help collecting data during the three field campaigns. Ian Willis and one anonymous reviewer are thanked for through and constructive reviews, which helped improve this study.

4.7 References

Benn, D Gulley, J Luckman, A Adamek, A and Glowacki, PS. 2009. Englacial drainage systems formed by hydrologically driven crevasse propagation. Journal of Glaciology 55: 513-523.

Benn, DI Bolch, T Hands, K Gulley, J Luckman, A Nicholson, LI Quincey, D Thompson, S Toumi, R and Wiseman, S. 2012. Response of debris-covered glaciers in the Mount Everest region to recent warming, and implications for outburst flood hazards. Earth-Science Reviews 114: 156-174. http://dx.doi.org/10.1016/j.earscirev.2012.03.008

Benn, DI Thompson, S Gulley, J Mertes, J Luckman, A and Nicholson, L. 2017. Structure and evolution of the drainage system of a Himalayan debris-covered glacier, and its relationship with patterns of mass loss. The Cryosphere Discuss. 2017: 1-43. 10.5194/tc-2017-29

Benn, DI Wiseman, S and Hands, KA. 2001. Growth and drainage of supraglacial lakes on debris-mantled Ngozumpa Glacier, Khumbu Himal, Nepal. Journal of Glaciology 47: 626-638. 10.3189/172756501781831729

Biggs, J Williams, P Whitfield, M Nicolet, P and Weatherby, A. 2005. 15 years of pond assessment in Britain: results and lessons learned from the work of Pond Conservation. Aquatic Conservation: Marine and Freshwater Ecosystems 15: 693-714. 10.1002/aqc.745

Bolch, T Pieczonka, T and Benn, DI. 2011. Multi-decadal mass loss of glaciers in the Everest area (Nepal Himalaya) derived from stereo imagery. The Cryosphere 5: 349-358. 10.5194/tc-5-349-2011

Box, JE and Ski, K. 2007. Remote sounding of Greenland supraglacial melt lakes: implications for subglacial hydraulics. Journal of Glaciology 53: 257-265. 10.3189/172756507782202883

Carrivick, JL and Tweed, FS. 2013. Proglacial lakes: character, behaviour and geological importance. Quaternary Science Reviews 78: 34-52. http://dx.doi.org/10.1016/j.quascirev.2013.07.028

Carrivick, JL and Tweed, FS. 2016. A global assessment of the societal impacts of glacier outburst floods. Global and Planetary Change 144: 1-16. http://dx.doi.org/10.1016/j.gloplacha.2016.07.001

Cook, SJ and Quincey, DJ. 2015. Estimating the volume of Alpine glacial lakes. Earth Surf. Dynam. 3: 559-575.

Fujita, K Sakai, A Nuimura, T Yamaguchi, S and Sharma, RR. 2009. Recent changes in Imja Glacial Lake and its damming moraine in the Nepal Himalaya revealed by in situ surveys and multi-temporal ASTER imagery. Environmental Research Letters 4: 1-7. 10.1088/1748-9326/4/4/045205

Gades, A Conway, H and Nereson, N. 2000. Radio echo-sounding through supraglacial debris on Lirung and Khumbu Glaciers, Nepal Himalayas. In: IAHS Publ.

264 (Symposium at Seattle 2000 – Debris-Covered Glaciers), Seattle, Washington, U.S.A. IAHS Publication: 13-22.

Gardelle, J Arnaud, Y and Berthier, E. 2011. Contrasted evolution of glacial lakes along the Hindu Kush Himalaya mountain range between 1990 and 2009. Global and Planetary Change 75: 47-55. http://dx.doi.org/10.1016/j.gloplacha.2010.10.003

Gulley, J Benn, D Müller, D and Luckman, A. 2009a. A cut-and-closure origin for englacial conduits in uncrevassed regions of polythermal glaciers. Journal of Glaciology 55: 66-80.

Gulley, J and Benn, DI. 2007. Structural control of englacial drainage systems in Himalayan debris-covered glaciers. Journal of Glaciology 53: 399-412. 10.3189/002214307783258378

Gulley, JD Benn, DI Screaton, E and Martin, J. 2009b. Mechanisms of englacial conduit formation and their implications for subglacial recharge. Quaternary Science Reviews 28: 1984-1999. 10.1016/j.quascirev.2009.04.002

Horodyskyj, U. 2015. Contributing Factors to Ice Mass Loss on Himalayan Debris-covered Glaciers. PhD thesis, University of Colorado, Boulder.

Inoue, J and Yoshida, M. 1980. Ablation and heat exchange over the khumbu glacier. Journal of the Japanese Society of Snow and Ice 39: 7-14.

Iwata, S, Watanabe, O. and Fushimi, H. 1980. Surface Morphology in the Ablation Area of the Khumbu Glacier. Seppyo, 41 (Special issue) 9-17.

Kattelmann, R. 2003. Glacial lake outburst floods in the Nepal Himalaya: A manageable hazard? Natural Hazards 28: 145-154. 10.1023/a:1021130101283

Kirkbride, MP. 1993. The temporal significance of transitions from melting to calving termini at glaciers in the central Southern Alps of New Zealand. The Holocene 3: 232-240. 10.1177/095968369300300305

Komori, J. 2008. Recent expansions of glacial lakes in the Bhutan Himalayas. Quaternary International 184: 177-186. http://dx.doi.org/10.1016/j.quaint.2007.09.012

Kraaijenbrink, P Meijer, SW Shea, JM Pellicciotti, F de Jong, SM and Immerzeel, WW. 2016. Seasonal surface velocities of a Himalayan glacier derived by automated correlation of unmanned aerial vehicle imagery. Annals of Glaciology 57: 103-113.

Lamsal, D Sawagaki, T Watanabe, T and Byers, AC. 2016. Assessment of glacial lake development and prospects of outburst susceptibility: Chamlang South Glacier, eastern Nepal Himalaya. Geomatics, Natural Hazards and Risk 7: 403-423. 10.1080/19475705.2014.931306

Liu, Q Christoph, M and Shiyin, L. 2015. Distribution and interannual variability of supraglacial lakes on debris-covered glaciers in the Khan Tengri-Tumor Mountains, Central Asia. Environmental Research Letters 10: 1-10.

Mertes, JR Thompson, SS Booth, AD Gulley, JD and Benn, DI. 2016. A conceptual model of supraglacial lake formation on debris-covered glaciers based on GPR facies analysis. Earth Surface Processes and Landforms 42: 903–914 10.1002/esp.4068

Miles, ES Pellicciotti, F Willis, IC Steiner, JF Buri, P and Arnold, NS. 2016a. Refined energy-balance modelling of a supraglacial pond, Langtang Khola, Nepal. Annals of Glaciology 57: 29-40.

Miles, ES Willis, IC Arnold, NS Steiner, J and Pellicciotti, F. 2016b. Spatial, seasonal and interannual variability of supraglacial ponds in the Langtang Valley of Nepal, 1999–2013. Journal of Glaciology 63: 1-18. 10.1017/jog.2016.120

Moussavi, MS Abdalati, W Pope, A Scambos, T Tedesco, M MacFerrin, M and Grigsby, S. 2016. Derivation and validation of supraglacial lake volumes on the Greenland Ice Sheet from high-resolution satellite imagery. Remote Sensing of Environment 183: 294-303. http://dx.doi.org/10.1016/j.rse.2016.05.024

Naito, N Nakawo, M Kadota, T and Raymond, CF. 2000. Numerical simulation of recent shrinkage of Khumbu Glacier, Nepal Himalayas. In: Nakawo, M.Raymond, C.F. and Fountain, A., eds. IAHS Publ. 264 (Symposium at Seattle 2000 – Debris-Covered Glaciers), Seattle, Washington, U.S.A. IAHS Publication, 245-254.

Narama, C Daiyrov, M Tadono, T Yamamoto, M Kääb, A Morita, R and Ukita, J. 2017. Seasonal drainage of supraglacial lakes on debris-covered glaciers in the Tien Shan Mountains, Central Asia. Geomorphology 286: 133-142. http://dx.doi.org/10.1016/j.geomorph.2017.03.002

Nicholson, L and Benn, DI. 2013. Properties of natural supraglacial debris in relation to modelling sub-debris ice ablation. Earth Surface Processes and Landforms 38: 490-501. 10.1002/esp.3299

Nie, Y Liu, Q and Liu, S. 2013. Glacial Lake Expansion in the Central Himalayas by Landsat Images, 1990–2010. PLoS ONE 8: 1-8. 10.1371/journal.pone.0083973

Pellicciotti, F Stephan, C Miles, E Herreid, S Immerzeel, WW and Bolch, T. 2015. Mass-balance changes of the debris-covered glaciers in the Langtang Himal, Nepal, from 1974 to 1999. Journal of Glaciology 61: 373-386.

Pope, A Scambos, TA Moussavi, M Tedesco, M Willis, M Shean, D and Grigsby, S. 2016. Estimating supraglacial lake depth in West Greenland using Landsat 8 and

comparison with other multispectral methods. The Cryosphere 10: 15-27. 10.5194/tc-10-15-2016

Purdie, H Bealing, P Tidey, E Gomez, C and Harrison, J. 2016. Bathymetric evolution of Tasman Glacier terminal lake, New Zealand, as determined by remote surveying techniques. Global and Planetary Change 147: 1-11. http://dx.doi.org/10.1016/j.gloplacha.2016.10.010

Quincey, DJ Luckman, A and Benn, D. 2009. Quantification of Everest region glacier velocities between 1992 and 2002, using satellite radar interferometry and feature tracking. Journal of Glaciology 55: 596-606.

Quincey, DJ Richardson, SD Luckman, A Lucas, RM Reynolds, JM Hambrey, MJ and Glasser, NF. 2007. Early recognition of glacial lake hazards in the Himalaya using remote sensing datasets. Global and Planetary Change 56: 137-152. http://dx.doi.org/10.1016/j.gloplacha.2006.07.013

Ragettli, S Bolch, T and Pellicciotti, F. 2016. Heterogeneous glacier thinning patterns over the last 40 years in Langtang Himal, Nepal. The Cryosphere 10: 2075-2097. 10.5194/tc-10-2075-2016

Reynolds, JM. 2000. On the formation of supraglacial lakes on debris-covered glaciers. In: Nakawo, M.Raymond, C.F. and Fountain, A., eds. IAHS Publ. 264 (Symposium at Seattle 2000 – Debris-Covered Glaciers), Seattle, Washington, U.S.A. IAHS Publishing, 153-161.

Rohl, K. 2008. Characteristics and evolution of supraglacial ponds on debris-covered Tasman Glacier, New Zealand. Journal of Glaciology 54: 867-880.

Rounce, DR Byers, AC Byers, EA and McKinney, DC. 2017. Brief communication: Observations of a glacier outburst flood from Lhotse Glacier, Everest area, Nepal. The Cryosphere 11: 443-449. 10.5194/tc-11-443-2017

Rounce, DR McKinney, DC Lala, JM Byers, AC and Watson, CS. 2016. A new remote hazard and risk assessment framework for glacial lakes in the Nepal Himalaya. Hydrol. Earth Syst. Sci. 20: 3455-3475. 10.5194/hess-20-3455-2016

Sakai, A Nishimura, K Kadota, T and Takeuchi, N. 2009. Onset of calving at supraglacial lakes on debris-covered glaciers of the Nepal Himalaya. Journal of Glaciology 55: 909-917.

Sakai, A Takeuchi, N Fujita, K and Nakawo, M. 2000. Role of supraglacial ponds in the ablation process of a debris-covered glacier in the Nepal Himalayas. In: Nakawo, M.Raymond, C.F. and Fountain, A., eds. IAHS Publ. 264 (Symposium at Seattle 2000 – Debris-Covered Glaciers), Seattle, Washington, U.S.A. IAHS Publishing, 119-130.

Salerno, F Thakuri, S D'Agata, C Smiraglia, C Manfredi, EC Viviano, G and Tartari, G. 2012. Glacial lake distribution in the Mount Everest region: Uncertainty of measurement and conditions of formation. Global and Planetary Change 92-93: 30-39. 10.1016/j.gloplacha.2012.04.001

Shrestha, BB and Nakagawa, H. 2014. Assessment of potential outburst floods from the Tsho Rolpa glacial lake in Nepal. Natural Hazards 71: 913-936. 10.1007/s11069-013-0940-3

Somos-Valenzuela, MA McKinney, DC Byers, AC Rounce, DR Portocarrero, C and Lamsal, D. 2014a. Assessing downstream flood impacts due to a potential GLOF from Imja Lake in Nepal. Hydrol. Earth Syst. Sci. Discuss. 11: 13019-13053. 10.5194/hessd-11-13019-2014

Somos-Valenzuela, MA McKinney, DC Rounce, DR and Byers, AC. 2014b. Changes in Imja Tsho in the Mount Everest region of Nepal. The Cryosphere 8: 1661-1671. 10.5194/tc-8-1661-2014

Strozzi, T Wiesmann, A Kääb, A Joshi, S and Mool, P. 2012. Glacial lake mapping with very high resolution satellite SAR data. Natural Hazards and Earth System Sciences 12: 2487-2498. 10.5194/nhess-12-2487-2012

Sugiyama, S Minowa, M Sakakibara, D Skvarca, P Sawagaki, T Ohashi, Y Naito, N and Chikita, K. 2016. Thermal structure of proglacial lakes in Patagonia. Journal of Geophysical Research: Earth Surface: p2016JF004084. 10.1002/2016JF004084

Takeuchi, N Sakai, A Kohshima, S Fujita, K and Nakawo, M. 2012. Variation in Suspended Sediment Concentration of Supraglacial Lakes on Debris Covered Area of the Lirung Glacier in the Nepal Himalayas. Global Environmental Research 16: 95-104.

Thakuri, S Salerno, F Smiraglia, C Bolch, T D'Agata, C Viviano, G and Tartari, G. 2014. Tracing glacier changes since the 1960s on the south slope of Mt. Everest (central Southern Himalaya) using optical satellite imagery. Cryosphere 8: 1297-1315. 10.5194/tc-8-1297-2014

Thompson, S Benn, D Mertes, J and Luckman, A. 2016. Stagnation and mass loss on a Himalayan debris-covered glacier: processes, patterns and rates. Journal of Glaciology 62: 467-485. doi:10.1017/jog.2016.37

Thompson, SS Benn, DI Dennis, K and Luckman, A. 2012. A rapidly growing moraine-dammed glacial lake on Ngozumpa Glacier, Nepal. Geomorphology 145: 1-11. 10.1016/j.geomorph.2011.08.015

Wang, WC Xiang, Y Gao, Y Lu, AX and Yao, TD. 2015. Rapid expansion of glacial lakes caused by climate and glacier retreat in the Central Himalayas. Hydrological Processes 29: 859-874. 10.1002/hyp.10199

Watanabe, T Ives, JD and Hammond, JE. 1994. Rapid Growth of a Glacial Lake in Khumbu Himal, Himalaya: Prospects for a Catastrophic Flood. Mountain Research and Development 14: 329-340. 10.2307/3673729

Watson, CS Quincey, DJ Carrivick, JL and Smith, MW. 2016. The dynamics of supraglacial ponds in the Everest region, central Himalaya. Global and Planetary Change 142: 14-27. http://dx.doi.org/10.1016/j.gloplacha.2016.04.008

Watson, CS Quincey, DJ Carrivick, JL and Smith, MW. 2017. Ice cliff dynamics in the Everest region of the Central Himalaya. Geomorphology 278: 238-251. http://dx.doi.org/10.1016/j.geomorph.2016.11.017

Watson, CS Quincey, DJ Smith, MW Carrivick, JL Rowan, AV and James, M. In press. Quantifying ice cliff evolution with multi-temporal point clouds on the debris-covered Khumbu Glacier, Nepal. Journal of Glaciology. DOI: 10.1017/jog.2017.47

Wessels, RL Kargel, JS and Kieffer, HH. 2002. ASTER measurement of supraglacial lakes in the Mount Everest region of the Himalaya. Annals of Glaciology 34: 399-408. 10.3189/172756402781817545

Xin, W Shiyin, L Haidong, H Jian, W and Qiao, L. 2012. Thermal regime of a supraglacial lake on the debris-covered Koxkar Glacier, southwest Tianshan, China. Environmental Earth Sciences 67: 175-183. 10.1007/s12665-011-1490-1

Zhang, G Yao, T Xie, H Wang, W and Yang, W. 2015. An inventory of glacial lakes in the Third Pole region and their changes in response to global warming. Global and Planetary Change 131: 148-157. http://dx.doi.org/10.1016/j.gloplacha.2015.05.013

Chapter 5
Ice cliff dynamics in the Everest region of the Central Himalaya

C. Scott Watson, Duncan J. Quincey, Jonathan L. Carrivick, and Mark W. Smith

Published in Geomorphology. 2017. 278: 238−251

DOI: 10.1016/j.geomorph.2016.11.017

5.1 Abstract

The importance of ice cliffs for glacier-scale ablation on debris-covered glaciers is now widely recognised. However, a paucity of data exists to describe the spatio-temporal distribution of ice cliffs. In this study we analysed the position and geometry of 8,229 ice cliffs and 5,582 supraglacial ponds on 14 glaciers in the Everest region between 2000 and 2015. We observed notable ice cliff and pond spatial coincidence. On average across our study glaciers, 77% of supraglacial pond area was associated with an adjacent ice cliff, and 49% of ice cliffs featured an adjacent supraglacial pond. The spatial density of ice cliffs was not directly related to glacier velocity, but did peak within zones of active ice. Furthermore, we found that ice cliff density was glacier-specific, temporally variable, and was positively correlated with surface lowering and decreasing debris thickness for individual glaciers. Ice cliffs predominantly had a north-facing (commonly north-westerly) aspect, which was independent of glacier flow direction, thereby signifying a strong solar radiation control on cliff evolution. Independent field observations indicated that cliff morphology was related to aspect, local debris thickness, and presence of a supraglacial pond, and highlighted the importance of surface runnel formation, which acts as a preferential pathway for meltwater and debris fluxes. Overall, by coupling remote sensing and in-situ observations it has been possible to capture local and glacier-scale ice cliff dynamics across 14 glaciers, which is necessary if explicit parameterisation of ice cliffs in dynamic glacier models is to be achieved.

5.2 Introduction

A negative glacier mass balance regime prevails across the central and eastern Himalaya (e.g. Bolch et al., 2011; Bolch et al., 2012; Kääb et al., 2012; Nuimura et al., 2012; Kääb et al., 2015), and this is expected to continue under projected climate change (Chaturvedi et al., 2014; Zhao et al., 2014). This mass loss will lead to increasingly seasonal and declining water resources towards the end of the century (Lutz et al., 2014; Shea and Immerzeel, 2016; Soncini et al., 2016). Additionally, as proglacial lakes become established during deglaciation, assessments of glacial lake outburst flood hazards will become increasingly pertinent (Benn et al., 2012; Carrivick and Tweed, 2013).

Heavily debris-covered glaciers predominantly respond to negative glacier mass balance regimes via surface lowering, rather than by up-valley retreat of a glacier terminus (Scherler et al., 2011; Benn et al., 2012; Thakuri et al., 2014; Racoviteanu et al., 2015). Spatio-temporally heterogeneous debris-cover (Zhang et al., 2011; Nicholson and Benn, 2013) controls patterns of melt by locally insulating the glacier where debris exceeds a critical thickness, which is typically just a few centimetres (Östrem, 1959; Mattson et al., 1993; Nicholson and Benn, 2006). This means that maximum debris-covered Himalayan glacier surface lowering rates are most commonly found in the mid and upper parts of this debris-covered area because debris thickness generally decreases up-glacier (Nakawo et al., 1999). However, whilst considerable local-scale heterogeneity in supraglacial debris and other supraglacial features such as ponds and ice cliffs has been acknowledged (e.g. Immerzeel et al., 2014; Pellicciotti et al., 2015; Ye et al., 2015), a full spatio-temporal analysis of these supraglacial features has yet to be made.

A quantitative assessment of the evolution of supraglacial parts of Himalayan glacier systems is urgently required because diminishing ice surface gradients and consequently reduced driving stress of debris- covered glaciers creates preferential conditions for supraglacial pond formation and expansion (Scherler et al., 2011; Benn et al., 2012). Indeed, several authors have documented a net increase in supraglacial pond area over recent decades (e.g. Gardelle et al., 2011; Nie et al., 2013; Wang et al., 2015; Watson et al., 2016). These supraglacial ponds can efficiently absorb and transmit thermal energy to adjacent ice cliffs (Sakai et al., 2000; Miles et al., 2016), and promote cliff calving rates of tens of metres per year (Table 5.1) (Benn et al., 2001). The resultant enhanced ice mass loss in shallow ice surface gradient zones can lead to a positive feedback cycle that may ultimately produce large glacial lakes (Reynolds, 2000; Bolch et al., 2011; Benn et al., 2012). The aim of this study is to conduct a remote sensing analysis investigating the spatio-temporal dynamics of ice

cliffs in the Everest region, which is informed by a summary of the existing ice cliff literature. Specifically we investigate: (1) the spatio-temporal distribution and aspect of ice cliffs; (2) the spatial coincidence of ice cliffs and supraglacial ponds; (3) associations between ice cliffs, glacier surface lowering, and debris-cover; (4) strategies for monitoring ice cliff evolution.

Table 5.1. Observations of ice cliff retreat rates and characteristics on debris-covered glaciers

Reference	Location	Typical cliff melt rates (cm d^{-1}) M – modelled, O – Observed	Summary
Brun et al. (2016)	Lirung Glacier, Nepal	Monsoon: 3.8 – 3.1 O Post-monsoon: 1.0 O	• Calculated ice cliff volume losses by comparing five ice cliff faces over a year. The study cliffs were north-facing.
Buri et al. (2016)	Lirung Glacier, Nepal	Pre-monsoon: 1.2 – 8.6 M Monsoon: 0.9 – 7.9 M Post monsoon: 0.6 – 4.7 M	• Incoming longwave radiation was higher than the total incoming shortwave flux, due to radiation emitted by the surrounding terrain • Two cliffs occupied 0.09% of the debris-covered area and accounted for 1.23% of modelled total glacier melt
Steiner et al. (2015)	Lirung Glacier, Nepal	Pre-monsoon: 3.3 – 8.6 O Post-Monsoon: 0.2 – 1.3 O	• High spatial and temporal variability in cliff melt was observed • The role of local topography for cliff shading and increasing longwave radiation fluxes was an important consideration
Juen et al. (2014)	Koxkar Glacier, China		• Ice cliffs occupied 1.7% of the debris-covered area and accounted for 12% of the sub-debris ablation and 2.5% of the total glacier ablation

Reid and Brock (2014)	Miage Glacier, Italy	5.9 – 8.1 O	• Mapped cliffs occupied ~1.3% of the debris-covered area and accounted for ~7.4 % of modelled total ablation
Thompson et al. (2012)	Ngozumpa Glacier, Nepal		• Retreat rates of 20–50 m a^{-1} (2008–2010) of a cliff beside Spillway Lake were attributed to ice cliff calving
Han et al. (2010)	Koxkar Glacier, China	3 – 10 O	• 38 cliffs observed • Cliffs accounted for ~7.3% of modelled debris-covered area runoff • There was a strong correlation between backwasting rate and daily mean temperature (R^2 = 0.84) • Shortwave radiation was the most important energy flux for cliff ablation
Rohl (2006)	Tasman Glacier, New Zealand	10 – 30 O (thermal undercutting)	• A mean notch formation rate of 15 cm d^{-1} was observed during the summer • A mean calving rate of 34 m a^{-1} was observed
Sakai et al. (2002)	Lirung & Khumbu Glaciers, Nepal		• Mapped cliffs occupied ~2.6% of Khumbu Glacier debris-covered area. • Cliffs accounted for ~20 % of the debris-covered area ablation • North-facing cliffs were most common
Benn et al. (2001)	Ngozumpa Glacier, Nepal	Post Monsoon: 3.0 – 4.5 O (13.7 – 14.9 m a^{-1})	• Calving retreat initiated on cliffs >15 m high • Mean calving retreat rates were 31–52 m a^{-1} • Subaerial melting was 20–50% of the calving retreat rate
Sakai et al. (1998)	Lirung Glacier, Nepal	Monsoon: 7.2 O	• Mapped cliffs occupied <2% of the debris-covered area and accounted for 69% of modelled total ablation

Inoue and Yoshida (1980)	Khumbu Glacier, Nepal	Monsoon: Up to 4.5 O	• Solar radiation was found to be most important for cliff ablation. Calving cliffs were observed

5.3 Previous work

5.3.1 Ice cliff and supraglacial pond inclusion into modelling studies

Quantifying ice cliff and supraglacial pond dynamics is important because studies modelling future glacier evolution do not fully incorporate these ice ablation processes (e.g. Rowan et al., 2015; Shea et al., 2015; Soncini et al., 2016). Douglas et al. (2016) parameterise ice cliffs as sources of locally enhanced melt by using an estimate of ice cliff distribution on the Khumbu Glacier but most studies calibrate glacier mass balance based on geodetic or previously-published estimates and thus account for the role of ice cliffs and ponds implicitly, meaning changes in their distribution, occurrence, and feedbacks are not represented. Furthermore, estimates of glacier volume loss from different modelling studies using the same climatic scenarios are not consistent. For example, Shea et al. (2015) estimated a 84% mean decrease in glacier volume for the Everest region to 2100 under an RCP4.5 scenario. For the Khumbu Glacier, Rowan et al. (2015) predict a volume loss of 8 to 10%, whereas Soncini et al. (2016) predict 54%, and Douglas et al. (2016) predict 72–75%. Therefore, an improved process-based understanding of the surface dynamics of heavily debris-covered Himalayan glaciers would help refine model parameterisation.

5.3.2 Observations of ice cliff retreat

Direct observations of ice cliff retreat are spatially and temporally limited, but nonetheless demonstrate their importance for ablation on debris-covered glaciers (Table 5.1). Ablation stake measurements have supported numerical models of cliff evolution and quantification of ice cliff importance relative to sub-debris melt (e.g. Han et al., 2010; Reid and Brock, 2014; Steiner et al., 2015; Buri et al., 2016). Buri et al. (2016) estimated that total ice cliff melt was 13 times higher than sub-debris melt in the Langtang region. Similarly, recent studies using multi-temporal digital elevation model (DEM) differencing have revealed high rates of localised surface lowering around ice cliffs and supraglacial ponds (Immerzeel et al., 2014; Pellicciotti et al., 2015; Thompson et al., 2016). For the Ngozumpa Glacier in the Everest region, Thompson et al. (2016) partitioned the observed surface lowering from fine-resolution DEMs of difference into respective contributions from ice cliffs, supraglacial ponds, and sub-debris melt. Here, cliffs covered ~5% of the debris-covered area but contributed ~40% to observed surface lowering. Additionally, the majority of cliffs were

north-facing, similar to the observations of Sakai et al. (2002) on the southerly flowing Lirung and Khumbu glaciers.

5.3.2 Ice cliff energy balance

Little is known about the relationship between radiation fluxes and cliff formation, persistence, and decay. A higher solar radiation receipt on south-facing cliffs is expected to cause their rapid decay and burial under debris following progressive slope angle lowering, which may explain why few south-facing cliffs are observed (Sakai et al., 2002). In contrast, ice cliff persistence is likely to be favoured on shaded north-facing slopes (Sakai et al., 2002; Steiner et al., 2015). The longwave radiation component of surface energy balance on heavily debris-covered glaciers was shown to be large by Steiner et al. (2015) and Buri et al. (2016) due to emissions from surrounding debris mounds adjacent to the base of ice cliffs. This is due to the debris-cover reaching high temperatures during the day, in contrast to clean ice (Nicholson and Benn, 2006; Steiner et al., 2015). On north-facing cliffs, a high longwave radiation input at the cliff base and low direct solar radiation input at the cliff top appears to maintain a steep cliff angle, favouring cliff persistence (Sakai et al., 2002). However, the monsoon dominated melt season of the central and eastern Himalaya complicates the energy balance due to influence of cloud cover (Sakai et al., 1998; Nicholson and Benn, 2013), which reduces the direct shortwave radiative flux but also reduces ambient temperature decline through the night (Steiner and Pellicciotti, 2016), potentially prolonging cliff melt.

5.4 Study area

The Everest region spans the Nepal/Tibet border in the central Himalaya (Figure 5.1). Warming temperatures and reduced precipitation (Yang et al., 2006; Shrestha and Aryal, 2011; Yang et al., 2011; Salerno et al., 2015) have resulted in a widespread negative mass balance regime (Bolch et al., 2008; Bolch et al., 2011; Benn et al., 2012; Ye et al., 2015) (Table 5.2). In this study, we focus on the debris-covered zones of 14 glaciers (Figure 5.1). These glaciers range in size, predominant flow direction and in mass balance, and are amongst the highest altitude glaciers in the world (Table 5.2). Additionally, we use observations of ice cliffs on the Khumbu Glacier photographed during field campaigns in October/ November 2015 and May 2016 to investigate cliff morphology and fine-scale melt processes.

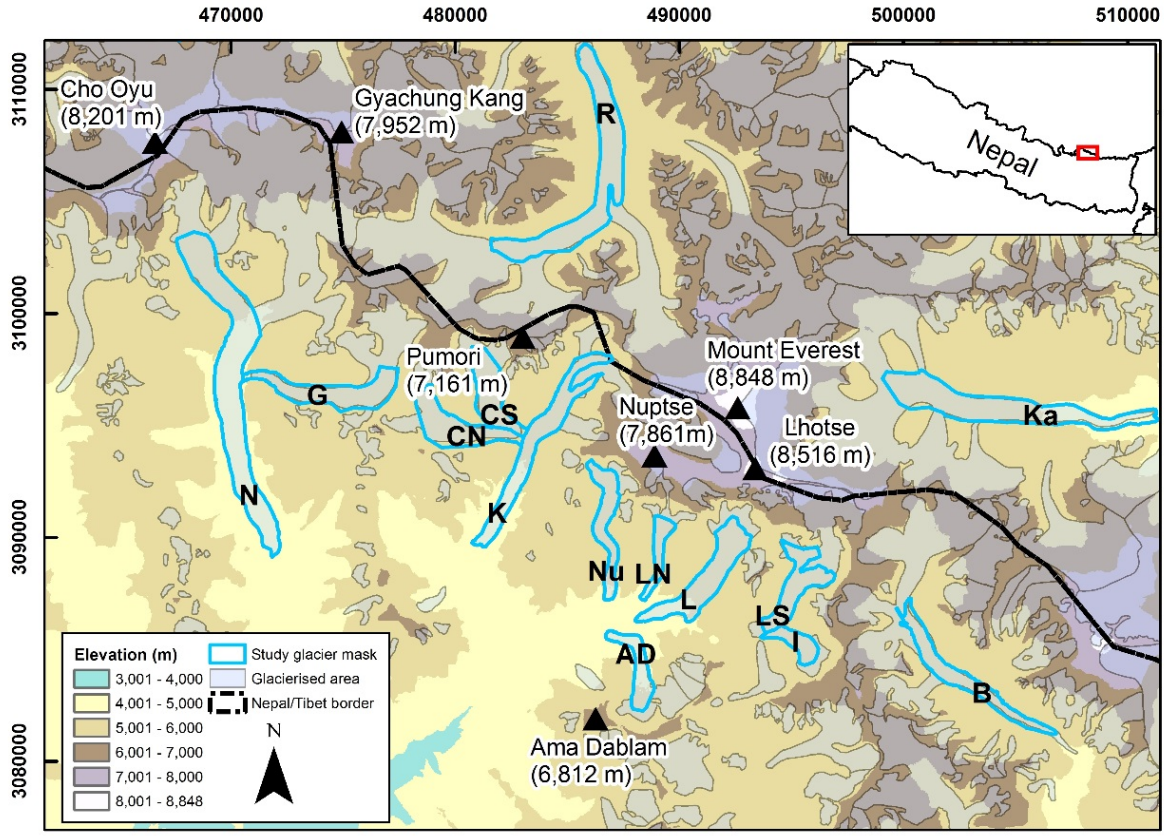

Figure 5.1. Study glaciers in the Everest region of Nepal/Tibet. The study masks broadly represent the debris-covered area of each glacier. AD – Ama Dablam Glacier, B – Barun Glacier, CN – Changri Nup Glacier, CS – Changri Shar Glacier, G – Gaunara Glacier, I – Imja Glacier, Ka – Kangshung Glacier, K – Khumbu Glacier, L – Lhotse Glacier, LN – Lhotse Nup Glacier, LS - Lhotse Shar Glacier, N- Ngozumpa Glacier, Nu – Nuptse Glacier, and R - Rongbuk Glacier. Grid is UTM zone 45N.

5.5 Datasets and methods

5.5.1 Ice cliff and supraglacial pond classification and analysis

True-colour orthorectified satellite imagery (<2 m spatial resolution) of the Everest region was accessed through Google Earth Pro. Images from December 2000 to June 2015 provided multi-temporal coverage for most of our study glaciers (Figure 5.2). The core imagery was selected based on a visual inspection of its quality (ice cliff contrast with the surrounding debris, snow cover, and presence of shadows) rather than acquisition date. Ice cliff presence is not seasonal in contrast to supraglacial ponds, which expand during the summer melt season. Glacier outlines were modified from the South Asia – East Randolph Glacier Inventory 5.0 (Pfeffer et al., 2014) to reflect the debris-covered area of each glacier, which were used as study masks. These masks excluded areas of heavily crevassed ‘dirty-ice’ where ice cliffs could not be clearly delineated, and areas of avalanche deposits or seasonal snow cover, both of

which occurred at the debris to clean-ice transition. The study masks for the Rongbuk and Kangshung glaciers stopped below the transition from debris-covered to clean-ice due to data availability, omitting ~4 km^2 and ~3 km^2 of debris-covered area respectively.

All ice cliffs and supraglacial ponds were manually delineated in Google Earth Pro by one operator and checked on independent days until no further edits were required. We define an ice cliff as any area of exposed ice, whether this is clean ice or dirty (i.e. with a thin layer of debris on the surface). Ice cliffs were digitised along the length of their top edge from left to right with the cliff facing outward (Figure 5.3). Supplementary satellite imagery was used where available to crosscheck the cliffs (Figure 5.2) and a total of 8,229 cliffs and 5,582 supraglacial ponds were digitised (Supplementary Table 5.1).

Glacier centrelines were automatically calculated in ArcGIS using the study masks and the 'Collapse Dual Lines to Centerline' tool (cf. Haritashya et al., 2015). Glacier centrelines were used to calculate glacier length and mean flow direction. Glacier surface gradients were calculated using the length and elevation change of the study masks. Ice cliffs were segmented by vertices in ArcGIS and the outward looking aspect of each segment was calculated. These segments were used in subsequent analysis to preserve the cliff-scale variation, rather than taking a mean across each cliff. Cliff length was summed per glacier and into 500 m distance bins, which started at the glacier terminus and accounted for centreline curvature. We calculated cliff length per unit area as a cliff density metric, which is referred to herein as cliff density. The spatial coincidence between ice cliffs and supraglacial ponds was assessed using a 30 m directional buffer from each cliff top edge. The buffer was used to extract ponds that intersected with the buffer polygon since cliff geometry and hence the distance between the cliff top edge and potential pond was unknown (Supplementary Figure 5.1). Taking 30° as the debris angle of repose (Sakai et al., 1998) and a cliff height of 15.5 m (a mean from the Ngozumpa Glacier observed by Thompson et al., 2016), a theoretical pond would be at least 27 m from the top edge of the cliff. Furthermore, 15 m is suggested as the threshold for calving initiation (Benn et al., 2001) and hence should represent an approximate upper bound for steeply sloping cliff faces. The buffer size was also supported by our field-based and satellite observations.

Table 5.2. Study glacier section characteristics

Glacier	Area (km^2)[a]	Length (km) [a]	Min – max elevation (range) (m) [a]	Gradient (º) [a]	Mean flow direction (º) [a]	Glacier Geodetic mass balance estimate

						(m.w.e. a^{-1})
Ama Dablam[b]	2.29	4.44	4,769 – 5,084 (315)	1.6	335	-0.29 ± 0.08*
Barun	3.89	9.17	5,018 – 5,453 (435)	1.5	129	-
Changri Nup[b]	4.62	5.75	5,057 – 5,540 (483)	1.6	118	-0.28 ± 0.08*
Changri Shar[b]	2.75	4.84	5,074 – 5,436 (362)	1.6	149	-0.28 ± 0.08*
Gaunara[b]	4.33	7.70	4,983 – 5,432 (449)	1.6	266	-
Imja	1.18	2.56	5,023 – 5,187 (164)	1.6	305	-0.50 ± 0.09*
Kangshung	10.0	12.1	4,586 – 5,377 (791)	1.6	94	-
Khumbu[b]	6.54	10.9	4,856 – 5,446 (590)	1.6	215	-0.27 ± 0.08*
Lhotse	5.76	6.73	4,815 – 5,245 (430)	1.6	230	-0.26 ± 0.08*
Lhotse Nup[b]	1.40	3.88	4,954 – 5,210 (256)	1.6	197	-0.18 ± 0.07*
Lhotse Shar	3.03	4.05	5,008 – 5,329 (321)	1.6	229	-0.50 ± 0.09*
Ngozumpa[b]	15.1	15.8	4,668 – 5,241 (573)	1.5	165	-
Nuptse[b]	3.04	6.19	4,962 – 5,554 (592)	1.6	178	-0.25 ± 0.08*
Rongbuk[b]	8.83	13.0	5,174 – 5,526 (352)	1.5	24	-0.42 ± 0.27**

a. Statistics are calculated for the study glacier masks of each glacier, which broadly represent the debris-covered area of each glacier.
b. Indicates glaciers with velocity data.

* 1970 – 2007 from Bolch et al. (2011). Note that Lhotse Shar and Imja, and Changri Nup and Changri Shar glaciers are not separated by Bolch et al. (2011).

** 1974–2006 from Ye et al. (2015)

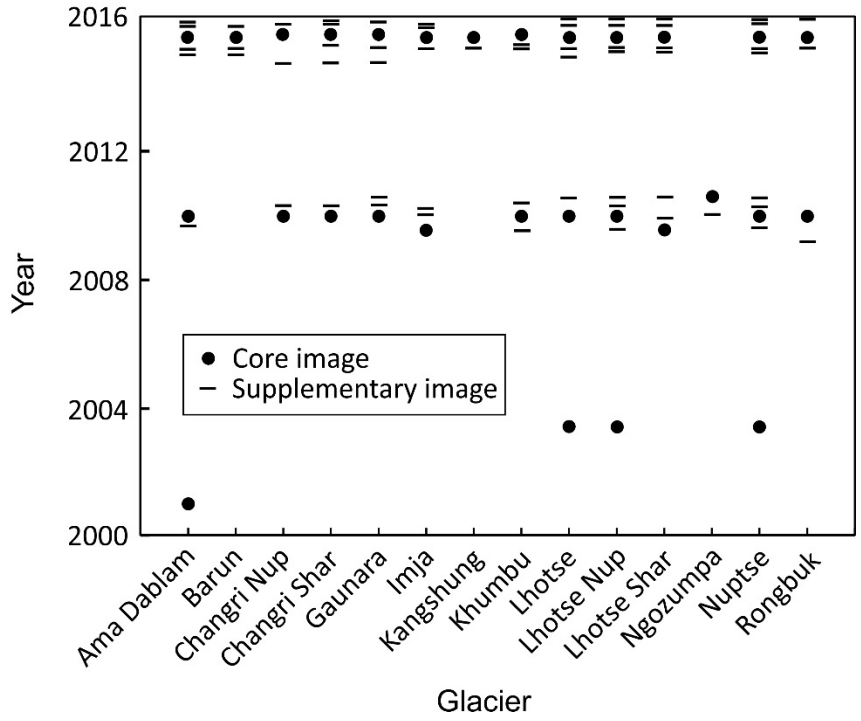

Figure 5.2. Temporal and spatial coverage of the satellite imagery used in this study. Ice cliffs were digitised on core images, using supplementary images for cross-referencing.

5.5.1.1 Glacier surface elevation change and debris-thickness

We used surface elevation change data of glaciers in the Everest region (2000 to 2015) from King et al. (2016) and the modelled debris thickness data of Rounce and McKinney (2014) to assess relationships with ice cliff density. The surface lowering and debris thickness data had coverage for nine and seven glaciers respectively and both datasets were generated at 30 m resolution. King et al. (2016) derived surface lowering data through the subtraction of an 8 m resolution 2015 DEM (resampled to 30 m) generated and distributed by the Polar Geospatial Centre at the University of Minnesota, and the co-registered 30 m resolution 2000 Shuttle Radar Topographic Mission (SRTM) DEM version 3.0. The modelled debris-thickness data of Rounce and McKinney (2014) were derived using an energy balance model and Landsat 7 Enhanced Thematic Mapper Plus (ETM+) satellite imagery (2002 to 2009). Modelled debris thicknesses were comparable with field-based measurements in the region, although the approach is only suitable for determining thicknesses below 0.5 m and hence provides a lower bound estimate (Foster et al., 2012; Rounce and McKinney, 2014). Notably however, ablation is negligible at debris thicknesses above 0.5 m (Mattson et al., 1993).

5.5.1.2 Glacier velocity

Glacier velocities were calculated by tracking surface features between a pair of TerraSAR-X images acquired approximately twelve months apart (18th January 2015 and 5th January 2016). We used a cross-correlation algorithm (Luckman et al., 2007) to identify displaced features using a pattern size (window) of 64 × 64 pixels within a search area of 128 × 128 pixels, equating to approximately 450 × 575 m and 900 × 1150 m on the ground respectively. Scene availability limited our analysis to nine of the fourteen studied glaciers (Table 5.2) but the density of matches on those nine glaciers was excellent given the abundance of surface features. Measured displacements were filtered to remove clear blunders and scaled to annual velocities using the time separation of the images. They were then projected onto a UTM grid at 8 m spatial resolution. We estimated the precision of the method to be approximately half a pixel and thus removed all data points <3 m a^{-1} from our subsequent analysis.

5.5.1.3 Uncertainty assessment

Ice cliff length uncertainty is influenced by image resolution, operator ambiguity in the identification of a cliff, and operator digitisation of the cliff. In this study, we used fine-resolution imagery of comparable resolution where cliffs were clearly visible and one operator undertook all of the analysis. Therefore the latter process, cliff digitisation, is likely to be the main source of uncertainty. To assess the operator error in cliff digitisation, 60 cliffs were randomly selected in each of the core images and repeat digitised. No systematic bias was observed between images in this analysis suggesting that the operator was consistent throughout (Supplementary Figure 5.2). The standard deviation of cliff differences ranged from 4.1 to 8.9 m, which we use as an indication of ice cliff delineation repeatability, although we are aware that potential omissions or commissions are not considered.

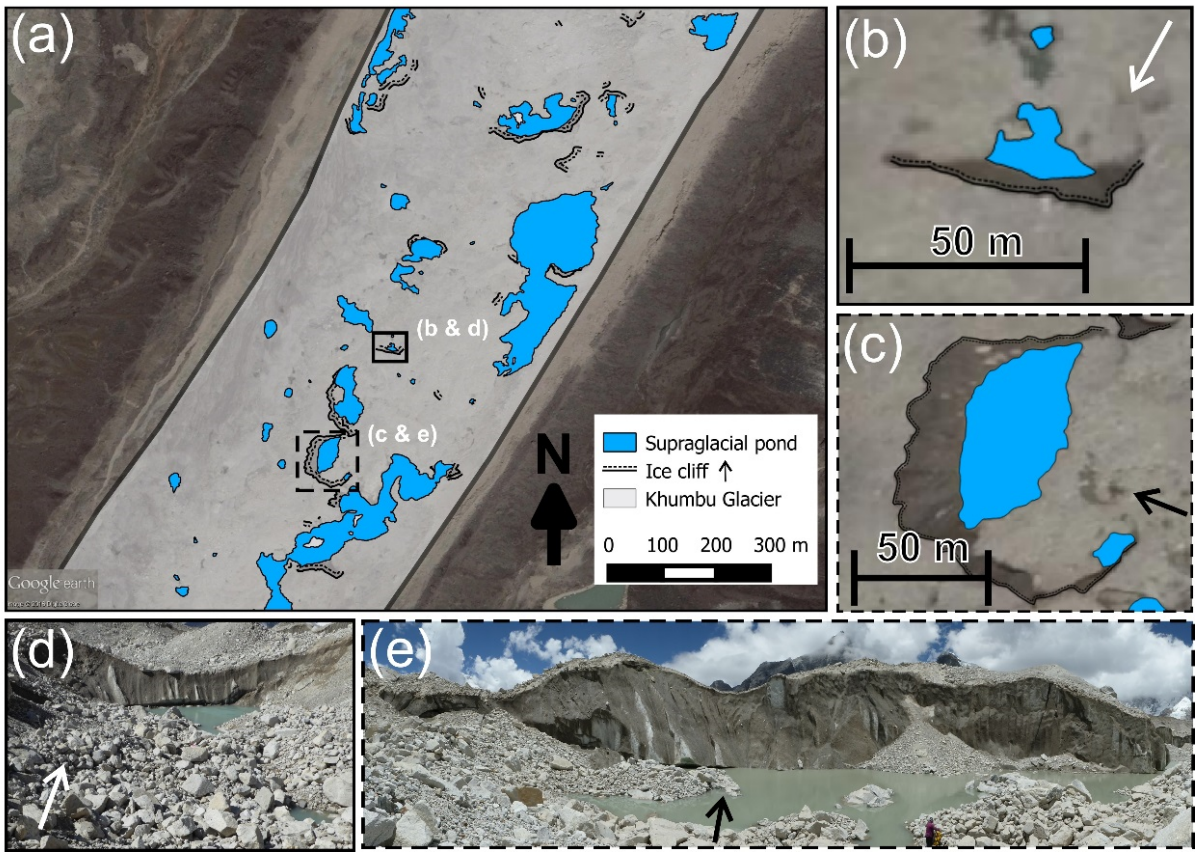

Figure 5.3. Ice cliffs and supraglacial ponds digitised on the Khumbu Glacier. (a) Digitised ice cliffs and supraglacial ponds overlaid on respective Google Earth imagery. Ice cliff aspect is indicated by the offset dotted line. (b) A north-facing cliff and pond, and (c) an easterly facing cliff and pond. Respective cliff photographs and viewing directions are shown in (d) and (e).

5.5.2 Field observations from the Khumbu Glacier

Six ice cliffs were photographed during field campaigns on the Khumbu Glacier (Oct–Nov 2015 and May 2016) and whilst this was initially to ground-truth the remotely-sensed observation the images also revealed and characterised the variable morphology of cliffs. In particular we explored ice cliff coincidence with supraglacial ponds, cliff shape, meltwater generation and drainage patterns, and evidence of evolutionary characteristics.

5.6 Results

5.6.1 Ice cliff and supraglacial pond density and spatial coincidence

The density of supraglacial ponds (ponded area as a percentage of glacier area) and ice cliffs (cliff length per glacier area) was variable across our study glaciers and through time (Figure 5.4). The highest cliff densities were on Lhotse Shar and Imja glaciers with 7.4 and 7.1mm/m^2 respectively. Similarly, the greatest cliff density

changes were on Lhotse Shar and Imja glaciers, which both featured a notable decrease in ice cliffs over the study period. When ranked, a high cliff density did not necessarily equate to high pond density. Cliff density was unrelated to glacier gradient, which displayed little inter-glacier variability (1.5–1.6°), or mean glacier flow direction. Bolch et al. (2011) found Lhotse Shar/Imja Glacier to have the most negative mass balance reported for our study glaciers (−0.50±0.9 m.w.e. a^{-1}), and Lhotse Nup to have the least negative (-0.18±0.07 m.w.e. a^{-1}) (Table 5.2). Similarly, we found these glaciers to have the highest and lowest cliff densities respectively (Figure 5.4b).

The area of supraglacial ponds with a coincident ice cliff far exceeded the area of those without (Figure 5.4a). Ponds accounted for between 1% (Ama Dablam 2000) and 7% (Changri Nup 2015) of glacier area, and between 43% (Nuptse 2009) and 95% (Changri Nup 2015) of pond area had an adjacent ice cliff, with a mean of 77% (Figure 5.4a). On average across our study glaciers, 51% of the total number of ponds had a coincident ice cliff and larger ponds were more likely to feature an ice cliff (Table 5.3, Supplementary Figure 5.3). Similarly, on average 49% of ice cliffs had a coincident pond. Generally, longer cliffs were most likely to have a coincident pond and larger ponds were most likely to have a coincident cliff (Figure 5.5, Supplementary Figure 5.3). Notably (with the exception of Ama Dablam Glacier with longer cliffs) cliffs 20–40 m in length were most frequent across our study glaciers.

5.6.2 Ice cliff aspect

Ice cliffs were shown to be strongly dependent on aspect and strongly independent of glacier flow direction (Figure 5.6). North-facing ice cliffs prevailed, although a slight deviation was observed on Kangshung and Barun glaciers, which flow in an easterly direction and predominantly featured north easterly facing cliffs. In contrast, cliffs mostly faced northwest on the remaining study glaciers despite a range of flow directions. The maximum intra-glacier change in cliff aspect (80°) was on Lhotse Shar Glacier (2009 to 2015). Temporal changes in cliff aspect were variable by glacier for both the magnitude and direction of change (Figure 5.6). Several glaciers displayed little temporal change in the overall mean cliff aspect (<20°) e.g. Gaunara, Changi Nup, Changri Shar, and Lhotse Nup glaciers, whereas others displayed large changes (≥20°) e.g. Lhotse Shar, Imja, Rongbuk, Khumbu, Nuptse, Ama Dablam and Lhotse glaciers (Figure 5.6). Additionally, we note that several glaciers exhibited a decline in north-facing cliffs over our study period. Whether these are recent or long-standing changes is not clear because of the limited temporal resolution of our data.

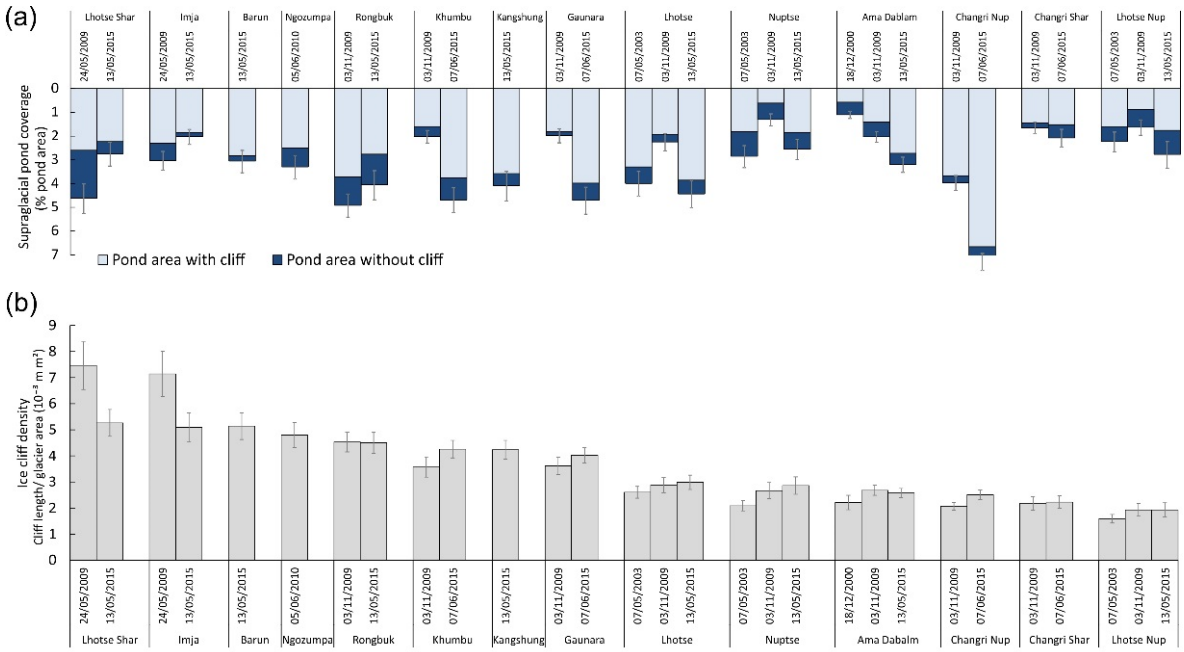

Figure 5.4. (a) Supraglacial pond coverage per glacier for ponds with and without associated ice cliffs; lake area at the termini of Lhotse Shar, Imja, Ngozumpa and Rongbuk glaciers is excluded for clarity and error bars represent a ±1 m pond boundary uncertainty. (b) Ice cliff density ranked high to low by glacier. Error bars represent the standard deviation of cliff length differences from the repeat digitisation analysis (Supplementary Figure 5.2).

5.6.3 Spatial distribution of ice cliffs

Ice cliff density generally increased up-glacier from the terminus and peaked in the upper region of the study masks (Figure 5.7), which were areas below peak velocity, and of thin or decreasing debris-thickness (Figure 5.8). However, seven of our study glaciers displayed an increasing trend with distance from the terminus, followed by a decrease into the transition zone between clean and debris-covered ice (e.g. Lhotse Shar, Barun, Ngozumpa, Khumbu, Lhotse, Nuptse, and Lhotse Nup). Temporal change in cliff length was generally evident along the full length of each study glacier, even for glaciers with no or slow flow around their termini (e.g. Rongbuk, Khumbu, Gaunara, Nuptse, Changri Nup and Lhotse Nup glaciers). We did not observe a relationship between distance up-glacier from the terminus and the distribution of ice cliff lengths. Overall, ice cliff development and persistence appears to be independent of glacier surface velocity although cliff density did peak within zones of active ice.

There were clear relationships between cliff density, surface lowering, and modelled debris thickness, within and between each glacier (Figure 5.8). Debris thickness decreased up-glacier from the terminus from a maximum depth not exceeding 0.6m (noting the methodological limitation). Surface lowering rates increased up-glacier from the terminus before plateauing and in some cases decreased again towards the

up-glacier end of the study mask. Cliff density increased from the terminus alongside surface lowering and we observed statistically significant correlations for this rising limb (e.g. blue line Figure 5.8a, b, c, f, i). After surface lowering plateaued, cliff density also plateaued or began to decrease (Figure 5.8a, b, c, f). In contrast to this prevailing trend, Lhotse Shar and Imja Glaciers featured high initial surface lowering rates at the terminus, which decreased up-glacier (Figure 5.8g, h)

Table 5.3. Summary data of the spatial coincidence between ice cliffs and supraglacial ponds

Ice cliffs with a supraglacial pond	49 %
Ice cliffs without a supraglacial pond	51 %
Supraglacial ponds with an ice cliff	51 %
Supraglacial ponds without an ice cliff	49 %

5.7 Discussion

The importance of ice cliffs for ablation on heavily debris-covered glaciers has long been suggested (e.g. Inoue and Yoshida, 1980). However, spatial and temporal measurements of ice cliff melt and calving retreat are exceptionally limited, owing to hazardous access to the cliff faces and the non-trivial task of working on debris-covered glaciers. Nonetheless, explicit parametrisation of ice cliff processes within ice dynamics models for projecting glacier evolution requires data on (1) ice cliff distribution and characteristics at a glacier-scale, and (2) multi-temporal cliff-scale observations of their 3D evolution. Our results address (1), revealing ice cliff distribution, short-term temporal change, and relationships with glacier surface dynamics in the Everest region. Using our remote sensing analysis and observations of ice cliffs on the Khumbu Glacier, we are able to propose strategies for addressing (2).

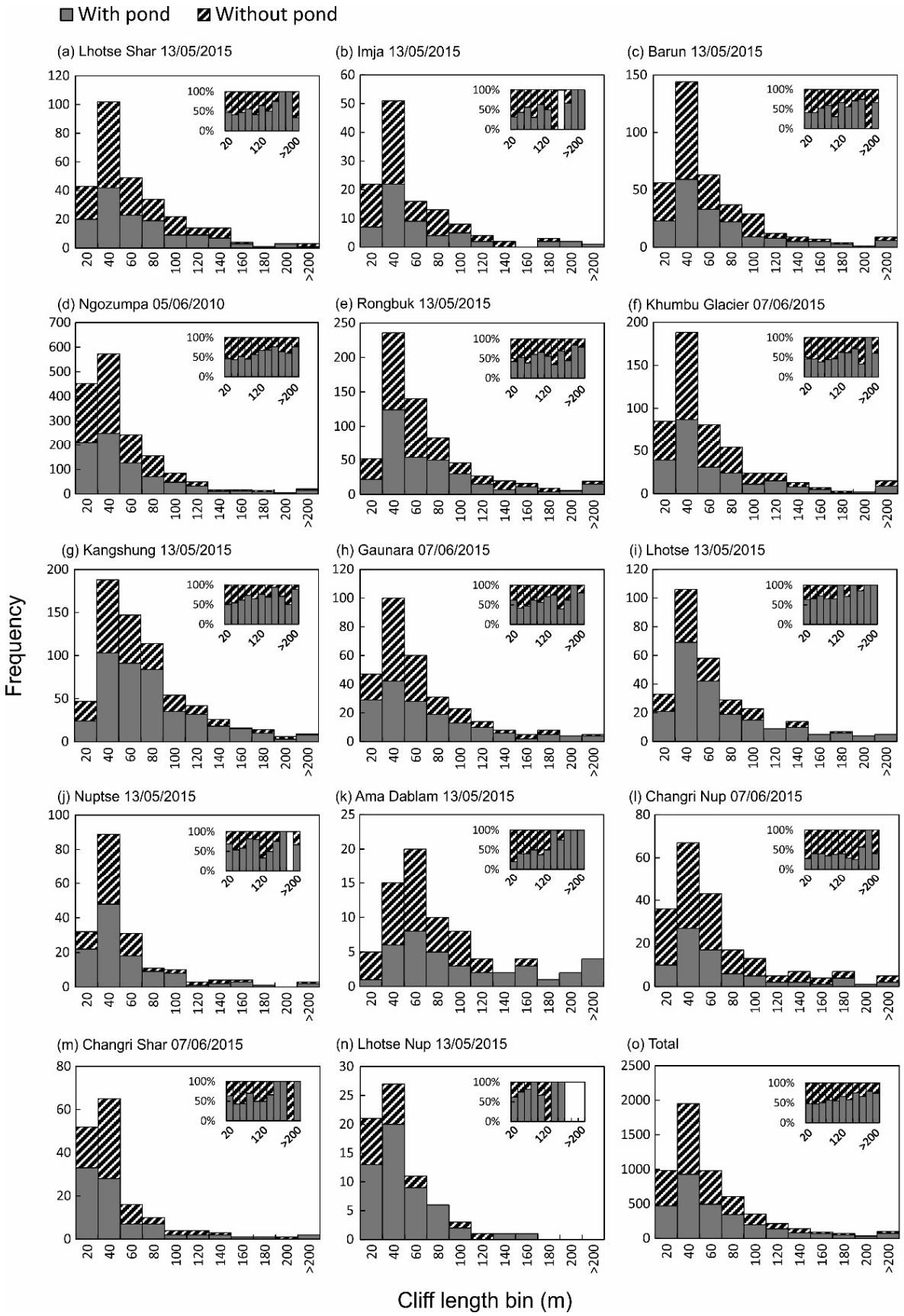

Figure 5.5. Size distribution of ice cliffs and coincidence with supraglacial ponds, for the most recent time period for each glacier. Insets show the same data as a percentage distribution.

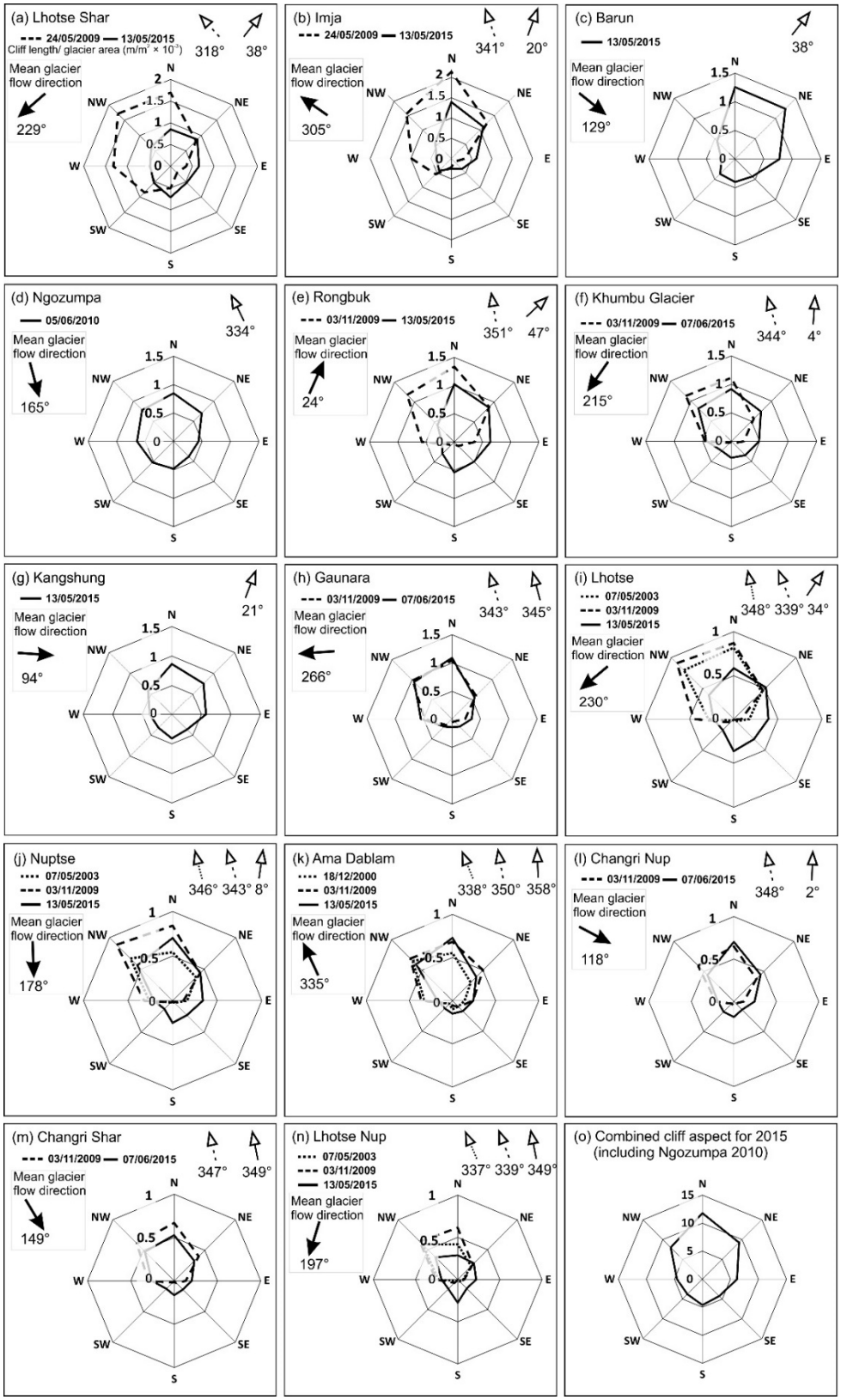

Figure 5.6. Aspect roses for each glacier showing cliff length per glacier area ($m/m^2 \times 10^{-3}$). Arrows indicate the mean cliff aspect for each time period. Note the different scale ranges.

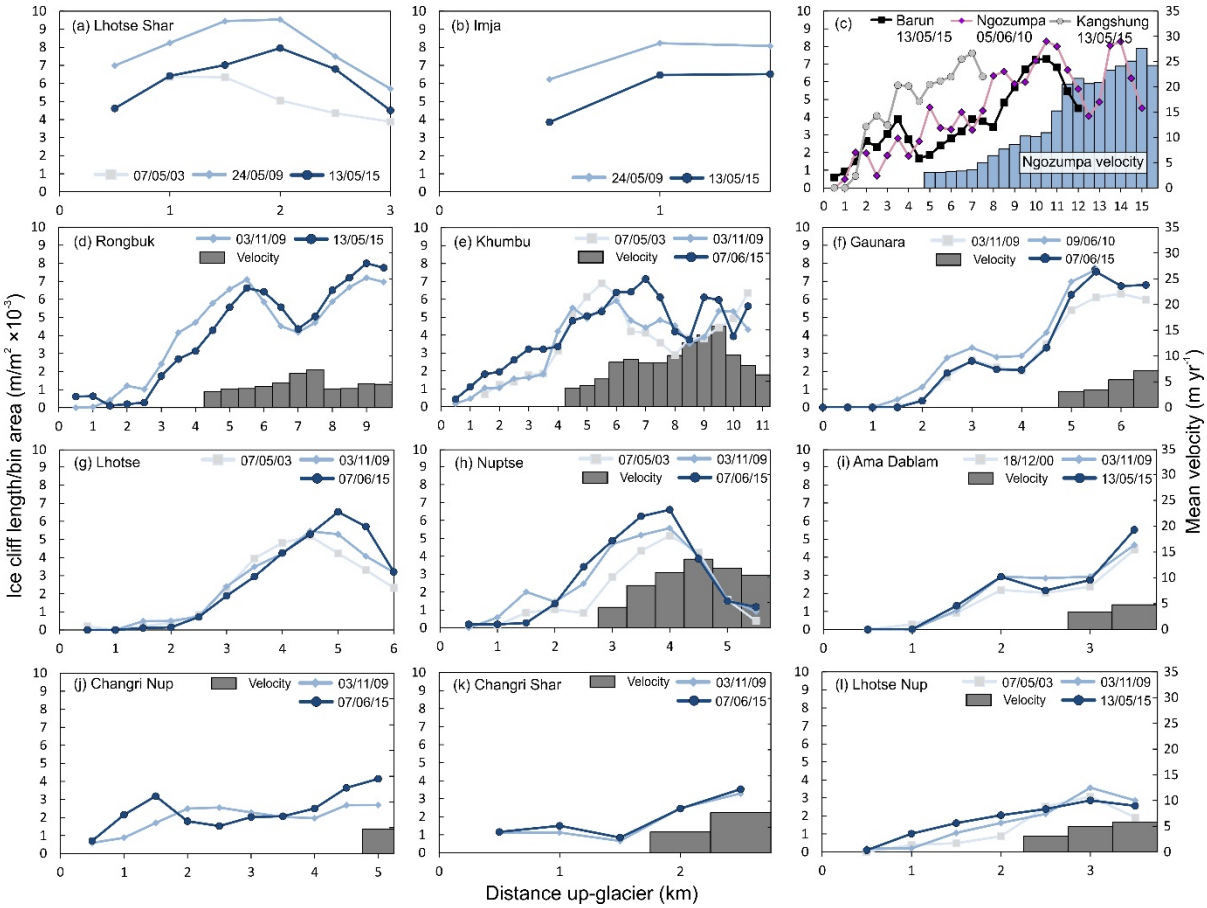

Figure 5.7. Ice cliff density with distance up-glacier from the terminus. The data represent a two-period moving average over 500 m distance bins. Velocity data are shown for the Ngozumpa, Rongbuk, Khumbu, Gaurana, Nuptse, Ama Dablam, Changri Nup, Changri Shar, and Lhotse Nup glaciers. Glaciers with a single time period (Barun, Ngozumpa and Kangshung) are shown on panel (c), with the velocity data from Ngozumpa Glacier. The date format is dd/mm/yy.

5.7.1 Ice cliff dynamics

Ice cliffs are observed to form on debris-covered glaciers through two main processes: (1) steepening of slopes beyond the gradient required to hold debris (Sakai et al., 1998; Benn et al., 2007), and (2) the collapse of englacial conduits or voids creating a surface depression bordered by an arc of exposed ice (Kirkbride, 1993). To assess ice cliff dynamics at a glacier-scale we consider the spatial density of ice cliffs; spatial coincidence of ice cliffs with supraglacial ponds; cliff aspect; spatial distribution and relationship with glacier velocity, surface lowering and debris-cover; and cliff-scale morphology.

5.7.1.1 Ice cliff density

Ice cliffs were most prevalent on Lhotse Shar Glacier, and least on Lhotse Nup Glacier (Figure 5.4), which featured the most and least negative mass balance regimes respectively (Table 5.2). High cliff density, or the proportion of bare ice on the debris-

covered surface, is expected to be associated with high glacier surface lowering, as suggested by DEMs of difference (e.g. Immerzeel et al., 2014; Pellicciotti et al., 2015). This situation reflects 'regime 2' glaciers described by Benn et al. (2012) where ice flux down-glacier is exceeded by mass loss in the ablation zone where ice cliffs and ponds prevail. However, comparisons between published glacier mass balance data and cliff density patterns from the current study are complicated since the available mass balance estimates either have a temporal interval greater than a decade or, conversely, shorter time periods feature high uncertainty (Bolch et al., 2011; Nuimura et al., 2012).

The ice cliff dataset presented in this study spans only the most recent decade and historic ice cliff distribution is unknown, although we note for the Khumbu Glacier that contemporary ice cliff distribution is visually comparable to that mapped in the late 1970s by Iwata et al. (1980). A fine-resolution contemporary DEM of difference is currently lacking for the Everest region, which would allow a more robust assessment of the association between ice cliffs and surface elevation change at a glacier scale (e.g. Thompson et al., 2016).

5.7.1.2 Spatial coincidence of ice cliffs and supraglacial ponds

Supraglacial ponds covered between 1% (Ama Dablam 2000) and 7% (Changri Nup 2015) of glacier area (Figure 5.4a). The percentage of pond area with a coincident ice cliff ranged from 43% (Nuptse 2009) to 95% (Changri Nup 2015). Lower pond-cliff coincidence is expected for non-monsoonal time periods (e.g. Nuptse November 2009), since ponds are expected to attain their maximum size in the preceding summer melt season (e.g. Watson et al., 2016) and ice-contact ponds are most seasonal (Benn et al., 2001). Across our study glaciers, 30 to 76% of ice cliffs featured a coincident pond, with a mean of 49%. Cliffs of all sizes were spatially coincident with supraglacial ponds, although this coincidence was generally greater for longer cliffs (Figure 5.5). Overall, the observed high pond-cliff coincidence supports the formation mechanism hypothesis of ice cliffs by englacial conduit or void collapse and the creation of a hollow in which a pond can develop (Kirkbride, 1993). A similarly high coincidence was reported by Thompson et al. (2016) on the Ngozumpa Glacier where 75% of cliffs bordered a pond.

Increasing supraglacial water storage in the region (Watson et al., 2016) promoted by low gradient debris-covered tongues (e.g. Reynolds, 2000; Quincey et al., 2007; Salerno et al., 2012) suggests that the importance of the observed cliff–pond interaction will become increasingly pertinent in coming decades, especially if there is a trajectory towards calving retreat. The transition of cliffs from melt-driven to rapid calving retreat is likely to increase as ponds coalesce to exceed the ~80 m fetch

threshold proposed for calving initiation (Sakai et al., 2009), which can increase cliff recession threefold (Benn et al., 2001). We observed calving events on ice cliffs with ponds smaller than this threshold (e.g. Figure 5.3e, 10f), where small calving events likely accompanied the thermal undercutting of the cliff face. Furthermore, seasonal expansion and drainage of supraglacial ponds transmits the absorbed thermal energy englacially, which can promote conduit collapse and subsequent cliff formation (Sakai et al., 2000; Miles et al., 2016), hence some consideration of how processes impact on and feedback to one another is also paramount for the accurate projection of glacier evolution.

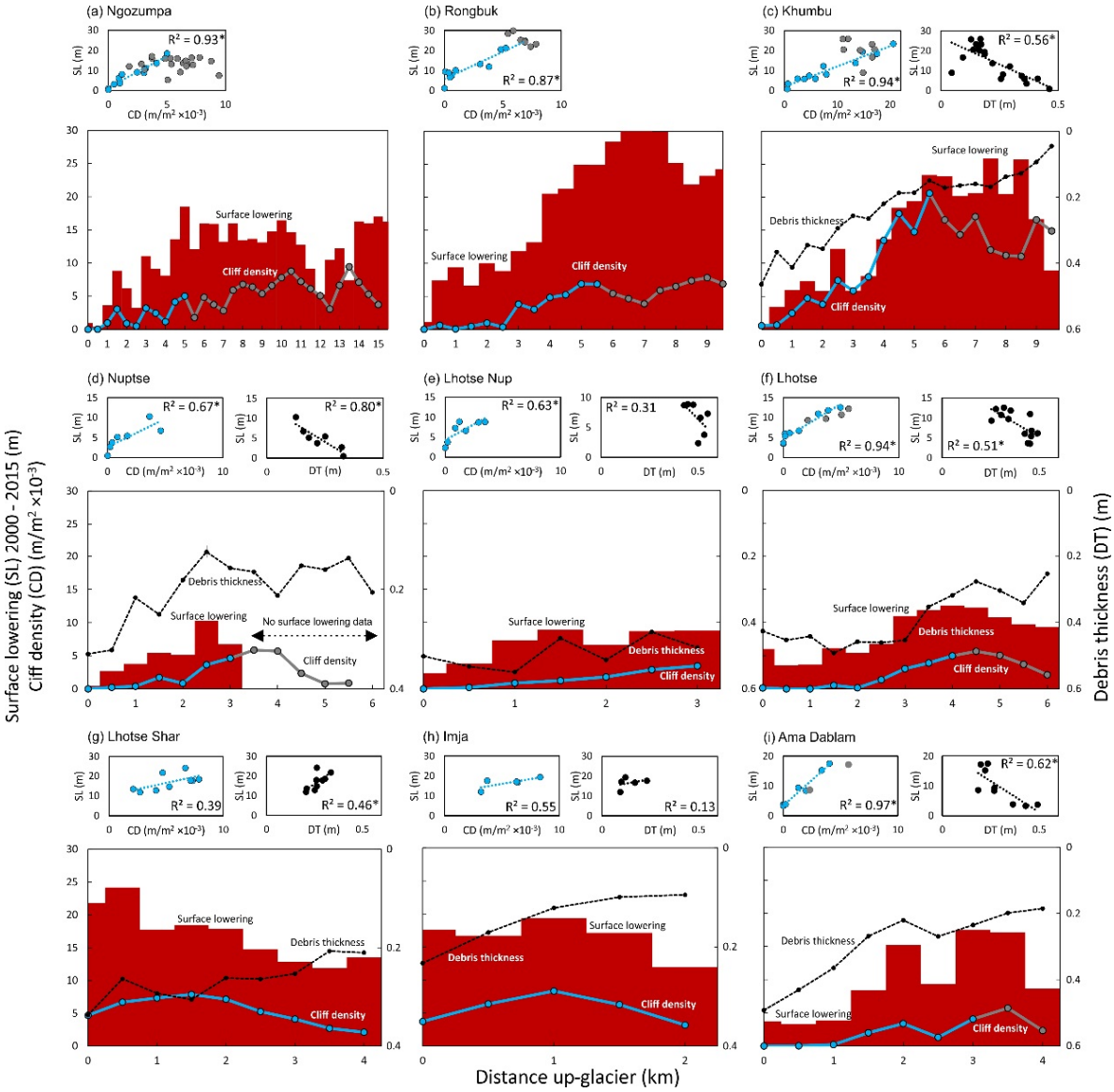

Figure 5.8. Spatial distribution of mean surface lowering, mean cliff density, and mean debris thickness with distance up-glacier from the terminus in 500 m distance bins. Correlations are shown for cliff density and surface lowering (light blue), and debris thickness and surface lowering (black). '*' indicates statistical significance ($P < 0.05$). Debris thickness data were unavailable for Ngozumpa and Rongbuk glaciers. The change from blue to grey lines represents the hypothesised transition from high to moderate influence of ice cliffs for ablation, relative to sub-debris melt.

5.7.1.3 Ice cliff aspect

Ice cliffs were observed to be predominantly north-facing across all 14 glaciers (Figure 5.6). North-facing cliffs were found to prevail on the southerly flowing Lirung and Khumbu glaciers by Sakai et al. (2002), on the Koxkar Glacier by Han et al. (2010), and more recently on the Ngozumpa Glacier by Thompson et al. (2016). Our results demonstrate that this trend prevails throughout the Everest region of the Himalaya irrespective of glacier flow direction.

Our results support the prevailing hypothesis that south-facing cliffs may decay rapidly due to a high solar radiation receipt, hence explaining their reduced occurrence (Sakai et al., 2002). In contrast, north-facing cliffs may persist due to shading of the cliff face (Sakai et al., 2002; Steiner et al., 2015). Debris mounds on high-relief debris-covered glaciers emit a large longwave radiation flux to the base of adjacent ice cliffs (Steiner et al., 2015; Buri et al., 2016). On north-facing cliffs this longwave radiation receipt could act to maintain a steep slope angle and hence promote persistence (Sakai et al., 2002). In contrast, high solar radiation receipt on south-facing cliffs promotes a lowering of the cliff slope and hence burial by debris once below a critical angle of ~30° (Sakai et al., 1998; Benn et al., 2007). However, increased temporal resolution is required to track the lifespan of individual cliffs and reveal the timescale of south-facing cliff decay, which could occur within a year given the high retreat rates observed (Table 5.1).

5.7.1.4 Spatial distribution of ice cliffs

We observed a generally increasing trend of ice cliff density with distance from glacier termini and several glaciers displayed peak cliff occurrence in their upper reach, followed by a decreasing trend (Figure 5.7). Velocity data for nine of our study glaciers showed an increasing trend up-glacier from stagnant lower reaches comparable to Quincey et al. (2009), though we did not observe a clear association between cliff occurrence and glacier velocity. The stagnant ice zones (i.e. those flowing at a rate lower than the noise in our data) ranged from 2.0 (Lhotse Nup) to 4.5 km (Gaunara & Ngozumpa) up-glacier from the respective termini. Ice cliffs were spatially and temporally variable in these slow-flowing regions, indicating that the glacier surface is still actively collapsing into conduits and promoting cliff formation (e.g. Gulley and Benn, 2007). Notable surface lowering here supports this observation and we reveal a statistically significant positive correlation between ice cliff density and surface lowering for six of the nine study glaciers with available data (blue line, Figure 5.8a, b, c, d, f, i).

Available debris thickness data show a decreasing trend up-glacier (Rounce and McKinney, 2014) and we suggest that the plateau of surface lowering marks a transition from high to moderate influence of ice cliffs for ablation, relative to sub-debris melt (grey line in Figure 5.8 and zone 2 to 3 in Figure 5.9). Debris thickness is known to be locally heterogeneous but generally decreases up-glacier from a thickness of several metres at the terminus, indicating that the debris acts to reduce ablation across the majority of the debris-covered zone by insulating the ice beneath (Nakawo et al., 1986; Benn et al., 2012; Nicholson and Benn, 2013; Rounce and McKinney, 2014). Debris-thicknesses in Figure 5.8 do not exceed 0.6 m, which reflects a methodological

limitation in model estimates (Foster et al., 2012; Rounce and McKinney, 2014). Nevertheless, the relative trend observed up-glacier matches that expected for a debris-covered glacier. Generally weaker correlations between debris thickness and cliff density lend support to cliff density having a larger influence over surface lowering on the lower tongues, although there is clearly an interaction between all three variables. The surface lowering associated with the prevalence of a thin debris layer further up-glacier increasingly masks the contribution of ice cliffs (Figure 5.9), i.e. the two surface lowering signals cannot be separated. This observation is supported by Thompson et al. (2016) who found an increasing importance of sub-debris melt and decreasing importance of ice cliff retreat with distance up the Ngozumpa Glacier, although data were only reported for the lower 6 km.

The relationship between cliff density and surface lowering was not clear on Lhotse Nup Glacier or on the lake-calving Lhotse Shar and Imja glaciers (Figure 5.8). These three glaciers were the smallest in our study. A relatively uniform high debris thickness (>0.4m) on Lhotse Nup Glacier likely inhibits cliff formation here since supraglacial pond coverage is similarly low (Figure 5.4a). Several studies have identified highest rates of surface lowering at the terminus of the lake-calving Lhotse Shar Glacier (Bolch et al., 2011; Nuimura et al., 2012; Thakuri et al., 2016) comparable to our results (Figure 5.8g). This trend contrasts with other glaciers in the region where highest rates are further up-glacier. Nuimura et al. (2012) hypothesised that reduced ice compression could be implicated in a reduction in emergence velocity, which contributes towards this high surface lowering signal at the terminus. Active flow along the length of Lhotse Shar Glacier also supports this hypothesis (Thakuri et al., 2016). Similarly, a larger dataset of lake-calving glaciers analysed by King et al. (2016) also revealed high rates of terminus surface lowering.

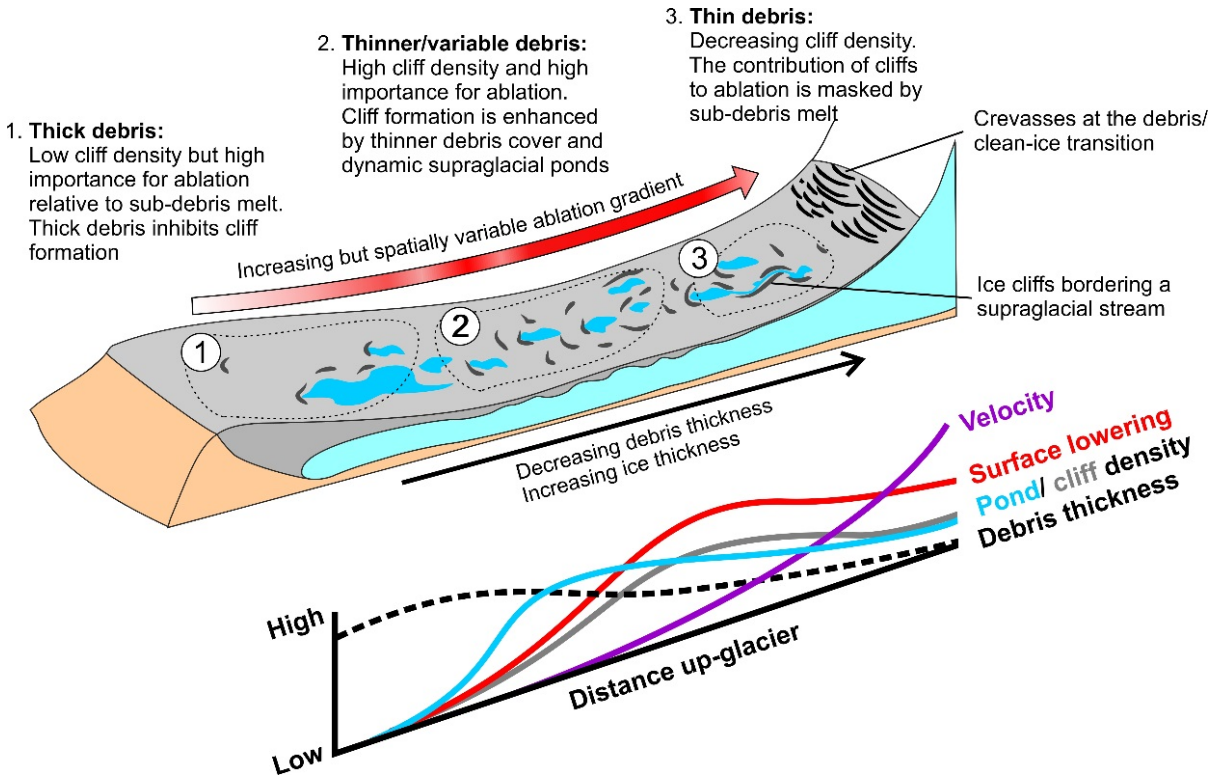

Figure 5.9. The interaction and associated ablation between ice cliffs, supraglacial ponds, and debris thickness on a debris-covered glacier.

5.7.2 Debris-covered glacier evolution

It is important to be able to characterise the interaction between ice cliffs, supraglacial ponds, debris thickness, and surface lowering when considering future glacier evolution, especially where the number of cliffs and ponds displays an increasing trend (Figure 5.4) (Rowan et al., 2015; Watson et al., 2016). A temporal up-glacier migration in the occurrence of cliffs is not apparent in our relatively short dataset, yet might be expected to accompany predicted volume loss in the coming century. In practical terms, the observations of cliff density, spatial dynamics and relationships, and cliff aspect presented in this study could be used to inform a glacier-specific and spatial parameterisation of ice cliff ablation when combined with local observations of cliff retreat (Table 5.1). However, knowledge of respective cliff areas is still lacking unless corresponding DEMs are available. Additionally, even with corresponding DEMs, the surface topography of steep cliff faces is likely to be poorly represented (Kolecka, 2012). Therefore, investigating a relationship between cliff length and mean cliff height could improve the utility of remote-sensing observations, especially since we observe similar frequency distributions of cliff length for each of our study glaciers (Figure 5.5). Here, cliffs between 21 and 40 m in length were most common. Relationships between surface lowering, cliff density, and debris thickness were apparent in this study using a 30 m resolution dataset. However, it is clear that an increased spatial coverage of

fine-resolution DEM differencing (e.g. Thompson et al., 2016), combined with local-scale observations of retreat, is the best strategy to further investigate their spatial and temporal significance.

5.7.3 Strategies for monitoring cliff evolution

The remote sensing analysis presented in this study reveals planimetric ice cliff dynamics but does not represent the heterogeneity of ice cliff morphologies that we observed in the field. Our field observations indicate that an ablation gradient is likely to be present on crescentic cliffs, which span a range of aspects (Figure 5.10). We identified meltwater runnel formation on several of these cliffs, which act as preferential pathways for meltwater and debris fluxes (falling debris and saturated debris flows). Runnel persistence is likely to be governed by the background rate of cliff melt, which determines the rate at which the runnel can incise, similar to the formation process of supraglacial streams (Hambrey, 1977), and the supply of meltwater and debris down the cliff face. Once established, the runnels create local topographic shading which may act as a positive feedback by slowing the decay of adjacent ridges bounding the runnel (e.g. Figure 5.10b). Where the background rate of cliff melt is low and winter refreeze persists on the cliff face, meltwater and debris conveyance may be the dominant ablative mechanism. This observed morphological heterogeneity is not considered in the top-edge delineation of an ice cliff, or in point-ablation stake measurements since placements are potentially spatially biased due to safety concerns (e.g. placement away from areas of falling or unstable debris). Therefore cliff parameterisation in dynamic glacier models still requires an improved processed-based understanding of cliff formation and evolution from field observations.

Isolating the magnitude of ice cliff retreat through multi-temporal observations is becoming possible with fine-resolution stereo imagery (e.g. Thompson et al., 2016) or low cost aerial surveys (e.g. Immerzeel et al., 2014; Brun et al., 2016). However, the steeply sloping cliff faces are likely to be poorly represented in commonly used 2D DEMs (Kolecka, 2012). Alternatively, fully 3D surveys could be pursued following a Structure from Motion with Multi-View Stereo workflow (e.g. Smith et al., 2015) and 3D point cloud differencing (Lague et al., 2013) to reveal the spatial and temporal retreat dynamics across a range of cliff aspects. This technology facilitates comparisons at a spatial resolution comparable to that at which the processes are operating (Passalacqua et al., 2015) and cloud-to-cloud differencing is available in open source software (e.g. CloudCompare). These 3D measurements of cliff retreat could then be coupled to remote sensing observations of cliff spatio-temporal distribution for

inclusion into dynamic glacier models, or used to validate cliff-scale grid-based models (e.g. Buri et al., 2016).

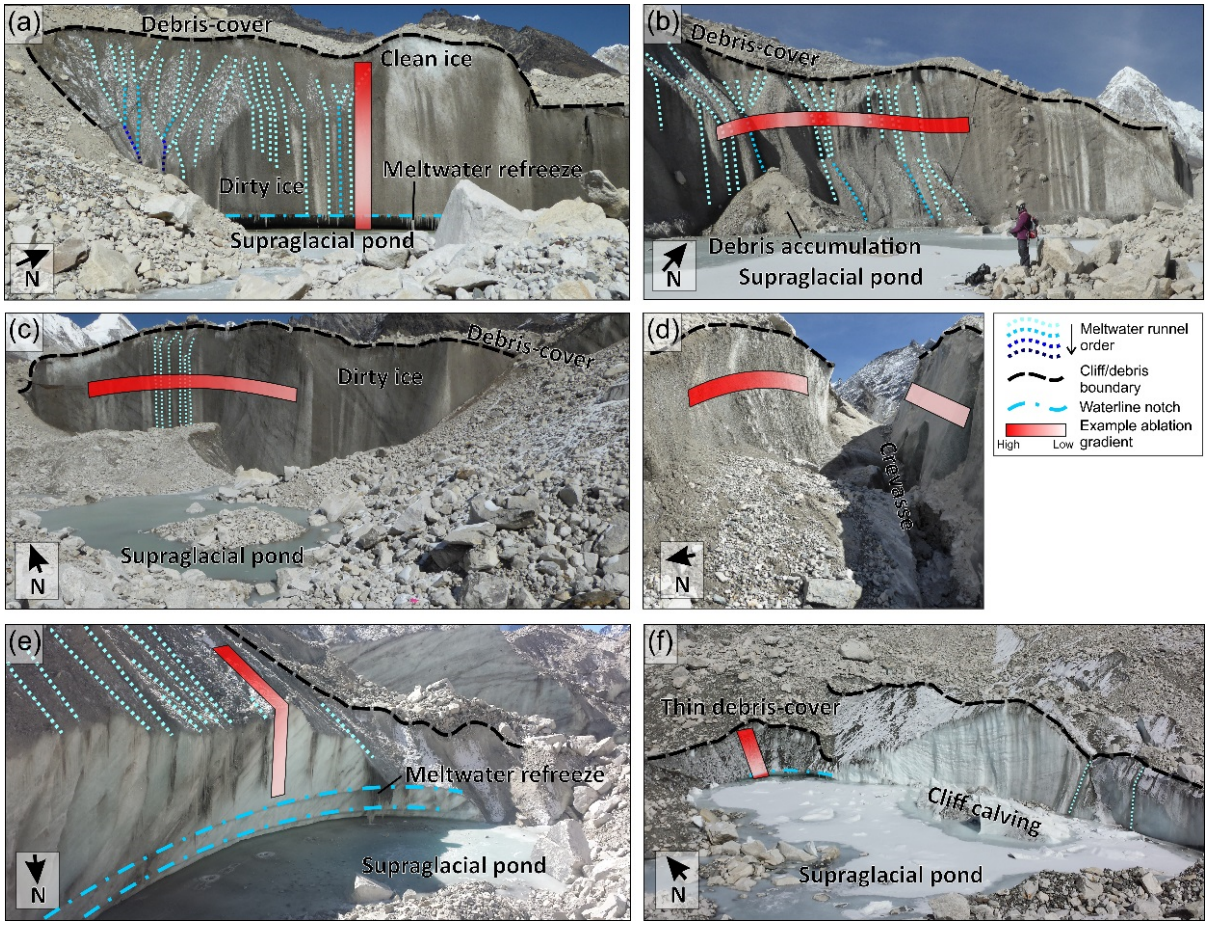

Figure 5.10. Examples of ice cliffs on the Khumbu Glacier. (a) An easterly facing cliff with well-developed meltwater channels, (b) a south-easterly facing cliff with well-developed meltwater runnels, (c) a south-facing cliff with limited meltwater runnels, (d) adjacent south- and north-facing cliffs with no meltwater runnels, (e) a cliff with historic water level notches revealing seasonal pond drainage, and (f) a south-facing debris-covered cliff and a west-facing clean-ice cliff with evidence of recent calving. Indicative ablation gradients are suggested from visual observations of cliff morphology and meltwater flows.

5.8 Conclusion and future work

We have presented the first spatio-temporally detailed analysis of ice cliff distribution and geometry characteristics for 14 debris-covered glaciers in the Everest region. Our results show that whilst ice cliffs are present across most of the debris-covered parts of these glaciers, their density is spatio-temporally variable and not clearly linked to glacier surface velocity. Therefore, ice cliffs do not appear to form preferentially on stagnating tongues where supraglacial ponds coalesce. However, we observed high spatial coincidence of ice cliffs and supraglacial ponds, highlighting the importance of

the cliff–pond interaction and the potential transition from subaerial to calving ice cliff retreat, which is a transition that can increase cliff recession rates threefold (Benn et al., 2001). Supraglacial pond expansion in the region suggests this interaction may becoming increasingly pertinent (Watson et al., 2016).

The predominance of north-facing cliffs irrespective of glacier flow direction supports a strong solar radiation control on cliff evolution (e.g. Sakai et al., 2002). Here, a high direct solar radiation receipt on south-facing cliffs can promote rapid decay and burial under debris, whilst shaded north-facing cliffs can persist. However, increased temporal resolution is required to confirm the timescale over which this south-facing cliff decay occurs, compared to the temporal longevity of north-facing cliffs. Determining the interaction between cliff density, surface lowering, debris thickness, cliff aspect, energy balance fluxes, and the influence of supraglacial ponds, would all benefit from fully 3D multi-temporal observations of cliff evolution. By coupling remote sensing and in-situ observations it is possible to capture processes operating at multiple spatial scales on the heterogeneous cliff faces, which is necessary if the proper parameterisation of ice cliffs in dynamic glacier models is to be addressed.

To summarise, our main findings are:

(1) A high spatial coincidence of supraglacial ponds and ice cliffs where on average across the study glaciers 77% of supraglacial pond area had an adjacent ice cliff, and 49% of ice cliffs had an adjacent supraglacial pond.

(2) An increase in ice cliff density with distance up-glacier from the terminus to peak in the zone of observable glacier movement (velocity >3 m a^{-1}), before a decline towards the transition zone from debris to clean-ice.

(3) A spatial density of ice cliffs that is glacier-specific, and that is positively correlated with surface lowering and decreasing debris thickness up-glacier.

(4) A predominance of north-facing ice cliffs irrespective of glacier flow direction.

Acknowledgements

C.S.W acknowledges support from the School of Geography at the University of Leeds, theMount Everest Foundation, the Royal Geographical Society (with IBG), the British Society for Geomorphology, the Petzl Foundation, and water@leeds. TerraSAR-X images were supplied by the European Space Agency under Category-1 Proposal Id. 32600 and we thank Adrian Luckman for use of his feature tracking code. Dhananjay Regmi and Himalayan Research Expeditions are thanked for invaluable support during fieldwork and for obtaining research permits. Owen King and David Rounce provided access to surface elevation change and debris-thickness

datasets respectively. We thank I.S. Evans and two anonymous reviewers for comments, which helped improved this study.

5.9 References

Benn, D.I. Bolch, T. Hands, K. Gulley, J. Luckman, A. Nicholson, L.I. Quincey, D. Thompson, S. Toumi, R. and Wiseman, S. 2012. Response of debris-covered glaciers in the Mount Everest region to recent warming, and implications for outburst flood hazards. *Earth-Science Reviews.* **114**(1–2), 156-174.

Benn, D.I. Warren, C.R. and Mottram, R.H. 2007. Calving processes and the dynamics of calving glaciers. *Earth-Science Reviews.* **82**(3-4), 143-179.

Benn, D.I. Wiseman, S. and Hands, K.A. 2001. Growth and drainage of supraglacial lakes on debris-mantled Ngozumpa Glacier, Khumbu Himal, Nepal. *Journal of Glaciology.* **47**(159), 626-638.

Bolch, T. Buchroithner, M. Pieczonka, T. and Kunert, A. 2008. Planimetric and volumetric glacier changes in the Khumbu Himal, Nepal, since 1962 using Corona, Landsat TM and ASTER data. *Journal of Glaciology.* **54**(187), 592-600.

Bolch, T. Kulkarni, A. Kääb, A. Huggel, C. Paul, F. Cogley, J.G. Frey, H. Kargel, J.S. Fujita, K. Scheel, M. Bajracharya, S. and Stoffel, M. 2012. The State and Fate of Himalayan Glaciers. *Science.* **336**(6079), 310-314.

Bolch, T. Pieczonka, T. and Benn, D.I. 2011. Multi-decadal mass loss of glaciers in the Everest area (Nepal Himalaya) derived from stereo imagery. *The Cryosphere.* **5**(2), 349-358.

Brun, F. Buri, P. Miles, E.S. Wagnon, P. Steiner, J.F. Berthier, E. Ragettli, S. Kraaijenbrink, P. Immerzeel, W.W. and Pellicciotti, F. 2016. Quantifying volume loss from ice cliffs on debris-covered glaciers using high-resolution terrestrial and aerial photogrammetry. *Journal of Glaciology.* **FirstView**, 1-12.

Buri, P. Pellicciotti, F. Steiner, J.F. Miles, E.S. and Immerzeel, W.W. 2016. A grid-based model of backwasting of supraglacial ice cliffs on debris-covered glaciers. *Annals of Glaciology* **57**(71), 199-211.

Carrivick, J.L. and Tweed, F.S. 2013. Proglacial lakes: character, behaviour and geological importance. *Quaternary Science Reviews.* **78**, 34-52.

Chaturvedi, R.K. Kulkarni, A. Karyakarte, Y. Joshi, J. and Bala, G. 2014. Glacial mass balance changes in the Karakoram and Himalaya based on CMIP5 multi-model climate projections. *Climatic Change.* **123**(2), 315-328.

Douglas, J.S. Huss, M. Swift, D.A. Jones, J.M. and Salerno, F. 2016. Incorporating Distributed Debris Thickness in a Glacio-Hydrological Model: Khumbu Himalaya, Nepal. *The Cryosphere Discuss.* **2016**, 1-35.

Foster, L.A. Brock, B.W. Cutler, M.E.J. and Diotri, F. 2012. A physically based method for estimating supraglacial debris thickness from thermal band remote-sensing data. *Journal of Glaciology.* **58**(210), 677-691.

Gardelle, J. Arnaud, Y. and Berthier, E. 2011. Contrasted evolution of glacial lakes along the Hindu Kush Himalaya mountain range between 1990 and 2009. *Global and Planetary Change.* **75**(1–2), 47-55.

Gulley, J. and Benn, D.I. 2007. Structural control of englacial drainage systems in Himalayan debris-covered glaciers. *Journal of Glaciology.* **53**(182), 399-412.

Hambrey, M.J. 1977. Supraglacial drainage and its relationship to structure, with particular reference to Charles Rabots Bre, Okstindan, Norway. *Norsk Geografisk Tidsskrift - Norwegian Journal of Geography.* **31**(2), 69-77.

Han, H. Wang, J. Wei, J. and Liu, S. 2010. Backwasting rate on debris-covered Koxkar glacier, Tuomuer mountain, China. *Journal of Glaciology.* **56**(196), 287-296.

Haritashya, U.K. Pleasants, M.S. and Copland, L. 2015. Assessment of the evolution in velocity of two debris-covered glaciers in Nepal and New Zealand. *Geografiska Annaler: Series A, Physical Geography.* **97**(4), 737–751.

Immerzeel, W.W. Kraaijenbrink, P.D.A. Shea, J.M. Shrestha, A.B. Pellicciotti, F. Bierkens, M.F.P. and de Jong, S.M. 2014. High-resolution monitoring of Himalayan glacier dynamics using unmanned aerial vehicles. *Remote Sensing of Environment.* **150**, 93-103.

Inoue, J. 1977. Mass Budget of Khumbu Glacier. *Journal of the Japanese Society of Snow and Ice.* **39**(Special), 15-19.

Inoue, J. and Yoshida, M. 1980. Ablation and heat exchange over the khumbu glacier. *Journal of the Japanese Society of Snow and Ice.* **39**, 7-14.

Iwata, S., Watanabe, O. and Fushimi, H. 1980. Surface Morphology in the Ablation Area of the Khumbu Glacier. *Seppyo, 41 (Special issue).* **9-17**.

Juen, M. Mayer, C. Lambrecht, A. Han, H. and Liu, S. 2014. Impact of varying debris cover thickness on ablation: a case study for Koxkar Glacier in the Tien Shan. *The Cryosphere.* **8**(2), 377-386.

Kääb, A. Berthier, E. Nuth, C. Gardelle, J. and Arnaud, Y. 2012. Contrasting patterns of early twenty-first-century glacier mass change in the Himalayas. *Nature.* **488**(7412), 495-498.

Kääb, A. Treichler, D. Nuth, C. and Berthier, E. 2015. Brief Communication: Contending estimates of 2003-2008 glacier mass balance over the Pamir–Karakoram–Himalaya. *The Cryosphere.* **9**(2), 557-564.

King, O. Quincey, D.J. Carrivick, J.L. and Rowan, A.V. 2016. Spatial variability in mass change of glaciers in the Everest region, central Himalaya, between 2000 and 2015. *The Cryosphere Discuss.* **2016**, 1-35.

Kirkbride, M.P. 1993. The temporal significance of transitions from melting to calving termini at glaciers in the central Southern Alps of New Zealand. *The Holocene.* **3**(3), 232-240.

Kolecka, N. 2012. Vector algebra for Steep Slope Model analysis. *Landform Analysis.* **21**, 17-25.

Lague, D. Brodu, N. and Leroux, J. 2013. Accurate 3D comparison of complex topography with terrestrial laser scanner: Application to the Rangitikei canyon (N-Z). *ISPRS Journal of Photogrammetry and Remote Sensing.* **82**, 10-26.

Lutz, A.F. Immerzeel, W.W. Shrestha, A.B. and Bierkens, M.F.P. 2014. Consistent increase in High Asia's runoff due to increasing glacier melt and precipitation. *Nature Clim. Change.* **4**(7), 587-592.

Mattson, L.E. Gardner, J.S. and Young, G.J. 1993. Ablation of debris covered glaciers: An example from the Rakhiot Glacier, Punjab Himalaya. In: Young, G.J., ed. *Snow and Glacier Hydrology (Proceedings of the Kathmandu Symposium, November 1992)*, *Kathmandu, Nepal*. IAHS Publishing, 289-296.

Miles, E.S. Pellicciotti, F. Willis, I.C. Steiner, J.F. Buri, P. and Arnold, N.S. 2016. Refined energy-balance modelling of a supraglacial pond, Langtang Khola, Nepal. *Annals of Glaciology.* **57**(71), 29-40.

Nakawo, M. Iwata, S. Watanabe, O. and Yoshida, M. 1986. Processes which distribute supraglacial debris on the Khumbu Glacier, Nepal Himalaya. *Annals of Glaciology.* **8**, 129-131.

Nakawo, M. Yabuki, H. and Sakai, A. 1999. Characteristics of Khumbu Glacier, Nepal Himalaya: recent change in the debris-covered area. *Annals of Glaciology.* **28**(1), 118-122.

Nicholson, L. and Benn, D.I. 2006. Calculating ice melt beneath a debris layer using meteorological data. *Journal of Glaciology.* **52**(178), 463-470.

Nicholson, L. and Benn, D.I. 2013. Properties of natural supraglacial debris in relation to modelling sub-debris ice ablation. *Earth Surface Processes and Landforms.* **38**(5), 490-501.

Nie, Y. Zhang, Y. Ding, M. Liu, L. and Wang, Z. 2013. Lake change and its implication in the vicinity of Mt. Qomolangma (Everest), central high Himalayas, 1970–2009. *Environmental Earth Sciences.* **68**(1), 251-265.

Nuimura, T. Fujita, K. Yamaguchi, S. and Sharma, R.R. 2012. Elevation changes of glaciers revealed by multitemporal digital elevation models calibrated by GPS survey in the Khumbu region, Nepal Himalaya, 1992-2008. *Journal of Glaciology.* **58**(210), 648-656.

Östrem, G. 1959. Ice Melting under a Thin Layer of Moraine, and the Existence of Ice Cores in Moraine Ridges. *Geografiska Annaler.* **41**(4), 228-230.

Passalacqua, P. Belmont, P. Staley, D.M. Simley, J.D. Arrowsmith, J.R. Bode, C.A. Crosby, C. DeLong, S.B. Glenn, N.F. Kelly, S.A. Lague, D. Sangireddy, H. Schaffrath, K. Tarboton, D.G. Wasklewicz, T. and Wheaton, J.M. 2015. Analyzing high resolution topography for advancing the understanding of mass and energy transfer through landscapes: A review. *Earth-Science Reviews.* **148**, 174-193.

Pellicciotti, F. Stephan, C. Miles, E. Herreid, S. Immerzeel, W.W. and Bolch, T. 2015. Mass-balance changes of the debris-covered glaciers in the Langtang Himal, Nepal, from 1974 to 1999. *Journal of Glaciology.* **61**(226), 373-386.

Pfeffer, W.T. Arendt, A.A. Bliss, A. Bolch, T. Cogley, J.G. Gardner, A.S. Hagen, J.O. Hock, R. Kaser, G. Kienholz, C. Miles, E.S. Moholdt, G. Molg, N. Paul, F. Radic, V. Rastner, P. Raup, B.H. Rich, J. Sharp, M.J. and Randolph, C. 2014. The Randolph Glacier Inventory: a globally complete inventory of glaciers. *Journal of Glaciology.* **60**(221), 537-552.

Quincey, D.J. Luckman, A. and Benn, D. 2009. Quantification of Everest region glacier velocities between 1992 and 2002, using satellite radar interferometry and feature tracking. *Journal of Glaciology.* **55**(192), 596-606.

Quincey, D.J. Richardson, S.D. Luckman, A. Lucas, R.M. Reynolds, J.M. Hambrey, M.J. and Glasser, N.F. 2007. Early recognition of glacial lake hazards in the Himalaya using remote sensing datasets. *Global and Planetary Change.* **56**(1–2), 137-152.

Racoviteanu, A.E. Arnaud, Y. Williams, M.W. and Manley, W.F. 2015. Spatial patterns in glacier characteristics and area changes from 1962 to 2006 in the Kanchenjunga–Sikkim area, eastern Himalaya. *The Cryosphere.* **9**(2), 505-523.

Reid, T.D. and Brock, B.W. 2014. Assessing ice-cliff backwasting and its contribution to total ablation of debris-covered Miage glacier, Mont Blanc massif, Italy. *Journal of Glaciology.* **60**(219), 3-13.

Reynolds, J.M. 2000. On the formation of supraglacial lakes on debris-covered glaciers. In: Nakawo, M.Raymond, C.F. and Fountain, A., eds. *IAHS Publ. 264 (Symposium at Seattle 2000 – Debris-Covered Glaciers)*, *Seattle, Washington, U.S.A*. IAHS Publishing, 153-161.

Rohl, K. 2006. Thermo-erosional notch development at fresh-water-calving Tasman Glacier, New Zealand. *Journal of Glaciology.* **52**(177), 203-213.

Rounce, D.R. and McKinney, D.C. 2014. Debris thickness of glaciers in the Everest area (Nepal Himalaya) derived from satellite imagery using a nonlinear energy balance model. *The Cryosphere.* **8**(4), 1317-1329.

Rowan, A.V. Egholm, D.L. Quincey, D.J. and Glasser, N.F. 2015. Modelling the feedbacks between mass balance, ice flow and debris transport to predict the response to climate change of debris-covered glaciers in the Himalaya. *Earth and Planetary Science Letters.* **430**, 427-438.

Sakai, A. Nakawo, M. and Fujita, K. 1998. Melt rate of ice cliffs on the Lirung Glacier, Nepal Himalayas. *Bulletin of Glaciological Research.* **16**, 57-66.

Sakai, A. Nakawo, M. and Fujita, K. 2002. Distribution characteristics and energy balance of ice cliffs on debris-covered glaciers, Nepal Himalaya. *Arctic Antarctic and Alpine Research.* **34**(1), 12-19.

Sakai, A. Nishimura, K. Kadota, T. and Takeuchi, N. 2009. Onset of calving at supraglacial lakes on debris-covered glaciers of the Nepal Himalaya. *Journal of Glaciology.* **55**(193), 909-917.

Sakai, A. Takeuchi, N. Fujita, K. and Nakawo, M. 2000. Role of supraglacial ponds in the ablation process of a debris-covered glacier in the Nepal Himalayas. In: Nakawo, M.Raymond, C.F. and Fountain, A., eds. *IAHS Publ. 264 (Symposium at Seattle 2000 – Debris-Covered Glaciers)*, *Seattle, Washington, U.S.A*. IAHS Publishing, 119-130.

Salerno, F. Guyennon, N. Thakuri, S. Viviano, G. Romano, E. Vuillermoz, E. Cristofanelli, P. Stocchi, P. Agrillo, G. Ma, Y. and Tartari, G. 2015. Weak precipitation, warm winters and springs impact glaciers of south slopes of Mt. Everest (central Himalaya) in the last 2 decades (1994–2013). *The Cryosphere.* **9**(3), 1229-1247.

Salerno, F. Thakuri, S. D'Agata, C. Smiraglia, C. Manfredi, E.C. Viviano, G. and Tartari, G. 2012. Glacial lake distribution in the Mount Everest region: Uncertainty of

measurement and conditions of formation. *Global and Planetary Change.* **92-93**, 30-39.

Scherler, D. Bookhagen, B. and Strecker, M.R. 2011. Spatially variable response of Himalayan glaciers to climate change affected by debris cover. *Nature Geosci.* **4**(3), 156-159.

Shea, J.M. and Immerzeel, W.W. 2016. An assessment of basin-scale glaciological and hydrological sensitivities in the Hindu Kush–Himalaya. *Annals of Glaciology.* **57**(71), 308-318.

Shea, J.M. Immerzeel, W.W. Wagnon, P. Vincent, C. and Bajracharya, S. 2015. Modelling glacier change in the Everest region, Nepal Himalaya. *The Cryosphere.* **9**(3), 1105-1128.

Shrestha, A.B. and Aryal, R. 2011. Climate change in Nepal and its impact on Himalayan glaciers. *Regional Environmental Change.* **11**, 65-77.

Smith, M.W. Carrivick, J.L. and Quincey, D.J. 2015. Structure from motion photogrammetry in physical geography. *Progress in Physical Geography.*

Soncini, A. Bocchiola, D. Confortola, G. Minora, U. Vuillermoz, E. Salerno, F. Viviano, G. Shrestha, D. Senese, A. Smiraglia, C. and Diolaiuti, G. 2016. Future hydrological regimes and glacier cover in the Everest region: The case study of the upper Dudh Koshi basin. *Science of The Total Environment.* **565**, 1084-1101.

Steiner, J.F. and Pellicciotti, F. 2016. Variability of air temperature over a debris-covered glacier in the Nepalese Himalaya. *Annals of Glaciology.* **57**(71), 295-307.

Steiner, J.F. Pellicciotti, F. Buri, P. Miles, E.S. Immerzeel, W.W. and Reid, T.D. 2015. Modelling ice-cliff backwasting on a debris-covered glacier in the Nepalese Himalaya. *Journal of Glaciology.* **61**(229), 889-907.

Thakuri, S. Salerno, F. Bolch, T. Guyennon, N. and Tartari, G. 2016. Factors controlling the accelerated expansion of Imja Lake, Mount Everest region, Nepal. *Annals of Glaciology.* **57**(71), 245-257.

Thakuri, S. Salerno, F. Smiraglia, C. Bolch, T. D'Agata, C. Viviano, G. and Tartari, G. 2014. Tracing glacier changes since the 1960s on the south slope of Mt. Everest (central Southern Himalaya) using optical satellite imagery. *Cryosphere.* **8**(4), 1297-1315.

Thompson, S. Benn, D. Mertes, J. and Luckman, A. 2016. Stagnation and mass loss on a Himalayan debris-covered glacier: processes, patterns and rates. *Journal of Glaciology.* **FirstView**, 1-19.

Thompson, S.S. Benn, D.I. Dennis, K. and Luckman, A. 2012. A rapidly growing moraine-dammed glacial lake on Ngozumpa Glacier, Nepal. *Geomorphology.* **145**, 1-11.

Wang, W.C. Xiang, Y. Gao, Y. Lu, A.X. and Yao, T.D. 2015. Rapid expansion of glacial lakes caused by climate and glacier retreat in the Central Himalayas. *Hydrological Processes.* **29**(6), 859-874.

Watson, C.S. Quincey, D.J. Carrivick, J.L. and Smith, M.W. 2016. The dynamics of supraglacial ponds in the Everest region, central Himalaya. *Global and Planetary Change.* **142**, 14-27.

Yang, X. Zhang, T. Qin, D. Kang, S. and Qin, X. 2011. Characteristics and Changes in Air Temperature and Glacier's Response on the North Slope of Mt. Qomolangma (Mt. Everest). *Arctic, Antarctic, and Alpine Research.* **43**(1), 147-160.

Yang, X. Zhang, Y. Zhang, W. Yan, Y. Wang, Z. Ding, M. and Chu, D. 2006. Climate change in Mt. Qomolangma region since 1971. *Journal of Geographical Sciences.* **16**(3), 326-336.

Ye, Q. Bolch, T. Naruse, R. Wang, Y. Zong, J. Wang, Z. Zhao, R. Yang, D. and Kang, S. 2015. Glacier mass changes in Rongbuk catchment on Mt. Qomolangma from 1974 to 2006 based on topographic maps and ALOS PRISM data. *Journal of Hydrology.* **530**, 273-280.

Zhang, Y. Fujita, K. Liu, S. Liu, Q. and Nuimura, T. 2011. Distribution of debris thickness and its effect on ice melt at Hailuogou glacier, southeastern Tibetan Plateau, using in situ surveys and ASTER imagery. *Journal of Glaciology.* **57**(206), 1147-1157.

Zhao, L. Ding, R. and Moore, J.C. 2014. Glacier volume and area change by 2050 in high mountain Asia. *Global and Planetary Change.* **122**, 197-207.

Chapter 6
Quantifying ice cliff evolution with multi-temporal point clouds on the debris-covered Khumbu Glacier, Nepal

C. Scott Watson, Duncan J. Quincey, Mark W. Smith, *Jonathan L. Carrivick, Ann V. Rowan, and Mike James*

Journal of Glaciology. 2017.

DOI: 10.1017/jog.2017.47

6.1 Abstract

Measurements of glacier ice cliff evolution are sparse, but where they do exist, they indicate that such areas of exposed ice contribute a disproportionate amount of melt to the glacier ablation budget. We used Structure from Motion photogrammetry with Multi-View Stereo to derive 3-D point clouds for nine ice cliffs on Khumbu Glacier, Nepal (in November 2015, May 2016 and October 2016). By differencing these clouds, we could quantify the magnitude, seasonality and spatial variability of ice cliff retreat. Mean retreat rates of 0.30–1.49 cm d^{-1} were observed during the winter interval (November 2015–May 2016) and 0.74–5.18 cm d^{-1} were observed during the summer (May 2016– October 2016). Four ice cliffs, which all featured supraglacial ponds, persisted over the full study period. In contrast, ice cliffs without a pond or with a steep back-slope degraded over the same period. The rate of thermo-erosional undercutting was over double that of subaerial retreat. Overall, 3-D topographic differencing allowed an improved process-based understanding of cliff evolution and cliff-pond coupling, which will become increasingly important for monitoring and modelling the evolution of thinning debris-covered glaciers.

6.2 Introduction

In coming decades, ongoing mass loss from Himalayan glaciers and changing runoff trends will affect the water resources of over a billion people, including those who require it for agricultural, energy production, and domestic usage (Immerzeel and others, 2009; Immerzeel and others, 2010; Lutz and others, 2014; Mukherji and others, 2015; Shea and Immerzeel, 2016). A negative mass balance regime prevails across glaciers in the central and eastern Himalaya (Bolch and others, 2011; Fujita and Nuimura, 2011; Benn and others, 2012; Kääb and others, 2012; Kääb and others, 2015; King and others, 2017), which are widely recognised to be out of equilibrium with current climate (Yang and others, 2006; Shrestha and Aryal, 2011; Salerno and others, 2015). Deglaciation is leading to the development of large proglacial lakes, which may expand rapidly through ice cliff calving (Bolch and others, 2008; Benn and others, 2012; Thompson and others, 2012; Thakuri and others, 2016), and pose potential glacial lake outburst flood hazards (e.g. Carrivick and Tweed, 2013; Carrivick and Tweed, 2016; Rounce and others, 2016; Rounce and others, 2017).

Debris-covered glaciers have a hummocky, pitted surface, caused by variable melt rates under different debris thicknesses, and include extensive coverage of ice cliffs and supraglacial ponds (Hambrey and others, 2008; Thompson and others, 2016; Watson and others, 2016; Watson and others, 2017). Studies using Digital Elevation Model (DEM) differencing to quantify elevation change over debris-covered tongues have revealed an association between glacier surface lowering and the presence of ice cliffs and supraglacial ponds (Immerzeel and others, 2014; Pellicciotti and others, 2015; Ragettli and others, 2016; Thompson and others, 2016), confirming historical ice cliff observations (e.g. Inoue and Yoshida, 1980; Sakai and others, 1998; Benn and others, 2001; Sakai and others, 2002). However, raster-based DEMs generally give a poor representation of steep slopes or steeply-sloping topography (Kolecka, 2012) and their differencing incorporates a mixed signal containing surface elevation change related to debris cover, ice cliff dynamics, supraglacial ponds, and glacier emergence velocity (Vincent and others, 2016).

Models of glacier evolution do not consider pond dynamics or ice cliff dynamics explicitly, because this requires an understanding of their spatio-temporal distribution (e.g. Sakai and others, 2002; Watson and others, 2017), energy balance modelling of the ice cliff surface (e.g. Reid and Brock, 2014; Steiner and others, 2015; Buri and others, 2016b; Buri and others, 2016a), and cliff-scale observations of retreat rates (e.g. Brun and others, 2016). Several studies have exploited topographic models derived from unmanned aerial vehicle surveys of Lirung Glacier in the Langtang region of Nepal, to make substantial progress towards understanding ice cliff dynamics

(Immerzeel and others, 2014; Steiner and others, 2015; Brun and others, 2016; Buri and others, 2016b; Buri and others, 2016a; Miles and others, 2016a). However, techniques to perform direct comparisons of multi-temporal point clouds without simplification have yet to be exploited.

In this study, we explore ice cliff evolution using multi-temporal point clouds obtained on Khumbu Glacier, Nepal. Specifically we: (1) quantify the retreat of ice cliffs for pre-monsoon and monsoon time periods; (2) compare the spatial variation in retreat across ice cliff faces; and (3) assess the change in ice cliff morphology through time in relation to local topography and the presence of supraglacial ponds.

6.3 Study site

Field data were obtained on Khumbu Glacier in the Everest region of Nepal during three field campaigns (post-monsoon November 2015, pre-monsoon May 2016, and late-monsoon October 2016). The November 2015 to May 2016 and May 2016 to October 2016 survey intervals are referred to as ‘winter’ and ‘summer’ respectively. The Indian summer monsoon spans the months of June to mid-October (Bollasina and others, 2002; Bonasoni and others, 2008) and is when ~80% of annual precipitation falls (Wagnon and others, 2013).

Khumbu Glacier is ~17 km long, of which the lower 10 km is debris covered (Fig. 6.1) and the lower ~4 km is essentially stagnant (Quincey and others, 2009). Supraglacial debris thickness is >2 m in this stagnating region and decreases up-glacier (Nakawo and others, 1986; Rowan and others, 2015). However, the thickness of the debris layer is locally heterogeneous owing to the pitted surface and the presence of ice cliffs and supraglacial ponds. We studied nine ice cliffs on the lower debris-covered glacier (Fig. 6.1), which is a region of particular interest since supraglacial ponds have begun to coalesce here over the past five years (Watson and others, 2016), and a large glacial lake is expected to form (Naito and others, 2000; Bolch and others, 2011; Haritashya and others, 2015).

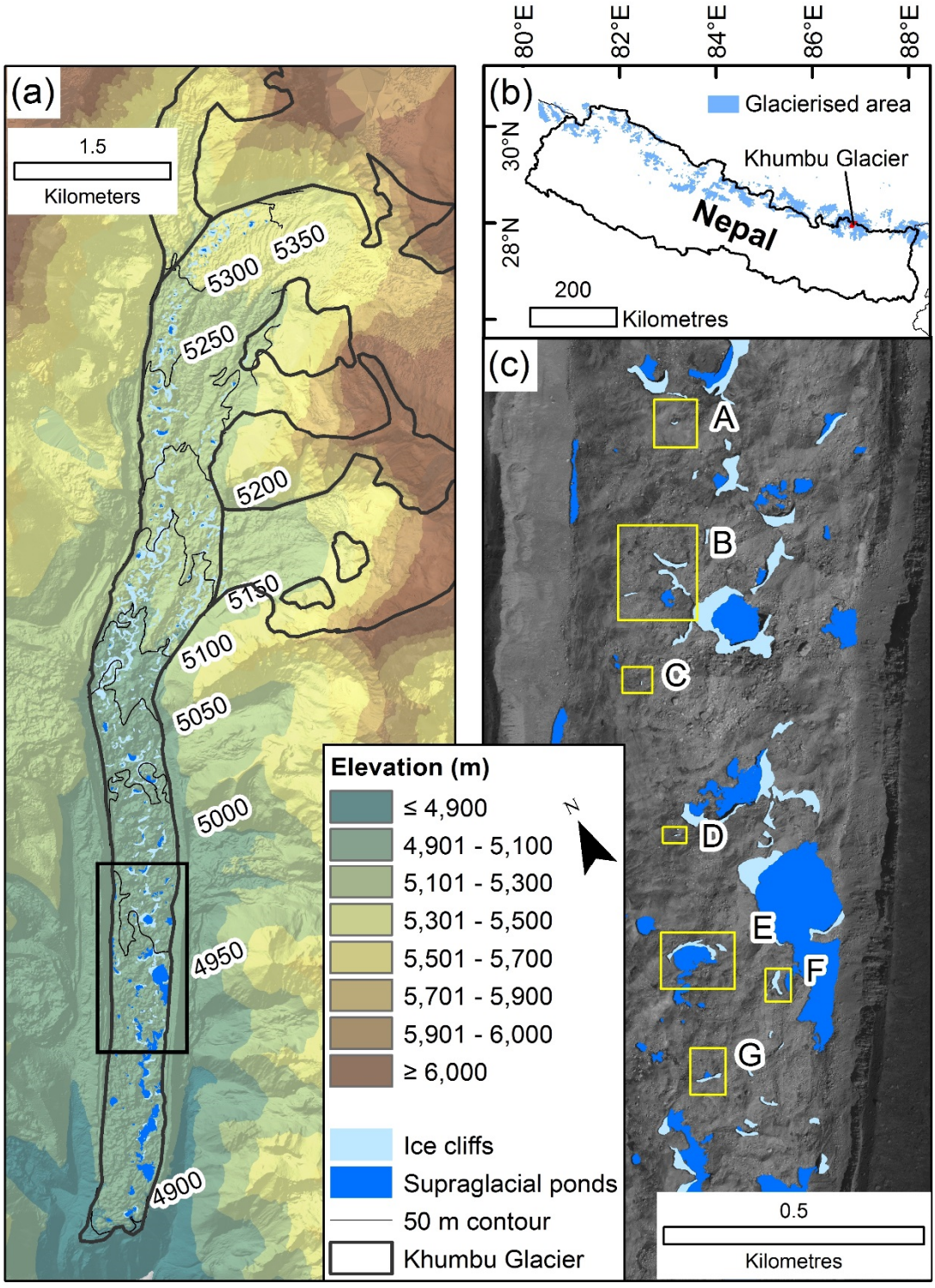

Figure. 6.1. Ice cliffs and supraglacial ponds on Khumbu Glacier (a), located in eastern Nepal (b). Inset boxes show the location and ID of the ice cliffs surveyed (c). Cliff sites B and D included both northerly- and southerly-facing ice cliffs. The panchromatic background image is from the Pleiades satellite (07/10/2015), and corresponding ice cliffs and ponds are shown. Khumbu Glacier flows in a southerly direction.

6.4 Data and methods

6.4.1 Data collection

Terrestrial photographic surveys of nine ice cliffs were carried out during the three field campaigns. Our study cliffs represented approximately 2% of the total ice cliff extent on Khumbu Glacier, based on the top-edge cliff delineation of Watson and others (2017). We sought to survey cliffs that were broadly representative of the range of cliffs found on Khumbu Glacier, with and without supraglacial ponds, of variable aspect, and of variable size, noting the terrestrial survey constraints that precluded surveys of very large cliffs. Four of our nine study cliffs had a supraglacial pond present during the initial survey and the mean length of ice cliffs was 57 m. This compares to the observation that on Khumbu Glacier 47% of ice cliffs were associated with a pond in 2015, and cliffs had a mean length of 54 m (Watson and others, 2017). We note from Watson and others (2017) that cliffs 20−40 m in length were most common, but that some cliffs exceeded 200 m in length.

Two out of the seven individual study sites (Fig. 6.1) included both northerly- and southerly-facing cliff faces. These southerly-facing cliffs are labelled '-SF' hereafter. Within the first two field campaigns, surveys were conducted at intervals of 7–11 days at cliffs C, D, E and F, which are referred to as 'weekly' surveys. 'Seasonal' surveys refer to those between field campaigns. Each survey typically took <1 hour and 122–564 photos were taken of each ice cliff with a highly convergent geometry (Fig. 6.2a) using a Panasonic DMC-TZ60 18.1 megapixel digital camera. In order to capture the surrounding topography, each photo was taken from a different position but was not necessarily orientated towards the ice cliff. High-contrast temporary ground control points (GCPs) (number of GCPs (n) = 6–15) were distributed around each ice cliff to encompass the survey area extents and surveyed using a Leica GS10 global navigation satellite system (GNSS). Each GCP was occupied in static mode for ~5 minutes. A base station was located on the lateral moraine of the glacier <2 km from our survey sites for the duration of each field campaign and was set to record each day.

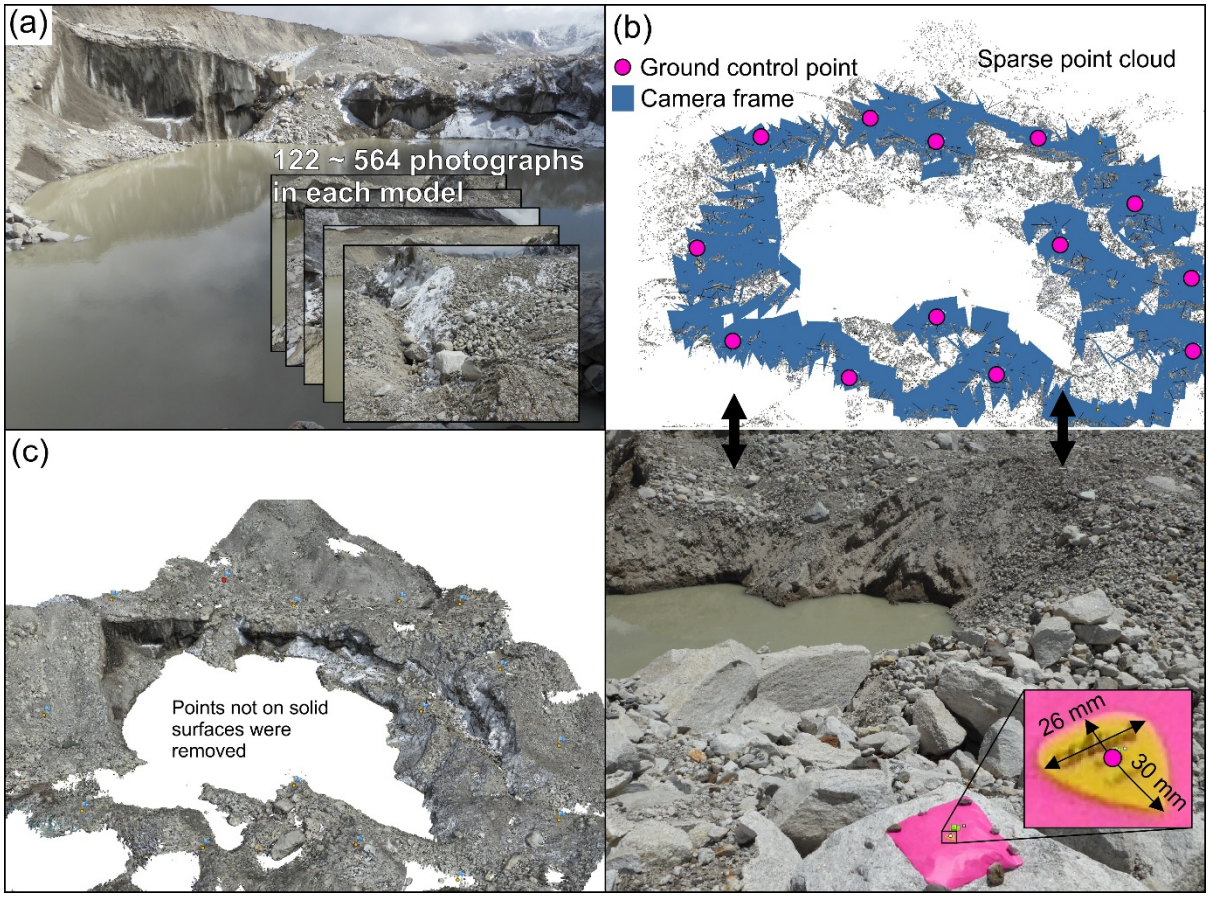

Figure. 6.2. The generation and georeferencing of ice cliff point clouds. Photographs of each ice cliff (a) were aligned to produce a sparse point cloud, which was georeferenced using high-contrast pink and yellow markers (b). Dense point clouds were produced and manually edited to remove points not on solid surfaces (e.g. supraglacial ponds) (c).

6.4.2 Post-processing

Our GNSS base station data were post-processed against the Syangboche permanent station (27.8142 N, 86.7125 E) located ~20 km from our field site using Global Positioning System (GPS) and GLObal NAvigation Satellite System (GLONASS) satellites. Our field GCPs were then adjusted with reference to the field base station data following a relative carrier phase positioning strategy. The mean 3D positional uncertainty was 3.9 mm across all our GCPs (n = 281).

Photographs were input into Agisoft PhotoScan 1.2.3 to derive 3D point clouds of the ice cliff topography following a Structure-from-Motion with Multiview Stereo (SfM-MVS) workflow (e.g. James and Robson, 2012; Westoby and others, 2012; Smith and others, 2015). First, photographs were aligned to produce a sparse point cloud by matching coincident features. This stage also estimated internal camera lens distortion parameters and scene geometry using a bundle adjustment with high redundancy, owing to large overlapping photographic datasets (Westoby and others, 2012). Only

points with a reprojection error of <0.6 were retained and clear outliers (e.g. areas of shadow under overhanging cliffs) were removed manually. Second, GCPs were identified in each photograph to georeference the sparse cloud. GCP placement accuracy was <10 mm (e.g. Fig. 6.2b). Uncertainties from GCP placement and the post-processed coordinates were used as weights to optimise the point cloud georeferencing to minimise root-mean-square error (RMSE) (Javernick and others, 2014; Stumpf and others, 2015; Smith and others, 2016; Westoby and others, 2016). Third, a dense point cloud was produced using PhotoScan's multiview stereo (MVS) algorithm (Fig. 6.3). The dense cloud was subsequently edited to remove points that were not on solid surfaces (e.g. on supraglacial ponds) and clear outliers. All PhotoScan's processes were run on high quality settings. Georeferencing uncertainty in the final point clouds was <0.035 m (RMSE; Table 6.1). The final point clouds were sub-sampled using an octree filter in CloudCompare to unify point density across the surveys for each individual ice cliff. Subsequent point cloud densities ranged between 2,185–14,581 points per m^2.

Table 6.1. Summary statistics for each ice cliff model

Cliff ID	Survey date	Georeferencing RMSE (m) / (number of GCPs)	Tie point RMSE (pixels)	Co-registration RMSE (m) / (number of GCPs)	
				May 2016 to November 2015	October 2016 to May 2016
A	08/11/2015	0.017 (10)	0.96	*	
	13/05/2016	0.015 (7)	0.75	*0.050 (7)	*
	05/10/2016	0.014 (8)	0.73		*0.262 (8)
B	03/11/2015	0.025 (14)	0.97	*	
	16/05/2016	0.013 (14)	0.98	*0.070 (12)	*
	05/10/2016	0.012 (14)	0.84		*0.334 (11)
C	03/11/2015	0.012 (6)	1.05	*	
	10/11/2015	0.016 (7)	1.03		
	16/05/2016	0.011 (7)	0.92	*0.025 (7)	*
	25/05/2016	0.013 (7)	0.87		
	03/10/2016	0.016 (6)	0.86		*0.183 (6)

D	01/11/2015	0.016 (8)	1.05	*	
	10/11/2015	0.012 (8)	0.96		
	15/05/2016	0.011 (8)	0.80	*0.100 (6)	*
	25/05/2016	0.011 (8)	0.71		
	03/10/2016	0.011 (7)	0.68		*0.176 (6)
E	01/11/2015	0.034 (15)	0.87		
	12/11/2015	0.011 (15)	0.85	*	
	15/05/2016	0.018 (15)	0.84	*0.122 (9)	*
	26/05/2016	0.014 (15)	0.81		
	04/10/2016	0.013 (14)	0.89		*0.140 (9)
F	04/11/2015	0.012 (8)	1.14	*	
	14/11/2015	0.017 (9)	1.02		
	14/05/2016	0.008 (9)	1.05	*0.041 (8)	*
	25/05/2016	0.010 (9)	0.96		
	04/10/2016	0.007 (8)	1.02		*0.186 (8)
G	07/11/2015	0.017 (7)	0.98	*	
	15/05/2016	0.004 (6)	0.91	*0.031 (7)	*
	03/10/2016	0.011 (8)	1.01		*0.224 (7)

*For point cloud differencing, May 2016 data were co-registered with November 2015, and October 2016 were co-registered with May 2016

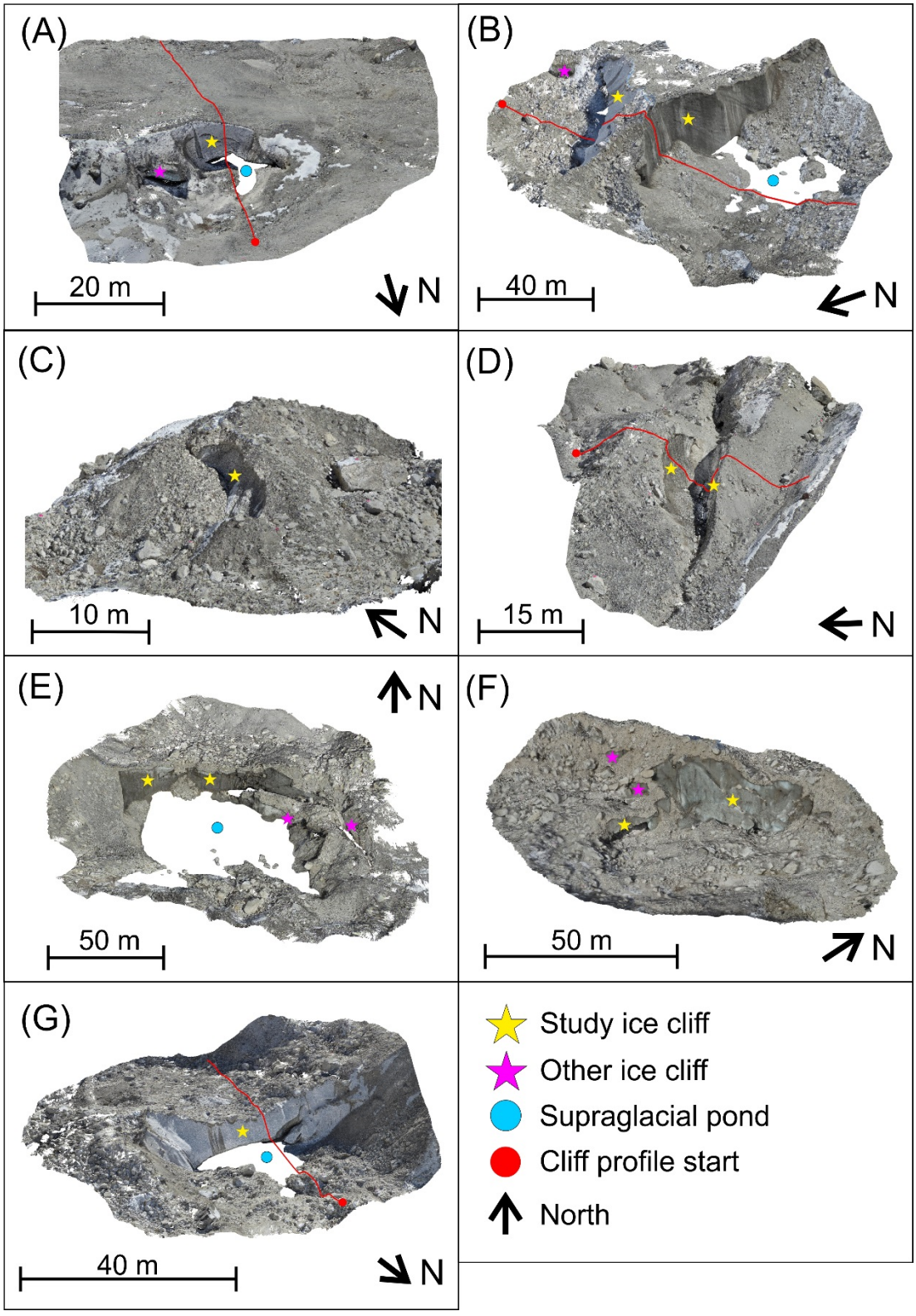

Figure. 6.3. Oblique views of the 3D ice cliff point clouds in November 2015. Cliff IDs correspond to Table 6.1 and Figure 6.1. The profiles (red lines) correspond to Figure 6.7.

6.4.3 Ice cliff displacement

6.4.3.1 Ice cliff surveys between field campaigns

The study cliffs were located down-glacier of the expected active−inactive ice transition on Khumbu Glacier (Quincey and others, 2009). However, small magnitude displacements (<3 m a^{-1}) were observed in this region from dGPS surveys of tagged boulders (Supplementary Fig. 6.1). Therefore, to correct for ice cliff displacement between field campaigns (November 2015 to May 2016 and May 2016 to October 2016) we co-registered point clouds using image features that could be identified in multiple surveys (e.g. identifiable marks on boulders). For each survey, the coordinates were derived for these features (as 'Markers' in PhotoScan), enabling a transform (2D translation-rotation) to be calculated to co-register the later model with the earlier one. The RMSE between these co-registered features are reported in Table 6.1, and were used as the total error (*ET*) in subsequent point cloud differencing. Co-registration errors were subject to sub-debris melt over each differencing period; however, thick debris cover (1−>2 m) (Nakawo and others, 1986) and low sub-debris melt rates of 0.0015 m d^{-1} (Inoue and Yoshida, 1980) over our study area minimised these errors. Glacier emergence velocity could not be calculated for this study; however, this is expected to be low for the slow-moving and gently-sloping debris-covered study area (Nuimura and others, 2012).

6.4.3.2 Ice cliff surveys within field campaigns

To account for cliff displacement between repeat surveys within each field campaign (e.g. Cliff C 03/11/2015 and 10/11/2015), we take the mean daily displacement of the respective cliff between field campaigns (e.g. 0.0023 m d^{-1}) and multiply this by the time-separation of the repeat models (e.g. seven days). The resulting shift (e.g. 0.0161 m) was treated as an additional uncertainty in addition to the respective georeferencing errors. We did not shift these models as described in section 3.3.1, since the expected displacement was <0.04 m for all ice cliffs, which was similar to the uncertainty in identifying coincident features in each model.

To calculate the total error (*ET*) for each cliff model comparison within a field campaign, the individual errors were propagated using (1):

$$(1)\ E_T = \sqrt{GE_{C1}^2 + GE_{C2}^2 + DE_{C1-C2}^2}$$

Where GE_{C1} and GE_{C2} are the georeferencing RMS errors associated with clouds *C1* and *C2*, and $DE_{C1\text{-}C2}$ is the displacement error between clouds *C1* and *C2*.

6.4.4 Point cloud characteristics and differencing

The mean slope and aspect of ice cliffs were calculated in CloudCompare using the dip direction and angle tool. The aspect of overhanging cliff sections required correction through 180°. The area of cliffs was calculated by fitting a mesh to each point cloud using the Poisson Surface Reconstruction tool in CloudCompare (Kazhdan and Hoppe, 2013).

Cloud-to-cloud differencing was carried out in the open source CloudCompare software using the Multiscale Model to Model Cloud Comparison (M3C2) method (e.g. Barnhart and Crosby 2013; Lague and others, 2013; Gomez-Gutierrez and others, 2015; Stumpf and others, 2015; Westoby and others, 2016). M3C2 was created by Lague and others (2013) to quantify the 3D distance between two point clouds along the normal surface direction and provide a 95% confidence interval based on the point cloud roughness and co-registration uncertainty. The method is therefore ideally suited to quantifying statistically significant ice cliff evolution where the geometry changes in 3D, and is robust to changes in point density and point cloud noise (Barnhart and Crosby, 2013; Lague and others, 2013).

For point clouds derived from photogrammetric techniques, uncertainty is spatially variable but highly correlated locally, since points in close proximity to one another are derived from the same images (James and others, 2017). Thus, although point-cloud roughness could represent a component of the measurement precision required to derive confidence intervals, it would not include broader photogrammetric contributions. In order to visualise spatially variable photogrammetric and georeferencing precision, we derived 3D precision maps for May 2016 study cliffs using the method of James and others (2017) (Supplementary Fig. 6.2). Repeated bundle adjustments implemented in PhotoScan (4000 Monte Carlo iterations) were applied to the sparse point cloud of each ice cliff using GCP and tie point uncertainties. Point precision estimates were then interpolated onto a 1 m raster grid in sfm_georef v3.0 (James and Robson, 2012; James and others, 2017). Large uncertainties were apparent at the survey edges (e.g. Cliff A, C, D, E), and around supraglacial ponds (e.g. Cliff E) due to poor photograph coverage. In contrast, the mean precision estimates ranged from 7−38 mm and were uniform across individual cliff faces. Hence, given the large magnitudes of the measured ice cliff changes, the M3C2-PM (Precision Maps) variant based on photogrammetry-derived precision maps was not required and the native M3C2 algorithm, implemented in CloudCompare, was used throughout.

M3C2 requires two user-defined parameters: (1) the normal scale *D*, which is used to calculate surface normals for each point and is dependent upon surface roughness and point cloud geometry, and (2) the projection scale d over which the cloud-to-cloud

distance calculation is averaged, which should be large enough to average a minimum of 30 points (Lague and others, 2013). We estimated the normal scale *D* for each point cloud following a trial-and-error approach similar that of Westoby and others (2016), to reduce the estimated normal error, *Enorm* (%), through refinement of a rescaled measure of the normal scale *n*(*i*):

$$(2)\ n(i) = \frac{D}{\sigma_i(D)}$$

n(i) is the normal scale D divided by the roughness *σ* measured at the same scale around *i.* Where *n(i)* falls in the range 20–25, *Enorm* <2% (Lague and others, 2013). In this study, normal scales *D* ranged from 1.5−8 m and the projection scale *d* was fixed at 0.3 m. The Level of Detection (LoD) threshold for a 95% confidence level is given by:

$$(3)\ LOD_{95\%}\ (d) = \pm 1.96\left(\sqrt{\frac{\sigma_1(d)^2}{n_1} + \frac{\sigma_2(d)^2}{n_2}} + reg\right)$$

where σ_1 and σ_2 represent the roughness of each point in sub-clouds of diameter *d* and size n_1 and n_2, and *reg* is the cloud-to-cloud co-registration error, for which *ET* is substituted. The error is assumed to be isotropic and spatially uniform across the dataset (Lague and others, 2013).

Distance calculations were masked to exclude points where the change was lower than the Level of Detection (LoD) threshold and were clipped to individual ice cliff faces. Ice cliff retreat rates were divided by respective survey intervals to derive daily retreat rates. Since cliffs often exhibited large changes in geometry between surveys, some cliff normals at time one intersected debris cover at time two. The total retreat of the cliff face was therefore reported, in addition to cliff-to-cliff retreat (i.e. where cliff normals at time one intersected a cliff at time two).

6.4.5 Other data

Volumetric loss due to ice cliff retreat was estimated from DEM differencing using point clouds gridded at 0.5 m. Cliff retreat rates were also calculated using these volumetric changes for comparison with M3C2 retreat rates, by dividing the volume loss over the respective time period by the cliff area. The zone of ice cliff retreat was defined as the area connected by cliff outlines at respective time periods. Where a cliff partially or completely degraded and hence was not represented by an outline at time two, the zone of cliff retreat was estimated using M3C2 distance measurements (representing spatially variable ice cliff retreat) from the cliff at time one. These distance measurements were used to define a variable-width buffer in ArcGIS to delineate the maximum extent of ice cliff retreat.

The drainage of the supraglacial pond adjacent to Cliff E provided an opportunity to reconstruct the bathymetry and maximum pond depth using the historic water level from May 2016, with the assumption that subaqueous basal melt and debris inputs to the basin were minimal. Additionally, air temperature at 1 m above the surface was recorded at 20 minute intervals on Khumbu Glacier using a Solinst Barologger Edge, which was sited behind Cliff G. Measurements were recorded from October 2015 to October 2016; however, the station collapsed in August 2016 due to the retreat of Cliff G. The logger was found in an air pocket buried by debris, hence data shown after this collapse revealed a subdued diurnal temperature cycle.

6.5 Results

6.5.1 Summary ice cliff characteristics

Ice cliffs: ranged from 4 to 23 m in height; were all within a 43 m elevation range; had mean slopes of 50 to 73°; and were of variable aspect, with both northerly- and southerly-facing cliffs represented (Fig. 6.4, Table 6.2). Of the four cliffs with a supraglacial pond present in November 2015, only Cliff B-SF had a pond remaining in October 2016. Overall, four study cliffs persisted throughout the study period and the other five were buried under debris between May 2016 and October 2016 (Fig. 6.4c).

Table 6.2. Ice cliff characteristics in November 2015

Cliff ID	Elevation (m)	Surface area (m^2)	Maximum height (m)	Mean slope (°)	Mean aspect (°)
A[1,2]	4959	85	5	56	5
B[2]	4939	1,278	17	54	37
B–SF[1,2,3]	4933	1,313	23	73	235
C	4941	34	4	58	266
D	4933	56	4	57	15
D– SF	4935	37	5	63	210
E[1,2]	4926	782	15	65	161
F*	4916	757	13	58	132
G[1,2]	4923	357	10	50	1

[1,2,3] indicate the presence of a supraglacial pond during (1) November 2015, (2) May 2016, and (3) October 2016 surveys. *A supraglacial pond was

present at Cliff F prior to field surveys based on Pleiades imagery (Figure.6.1)

The mean slope, maximum cliff height, cliff area, and mean cliff aspect were evaluated across our study period (Fig. 6.4). Southerly-facing cliffs generally featured higher mean slopes, and the greatest changes in cliff slope were observed on southerly-facing cliffs B-SF and E (Fig. 6.4a). Maximum cliff height reduced for all cliffs over the study period, although this change was generally small for those cliffs that persisted through the study. Cliff E, which lost ~5 m in height over summer (Fig. 6.4b), was an exception. Notably, persistent cliffs had a starting height greater than 10 m; however, we note that Cliff F decayed, despite a starting height greater than 10 m. With the exception of Cliff B-SF which increased in area, all other cliffs declined in area over the study; however, the rate of this area loss varied from cliff to cliff. Of the four cliffs persisting over the study, two were southerly-facing and two were northerly-facing and all had a supraglacial pond present for part of the study period (Table 6.2). However, pond dynamics between the observation dates were unknown. The largest changes in cliff aspect were for cliffs C and D-SF, which became increasingly northerly and westerly orientated by 25° and 23° respectively (Fig. 6.4d).

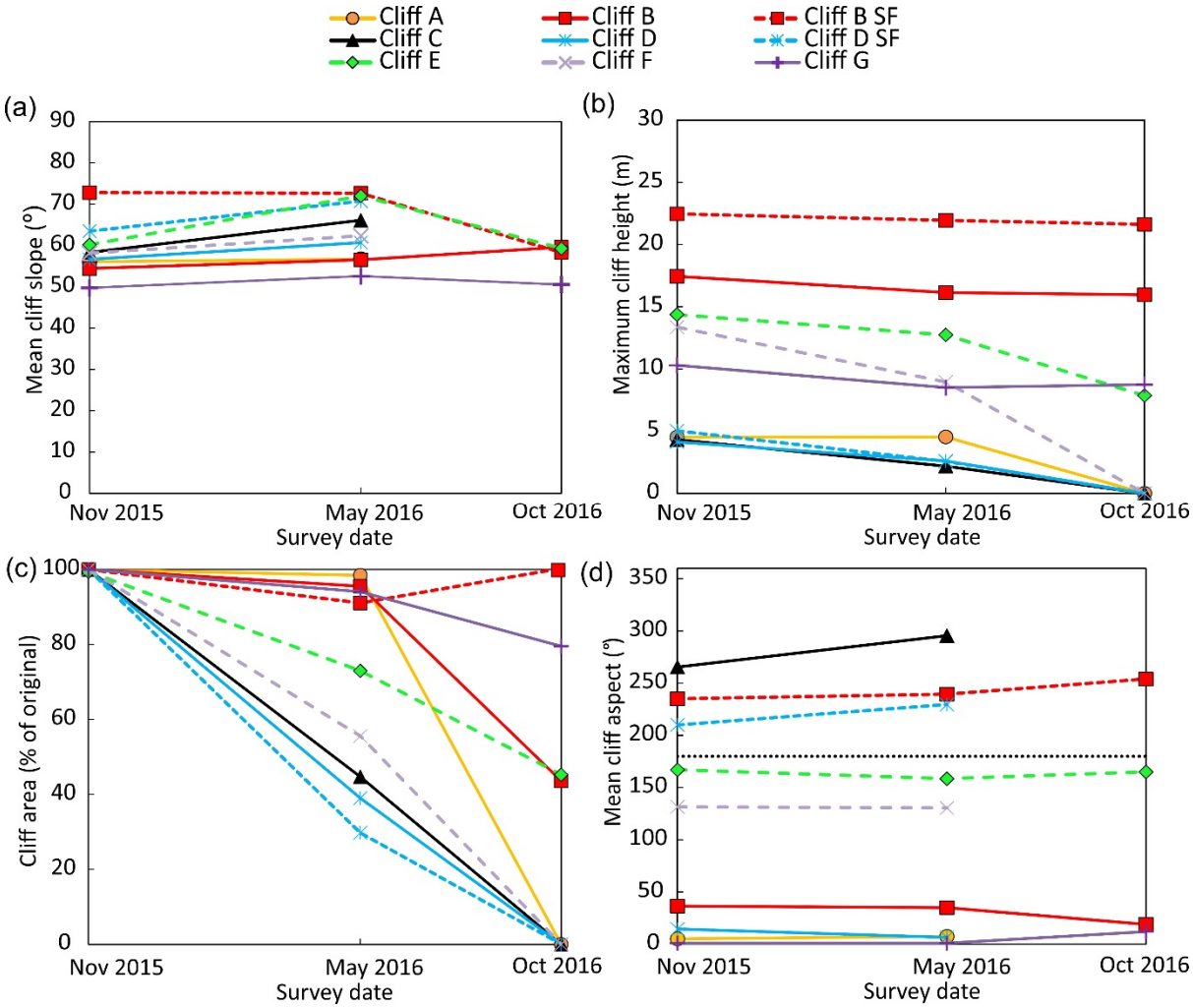

Figure. 6.4. The evolution of ice cliff mean slope (a), maximum height (b), area (c), and aspect (d) over the study period. Absolute cliff area change is shown in Supplementary Fig. 6.3.

6.5.2 Ice cliff retreat

With the exception of Cliff D-SF, cliff retreat rates were higher over summer than the preceding winter, which corresponds with consistently higher air temperatures during summer (Fig. 6.5, Table 6.3). Mean winter temperatures were generally below 0°C, whereas summer temperatures were generally above 0°C, although several discrete periods of positive air temperature also occurred in winter. Similarly, volumetric losses due to cliff retreat were generally higher during summer, although they were small where cliffs degraded (e.g. D-SF, Table 6.3). Notably, the M3C2- and DEM-based retreat rates were comparable for most cliffs.

The highest mean retreat rate occurred at Cliff B and B-SF during summer, although this was a combination of subaerial retreat and a large-scale cliff collapse involving a section of the cliff ~30 m in length. Excluding this cliff face, the highest mean retreat rates observed and the largest seasonal differences in retreat rates were from ice cliffs

with an adjacent supraglacial pond including cliffs A (1.75 cm d^{-1}), E (4.26 cm d^{-1}) and G (2.62 cm d^{-1}) (Fig. 6.5b). The retreat rates for weekly surveys were generally higher than seasonal retreat rates, with the exception of Cliff E (Fig. 6.5). Retreat rates for cliffs that degraded over the study period (A, C, D, D-SF, and F) included a transition to sub-debris melt during the summer, and hence were expected to have lower retreat rates and volume losses compared to persistent cliffs. Similarly, where cliffs partially degraded between survey intervals, the cliff-to-cliff retreat was generally greater than the total retreat rates, which included areas of cliff-to-debris transition (Table 6.3). Here, retreat rates attributed only to persistent areas of cliff ranged from 0.36−1.68 cm d^{-1} (winter), and 3.84−5.85 cm d^{-1} (summer).

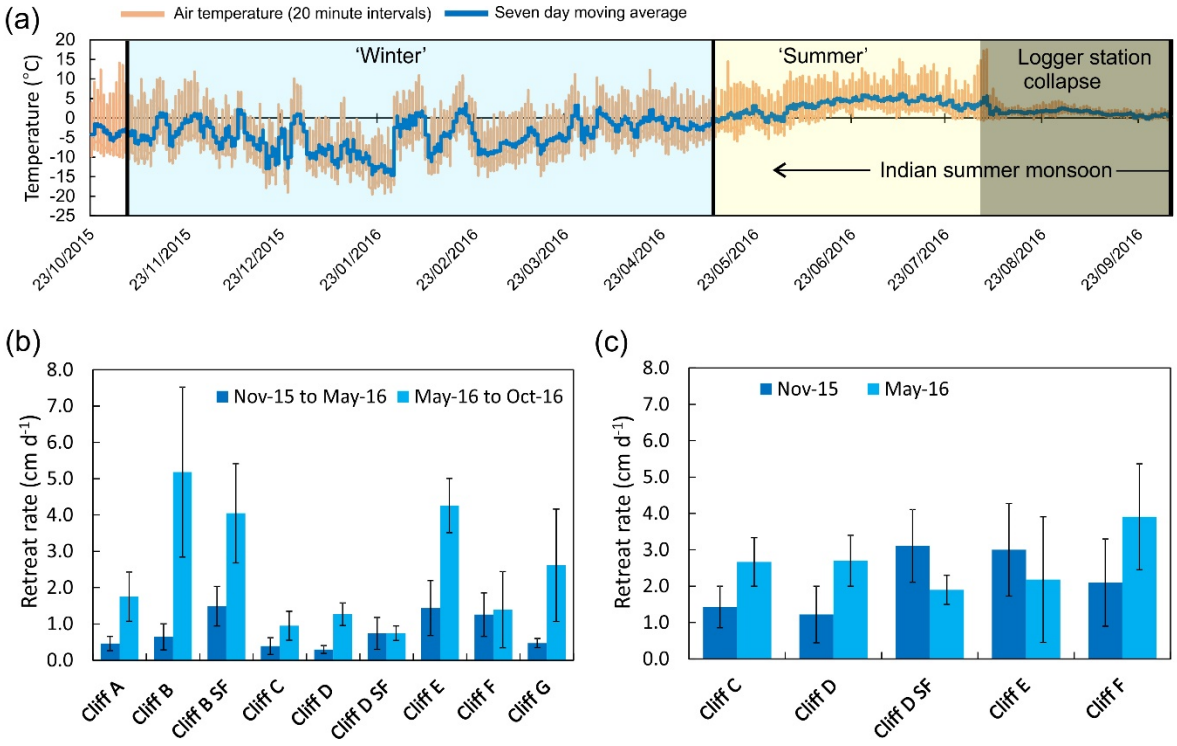

Figure. 6.5. (a) Air temperature at 1 m above the surface recorded at 20 minute intervals with a seven day moving average. Survey intervals are indicated by vertical black lines. The logger mounting collapsed due to ice cliff retreat in August 2016 (shaded area represents data when the logger was partially buried by debris). Mean ice cliff retreat rates for the seasonal (b), and weekly surveys (c). Error bars show one standard deviation.

Table 6.3. Mean ice cliff retreat rates and volume loss for winter and summer

Cliff ID	Nov 2015 to May 2016				May 2016 to Oct 2016			
	M3C2 retreat (cm d^{-1})	M3C2 retreat (cliff only)[1] (cm d^{-1})	DEM-based volume loss (m^3)	DEM-based retreat (cm d^{-1})	M3C2 retreat (cm d^{-1})	M3C2 retreat (cliff only)[1] (cm d^{-1})	DEM-based volume loss (m^3)	DEM-based retreat (cm d^{-1})
A	0.46	0.46	68	0.30	1.75	-	420	1.20
B	0.65	0.70	797	0.66	5.18	5.85	12426*	5.53
B–SF	1.49	1.55	3286	3.05	4.05	3.84		
C	0.39	0.58	22	0.36	0.95	-	38	0.97
D	0.30	0.36	28	0.34	1.27	-	63	1.18
D–SF	0.74	0.92	69	0.80	0.74	-	5	0.33
E	1.44	1.68	1779	2.58	4.26	4.70	2950	4.55
F	1.26	1.57	1238	1.32	1.39	-	643	1.93
G	0.47	0.49	315	0.63	2.62	4.10	1786	2.44

1. M3C2 retreat rates (cliff only) represent cliff-to-cliff retreat i.e. excluding areas where ice cliff normals at time one intersected with debris cover at time two (see Supplementary Table 6.1).

* Volume loss could not be separated at B and B-SF due to a calving event.

Across individual cliff faces, the observed retreat was related to the presence of supraglacial ponds, englacial conduits (expressed as an opening within or below ice cliff faces), cliff aspect, cliff slope, and the formation of runnels (Fig. 6.6). Mean winter ice cliff retreat showed a clear relationship with aspect and peaked at a south easterly aspect of 155º, although this was not the case during summer (Fig. 6.6h). Maximum retreat rates (10.65 cm d^{-1}) were observed at cliffs B and B-SF (Fig. 6.6b) where a notable calving event occurred in the summer. This was followed by northerly-facing Cliff G in association with a supraglacial pond, with maximum retreat rates of 6.18 cm d^{-1} in the zone of thermal undercutting (Fig. 6.6g). The surface of this pond was frozen between the November 2015 and May 2016 surveys and the pond had drained by October 2016.

Runnels were locations of locally differential retreat on the north-facing cliffs B and G during winter (Fig. 6.6b, g) and these cliffs also had the lowest mean initial slopes of 54° and 50° respectively (Table 6.2). During winter, the relative increase in retreat at Cliff G at locations of runnels was ~0.12−0.24 cm d^{-1} (Fig. 6.6g). However, the

presence of runnels was localised and, when considering the whole cliff, the rate of runnel retreat (~0.47−0.58 cm d^{-1}) was otherwise comparable to the mean retreat rate during winter (0.47 cm d^{-1}). Evidence of a vertical retreat gradient was apparent on several cliffs during winter (e.g. Fig. 6.6c, d, f), and was similar during summer, other than where thermal undercutting was apparent (e.g. Cliff G). Cliff B-SF featured the most apparent aspect-related control on retreat during winter with westerly facing ice melting at the slowest rate (~0.84 cm d^{-1}) compared to southerly faces (~2.62 cm d^{-1}, Fig. 6.6b). Cliff A featured an englacial conduit large enough to enable crouched access into a void behind the cliff face, which was the area of greatest retreat for this cliff (~4 cm d^{-1} during summer) as the void likely became exposed and degraded (Fig. 6.6a).

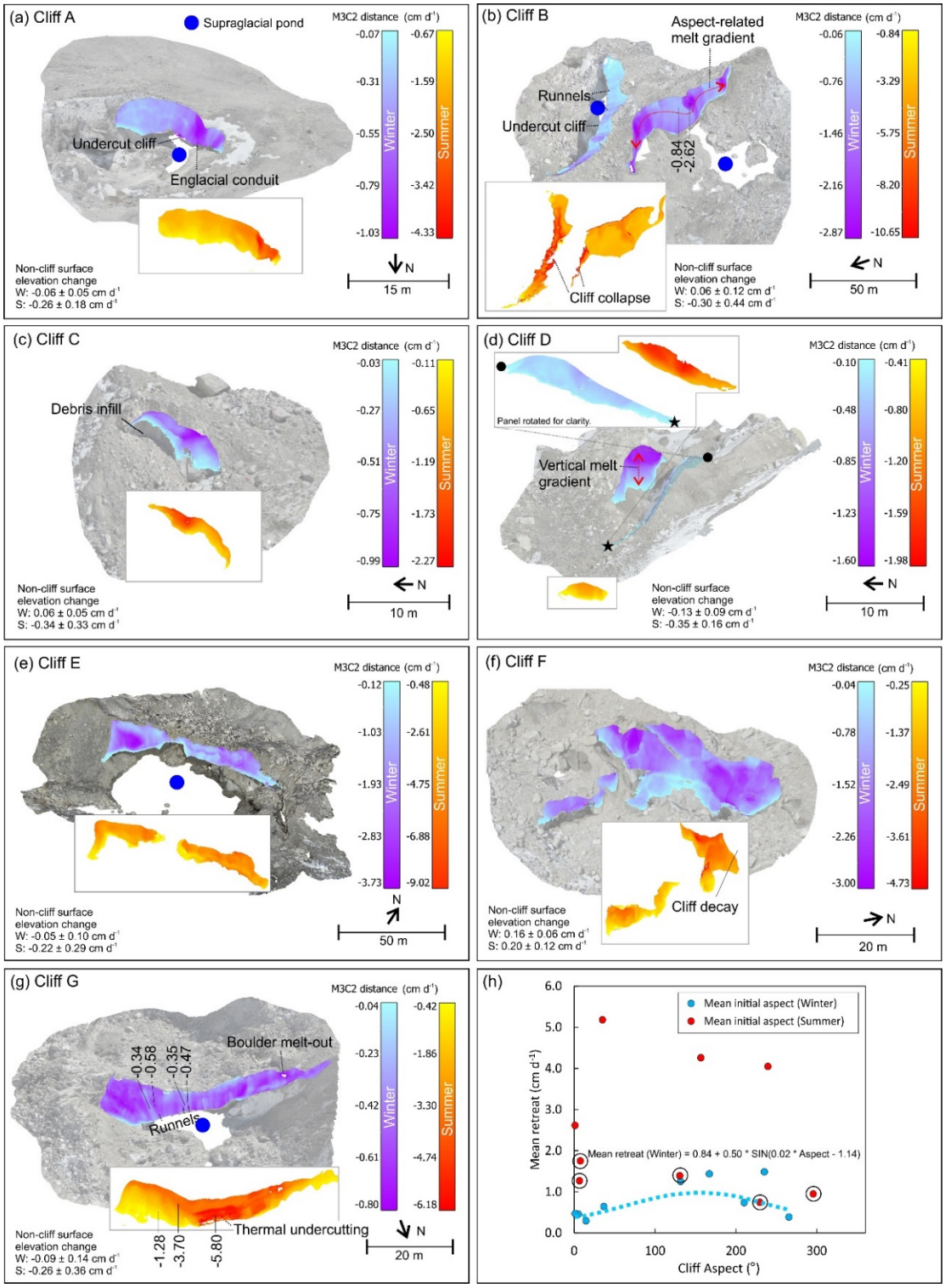

Figure. 6.6. Ice cliff retreat rates shown for winter (November 2015 to May 2016) and summer (May 2016 to October 2016). Note the different scale ranges. Distance measurements are clipped to the study cliffs and indicative values are shown for key features. The mean and standard deviation of non-cliff surface elevation changes are reported for winter (w) and summer (s). Ice cliff retreat rate and initial aspect for winter and summer differencing periods are shown in (h), with a sinusoidal regression line (winter). Circled points indicate ice cliffs that disappeared during summer.

6.5.3 Ice cliff evolutionary traits

2D profiles through selected ice cliffs revealed different characteristics of retreat, including ice cliff burial under debris, ice cliff collapse, and undercutting by adjacent supraglacial ponds (Fig. 6.7). Cliff A maintained a similar slope during its retreat over winter, although during summer the slope angle decreased to ~35°, which led to burial under debris (Fig. 6.7a). There was a small supraglacial pond shallower than 1 m adjacent to Cliff A in the November 2015 and May 2016 surveys, and an associated undercut notch. The pond drained prior to the October 2016 survey, and the steep cliff back-slope led to a relaxation of the cliff slope and hence degradation of Cliff A by October 2016.

The profile through Cliff B revealed greater retreat on the southerly face through winter, compared to the northerly face (Fig. 6.7b). A section of Cliff B collapsed prior to the final survey in October 2016, suggesting that the undercut notch caused the cliff to collapse in a northerly direction. The supraglacial pond in contact with Cliff B-SF expanded throughout the study and was in contact with the southerly face (although not at the 2D profile shown), which exposed a new ice cliff face and caused an increase in cliff area (Fig. 6.4c). A supraglacial pond was present at the northerly-facing Cliff B in May 2016; however, the water level was well below historic water cut notches.

The two opposing faces of Cliff D and D-SF both became buried over the study (Fig. 6.7c). The southerly-facing cliff retreated faster than the northerly face during winter; however, the steep back-slope and small area of this southerly face limited the retreat during summer. Debris infill was apparent in the May 2016 profile, caused by the retreat of the southerly face, which had an inwardly sloping cliff top.

Cliff E featured a supraglacial pond over 9.95 m deep, which drained over the summer. There was evidence of deepening towards the cliff faces at profiles 1 and 2 and thermal undercutting of both cliff faces (Fig. 6.8c, d). The pond at Cliff G also drained over the summer and was also associated with an undercut notch. Cliff G had a gentle back-slope and maintained a similar slope (50−54°) during retreat (Fig. 6.7d). The gentle back-slope of Cliff G allowed continued retreat, in contrast to cliffs A and D where a steep back-slope lead to cliff degradation.

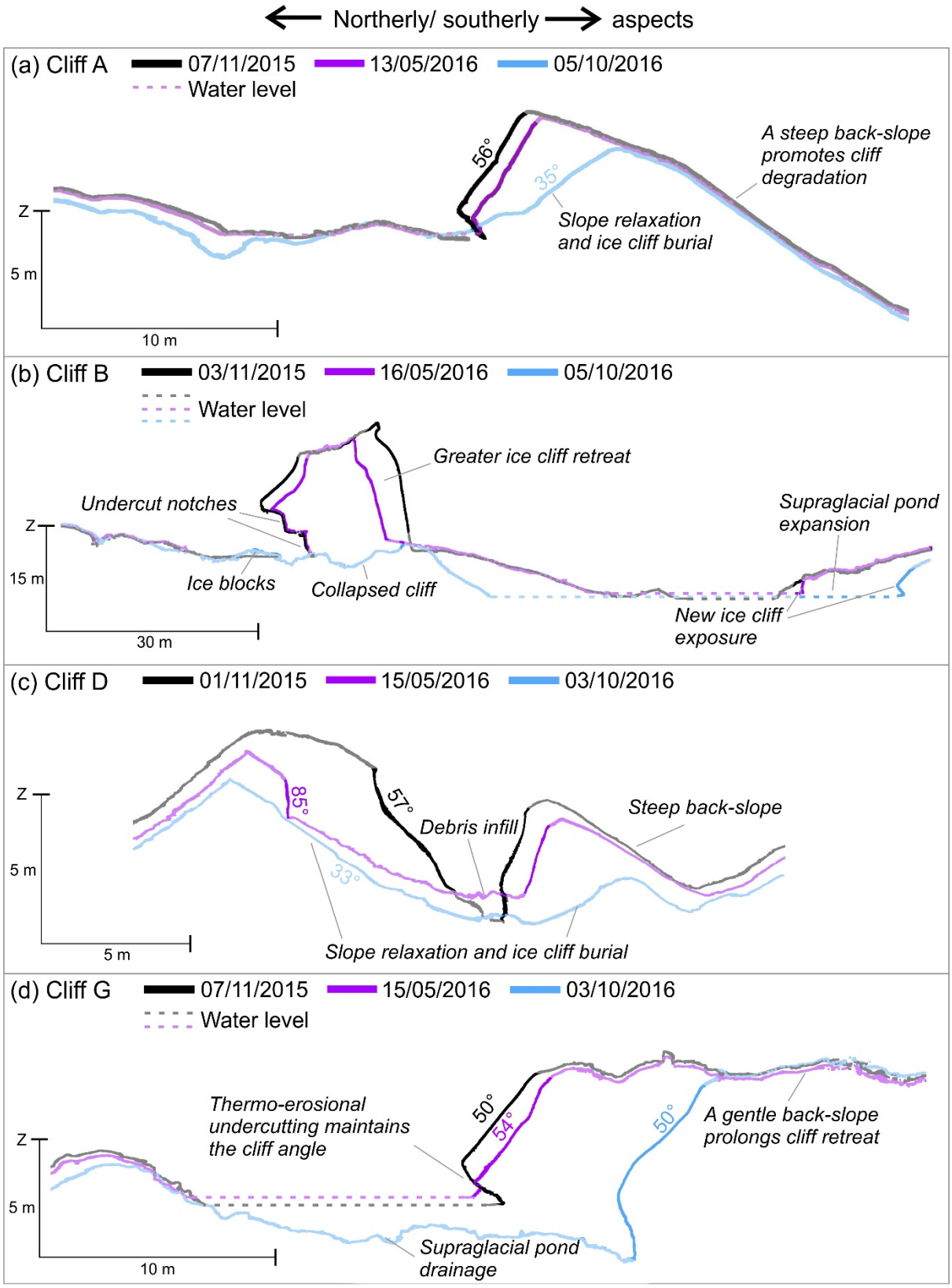

Figure. 6.7. 2D ice cliff profiles for selected cliffs revealing topographic change over the study period. Ice cliff faces are shown as lines without a transparency, whereas debris-covered areas and water levels are shown with transparency.

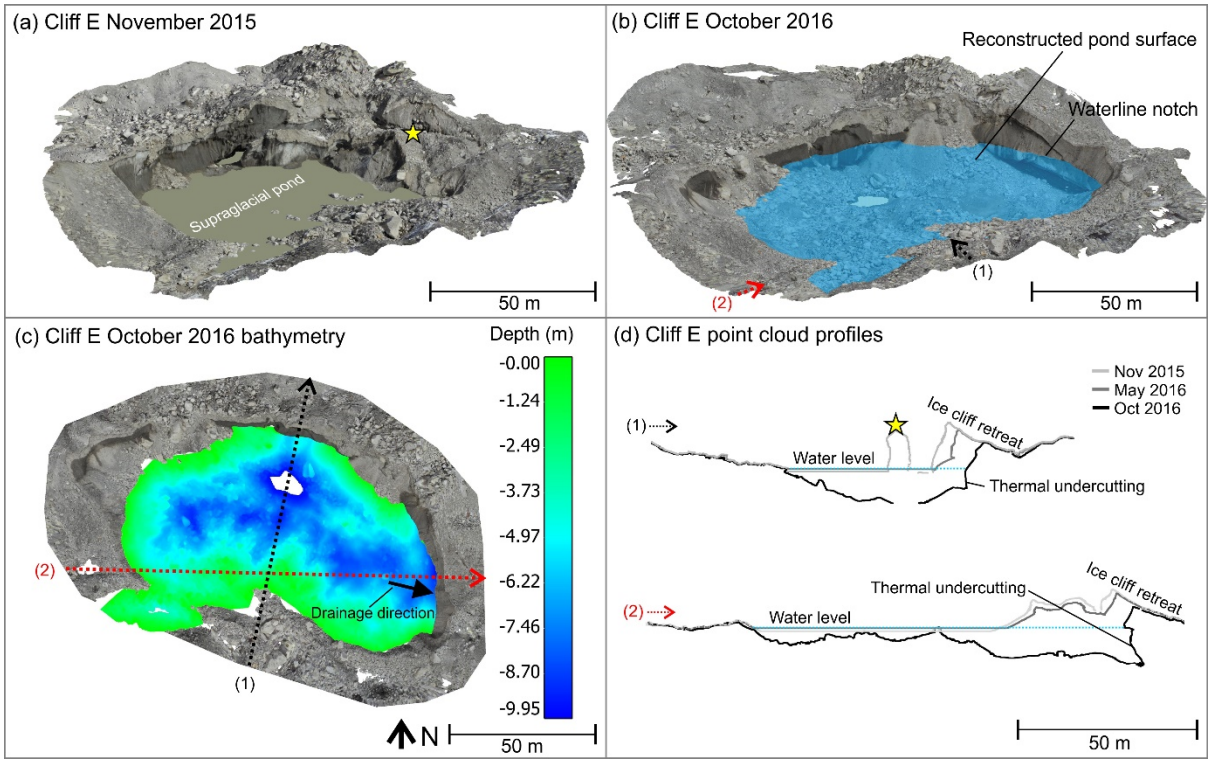

Figure. 6.8. The drainage of a supraglacial pond at Cliff E (a). The drained supraglacial pond provided an opportunity to reconstruct the historic bathymetry (b and c). The data gap at the deepest part of the pond (intersecting with Profile 1) was caused by the remnant presence of water, which had not drained, estimated to be <1 m in depth. Point cloud profiles revealed subaerial ice cliff retreat and thermo-erosional undercutting (d). The yellow star denotes an area of the cliff that was present in November 2015 (a), but had degraded by May 2016 (d).

6.6 Discussion

6.6.1 Multi-temporal ice cliff surveys

In this study we have presented the first application of 3D point cloud differencing to multi-temporal topographic surveys of ice cliffs, revealing evolutionary traits for a variety of ice cliffs present on the lower ablation area of Khumbu Glacier. This method has specific advantages for quantifying the importance of ice cliff retreat and the cliff−pond interaction when compared to previous approaches. First, the retreat attributed to ice cliffs is calculated along the normal direction of the cliff face, thereby minimising the conflation of topographic change from debris cover, ice cliffs and supraglacial ponds, that exists in vertical DEM differencing (e.g. Thompson and others, 2016). However, where a cliff decays between two survey dates, retreat calculations include topographic change related to processes in addition to cliff retreat such as sub-debris melt, hence short survey intervals are preferable. M3C2 allows quantification of the variability of retreat across a cliff face, for example in relation to slope and aspect (Buri and others, 2016a), the presence of runnels (Watson and

others, 2017), and supraglacial ponds (Miles and others, 2016a). Second, the mechanism controlling topographic change can be evaluated in three dimensions, revealing the role of ice cliff back-slope in ice cliff persistence, and thermo-erosional undercutting by supraglacial ponds.

6.6.2 Ice cliff retreat

Observations of ice cliff retreat have previously been obtained from point ablation stake measurements or using static markers on the back-slopes of ice cliffs (e.g. Inoue and Yoshida, 1980; Sakai and others, 1998; Purdie and Fitzharris, 1999; Sakai and others, 2002; Benn and others, 2001; Han and others, 2010; Reid and Brock, 2014; Steiner and others, 2015). Use of ablation stakes restricts assessment of the spatial variation in retreat across an ice cliff face, since stake placements are likely to be aligned vertically down the cliff face and biased towards areas of comparatively safer access. In comparison, Brun and others (2016) used multi-temporal fine-resolution topographic surveys to estimate the volumetric mass loss and mean retreat rates from five ice cliffs on the debris-covered Lirung Glacier. Their study cliffs were generally larger (maximum face size of 6441 m^2 compared to 1313 m^2 in this study), and at ~800 m lower elevation.

6.6.2.1 Ice cliff retreat through time

Four of nine ice cliffs, which all had a maximum height >10 m (Fig. 6.4b) and featured an adjacent supraglacial pond (Table 6.2), persisted over one year in this study. In contrast, all study cliffs of Brun and others (2016) persisted over one year and were all ≥9 m high. Mean retreat rates obtained in this study ranged from 0.30 to 1.49 cm d^{-1} (winter), and 0.74 to 5.18 cm d^{-1} (summer) and were comparable to those of Brun and others (2016), 0.70 to 1.20 cm d^{-1} (winter) and 2.2 to 4.5 cm d^{-1} (summer), despite the higher elevation and smaller size of our study cliffs. In our study, ice cliff retreat rates were generally higher during summer and for southerly-facing ice cliffs, and summer featured the largest variability in retreat rates amongst cliffs (Fig. 6.5b, c). Lower retreat rates during winter correspond with cooler air temperatures (Fig. 6.5a). Higher retreat rates during the November 2015 weekly surveys compared to respective seasonal surveys, reflected warmer temperatures before winter. Similarly, the May 2016 surveys generally had higher retreat rates than the May 2016 to October 2016 surveys (Fig. 6.5b, c). For cliffs C, D and F, this likely reflects cliff degradation before October 2016 and hence a transition from cliff retreat to sub-debris melt for part of the survey interval. The unknown date of cliff degradation is a limitation to assessing mass loss relating only to ice cliff retreat. However, the retreat rates for cliffs that partially degraded between surveys can be quantified by considering the total cliff retreat, which includes areas where the cliff degraded, and the cliff-to-cliff retreat,

where cliff normals at time one intersect a cliff at time two (Table 6.3, Supplementary Table 6.1). The former is representative of the total cliff evolution, which includes areas of ice cliff degrading and becoming buried by debris, whereas the latter is representative of the retreat rates for persisting areas of cliff.

Cliff B suffered a partial collapse of a ~30 m segment during summer, causing high mass loss due to the effect of this calving event (Fig. 6.5b, Table 6.3). Similarly high retreat rates May 2016 to October 2016 were observed at cliffs E and G, which both featured supraglacial ponds becoming active (i.e. thawed) during summer. The high variation in retreat rates over summer suggests that more frequent monitoring would be beneficial to assess cliff dynamics such as burial under debris and the interaction with seasonally expanding supraglacial ponds.

6.6.2.2 Cliff face variation in retreat

Visualising the spatial distribution of retreat across individual cliff faces revealed vertical and lateral gradients, and increased retreat attributed to supraglacial ponds during summer (Fig. 6.6). The influence of cliff aspect is apparent on Cliff B-SF, where a southerly face retreated 1.78 cm d^{-1} faster than an adjacent westerly face (Fig. 6.6b). Both the north-facing cliffs B and G displayed evidence of locally enhanced retreat attributed to the presence of vertical runnels observed during the winter surveys (Fig. 6.6b, g). Runnels were also observed by Watson and others (2017) on other ice cliffs on Khumbu Glacier. The low solar radiation receipt on northerly-facing cliffs during winter may mean that meltwater generated at the less shaded cliff top from sub-debris melt and from melt on the cliff face is able to incise runnels faster than the background rate of cliff retreat. In contrast, during summer the higher magnitude of retreat likely masks this influence of micro-scale cliff topography (Fig. 6.6), although the runnels may persist. Runnels also act as preferential pathways for debris slumping from the cliff top and differential retreat may also occur in response to albedo variations across the cliff face. The morphology of the cliff face, including runnel development and self-shading, is therefore likely to locally influence retreat rates as evidenced in this study, but should be explored further with additional 3D surveys in order to assess their importance seasonally, and at a glacier scale.

Cliff tops exhibited the highest retreat rates in several cases (e.g. Fig. 6.6c, d, f), which was also observed in the modelled retreat rates at two ice cliffs by Buri et al. (2016b). Cliff G also displayed a vertical gradient during the summer; however, this was locally reversed in the area undercut by a supraglacial pond (Fig. 6.6g).

6.6.2.3 The influence of aspect

Several studies have observed a prevalence of northerly-facing ice cliffs on debris-covered glaciers in the Northern Hemisphere, suggesting that solar radiation receipt plays a key role in controlling ice cliff development (Sakai and others, 2002; Kraaijenbrink and others, 2016b; Thompson and others, 2016; Watson and others, 2017). Southerly-facing ice cliffs are expected to decay quickly after formation due to high solar radiation receipt, whereas northerly-facing cliffs are more persistent (Sakai and others, 2002). Slope relaxation was apparent on southerly-facing cliffs B-SF and E, which decreased by 14 and 13° respectively; however, both of these cliffs persisted throughout the study period.

We observed highest ice cliff retreat rates on ice cliffs with a southeasterly aspect (155º) (Fig. 6.6h), although this trend was only apparent during winter. Also on Khumbu Glacier, Inoue and Yoshida (1980) revealed maximum ice cliff retreat at an aspect of ~190º. Cliff aspect likely has a stronger influence over cliff retreat in the winter due to the low solar angle and cliff self-shading (e.g. Steiner and others, 2015). Additionally, direct solar radiation receipt is reduced during the summer monsoon due to the prevalence of cloud cover (Supplementary Fig. 6.4). Therefore at this time, diffuse radiation, air temperature, and local ice cliff characteristics such as the presence of a supraglacial pond were likely stronger controls on ice cliff retreat than the cliff aspect. Shading from surrounding mountains would also affect the relationship between ice cliff melt rates and aspect, however, this should be similar for cliffs on the lower terminus of Khumbu Glacier, which are in a similar setting. Mountain ridges are present on both sides of Khumbu Glacier, although the greatest shading is from the southeast where the mountain ridge extends further south.

6.6.3 Local controls on ice cliff evolution

The back-slope of individual ice cliffs influences their longevity, since there is a finite volume of ice for the cliff to retreat into unless accompanied by simultaneous downwasting of a supraglacial pond. In our study, slope relaxation and cliff degradation (Fig. 6.4a, 6.7a and c) were observed on both northerly- and southerly-facing ice cliffs. This contrasts with the observations of Sakai and others (2002) where slope relaxation was a trait of southerly-facing ice cliffs, highlighting the importance of local topography and cliff characteristics, which determine the longevity of individual ice cliffs over an ablation season.

Several studies have observed strong spatial coincidence of ice cliffs and supraglacial ponds (Thompson and others, 2016; Watson and others, 2017) and notable subaqueous melt rates (Sakai and others, 2009; Miles and others, 2016a). The potential importance of ponds for enhancing ice cliff retreat on Himalayan debris-

covered glaciers is analogous to the ‘wandering lakes’ on Antarctic ice-cored moraines (e.g. Pickard, 1983). Thompson and others (2016) observed that 75% of ice cliffs were associated with a supraglacial pond on the Ngozumpa Glacier, and an average of 49% was observed by Watson and others (2017) across 14 glaciers in the Everest region of Nepal; however, these associations are likely to be seasonally variable. Our study revealed greater retreat for ice cliffs associated with a supraglacial pond, and mean retreat rates of pond-contact ice were estimated to be double that of subaerial retreat at Cliff G. However, the pond at Cliff G drained prior to the final survey such that the role of the pond could not be fully isolated from subaerial retreat. All persisting ice cliffs featured a supraglacial pond during their lifespan. We suggest that undercut notches allowed the cliff angle to be maintained during retreat, which promoted cliff persistence (e.g. Fig 6.7d, 6.8d). Therefore our observations, in addition to strong association of cliffs and ponds (e.g. Watson and others, 2017), suggest that supraglacial ponds are likely to play a key role in ice cliff retreat and persistence at a glacier scale. However, quantifying subaqueous retreat using point cloud differencing is hindered by submerged topography, and manual field measurements (e.g. Rohl, 2006) are restricted by falling debris. Additionally, we cannot comment on the spatial variation in the importance of ice cliff retreat, which likely decreases with distance up-glacier due to thinning debris cover (Thompson and others, 2016; Watson and others, 2017).

6.6.4 Implications for mass loss at a glacier scale

The ice cliff retreat rates observed in this study support previously observed associations between glacier surface lowering and the presence of ice cliffs and supraglacial ponds (Immerzeel and others, 2014; Pellicciotti and others, 2015; Thompson and others, 2016; Watson and others, 2017). Observed mean ice cliff retreat rates ranged from 0.30 (winter) to 5.18 cm d^{-1} (summer), which is much greater than sub-debris melt of 0.15 cm d^{-1} (Aug-1978) observed in a similar region of Khumbu Glacier by Inoue and Yoshida (1980). However, we note that these rates are not directly comparable since our observations represent surface-normal retreat, whereas sub-debris melt represents vertical lowering. The rate of surface lowering related to debris cover ranged from 0.03−0.31 cm d^{-1} on the nearby Ngozumpa Glacier based on the DEM differencing of Thompson and others (2016). However, surface lowering observed from DEM differencing is a function of sub-debris melt and emergence velocity. The latter was not quantified by Thompson et al. (2016), or in this study, but was shown to be +0.37 m w.e a^{-1} (water equivalent) on the debris-covered Changri Nup Glacier (Vincent and others, 2016).

The volumetric loss at ice cliffs is variable and highlights the requirement to up-scale our methodology to the glacier scale in order to capture the full size distribution of ice cliffs present (Table 6.3). Additionally, knowledge of fine spatio-temporal dynamics of supraglacial ponds is still limited, but reveals potentially large seasonal expansion and contraction of ponds (e.g. Miles and others, 2016b; Watson and others, 2016). This restricts efforts to model the ice cliff−pond interaction (Buri and others, 2016a), or to quantify subaqueous retreat with multi-temporal point clouds. Nonetheless, our results suggest that undercut notches can promote ice cliff persistence by maintaining the slope angle during retreat. However, this requires further investigation at a glacier scale and over longer time periods, with particular attention to the role of undercutting for promoting calving events. A SfM-MVS methodology using time-lapse imagery is one such approach that could provide high temporal resolution.

6.6.5 Future work

M3C2 offers new opportunities to quantify 3D topographic change on debris-covered glaciers and this could be used to explore debris redistribution and the formation of ice cliffs, which are currently limiting factors in modelling efforts (Buri and others, 2016a). Similarly, using point cloud data and M3C2 can address several problems related to fine spatio-temporal resolution DEM differencing, including the conflation of several processes contributing to the topographic change signal such as ice cliff retreat, sub-debris melt, and supraglacial pond basal melt. Debris thickness estimated along the top edge of the cliff could be accounted for when slumping into supraglacial ponds, which may otherwise be counted as mass loss in DEM differencing. Comparisons of coincident measurements of 3D and 2D topographic change would therefore be highly beneficial to fully quantify their limitations. Additionally, the topographic change could be explored further with a greater dataset of ice cliff observations, to quantify specific relationships between cliff retreat and variables such as local slope, aspect, and pond presence. However, our dataset demonstrates that ice cliff evolution is highly heterogeneous and that, when considering the dataset as a whole, the relationship between cliff retreat and slope, aspect, and pond presence would be highly complex. Moving forward, conceptualising ice cliff evolution requires both local observations as presented in this study, and glacier scale multi-temporal ice cliff datasets (e.g. Watson and others, 2017).

The M3C2 method is not without its own limitations since it is difficult to calculate volumetric mass loss due to the variable alignment of surface normals; however, such methods are likely to become available or can be developed independently for similar applications (e.g. Brun and others, 2016). Non-uniform glacier surface displacement also presents issues when co-registering multi-temporal point clouds; however, this is

arguably easier to achieve than using a DEM due to the availability of true-colour point data. However, DEMs and corresponding orthophotos can also be used for this correction (e.g. Kraaijenbrink and others, 2016a). Non-uniform glacier surface displacement is an important consideration if investigating lower magnitude processes such as sub-debris melt, which also requires quantification of glacier emergence velocity (Vincent and others, 2016). Emergence velocity is expected to be low on slow-moving low gradient debris-covered glacier tongues (Nuimura and others, 2011); however, positive surface elevation change was observed in this study (e.g. Fig. 6f), which was confirmed by independent dGPS boulder surveys (used in Supplementary Fig. 1). Additionally, point cloud precision estimates based on rigorous photogrammetric processing rather than surface roughness allow improved topographic change detection (James and others, 2017).

6.7 Conclusion

We have presented the first multi-temporal 3D analysis of ice cliff evolution using 3D point cloud differencing, which was necessary to quantify the spatial heterogeneity of retreat across individual cliff faces and their interaction with supraglacial ponds. Our results revealed the importance of a gentle cliff back-slope to allow continued retreat, and the role of supraglacial ponds in thermo-erosional undercutting, which maintains the cliff angle and delays burial under debris. Mean ice cliff retreat rates observed in this study ranged from 0.30–1.49 cm d^{-1} (winter), and 0.74–5.18 cm d^{-1} (summer). Additionally, the four ice cliffs persisting over our one year study period were all influenced by supraglacial ponds, and pond-contact ice was associated with a two-fold increase in retreat at Cliff G. Our findings add further evidence to the role of ice cliffs as ‘hot-spots’ of mass loss on heavily debris-covered glaciers and contribute to a previously sparse dataset of ice cliff observations, revealing local controls on cliff retreat which can be used to validate emerging models of ice cliff evolution (Brun and others, 2016; Buri and others, 2016a).

We observed an aspect-related control on ice cliff retreat during winter; however, local ice cliff characteristics masked any cliff-scale aspect related control on retreat during summer. We observed examples of northerly- and southerly-facing cliffs persisting, but also examples of cliff burial under debris. The controlling factors for ice cliff persistence appeared to be cliffs with a maximum height >10 m and with supraglacial pond influence. Nonetheless, the prevalence of northerly-facing cliffs on debris-covered glaciers in the northern hemisphere (Sakai and others, 2002; Brun and others, 2016; Watson and others, 2017) suggests that over longer timescales (e.g.

decadal) the persistence of northerly-facing cliffs is greater in response to self-shading and supraglacial pond association.

M3C2 point cloud differencing was shown to be an effective tool to quantify the spatio-temporal magnitude of retreat across ice cliff faces, and to offer a new opportunity to validate models of ice cliff evolution. It is also more practical than point-based ablation stake measurements. M3C2 could be applied to glacier scale point clouds to enable surface elevation change to be partitioned into surface-normal (ice cliff retreat) and vertical (sub-debris and subaqueous melt) components, and should be compared to the prevailing practice of DEM differencing. These 3D point cloud data provide a much more realistic representation of surface area compared to a planimetric DEM, and minimise the conflation of different topographic change signals that are common to DEM differencing.

ACKNOWLEDGEMENTS

C.S.W acknowledges support from the School of Geography at the University of Leeds, the Mount Everest Foundation, the British Society for Geomorphology, the Royal Geographical Society (with IBG), the Petzl Foundation, and water@leeds. The Natural Environment Research Council Geophysical Equipment Facility is thanked for loaning Global Navigation Satellite Systems receivers and technical assistance under loan numbers 1050, 1058, and 1065. Dhananjay Regmi and Himalayan Research Expeditions are thanked for fieldwork support including research permit acquisition, and Mahesh Magar is thanked for invaluable support during data collection. Patrick Wagnon is thanked for providing access to AWS data. This AWS has been funded by the French Service d'Observation GLACIOCLIM, the French National Research Agency (ANR) through ANR-13-SENV-0005-04/05-PRESHINE, and has been supported by a grant from Labex OSUG@2020 (Investissements d'avenir – ANR10 LABX56). CloudCompare (version 2.8, 2016) is GPL software retrieved from http://www.cloudcompare.org/. Pleiades images were supplied by Airbus Defence and Space through a Category-1 agreement with the European Space Agency (ID Nr. 32600). We thank two anonymous reviewers for thorough and constructive reviews.

6.8 References

Barnhart, T. and Crosby, B. 2013. Comparing two methods of surface change detection on an evolving thermokarst using high-temporal-frequency terrestrial laser scanning, selawik river, Alaska. Remote Sensing. **5**(6), pp.2813-2837.

Benn, D.I. Bolch, T. Hands, K. Gulley, J. Luckman, A. Nicholson, L.I. Quincey, D. Thompson, S. Toumi, R. and Wiseman, S. 2012. Response of debris-covered glaciers

in the Mount Everest region to recent warming, and implications for outburst flood hazards. Earth-Science Reviews. **114**(1–2), pp.156-174.

Benn, D.I. Wiseman, S. and Hands, K.A. 2001. Growth and drainage of supraglacial lakes on debris-mantled Ngozumpa Glacier, Khumbu Himal, Nepal. Journal of Glaciology. **47**(159), pp.626-638.

Bolch, T. Buchroithner, M.F. Peters, J. Baessler, M. and Bajracharya, S. 2008. Identification of glacier motion and potentially dangerous glacial lakes in the Mt. Everest region/Nepal using spaceborne imagery. Nat. Hazards Earth Syst. Sci. **8**(6), pp.1329-1340.

Bolch, T. Pieczonka, T. and Benn, D.I. 2011. Multi-decadal mass loss of glaciers in the Everest area (Nepal Himalaya) derived from stereo imagery. The Cryosphere. **5**(2), pp.349-358.

Bollasina, M. Bertolani, L. and Tartari, G. 2002. Meteorological observations in the Khumbu Valley, Nepal Himalayas. Bulletin of Glaciological Research. 19, pp.1-11.

Bonasoni, P. Laj, P. Angelini, F. Arduini, J. Bonafè, U. Calzolari, F. Cristofanelli, P. Decesari, S. Facchini, M.C. Fuzzi, S. Gobbi, G.P. Maione, M. Marinoni, A. Petzold, A. Roccato, F. Roger, J.C. Sellegri, K. Sprenger, M. Venzac, H. Verza, G.P. Villani, P. and Vuillermoz, E. 2008. The ABC-Pyramid Atmospheric Research Observatory in Himalaya for aerosol, ozone and halocarbon measurements. Science of The Total Environment. **391**(2–3), pp.252-261.

Brun, F. Buri, P. Miles, E.S. Wagnon, P. Steiner, J.F. Berthier, E. Ragettli, S. Kraaijenbrink, P. Immerzeel, W.W. and Pellicciotti, F. 2016. Quantifying volume loss from ice cliffs on debris-covered glaciers using high-resolution terrestrial and aerial photogrammetry. Journal of Glaciology. **62**(234), pp.684-695.

Buri, P. Miles, E.S. Steiner, J.F. Immerzeel, W.W. Wagnon, P. and Pellicciotti, F. 2016a. A physically-based 3D-model of ice cliff evolution over debris-covered glaciers. Journal of Geophysical Research: Earth Surface. **121**(12), pp.2471-2493.

Buri, P. Pellicciotti, F. Steiner, J.F. Miles, E.S. and Immerzeel, W.W. 2016b. A grid-based model of backwasting of supraglacial ice cliffs on debris-covered glaciers. Annals of Glaciology **57**(71), pp.199-211.

Carrivick, J.L. and Tweed, F.S. 2013. Proglacial lakes: character, behaviour and geological importance. Quaternary Science Reviews. **78**, pp.34-52.

Carrivick, J.L. and Tweed, F.S. 2016. A global assessment of the societal impacts of glacier outburst floods. Global and Planetary Change. **144**, pp.1-16.

Fujita, K. and Nuimura, T. 2011. Spatially heterogeneous wastage of Himalayan glaciers. Proceedings of the National Academy of Sciences of the United States of America. **108**(34), pp.14011-14014.

Gómez-Gutiérrez, Á. de Sanjosé-Blasco, J. Lozano-Parra, J. Berenguer-Sempere, F. and de Matías-Bejarano, J. 2015. Does HDR pre-processing improve the accuracy of 3D models obtained by means of two conventional SfM-MVS software packages? The case of the Corral del Veleta rock glacier. Remote Sensing. **7**(8), p10269.

Hambrey, M.J. Quincey, D.J. Glasser, N.F. Reynolds, J.M. Richardson, S.J. and Clemmens, S. 2008. Sedimentological, geomorphological and dynamic context of debris-mantled glaciers, Mount Everest (Sagarmatha) region, Nepal. Quaternary Science Reviews. **27**(25–26), pp.2361-2389.

Han, H. Wang, J. Wei, J. and Liu, S. 2010. Backwasting rate on debris-covered Koxkar glacier, Tuomuer mountain, China. Journal of Glaciology. **56**(196), pp.287-296.

Haritashya, U.K. Pleasants, M.S. and Copland, L. 2015. Assessment of the evolution in velocity of two debris-covered glaciers in Nepal and New Zealand. Geografiska Annaler: Series A, Physical Geography. **97**(4), pp.737–751.

Immerzeel, W.W. Droogers, P. de Jong, S.M. and Bierkens, M.F.P. 2009. Large-scale monitoring of snow cover and runoff simulation in Himalayan river basins using remote sensing. Remote Sensing of Environment. **113**(1), pp.40-49.

Immerzeel, W.W. Kraaijenbrink, P.D.A. Shea, J.M. Shrestha, A.B. Pellicciotti, F. Bierkens, M.F.P. and de Jong, S.M. 2014. High-resolution monitoring of Himalayan glacier dynamics using unmanned aerial vehicles. Remote Sensing of Environment. **150**, pp.93-103.

Immerzeel, W.W. van Beek, L.P.H. and Bierkens, M.F.P. 2010. Climate change will affect the asian water towers. Science. **328**(5984), pp.1382-1385.

Inoue, J. and Yoshida, M. 1980. Ablation and heat exchange over the Khumbu glacier. Journal of the Japanese Society of Snow and Ice. **39**, pp.7-14.

James, M.R. and Robson, S. 2012. Straightforward reconstruction of 3D surfaces and topography with a camera: Accuracy and geoscience application. Journal of Geophysical Research: Earth Surface. **117**(F03017), doi: 10.1029/2011JF002289.

James, M.R. Robson, S. and Smith, M.W. 2017. 3-D uncertainty-based topographic change detection with structure-from-motion photogrammetry: precision maps for ground control and directly georeferenced surveys. Earth Surface Processes and Landforms. DOI: 10.1002/esp.4125.

Javernick, L. Brasington, J. and Caruso, B. 2014. Modeling the topography of shallow braided rivers using Structure-from-Motion photogrammetry. Geomorphology. **213**, pp.166-182.

Kääb, A. Berthier, E. Nuth, C. Gardelle, J. and Arnaud, Y. 2012. Contrasting patterns of early twenty-first-century glacier mass change in the Himalayas. Nature. **488**(7412), pp.495-498.

Kääb, A. Treichler, D. Nuth, C. and Berthier, E. 2015. Brief Communication: Contending estimates of 2003-2008 glacier mass balance over the Pamir–Karakoram–Himalaya. The Cryosphere. **9**(2), pp.557-564.

Kazhdan, M. and Hoppe, H. 2013. Screened poisson surface reconstruction. ACM Transactions on Graphics (TOG). **32**(3), p29.

King, O. Quincey, D.J. Carrivick, J.L. and Rowan, A.V. 2017. Spatial variability in mass loss of glaciers in the Everest region, central Himalayas, between 2000 and 2015. The Cryosphere. **11**(1), pp.407-426.

Kolecka, N. 2012. Vector algebra for Steep Slope Model analysis. Landform Analysis. **21**, pp.17-25.

Kraaijenbrink, P. Meijer, S.W. Shea, J.M. Pellicciotti, F. de Jong, S.M. and Immerzeel, W.W. 2016a. Seasonal surface velocities of a Himalayan glacier derived by automated correlation of unmanned aerial vehicle imagery. Annals of Glaciology. **57**(71), pp.103-113.

Kraaijenbrink, P.D.A. Shea, J.M. Pellicciotti, F. Jong, S.M.d. and Immerzeel, W.W. 2016b. Object-based analysis of unmanned aerial vehicle imagery to map and characterise surface features on a debris-covered glacier. Remote Sensing of Environment. **186**, pp.581-595.

Lague, D. Brodu, N. and Leroux, J. 2013. Accurate 3D comparison of complex topography with terrestrial laser scanner: Application to the Rangitikei canyon (N-Z). ISPRS Journal of Photogrammetry and Remote Sensing. **82**, pp.10-26.

Lutz, A.F. Immerzeel, W.W. Shrestha, A.B. and Bierkens, M.F.P. 2014. Consistent increase in High Asia's runoff due to increasing glacier melt and precipitation. Nature Clim. Change. **4**(7), pp.587-592.

Miles, E.S. Pellicciotti, F. Willis, I.C. Steiner, J.F. Buri, P. and Arnold, N.S. 2016a. Refined energy-balance modelling of a supraglacial pond, Langtang Khola, Nepal. Annals of Glaciology. **57**(71), pp.29-40.

Miles, E.S. Willis, I.C. Arnold, N.S. Steiner, J. and Pellicciotti, F. 2016b. Spatial, seasonal and interannual variability of supraglacial ponds in the Langtang Valley of Nepal, 1999–2013. Journal of Glaciology. **63**(237), pp.1-18.

Mukherji, A. Molden, D. Nepal, S. Rasul, G. and Wagnon, P. 2015. Himalayan waters at the crossroads: issues and challenges. International Journal of Water Resources Development. **31**(2), pp.151-160.

Naito, N. Nakawo, M. Kadota, T. and Raymond, C.F. 2000. Numerical simulation of recent shrinkage of Khumbu Glacier, Nepal Himalayas. In: Nakawo, M.Raymond, C.F. and Fountain, A., eds. IAHS Publ. 264 (Symposium at Seattle 2000 – Debris-Covered Glaciers), Seattle, Washington, U.S.A. IAHS Publication, pp.245-254.

Nakawo, M. Iwata, S. Watanabe, O. and Yoshida, M. 1986. Processes which distribute supraglacial debris on the Khumbu Glacier, Nepal Himalaya. Annals of Glaciology. 8, pp.129-131.

Nuimura, T. Fujita, K. Fukui, K. Asahi, K. Aryal, R. and Ageta, Y. 2011. Temporal changes in elevation of the debris-covered ablation area of Khumbu Glacier in the Nepal Himalaya since 1978. Arctic Antarctic and Alpine Research. **43**(2), pp.246-255.

Nuimura, T. Fujita, K. Yamaguchi, S. and Sharma, R.R. 2012. Elevation changes of glaciers revealed by multitemporal digital elevation models calibrated by GPS survey in the Khumbu region, Nepal Himalaya, 1992-2008. Journal of Glaciology. **58**(210), pp.648-656.

Pellicciotti, F. Stephan, C. Miles, E. Herreid, S. Immerzeel, W.W. and Bolch, T. 2015. Mass-balance changes of the debris-covered glaciers in the Langtang Himal, Nepal, from 1974 to 1999. Journal of Glaciology. **61**(226), pp.373-386.

Pickard, J. 1983. Surface lowering of ice-cored moraine by wandering lakes. Journal of Glaciology. **29**(102), pp.338-342.

Purdie, J. and Fitzharris, B. 1999. Processes and rates of ice loss at the terminus of Tasman Glacier, New Zealand. Global and Planetary Change. **22**(1–4), pp.79-91.

Quincey, D.J. Luckman, A. and Benn, D. 2009. Quantification of Everest region glacier velocities between 1992 and 2002, using satellite radar interferometry and feature tracking. Journal of Glaciology. **55**(192), pp.596-606.

Ragettli, S. Bolch, T. and Pellicciotti, F. 2016. Heterogeneous glacier thinning patterns over the last 40 years in Langtang Himal, Nepal. The Cryosphere. **10**(5), pp.2075-2097.

Reid, T.D. and Brock, B.W. 2014. Assessing ice-cliff backwasting and its contribution to total ablation of debris-covered Miage glacier, Mont Blanc massif, Italy. Journal of Glaciology. **60**(219), pp.3-13.

Rohl, K. 2006. Thermo-erosional notch development at fresh-water-calving Tasman Glacier, New Zealand. Journal of Glaciology. **52**(177), pp.203-213.

Rounce, D. Watson, C. and McKinney, D. 2017. Identification of hazard and risk for glacial lakes in the Nepal Himalaya using satellite imagery from 2000–2015. Remote Sensing. **9**(7), 654; DOI:10.3390/rs9070654

Rounce, D.R. McKinney, D.C. Lala, J.M. Byers, A.C. and Watson, C.S. 2016. A new remote hazard and risk assessment framework for glacial lakes in the Nepal Himalaya. Hydrol. Earth Syst. Sci. **20**(9), pp.3455-3475.

Rowan, A.V. Egholm, D.L. Quincey, D.J. and Glasser, N.F. 2015. Modelling the feedbacks between mass balance, ice flow and debris transport to predict the response to climate change of debris-covered glaciers in the Himalaya. Earth and Planetary Science Letters. **430**, pp.427-438.

Sakai, A. Nakawo, M. and Fujita, K. 1998. Melt rate of ice cliffs on the Lirung Glacier, Nepal Himalayas. Bulletin of Glaciological Research. **16**, pp.57-66.

Sakai, A. Nakawo, M. and Fujita, K. 2002. Distribution characteristics and energy balance of ice cliffs on debris-covered glaciers, Nepal Himalaya. Arctic Antarctic and Alpine Research. **34**(1), pp.12-19.

Sakai, A. Nishimura, K. Kadota, T. and Takeuchi, N. 2009. Onset of calving at supraglacial lakes on debris-covered glaciers of the Nepal Himalaya. Journal of Glaciology. **55**(193), pp.909-917.

Salerno, F. Guyennon, N. Thakuri, S. Viviano, G. Romano, E. Vuillermoz, E. Cristofanelli, P. Stocchi, P. Agrillo, G. Ma, Y. and Tartari, G. 2015. Weak precipitation, warm winters and springs impact glaciers of south slopes of Mt. Everest (central Himalaya) in the last 2 decades (1994–2013). The Cryosphere. **9**(3), pp.1229-1247.

Shea, J.M. and Immerzeel, W.W. 2016. An assessment of basin-scale glaciological and hydrological sensitivities in the Hindu Kush–Himalaya. Annals of Glaciology. **57**(71), pp.308-318.

Shrestha, A.B. and Aryal, R. 2011. Climate change in Nepal and its impact on Himalayan glaciers. Regional Environmental Change. **11**, pp.65-77.

Smith, M.W. Carrivick, J.L. and Quincey, D.J. 2015. Structure from motion photogrammetry in physical geography. Progress in Physical Geography. **12**(2), pp.1-29.

Smith, M.W. Quincey, D.J. Dixon, T. Bingham, R.G. Carrivick, J.L. Irvine-Fynn, T.D.L. and Rippin, D.M. 2016. Aerodynamic roughness of glacial ice surfaces derived from high-resolution topographic data. Journal of Geophysical Research: Earth Surface. **121**(4), p2015JF003759.

Steiner, J.F. Pellicciotti, F. Buri, P. Miles, E.S. Immerzeel, W.W. and Reid, T.D. 2015. Modelling ice-cliff backwasting on a debris-covered glacier in the Nepalese Himalaya. Journal of Glaciology. **61**(229), pp.889-907.

Stumpf, A. Malet, J.P. Allemand, P. Pierrot-Deseilligny, M. and Skupinski, G. 2015. Ground-based multi-view photogrammetry for the monitoring of landslide deformation and erosion. Geomorphology. **231**, pp.130-145.

Thakuri, S. Salerno, F. Bolch, T. Guyennon, N. and Tartari, G. 2016. Factors controlling the accelerated expansion of Imja Lake, Mount Everest region, Nepal. Annals of Glaciology. **57**(71), pp.245-257.

Thompson, S. Benn, D. Mertes, J. and Luckman, A. 2016. Stagnation and mass loss on a Himalayan debris-covered glacier: processes, patterns and rates. Journal of Glaciology. **62**(233), pp.467-485.

Thompson, S.S. Benn, D.I. Dennis, K. and Luckman, A. 2012. A rapidly growing moraine-dammed glacial lake on Ngozumpa Glacier, Nepal. Geomorphology. **145**, pp.1-11.

Vincent, C. Wagnon, P. Shea, J.M. Immerzeel, W.W. Kraaijenbrink, P. Shrestha, D. Soruco, A. Arnaud, Y. Brun, F. Berthier, E. and Sherpa, S.F. 2016. Reduced melt on debris-covered glaciers: investigations from Changri Nup Glacier, Nepal. The Cryosphere. **10**(4), pp.1845-1858.

Wagnon, P. Vincent, C. Arnaud, Y. Berthier, E. Vuillermoz, E. Gruber, S. Ménégoz, M. Gilbert, A. Dumont, M. Shea, J.M. Stumm, D. and Pokhrel, B.K. 2013. Seasonal and annual mass balances of Mera and Pokalde glaciers (Nepal Himalaya) since 2007. The Cryosphere. **7**(6), pp.1769-1786.

Watson, C.S. Quincey, D.J. Carrivick, J.L. and Smith, M.W. 2016. The dynamics of supraglacial ponds in the Everest region, central Himalaya. Global and Planetary Change. **142**, pp.14-27.

Watson, C.S. Quincey, D.J. Carrivick, J.L. and Smith, M.W. 2017. Ice cliff dynamics in the Everest region of the Central Himalaya. Geomorphology. **278**, pp.238-251.

Westoby, M.J. Brasington, J. Glasser, N.F. Hambrey, M.J. and Reynolds, J.M. 2012. 'Structure-from-Motion' photogrammetry: A low-cost, effective tool for geoscience applications. Geomorphology. **179**, pp.300-314.

Westoby, M.J. Dunning, S.A. Woodward, J. Hein, A.S. Marrero, S.M. Winter, K. and Sugden, D.E. 2016. Interannual surface evolution of an Antarctic blue-ice moraine using multi-temporal DEMs. Earth Surf. Dynam. **4**(2), pp.515-529.

Yang, X. Zhang, Y. Zhang, W. Yan, Y. Wang, Z. Ding, M. and Chu, D. 2006. Climate change in Mt. Qomolangma region since 1971. Journal of Geographical Sciences. **16**(3), pp.326-336.

Chapter 7
Discussion

This thesis presents a holistic analysis of supraglacial pond and ice cliff dynamics using a combination of remote sensing imagery and field-based surveys and monitoring. The importance of supraglacial ponds and ice cliffs for ablation on debris-covered glaciers is only recently becoming apparent, using an unprecedented availability of fine-resolution imagery and field-based techniques to analyse glacier surface morphology. In the short-term, supraglacial ponds act to absorb thermal energy and transmit this to underlying ice, adjacent ice cliffs, and englacially during conduit interception and drainage. In the long-term, an increase in glacier surface water storage is coincident with a low gradient surface profile and the growth of ponds approaching the hydrological base-level, which is leading to the development of glacial lakes in the Everest region. I quantified these trends in addition to the association and interaction between supraglacial ponds and ice cliffs on debris-covered glaciers (Figure 7.1). This project has derived the first baseline fine-resolution dataset of spatio-temporal trends for supraglacial ponds and ice cliffs on debris-covered glaciers in the Everest region, in addition to quantifying local and glacier-scale characteristics and dynamics.

The following sections discuss the key findings from each paper presented in this thesis, which are linked together into a complete body of work. Detailed discussions of individual papers are found within respective chapters. Finally, I reflect on the methodological approach used and suggest directions for future work.

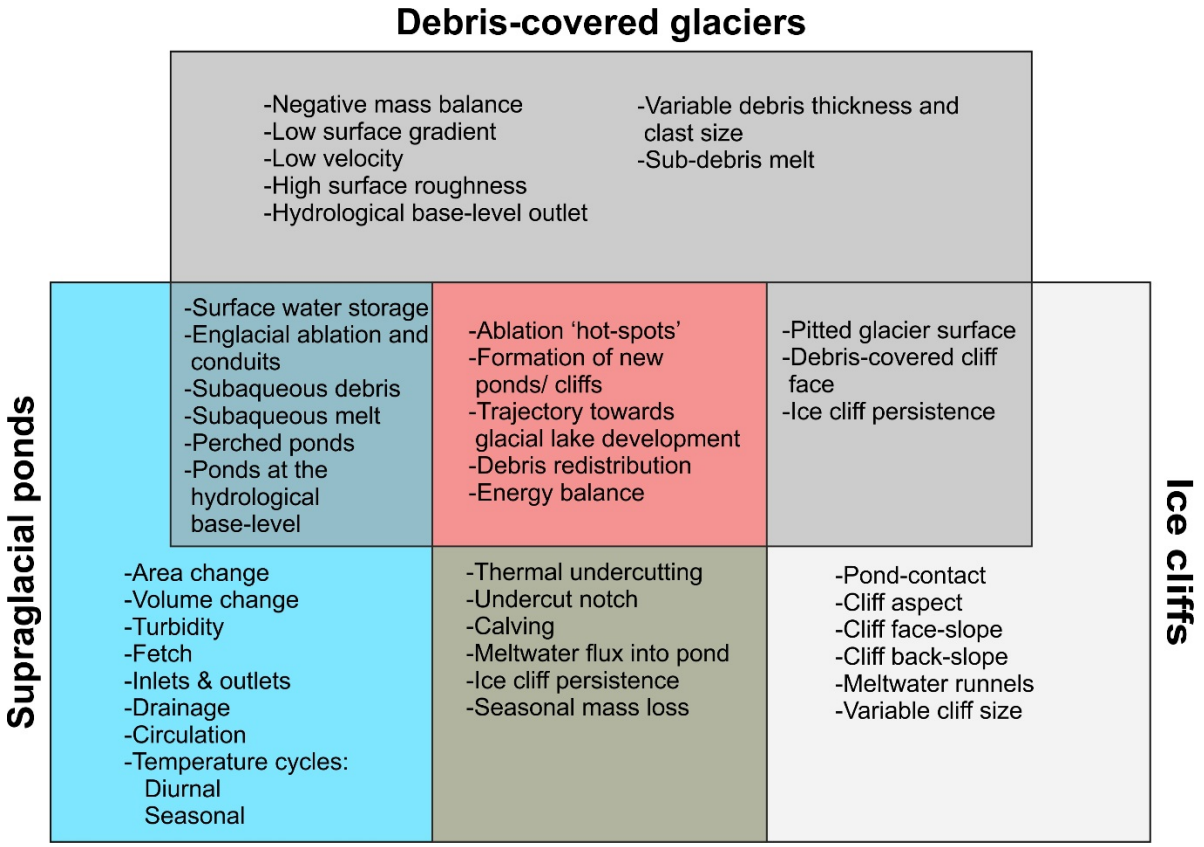

Figure 7.1 Conceptual diagram indicating the key characteristics and interactions between supraglacial ponds, ice cliffs, and debris-covered glaciers.

7.1 Long-term supraglacial pond dynamics

A net increase in glacier surface water storage, on glaciers with negative mass balance, can ultimately lead to the formation of large proglacial lakes behind terminal and lateral moraines (Benn et al., 2012; Linsbauer et al., 2016), raising concerns about GLOFs. The potential instability of moraine-dammed proglacial lakes is uncertain and the process chain potentially resulting in a GLOF event can only be preliminarily assessed remotely (Worni et al., 2012; Worni et al., 2014; Rounce et al., 2016; Rounce et al., 2017). Therefore assessing glacial lake development remains an active research field and with a growing dataset of fine-resolution imagery, studies are increasingly focussing on the development of supraglacial ponds to assess their role towards glacial ablation and as precursors to lake development.

Using medium-resolution imagery (e.g. 15 m ASTER or 30 m Landsat), glacial lakes can be effectively delineated across large regions and studies have revealed an increasing trend in lake area across the central Himalaya (Gardelle et al., 2011; Nie et al., 2013; Zhang et al., 2015; Nie et al., 2017). However, there is high uncertainty when delineating smaller supraglacial ponds that only comprise several pixels, which creates large uncertainty when assessing trends in supraglacial pond development,

especially on an inter- or intra-annual scale (Gardelle et al., 2011; Miles et al., 2016b). Fine-resolution imagery has only previously been used for supraglacial pond delineation for a single point in time, or in conjunction with medium-resolution imagery (e.g. Bolch et al., 2008). For this reason, the first paper presented in this thesis used an archive of fine-resolution satellite imagery of the Everest region to quantify supraglacial pond dynamics over the last ~15 years (Chapter 3, Watson et al., 2016).

A total of 9340 supraglacial ponds were delineated across nine glaciers in the Everest region. The number of ponds for individual glaciers ranged from 25 (Imja, December 2013) to 1,022 (Ngozumpa, June 2010). For comparison, a snapshot supraglacial pond distribution was analysed by Salerno et al. (2012) using 10 m ALOS AVNIR imagery from 2008. Fine-resolution imagery from 2008 was not available for use by Watson et al. (2016); however, from 2009 imagery it was clear that the number of ponds on any given glacier was probably underrepresented by Salerno et al. (2012). For example in November 2009, 185 and 545 ponds were present on Khumbu and Ngozumpa Glaciers respectively, whereas 32 and 108 were present in the analysis of Salerno et al. (2012). It could be argued that omission of smaller ponds is of little interest if they account for a small proportion of pond area at a glacier-scale and hence have little hydrological significance; however, I demonstrated this was not the case by analysing cumulative pond area distributions for each glacier. I revealed that 43−88% of pond area falls below a minimum detection threshold of four Landsat pixels (3600 m^2) (e.g. Gardelle et al., 2011) and 15−40% fall below a 900 m^2 threshold (Figures 3.8, 3.9). Potential omissions are related to the inclusion of mixed pixels along the pond boundary (e.g. Figure 1.2), irregular pond shorelines, and the size-distribution of ponds, which were variable between glaciers.

From the dataset of supraglacial pond development, I observed a net increase in ponded area for six of the nine glaciers (Figure 3.4, Table 3.3). This increasing trend was not as strong as that observed by Gardelle et al. (2011) using Landsat imagery (1990−2009). However, their analysis also included rapidly expanding proglacial lakes. Notably, my observations revealed high inter-annual and intra-annual variability in supraglacial pond area, with prominent increases in pond area and the number of ponds May−June. Whilst inter-annual changes were likely dominated by the number and magnitude of pond drainage events, seasonal expansion reflected meltwater generation during the summer ablation season in addition to precipitation inputs. Other recent studies have observed cyclical pond expansion during the melt season and decline approaching winter (Miles et al., 2016b; Narama et al., 2017), which highlights the englacial ablation potential of short-term pond variability (Sakai et al., 2000; Miles et al., 2016a). Notably, this seasonal expansion in ponded area was most prevalent in the mid- and upper- ablation area (e.g. Figure 3.5a, b), where empty pond basins

became occupied, and existing ponds expanded. In contrast, the supraglacial hydrology is well connected in the lower ablation area, so seasonal meltwater must be effectively conveyed to the outlet and off the glacier surface.

The persistence and expansion of ponds on the easterly margin of Khumbu Glacier (Figures 3.6a, 3.7b) is indicative of a trajectory towards large lake development. Here, I identified 66% increase in pond area (2009−2015), which is likely to occupy an overdeepened basin in the future and expand up-glacier from the terminus (Naito et al., 2000; Linsbauer et al., 2016). Notably, the rapidly expanding Spillway and Rongbuk Lakes (Thompson et al., 2012; Chen et al., 2014) both exhibited drainage events during the study (e.g. Figure 3.6b, c). This suggests that sub-basins of these lakes were perched above the hydrological base-level and likely drained upon interception with an englacial conduit, or that the hydrological base-level of the lake itself had lowered in response to drainage channel reorganisation.

My results demonstrated that supraglacial pond dynamics cannot be fully quantified using medium resolution imagery since many ponds are not adequately detected. However, the use of fine-resolution imagery is still hampered by poor temporal availability, especially during the summer monsoon where cloud-free conditions are intermittent. Nonetheless, the inter-annual and intra-annual variability I identified provides the framework for future supraglacial pond studies, which should be of fine spatio-temporal resolution and ideally be supplemented with field-based monitoring of pond dynamics.

7.2 Short-term supraglacial pond dynamics

Analyses of fine-resolution satellite imagery revealed increased supraglacial water storage during the ablation season (Chapter 3, Watson et al., 2016); however, the temporal resolution of imagery was insufficient to quantify the development of individual ponds over intra-annual timescales. Seasonal pond expansion and drainage has implications for subaqueous melt, englacial ablation, the creation of new surface depressions through englacial conduit collapse, and the thermo-erosional interaction between ponds and ice cliffs. Using field-based monitoring of supraglacial pond temperature and water level in addition to bathymetry surveys, I assessed short-term pond dynamics on Khumbu Glacier (Chapter 4, Watson et al., 2017b).

Empirical area-volume relationships are commonly used to estimate glacial lake volume when assessing the magnitude of potential GLOF events; however, data from which these relationships are derived does not yet extend down to the size distribution of supraglacial ponds commonly found on debris-covered glaciers (Cook and Quincey, 2015; Chapter 3, Watson et al., 2016). I derived a new empirical area-volume

relationship by incorporating my dataset of 24 surveyed supraglacial ponds with the existing dataset of Cook and Quincey et al. (2015). It was clear that the existing relationship extended well down to these smaller ponds (Figure 4.5b). Nonetheless, I used the new dataset to test the ability to predict the volume of individual ponds, revealing a mean difference between the pond volume and predicted pond volume of 22.8%, or 18.5% with an outlier removed. Notably, the mean of the predicted pond volumes (mean pond area of 14609 m^2) underestimated the pond volumes calculated using the bathymetry (mean pond area of 20801 m^2). This relationship between pond area and volume provides an opportunity to estimate glacier-scale water storage in conjunction with multi-temporal satellite imagery (Chapter 3, Watson et al., 2016). However, it is clear that variable pond morphology requires further assessment, and would benefit from surveys of ponds along the full debris-covered ablation area to better represent ponds at different stages of evolution, and of variable persistence. Nonetheless, with an increasing knowledge of pond volume and temperature variability, their ablative role could be quantified at a glacier-scale (Sakai et al., 2000; Miles et al., 2016a), and related to DEM differencing observations of surface lowering.

Most ponds either exist as ephemeral features that drain upon interception with an englacial conduit or expand through ice cliff retreat, such that multiple basins coalesce to form larger glacial lakes (Kirkbride, 1993; Richardson and Reynolds, 2000; Sakai et al., 2009). Therefore, the bathymetry of individual supraglacial ponds and their association with ice cliffs is indicative of likely evolutionary trajectories. Similar to the observations of Horodyskyj (2015) and Thompson et al. (2016) on Ngozumpa Glacier, pond depth was generally highest in the vicinity of ice cliffs (Figure 4.3, 4.4), and the deepest ponds observed had ice cliffs present (Table 4.2). Here, thermal undercutting of the cliff face is likely to maintain the pond-cliff coupling until the pond drains, or the volume of ice for the cliff to retreat into diminishes (Chapter 6, Watson et al., *2017c*). Debris slumping accompanies ice cliff retreat, creating turbid ponds with a low albedo that absorbs solar energy, which is transmitted to adjacent glacier ice or englacially if the pond drains. High rates of glacier surface lowering are therefore correlated with high pond and cliff densities (Ragettli et al., 2016; Thompson et al., 2016; Chapter 5, Watson et al., 2017a). On glaciers with a low surface gradient (e.g. Khumbu Glacier), pond persistence and expansion is indicative of a trajectory towards large glacial lake development (Chapter 3, Watson et al., 2016).

The stored thermal energy of a pond is related to the ablation during its persistence and potential drainage (Sakai et al., 2000; Miles et al., 2016a). In my study, supraglacial ponds with ice cliffs were generally close to zero degrees Celsius during summer and winter, whereas isolated ponds (i.e. without cliffs) were >4°C at the pond bed over winter (Figure 4.8). Of the three ponds that drained over the study, the pond

with the lowest temperature (K20) had the greatest englacial ablation potential (300.9× 10^3 kg) due to its large volume (Chapter 4, Watson et al., 2017b). The prevalence of ponds with ice cliffs at a glacier-scale that are likely to have large volumes, suggests that seasonal expansion and drainage is likely to be an important source of ablation on debris-covered glaciers.

Seasonal expansion and drainage is indicated from remote sensing satellite imagery but assessments are currently limited by temporal- (Chapter 3, Watson et al., 2016) or spatial-resolution (Miles et al., 2016b). Field-based instrumentation of three ponds with pressure transducers on Khumbu Glacier revealed precise water level fluctuations including seasonal summer peaks in June and July before sudden or gradual drainage (Figure 4.6). Water levels were stable, or declining over winter, suggesting englacial hydrology remains at least partially active over winter. However, all major pond drainage events occurred before winter. The complete drainage of pond K19 during the summer proceeded in two stages, with the initial event lasting seven days where the water level dropped by 3 m, and the later event lasting approximately two days. This drainage was coincident with that of a neighbouring pond (K20), suggesting the presence of englacial connectivity that was not apparent from the surface. These conduits enlarge during pond drainage and may collapse to leave a depression or ice cliff exposure (Gulley and Benn, 2007). Potential englacial ablation attributed to englacial conduits was apparent using fine-resolution DEM differencing on Lirung Glacier (e.g. Immerzeel et al., 2014). Therefore, the integration of pond dynamics with surface lowering data could begin to reveal the role of englacial ablation for glacier mass balance.

7.3 Spatio-temporal ice cliff characteristics

Ice cliffs are associated with locally high rates of mass loss compared to surrounding debris-cover (Inoue and Yoshida, 1980; Sakai et al., 1998), especially when undergoing calving retreat due to thermo-erosional undercutting by a supraglacial pond (Benn et al., 2001). However, it is only with recent DEM differencing using fine-resolution imagery that the association between the presence of ice cliffs, ponds, and glacier surface lowering is becoming apparent (Immerzeel et al., 2014; Ragettli et al., 2016; Thompson et al., 2016). I assessed the relationship between ice cliff density and glacier surface lowering, in addition to ice cliff characteristics and spatial distribution, for 14 glaciers in the Everest region (Chapter 5, Watson et al., 2017a).

The spatial distribution of ice cliffs on Khumbu Glacier were first mapped by Sakai et al. (2002) using field observations and the photogrammetrically-derived topographical map of Iwata et al. (1980). They observed a prevalence of northerly-facing ice cliffs,

attributed to greater solar radiation receipt and preferential decay of southerly-facing cliffs. I used the GoogleEarth archive of fine-resolution satellite imagery to map the distribution of ice cliffs and supraglacial ponds across 14 glaciers in the Everest region. With a large sample of glaciers I could assess spatial trends in ice cliff distribution, including the prevalence of northerly-facing cliffs, and the relationship with glacier surface elevation change, modelled debris-thickness, glacier velocity, and the presence of supraglacial ponds (Chapter 5, Watson et al., 2017a).

At a glacier-scale, ice cliff density was highest on Lhotse Shar Glacier and lowest on Lhotse Nup Glacier (Figure 5.4), which had the the most and least negative geodetic mass balance respectively (Table 5.2). Lhotse Shar is retreating under a calving regime as Imja Lake expands. There is little observable glacier flow near the terminus (Thakuri et al., 2016) and high rates of surface lowering in the lower ablation area (Figure 5.8g), in contrast to land-terminating glaciers where maximum surface lowering is in the mid-ablation area. Several of the other study glaciers fall under a regime 2 classification as described by Benn et al. (2012; their Fig. 19), where mass loss in the stagnating ablation zone exceeds ice flux from up-glacier (Figure 5.8). These thinning low gradient (Table 5.2) and low velocity ablation zones (e.g. Figure 5.7) are conducive to the development of supraglacial ponds (Reynolds, 2000; Quincey et al., 2007). Notably, I identified high spatial coincidence between ice cliffs and ponds, and an average of 49% of ice cliffs had an adjacent pond. Other cliffs may have once featured a pond which had subsequently drained, or alternatively the cliffs may have been exposed through debris-redistribution, rather than englacial conduit collapse. The association between ice cliffs and ponds is becoming especially pertinent on glaciers where supraglacial water storage is increasing (e.g. Chapter 3, Watson et al., 2016), since ice cliffs retreat ~2−3 times faster under a calving regime compared to subaerial retreat (Benn et al., 2001).

Highest ice cliff densities were observed in the mid-ablation areas of debris-covered glaciers, within the zone of active flow (Figure 5.7). In contrast, maximum supraglacial water storage was generally observed on the lower ablation area by Watson et al. (2016; Chapter 3), which was most pronounced for the larger glaciers that were studied (Khumbu, Ngozumpa, and Rongbuk) (Figure 3.5). Highest rates of surface lowering were positively correlated with cliff density but were also related to decreasing debris-thickness up-glacier (Figure 5.8). Maximum surface lowering rates were observed in the mid/upper debris-covered ablation areas, other than for Lhotse Shar and Imja glaciers, which were associated with Imja Lake and featured highest rates of surface lowering in the vicinity of the lake. My results suggested that in the lower/mid ablation areas, ice cliffs are likely to be important drivers of mass loss, due to thick debris-cover otherwise insulating the glacier ice beneath. Conversely, in the upper

ablation area, the debris cover is thinner and the contribution of ice cliffs is comparatively lower due to a higher 'background rate' of sub-debris melt (Figure 5.9). The high cliff–pond association I observed at a glacier-scale, in addition to evidence of pond deepening approaching ice cliffs (Chapter 4, Watson et al., 2017b), supports observations correlating high rates of surface lowering with the presence of cliffs and ponds on other glaciers in the Everest region (e.g. Thompson et al., 2016).

Ice cliffs were predominantly northerly facing irrespective of glacier flow direction (Figure 5.6). My observations support the prevailing hypothesis that north-facing cliffs persist through self-shading, a steep slope angle maintained through longwave radiation emission from adjacent debris, or the presence of a supraglacial pond at the cliff base, whereas a higher solar radiation receipt promotes flattening and burial by debris of southerly facing cliffs (Sakai et al., 2002; Steiner et al., 2015; Chapter 6, Watson et al., *2017c*). However, controls on ice cliff persistence cannot be fully explored without fine-resolution topographic datasets, which reveal the potential volume into which cliffs can retreat (Brun et al., 2016). Additionally, it was clear from field-based observations of ice cliff morphology on Khumbu Glacier that cliff faces were highly heterogeneous and exhibited vertical and lateral retreat gradients (Figure 5.10) (Chapter 5, Watson et al., 2017a). Cliff-scale variation in retreat rates cannot be quantified using DEM differencing, since isolating mass loss due to sub-debris melt, ice cliff retreat, and supraglacial pond expansion is problematic. Alternatively, 3D point cloud differencing can quantify complex topographic change along the surface normal direction (Lague et al., 2013) and therefore offers an opportunity to assess ice cliff evolution.

7.4 Ice cliff retreat and persistence

The spatio-temporal distribution and characteristics of ice cliffs was assessed using multi-temporal fine-resolution satellite imagery (Chapter 5, Watson et al., 2017a). However, without knowledge of the cliff morphology or retreat rates, the mass loss due to cliff retreat could not be determined. Similarly, developing a process-based understanding of the ice cliff development, and particularly the cliff–pond interaction requires field-based observations of cliff evolution. Efforts to model ice cliff evolution require a process-based understanding, in addition to field observations of ice cliff retreat for validation (Steiner et al., 2015; Brun et al., 2016; Buri et al., 2016a). 3D data generated from UAV photogrammetry were recently used to quantify the retreat of six ice cliffs on the small debris-covered Lirung Glacier (Brun et al., 2016). Whilst this approach provided estimates of volumetric mass loss due to cliff retreat, it could not reveal the spatial variation in this retreat across a cliff face in relation to aspect,

elevation, slope, micro-scale topography, and supraglacial ponds. An alternative 3D point cloud differencing method called M3C2 calculates the distance between two point clouds along the normal direction with a 95% confidence interval (Lague et al., 2013). I applied the M3C2 algorithm to multi-temporal point clouds of ice cliffs surveyed on Khumbu Glacier to present the first analysis of fully 3D ice cliff evolution. This allowed an assessment of the processes driving ice cliff evolution and the rates of ice cliff retreat for cliffs of variable size, aspect, slope, and pond presence (Chapter 6, Watson et al., *2017c*).

A terrestrial survey methodology meant that surveys were limited to cliffs that were accessible by foot for photographic surveys and GCP deployment. My study cliffs were therefore limited to smaller exposures and were located in the lower ablation area of Khumbu Glacier. Nonetheless, I aimed to survey cliffs that were broadly representative of a range of aspects, sizes, and supraglacial pond presence. The mean top-edge length of cliffs surveyed was 57 m, heights ranged from 4−23 m, and four of the nine study cliffs had a supraglacial pond present during the initial survey. For comparison, Watson et al. (2017a; Chapter 5) found 47% of ice cliffs were associated with a pond and cliffs had a mean length of 54 m using satellite-image based analyses on Khumbu Glacier.

Mean ice cliff retreat rates were 0.30−1.49 cm d^{-1} during winter and 0.74−5.18 cm d^{-1} during summer, which were comparable to those observed by Brun et al. (2016) on the debris-covered Lirung Glacier, Nepal. On average, the largest cliffs retreated ~5−9 m over the observation period. Notably, the observed retreat rates were up to an order of magnitude higher than observed sub-debris melt in a similar region of the glacier, which was estimated to be 0.15 cm d^{-1} (Aug-1978) by Inoue and Yoshida (1980). Four out of nine cliffs persisted over the one year study period, whilst the others disappeared under a layer of debris as their faces flattened during retreat. Observed cliff disappearance indicates a potentially high turnover rate for smaller cliffs (<~10 m high) during the summer monsoon when retreat rates are high. Persistent cliffs all featured a supraglacial pond through the study, or had been preconditioned by a pond (e.g. undercut). For cliffs with a pond present during the study, there was evidence that ponds were maintaining a steep cliff angle through undercutting and/or calving. Cliffs showing evidence of a historic pond (e.g. Cliff B-NF, Cliff F, Figures 6.6b,f, 6.7b) were undercut, which probably prolonged their existence. Variable cliff and pond persistence makes parameterising their role in dynamic glacier models problematic, since two similar cliffs could behave differently depending on the volume of ice for the cliff to recede into, and on adjacent pond dynamics. Similarly, although a relationship between mean cliff aspect and retreat rate was apparent over winter, this was not clear during summer (Figure 6.6h). Ideally, multiple datasets of ice cliffs from different

debris-covered glaciers would be combined into a meta-analysis to more robustly identify key trends; however, these datasets are currently sparse.

M3C2 cloud-to-cloud differencing revealed spatio-temporal trends in ice cliff evolution related to cliff aspect and shape, thermo-erosional undercutting of the cliff face by ponds, and runnel formation (Figure 6.6, 6.7). Spatial variation in cliff retreat rates were apparent from observations of cliff morphology (Chapter 5, Watson et al., 2017a). However, it has not hitherto been possible to quantify variation in retreat rates using traditional point ablation stake measurements of cliff retreat since the placement of ablation stakes is limited to areas of comparatively safe access to a cliff face, which is not conducive to capturing spatial variation in retreat rates. My cliff-scale observations were used to conceptualise scenarios of ice cliff evolution, revealing the role of cliff size, shape, aspect, and pond presence (Figure 7.2). However, based on my limited observations of ice cliff evolution I cannot assess glacier-scale variability in evolutionary trends. Therefore, I suggest that future integration between local observations and multi-temporal ice cliff datasets (e.g. Chapter 5, Watson et al., 2017a) would be highly beneficial. Especially since the highly heterogeneous cliff evolution I observed likely precludes simple relationships between their retreat rate and topographical parameters, although these were clearly apparent in some cases (Figure 6.6).

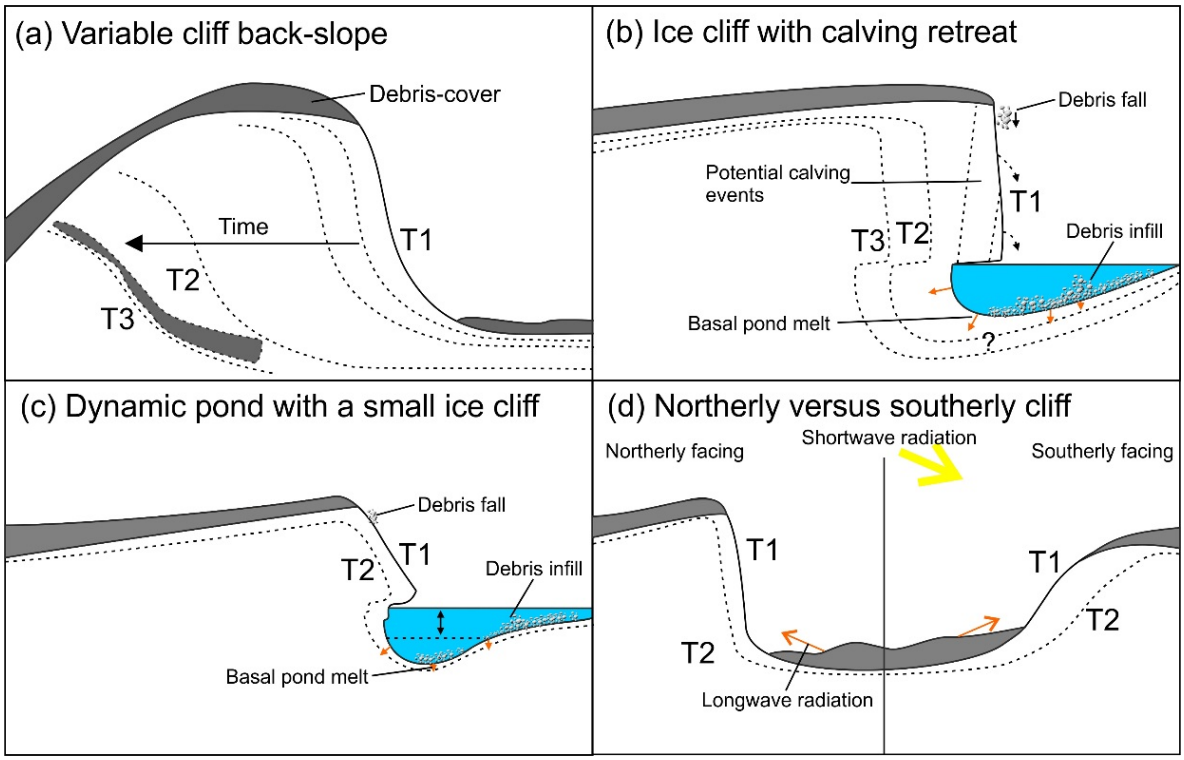

Figure 7.2. Example scenarios of ice cliff retreat on a debris-covered glacier. (a) A cliff with a variable back-slope and debris-thickness. (b) A cliff retreating under a calving regime in association with a supraglacial pond. (c) A small cliff retreating due to

subaqueous and subaerial melt. (d) Contrasting evolution of northerly and southerly facing ice cliffs.

7.5 Methodological considerations and future work

7.5.1 Remote sensing

The remote sensing analysis of supraglacial ponds was driven, but equally limited by, the availability of fine-resolution satellite imagery. The DigitalGlobe Foundation provided access to WorldView, GeoEye, and QuickBird satellite imagery in the Everest region of Nepal, which was supplemented using imagery available in GoogleEarth to increase temporal coverage. Imagery spanned >5 years for all glaciers, and >10 years for five glaciers. Acquisitions from late September to March were considered to be comparable since supraglacial hydrology was expected to be less active during the winter months. Acquisitions during summer months were analysed separately, since this is when seasonal pond expansion and drainage dominates (Chapter 4, Watson et al., 2017b). However, I noted from field observations of slumped ice plates around a pond boundary at least one case of continued englacial pond drainage in November 2015, despite a frozen surface.

The remote sensing analysis of ice cliffs was carried out using fine-resolution imagery in GoogleEarth, where the top edge of ice cliffs and all supraglacial ponds were delineated. The face of ice cliffs was not delineated since they have variable slope angles and some have overhanging sections, such that the area of ice cliff faces can only be reliably quantified using fully 3D data (e.g. a meshed point cloud) (Chapter 6, Watson et al., *2017c*). Nonetheless, the primary aim of Chapter 5 was to assess the spatial distribution and orientation of ice cliffs across the Everest region and this analysis was the first to assess multi-glacier and multi-temporal ice cliff characteristics. However, the temporal separation of satellite images was >5 years and limited to two acquisitions at most, which was insufficient to draw conclusions on temporal trends. Similarly, the short-term turnover of small ice cliffs indicated in Chapter 6 is likely to be missed.

7.5.2 Field-monitoring

Supraglacial ponds of varying characterises were instrumented with temperature sensors designed to characterise the pond thermal regime over one year, in addition to the deployment of three pressure transducers to monitor water level fluctuations. Ponds are of variable size, turbidity, hydrological connectivity, and ice cliff presence, and published data on their instrumentation is sparse. Nine ponds were therefore instrumented with 1−2 temperature sensors to capture inter-pond variability. I

expected ponds with ice cliffs to be well mixed, although assessing pond-scale trends such as temperature variation approaching an ice cliff face would have been a useful addition when assessing the role of ponds for promoting thermo-erosional undercutting.

A sonar-equipped USV was designed to collect georeferenced depth measurements across supraglacial ponds using a single beam sonar. Empirical area-volume scaling using bathymetry exists for large glacial lakes (Cook and Quincey, 2015), but not for the size distribution of supraglacial ponds encountered on debris-covered glaciers. The single beam sonar could not reveal information about the bottom composition of supraglacial ponds, in contrast to when using side-scan sonar or ground penetrating radar (e.g. Horodyskyj, 2015; Mertes et al., 2016), which is important for modelling subaqueous melt rates (Miles et al., 2016a). Nonetheless, 24 supraglacial ponds were surveyed in May 2016 and their bathymetries were used to derive a new empirical area-volume relationship. Repeat bathymetric surveys were not carried out here but could be used in the future to assess subaqueous melt rates and the evolution of ponds in association with ice cliffs.

Nine ice cliffs were surveyed on Khumbu Glacier (November 2015, May 2016 and October 2016) following a SfM-MVS workflow, which enabled 3D point cloud generation. These point clouds were georeferenced with a RMSE of ≤0.03 m owing to high quality differential GPS ground control; however, glacier displacement between field campaigns required these clouds to be co-registered, which increased georeferencing uncertainty to ≤0.33 m. Nonetheless, the observed retreat rates were at least an order of magnitude higher than this uncertainty. I could not instrument ice cliffs to capture energy fluxes (Figure 7.3a), but instead surveyed cliffs in a range of topographic settings, of variable aspects, and with and without supraglacial ponds. Ice cliff retreat rates were thought to be variable across individual faces and related to the formation of micro-scale topography such as runnels (Figure 5.10, 7.3b). Therefore I applied 3D point cloud differencing to ice cliffs for the first time to quantify the spatio-temporal variation in retreat rates (Chapter 6, Watson et al., *2017c*). My cliff surveys represented snap-shots of cliff morphology, hence the processes driving cliff retreat were inferred from topographic changes. A time-lapse camera set-up used as part of a SfM-MVS workflow would offer increased temporal resolution to observe processes driving retreat and supraglacial pond dynamics. However, the practicalities and high costs in applying such a method to multiple ice cliffs precluded time-lapse application in this instance. Snap-shot surveys meant that where a cliff fully or partially degraded over the study period, the date of burial under debris was not known. This degradation meant that the summer retreat rates presented for five cliffs also included a period of sub-debris melt once the cliff had become buried. For cliffs that only partially degraded,

the cliff-to-cliff rates of retreat were quantified separately from cliff-to-debris retreat. Undercut notches were only visible where a supraglacial pond had drained, hence estimating rates of thermo-erosional undercutting was only possible for one ice cliff (Cliff G), although this process was apparent on several cliffs. Nonetheless, due to frequent debris-fall it was not safe to collect manual measurements of undercut notch development, which require being in close proximity to the cliff face (e.g. Rohl, 2006).

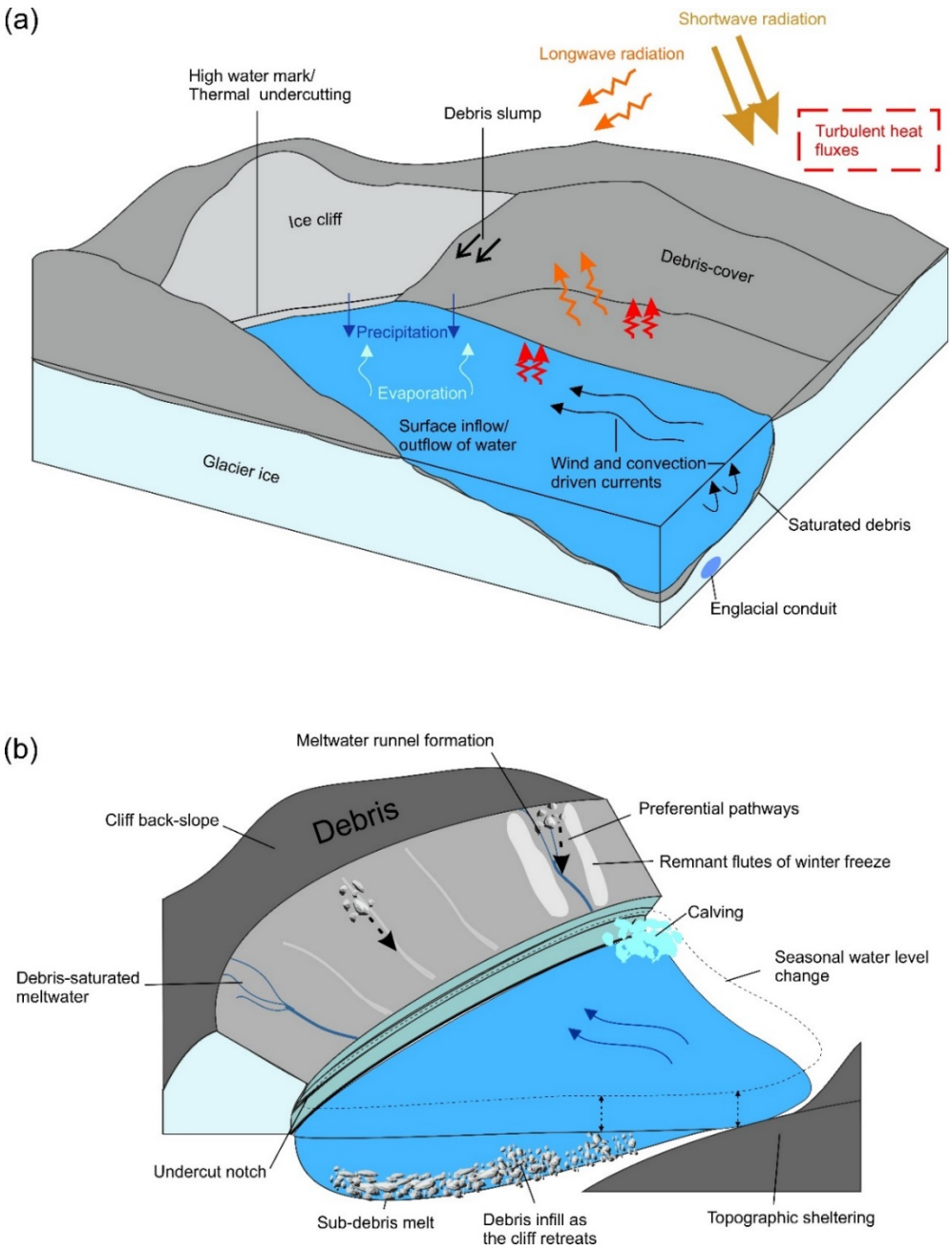

Figure 7.3. (a) Mass and energy fluxes driving supraglacial pond dynamics and interaction with ice cliffs. (b) An illustration of ice cliff morphology.

7.5.3 Future work

Through improving our process-based understanding of the evolution of supraglacial ponds and ice cliffs on Himalayan debris-covered glaciers I can suggest key directions for future work to better understand feedbacks between supraglacial ponds, ice cliffs, and debris-covered glaciers. I used remote sensing datasets to observe glacier-scale supraglacial pond and ice cliff dynamics, and to inform the methodology for local-scale observations. Moving forward, it is clear that by integrating both glacier-scale datasets of supraglacial pond and ice cliff dynamics (Chapters 3 and 5), and local observations (Chapters 4 and 6), the future development of debris-covered glaciers in the region can be better predicted. This is especially pertinent where glaciers display a net increase in water storage and are on a trajectory towards glacial lake development.

An increasing archive and acquisition programme of fine-resolution satellite imagery could enable seasonal pond dynamics to be investigated in greater detail to quantify the magnitude of seasonal pond expansion and drainage at a glacier-scale. For example, Planet Labs now have over 100 satellites in orbit with optical sensors imaging the Earth almost daily at 3 m resolution. However, at the time when ponds are most active during the Indian Summer Monsoon, frequent cloud cover limits usable acquisitions. Synthetic aperture radar (SAR) data, which is able to penetrate clouds, has only been applied to large glacial lakes thus far (Strozzi et al., 2012), but sensors such as TerraSAR-X offer fine-resolution acquisition capabilities. Due to the prevalence of high turbidity water, supraglacial pond bathymetry can only be assessed in the field (Chapter 4, Watson et al., 2017b), and multi-temporal surveys are currently limited to larger lakes (e.g. Spillway Lake on Ngozumpa Glacier) (Thompson et al., 2016). Knowledge of vertical pond development is therefore lacking, but clearly is linked to ice cliff retreat (Chapters 4 and 6). Assessing both vertical and lateral pond expansion is key to understanding the onset of the trajectory towards large glacial lake development as multiple ponds coalesce.

Fine-resolution satellite or UAV imagery enables semi-automatic classification of ice cliffs (e.g. Kraaijenbrink et al., 2016). However, only UAV or terrestrial photogrammetry can fully resolve the variable cliff morphology and this has thus far only been applied to small glaciers. Clearly there is merit in combining multiple datasets of labour-intensive field-based ice cliff observations to help parameterise and up-scale cliff modelling studies. Additionally, knowledge of spatio-temporal ice cliff distribution (Chapter 5, Watson et al., 2017a) combined with cliff-scale retreat rates (Brun et al., 2016; Chapter 6, Watson et al., *2017c*) could be used to investigate the magnitude of melt and turnover time of the debris-covered glacier surface by ice cliffs and supraglacial ponds. Partitioning glacier mass loss into components related to debris-

cover, ice cliffs, and supraglacial ponds is problematic using DEM differencing (e.g. Thompson et al., 2016), and is not possible where DEMs are differenced on a decadal timescale for mass balance estimates (Bolch et al., 2011; King et al., 2017). Therefore understanding the driving factors of observed surface lowering requires up-scaling of short-term cliff and pond dynamics. Ultimately, an improved process-based understanding of the role and feedbacks between debris-covered glacier morphology can inform models forecasting glacier evolution under future climate scenarios (e.g. Rowan et al., 2015; Shea et al., 2015).

Conclusion

In this thesis a remote sensing and field-based assessment of supraglacial ponds and ice cliffs were presented in the context of widespread negative mass balance of debris-covered glaciers in the Everest region. Spatio-temporal trends in the surface morphology of debris-covered glaciers were quantified and used to guide three field campaigns on Khumbu Glacier in the Everest region of Nepal. Through this work, the importance of debris-covered glacier surface morphology has been detailed by revealing local-scale evolution of supraglacial ponds and ice cliffs.

The characteristics of supraglacial ponds and ice cliffs were assessed across the Everest region using fine-resolution satellite imagery. Glacier-scale trends were analysed, such as the trajectory towards large lake development on Khumbu Glacier, and the role of ponds and cliffs were conceptualised in relation to glacier debris-thickness and mass loss. Field-based analyses focussed on the short-term local-scale evolution of supraglacial ponds and ice cliffs, and their potential ablative role due to englacial ablation. Using a holistic approach, it was clear that previous approaches considering long-term water storage trends miss annual and seasonal variability and numerous smaller ponds found on debris-covered glaciers. These omissions are particularly important when considering the role of draining supraglacial ponds towards englacial ablation and the formation of new ice cliffs and ponds. Regarding ice cliffs, the application of 3D point cloud differencing revealed ice cliff retreat was spatially and temporally heterogeneous, and that the presence of a pond and a shallow back-slope appeared key to ice cliff persistence. Evolutionary ice cliff scenarios were identified and conceptualised for several styles of cliff, suggesting that upscaling my local studies using glacier-scale 3D point clouds (e.g. from UAVs) is required to fully assess how glacier ablation is influenced by, and expressed through the surface morphology.

Overall, I have exploited several fine-resolution spatio-temporal datasets to improve our understanding of the interactions between cliffs, ponds, and the debris-covered surface. Additionally, I have demonstrated methods and generated the datasets required to work towards improved projections of debris-covered glacier evolution in the region that can explicitly consider surface features and their feedbacks.

In summary, this thesis has:

1. Quantified a variable trend of supraglacial water storage in the Everest region and revealed high seasonal and annual variability.
2. Revealed that Khumbu Glacier is developing a connected chain of ponds approaching the hydrological base level, which is indicative of a trajectory towards large lake development.

3. Highlighted that medium-resolution imagery is not suitable for assessing the size distribution of supraglacial ponds found on debris-covered glaciers.
4. Quantified examples of seasonal pond expansion and drainage on Khumbu Glacier, with large englacial ablation potentials.
5. Derived the first empirical area-volume relationship for supraglacial ponds.
6. Explored the differences in pond bathymetry relating to ice cliff presence and connectivity of ponds to the glacier hydrological network.
7. Quantified glacier-scale ice cliff distribution, their association with supraglacial ponds, and their relationship with surface lowering obtained from DEM differencing.
8. Revealed spatio-temporally variable ice cliff retreat using 3D point cloud differencing and explored the controlling factors on ice cliff persistence.
9. Detailed future research directions that integrate remote-sensing and field-based methods to move towards the parametrisation of surface dynamics in models of glacier evolution in a changing climate.

References (Chapters 1, 2, and 7)

Armstrong, R.L. 2010. The Glaciers of the Hindu Kush-Himalayan Region. A summary of the science regarding glacier melt, retreat in the Himalayan, Hindu Kush, Karakoram, Pamir, and Tien Shan mountain ranges. [Online]. Available from: http://lib.icimod.org/record/26917.

Bajracharya, B. Shrestha, A.B. and Rajbhandari, L. 2007. Glacial Lake Outburst Floods in the Sagarmatha Region. *Mountain Research and Development.* **27**(4), 336-344.

Bajracharya, S.R. and Mool, P. 2009. Glaciers, glacial lakes and glacial lake outburst floods in the Mount Everest region, Nepal. *Annals of Glaciology.* **50**(53), 81-86.

Barnhart, T. and Crosby, B. 2013. Comparing two methods of surface change detection on an evolving thermokarst using high-temporal-frequency terrestrial laser scanning, selawik river, Alaska. *Remote Sensing.* **5**(6), 2813-2837.

Benn, D.I. Bolch, T. Hands, K. Gulley, J. Luckman, A. Nicholson, L.I. Quincey, D. Thompson, S. Toumi, R. and Wiseman, S. 2012. Response of debris-covered glaciers in the Mount Everest region to recent warming, and implications for outburst flood hazards. *Earth-Science Reviews.* **114**(1–2), 156-174.

Benn, D.I. Wiseman, S. and Hands, K.A. 2001. Growth and drainage of supraglacial lakes on debris-mantled Ngozumpa Glacier, Khumbu Himal, Nepal. *Journal of Glaciology.* **47**(159), 626-638.

Bliss, A. Hock, R. and Radić, V. 2014. Global response of glacier runoff to twenty-first century climate change. *Journal of Geophysical Research: Earth Surface.* **119**(4), 717-730.

Bolch, T. Buchroithner, M.F. Peters, J. Baessler, M. and Bajracharya, S. 2008. Identification of glacier motion and potentially dangerous glacial lakes in the Mt. Everest region/Nepal using spaceborne imagery. *Nat. Hazards Earth Syst. Sci.* **8**(6), 1329-1340.

Bolch, T. Kulkarni, A. Kääb, A. Huggel, C. Paul, F. Cogley, J.G. Frey, H. Kargel, J.S. Fujita, K. Scheel, M. Bajracharya, S. and Stoffel, M. 2012. The State and Fate of Himalayan Glaciers. *Science.* **336**(6079), 310-314.

Bolch, T. Pieczonka, T. and Benn, D.I. 2011. Multi-decadal mass loss of glaciers in the Everest area (Nepal Himalaya) derived from stereo imagery. *The Cryosphere.* **5**(2), 349-358.

Bookhagen, B. and Burbank, D.W. 2006. Topography, relief, and TRMM-derived rainfall variations along the Himalaya. *Geophysical Research Letters.* **33**(8), 1-5.

Brun, F. Buri, P. Miles, E.S. Wagnon, P. Steiner, J.F. Berthier, E. Ragettli, S. Kraaijenbrink, P. Immerzeel, W.W. and Pellicciotti, F. 2016. Quantifying volume loss from ice cliffs on debris-covered glaciers using high-resolution terrestrial and aerial photogrammetry. *Journal of Glaciology.* **62**(234), 684-695.

Buri, P. Miles, E.S. Steiner, J.F. Immerzeel, W.W. Wagnon, P. and Pellicciotti, F. 2016a. A physically-based 3D-model of ice cliff evolution over debris-covered glaciers. *Journal of Geophysical Research: Earth Surface.* 2471-2493.

Buri, P. Pellicciotti, F. Steiner, J.F. Miles, E.S. and Immerzeel, W.W. 2016b. A grid-based model of backwasting of supraglacial ice cliffs on debris-covered glaciers. *Annals of Glaciology* **57**(71), 199-211.

Carrivick, J.L. and Tweed, F.S. 2013. Proglacial lakes: character, behaviour and geological importance. *Quaternary Science Reviews.* **78**, 34-52.

Carrivick, J.L. and Tweed, F.S. 2016. A global assessment of the societal impacts of glacier outburst floods. *Global and Planetary Change.* **144**, 1-16.

Chen, W. Doko, T. Liu, C. Ichinose, T. Fukui, H. Feng, Q. and Gou, P. 2014. Changes in Rongbuk lake and Imja lake in the Everest region of Himalaya. *ISPRS - International Archives of the Photogrammetry, Remote Sensing and Spatial Information Sciences.* 259-266.

Chen, W. Fukui, H. Doko, T. and Gu, X. 2013. Improvement of Glacial Lakes Detection under Shadow Environment Using ASTER Data in Himalayas, Nepal. *Chinese Geographical Science.* **23**(2), 216-226.

Chikita, K. Joshi, S.P. Jha, J. and Hasegawa, H. 2000. Hydrological and thermal regimes in a supraglacial lake: Imja, Khumbu, Nepal Himalaya. *Hydrological Sciences Journal-Journal Des Sciences Hydrologiques.* **45**(4), 507-521.

Chikita, K.A. 2007. Topographic effects on the thermal structure of Himalayan glacial lakes: Observations and numerical simulation of wind. *Journal of Asian Earth Sciences.* **30**(2), 344-352.

Cook, S.J. and Quincey, D.J. 2015. Estimating the volume of Alpine glacial lakes. *Earth Surf. Dynam.* **3**, 559-575.

Emmer, A. and Vilímek, V. 2013. Review Article: Lake and breach hazard assessment for moraine-dammed lakes: an example from the Cordillera Blanca (Peru). *Nat. Hazards Earth Syst. Sci.* **13**(6), 1551-1565.

Fujita, K. Sakai, A. Nuimura, T. Yamaguchi, S. and Sharma, R.R. 2009. Recent changes in Imja Glacial Lake and its damming moraine in the Nepal Himalaya revealed by in situ surveys and multi-temporal ASTER imagery. *Environmental Research Letters.* **4**, 1-7.

Gardelle, J. Arnaud, Y. and Berthier, E. 2011. Contrasted evolution of glacial lakes along the Hindu Kush Himalaya mountain range between 1990 and 2009. *Global and Planetary Change.* **75**(1–2), 47-55.

Gardelle, J. Berthier, E. and Arnaud, Y. 2012. Slight mass gain of Karakoram glaciers in the early twenty-first century. *Nature Geosci.* **5**(5), 322-325.

Gardelle, J. Berthier, E. Arnaud, Y. and Kääb, A. 2013. Region-wide glacier mass balances over the Pamir-Karakoram-Himalaya during 1999-2011. *Cryosphere.* **7**(4), 1263-1286.

Gardner, A.S. Moholdt, G. Cogley, J.G. Wouters, B. Arendt, A.A. Wahr, J. Berthier, E. Hock, R. Pfeffer, W.T. Kaser, G. Ligtenberg, S.R.M. Bolch, T. Sharp, M.J. Hagen, J.O. van den Broeke, M.R. and Paul, F. 2013. A Reconciled Estimate of Glacier Contributions to Sea Level Rise: 2003 to 2009. *Science.* **340**(6134), 852-857.

Gulley, J. and Benn, D.I. 2007. Structural control of englacial drainage systems in Himalayan debris-covered glaciers. *Journal of Glaciology.* **53**(182), 399-412.

Hambrey, M.J. Quincey, D.J. Glasser, N.F. Reynolds, J.M. Richardson, S.J. and Clemmens, S. 2008. Sedimentological, geomorphological and dynamic context of debris-mantled glaciers, Mount Everest (Sagarmatha) region, Nepal. *Quaternary Science Reviews.* **27**(25–26), 2361-2389.

Han, H. Wang, J. Wei, J. and Liu, S. 2010. Backwasting rate on debris-covered Koxkar glacier, Tuomuer mountain, China. *Journal of Glaciology.* **56**(196), 287-296.

Haritashya, U.K. Pleasants, M.S. and Copland, L. 2015. Assessment of the evolution in velocity of two debris-covered glaciers in Nepal and New Zealand. *Geografiska Annaler: Series A, Physical Geography.* **97**(4), 737–751.

Horodyskyj, U. 2015. *Contributing Factors to Ice Mass Loss on Himalayan Debris-covered Glaciers*. PhD thesis, University of Colorado, Boulder.

Huggel, C. Kääb, A. Haeberli, W. Teysseire, P. and Paul, F. 2002. Remote sensing based assessment of hazards from glacier lake outbursts: a case study in the Swiss Alps. *Canadian Geotechnical Journal.* **39**(2), 316-330.

ICIMOD. 2011. Glacial Lakes and Glacial Lake Outburst Floods in Nepal. [Online]. Available from: http://www.icimod.org/dvds/201104_GLOF/reports/final_report.pdf.

Immerzeel, W.W. Kraaijenbrink, P.D.A. Shea, J.M. Shrestha, A.B. Pellicciotti, F. Bierkens, M.F.P. and de Jong, S.M. 2014. High-resolution monitoring of Himalayan glacier dynamics using unmanned aerial vehicles. *Remote Sensing of Environment.* **150**, 93-103.

Immerzeel, W.W. van Beek, L.P.H. and Bierkens, M.F.P. 2010. Climate change will affect the asian water towers. *Science.* **328**(5984), 1382-1385.

Inoue, J. and Yoshida, M. 1980. Ablation and heat exchange over the Khumbu glacier. *Journal of the Japanese Society of Snow and Ice.* **39**, 7-14.

Iwata, S. Aoki, T. Kadiota, T. Seko, K. and Yamaguchi, S. 2000. Morphological evolution of the debris cover on Khumbu Glacier, Nepal, between 1978 and 1995. In: Nakawo, M.Raymond, C.F. and Fountain, A., eds. *IAHS Publ. 264 (Symposium at Seattle 2000 – Debris-Covered Glaciers)*, *Seattle, Washington, U.S.A*. IAHS Publication, 3-12.

Iwata, S., Watanabe, O. and Fushimi, H. 1980. Surface Morphology in the Ablation Area of the Khumbu Glacier. *Seppyo, 41 (Special issue).* **9-17**.

James, M.R. and Robson, S. 2012. Straightforward reconstruction of 3D surfaces and topography with a camera: Accuracy and geoscience application. *Journal of Geophysical Research: Earth Surface.* **117**(F3), 1-17.

Ji, L., Zhang, L, Wylie, B. 2009. Analysis of dynamic thresholds for the normalized difference water index. *Photogram. Eng. Remote Sen.* **75**, 1307–1317.

Juen, M. Mayer, C. Lambrecht, A. Han, H. and Liu, S. 2014. Impact of varying debris cover thickness on ablation: a case study for Koxkar Glacier in the Tien Shan. *The Cryosphere.* **8**(2), 377-386.

Kääb, A. Berthier, E. Nuth, C. Gardelle, J. and Arnaud, Y. 2012. Contrasting patterns of early twenty-first-century glacier mass change in the Himalayas. *Nature.* **488**(7412), 495-498.

Kääb, A. Treichler, D. Nuth, C. and Berthier, E. 2015. Brief Communication: Contending estimates of 2003-2008 glacier mass balance over the Pamir–Karakoram–Himalaya. *The Cryosphere.* **9**(2), 557-564.

Kattelmann, R. 2003. Glacial lake outburst floods in the Nepal Himalaya: A manageable hazard? *Natural Hazards.* **28**(1), 145-154.

King, O. Quincey, D.J. Carrivick, J.L. and Rowan, A.V. 2017. Spatial variability in mass loss of glaciers in the Everest region, central Himalayas, between 2000 and 2015. *The Cryosphere.* **11**(1), 407-426.

Kirkbride, M.P. 1993. The temporal significance of transitions from melting to calving termini at glaciers in the central Southern Alps of New Zealand. *The Holocene.* **3**(3), 232-240.

Kirkbride, M.P. and Warren, C.R. 1997. Calving processes at a grounded ice cliff. *Annals of Glaciology.* **24**, 116-121.

Kolecka, N. 2012. Vector algebra for Steep Slope Model analysis. *Landform Analysis.* **21**, 17-25.

Kraaijenbrink, P.D.A. Shea, J.M. Pellicciotti, F. Jong, S.M.d. and Immerzeel, W.W. 2016. Object-based analysis of unmanned aerial vehicle imagery to map and characterise surface features on a debris-covered glacier. *Remote Sensing of Environment.* **186**, 581-595.

Lague, D. Brodu, N. and Leroux, J. 2013. Accurate 3D comparison of complex topography with terrestrial laser scanner: Application to the Rangitikei canyon (N-Z). *ISPRS Journal of Photogrammetry and Remote Sensing.* **82**, 10-26.

Linsbauer, A. Frey, H. Haeberli, W. Machguth, H. Azam, M.F. and S., A. 2016. Modelling glacier-bed overdeepenings and possible future lakes for the glaciers in the Himalaya–Karakoram. *Annals of Glaciology.* **57**(71).

Liu, Q. Christoph, M. and Shiyin, L. 2015. Distribution and interannual variability of supraglacial lakes on debris-covered glaciers in the Khan Tengri-Tumor Mountains, Central Asia. *Environmental Research Letters.* **10**(1), 1-10.

Luckman, A. Quincey, D. and Bevan, S. 2007. The potential of satellite radar interferometry and feature tracking for monitoring flow rates of Himalayan glaciers. *Remote Sensing of Environment.* **111**(2-3), 172-181.

Lutz, A.F. Immerzeel, W.W. Shrestha, A.B. and Bierkens, M.F.P. 2014. Consistent increase in High Asia's runoff due to increasing glacier melt and precipitation. *Nature Clim. Change.* **4**(7), 587-592.

Mattson, L.E. Gardner, J.S. and Young, G.J. 1993. Ablation of debris covered glaciers: An example from the Rakhiot Glacier, Punjab Himalaya. In: Young, G.J., ed. *Snow and Glacier Hydrology (Proceedings of the Kathmandu Symposium, November 1992)*, *Kathmandu, Nepal*. IAHS Publishing, 289-296.

Meier, M.F. Dyurgerov, M.B. Rick, U.K. O'Neel, S. Pfeffer, W.T. Anderson, R.S. Anderson, S.P. and Glazovsky, A.F. 2007. Glaciers dominate Eustatic sea-level rise in the 21st century. *Science.* **317**(5841), 1064-1067.

Mertes, J.R. Thompson, S.S. Booth, A.D. Gulley, J.D. and Benn, D.I. 2016. A conceptual model of supraglacial lake formation on debris-covered glaciers based on GPR facies analysis. *Earth Surface Processes and Landforms.* **42**(6), 903–914

Miles, E.S. Pellicciotti, F. Willis, I.C. Steiner, J.F. Buri, P. and Arnold, N.S. 2016a. Refined energy-balance modelling of a supraglacial pond, Langtang Khola, Nepal. *Annals of Glaciology.* **57**(71), 29-40.

Miles, E.S. Willis, I.C. Arnold, N.S. Steiner, J. and Pellicciotti, F. 2016b. Spatial, seasonal and interannual variability of supraglacial ponds in the Langtang Valley of Nepal, 1999–2013. *Journal of Glaciology.* **63**(237), 1-18.

Mool, P.K. Bajracharya, S.R. and Joshi, S.P. 2001. Inventory of glaciers, glacial lakes and glacial lake outburst floods. Monitoring and early warning systems in the Hindu Kush-Himalayan Region: Nepal. [Online]. Available from: http://www.preventionweb.net/files/2370_InventoryGlaciers.pdf. 1-254.

Naito, N. Nakawo, M. Kadota, T. and Raymond, C.F. 2000. Numerical simulation of recent shrinkage of Khumbu Glacier, Nepal Himalayas. In: Nakawo, M.Raymond, C.F. and Fountain, A., eds. *IAHS Publ. 264 (Symposium at Seattle 2000 – Debris-Covered Glaciers)*, *Seattle, Washington, U.S.A*. IAHS Publication, 245-254.

Nakawo, M. Iwata, S. Watanabe, O. and Yoshida, M. 1986. Processes which distribute supraglacial debris on the Khumbu Glacier, Nepal Himalaya. *Annals of Glaciology.* **8**, 129-131.

Nakawo, M. and Young, G.J. 1982. Estimate of Glacier Ablation under a Debris Layer from Surface Temperature and Meteorological Variables. *Journal of Glaciology.* **28**(98), 29-34.

Narama, C. Daiyrov, M. Tadono, T. Yamamoto, M. Kääb, A. Morita, R. and Ukita, J. 2017. Seasonal drainage of supraglacial lakes on debris-covered glaciers in the Tien Shan Mountains, Central Asia. *Geomorphology.* **286**, 133-142.

National Environment Commission. 2009. Strategizing climate change for Bhutan. [Online]. [Accessed 26 March 2014]. Available from: http://www.rrcap.ait.asia/nsds/uploadedfiles/file/bhutan.pdf.

Nicholson, L. and Benn, D.I. 2006. Calculating ice melt beneath a debris layer using meteorological data. *Journal of Glaciology.* **52**(178), 463-470.

Nicholson, L. and Benn, D.I. 2013. Properties of natural supraglacial debris in relation to modelling sub-debris ice ablation. *Earth Surface Processes and Landforms.* **38**(5), 490-501.

Nie, Y. Liu, Q. and Liu, S. 2013. Glacial Lake Expansion in the Central Himalayas by Landsat Images, 1990–2010. *PLoS ONE.* **8**(12), 1-8.

Nie, Y. Sheng, Y. Liu, Q. Liu, L. Liu, S. Zhang, Y. and Song, C. 2017. A regional-scale assessment of Himalayan glacial lake changes using satellite observations from 1990 to 2015. *Remote Sensing of Environment.* **189**, 1-13.

Nuimura, T. Fujita, K. Yamaguchi, S. and Sharma, R.R. 2012. Elevation changes of glaciers revealed by multitemporal digital elevation models calibrated by GPS survey in the Khumbu region, Nepal Himalaya, 1992-2008. *Journal of Glaciology.* **58**(210), 648-656.

Östrem, G. 1959. Ice Melting under a Thin Layer of Moraine, and the Existence of Ice Cores in Moraine Ridges. *Geografiska Annaler.* **41**(4), 228-230.

Pellicciotti, F. Stephan, C. Miles, E. Herreid, S. Immerzeel, W.W. and Bolch, T. 2015. Mass-balance changes of the debris-covered glaciers in the Langtang Himal, Nepal, from 1974 to 1999. *Journal of Glaciology.* **61**(226), 373-386.

Pritchard, H.D. 2017. Asia's glaciers are a regionally important buffer against drought. *Nature.* **545**(7653), 169-174.

Quincey, D.J. Luckman, A. and Benn, D. 2009. Quantification of Everest region glacier velocities between 1992 and 2002, using satellite radar interferometry and feature tracking. *Journal of Glaciology.* **55**(192), 596-606.

Quincey, D.J. Richardson, S.D. Luckman, A. Lucas, R.M. Reynolds, J.M. Hambrey, M.J. and Glasser, N.F. 2007. Early recognition of glacial lake hazards in the Himalaya using remote sensing datasets. *Global and Planetary Change.* **56**(1–2), 137-152.

Radić, V. Bliss, A. Beedlow, A.C. Hock, R. Miles, E. and Cogley, J.G. 2014. Regional and global projections of twenty-first century glacier mass changes in response to climate scenarios from global climate models. *Climate Dynamics.* **42**(1-2), 37-58.

Radic, V. and Hock, R. 2011. Regionally differentiated contribution of mountain glaciers and ice caps to future sea-level rise. *Nature Geosci.* **4**(2), 91-94.

Ragettli, S. Bolch, T. and Pellicciotti, F. 2016. Heterogeneous glacier thinning patterns over the last 40 years in Langtang Himal, Nepal. *The Cryosphere.* **10**(5), 2075-2097.

Reid, T.D. and Brock, B.W. 2014. Assessing ice-cliff backwasting and its contribution to total ablation of debris-covered Miage glacier, Mont Blanc massif, Italy. *Journal of Glaciology.* **60**(219), 3-13.

Reynolds, J.M. 2000. On the formation of supraglacial lakes on debris-covered glaciers. In: Nakawo, M.Raymond, C.F. and Fountain, A., eds. *IAHS Publ. 264 (Symposium at Seattle 2000 – Debris-Covered Glaciers)*, *Seattle, Washington, U.S.A*. IAHS Publishing, 153-161.

Richardson, S.D. and Reynolds, J.M. 2000. An overview of glacial hazards in the Himalayas. *Quaternary International.* **65–66**, 31-47.

Rohl, K. 2006. Thermo-erosional notch development at fresh-water-calving Tasman Glacier, New Zealand. *Journal of Glaciology.* **52**(177), 203-213.

Rounce, D. Watson, C. and McKinney, D. 2017. Identification of hazard and risk for glacial lakes in the Nepal Himalaya using satellite imagery from 2000–2015. *Remote Sensing.* **9**(7).

Rounce, D.R. and McKinney, D.C. 2014. Debris thickness of glaciers in the Everest area (Nepal Himalaya) derived from satellite imagery using a nonlinear energy balance model. *The Cryosphere.* **8**(4), 1317-1329.

Rounce, D.R. McKinney, D.C. Lala, J.M. Byers, A.C. and Watson, C.S. 2016. A new remote hazard and risk assessment framework for glacial lakes in the Nepal Himalaya. *Hydrol. Earth Syst. Sci.* **20**(9), 3455-3475.

Rowan, A.V. Egholm, D.L. Quincey, D.J. and Glasser, N.F. 2015. Modelling the feedbacks between mass balance, ice flow and debris transport to predict the response to climate change of debris-covered glaciers in the Himalaya. *Earth and Planetary Science Letters.* **430**, 427-438.

Sakai, A. Nakawo, M. and Fujita, K. 1998. Melt rate of ice cliffs on the Lirung Glacier, Nepal Himalayas. *Bulletin of Glaciological Research.* **16**, 57-66.

Sakai, A. Nakawo, M. and Fujita, K. 2002. Distribution characteristics and energy balance of ice cliffs on debris-covered glaciers, Nepal Himalaya. *Arctic Antarctic and Alpine Research.* **34**(1), 12-19.

Sakai, A. Nishimura, K. Kadota, T. and Takeuchi, N. 2009. Onset of calving at supraglacial lakes on debris-covered glaciers of the Nepal Himalaya. *Journal of Glaciology.* **55**(193), 909-917.

Sakai, A. Takeuchi, N. Fujita, K. and Nakawo, M. 2000. Role of supraglacial ponds in the ablation process of a debris-covered glacier in the Nepal Himalayas. In: Nakawo, M.Raymond, C.F. and Fountain, A., eds. *IAHS Publ. 264 (Symposium at Seattle 2000 – Debris-Covered Glaciers)*, *Seattle, Washington, U.S.A*. IAHS Publishing, 119-130.

Salerno, F. Guyennon, N. Thakuri, S. Viviano, G. Romano, E. Vuillermoz, E. Cristofanelli, P. Stocchi, P. Agrillo, G. Ma, Y. and Tartari, G. 2015. Weak precipitation, warm winters and springs impact glaciers of south slopes of Mt. Everest (central Himalaya) in the last 2 decades (1994–2013). *The Cryosphere.* **9**(3), 1229-1247.

Salerno, F. Thakuri, S. D'Agata, C. Smiraglia, C. Manfredi, E.C. Viviano, G. and Tartari, G. 2012. Glacial lake distribution in the Mount Everest region: Uncertainty of measurement and conditions of formation. *Global and Planetary Change.* **92-93**, 30-39.

Scherler, D. Bookhagen, B. and Strecker, M.R. 2011. Spatially variable response of Himalayan glaciers to climate change affected by debris cover. *Nature Geosci.* **4**(3), 156-159.

Schwanghart, W. Worni, R. Huggel, C. Stoffel, M. and Korup, O. 2016. Uncertainty in the Himalayan energy–water nexus: estimating regional exposure to glacial lake outburst floods. *Environmental Research Letters.* **11**(7), 1-9.

Sharma, R.H. and Awal, R. 2013. Hydropower development in Nepal. *Renewable and Sustainable Energy Reviews.* **21**, 684-693.

Shea, J.M. Immerzeel, W.W. Wagnon, P. Vincent, C. and Bajracharya, S. 2015. Modelling glacier change in the Everest region, Nepal Himalaya. *The Cryosphere.* **9**(3), 1105-1128.

Smith, M.W. Carrivick, J.L. and Quincey, D.J. 2015. Structure from motion photogrammetry in physical geography. *Progress in Physical Geography.* 1-29.

Solomina, O.N. Bradley, R.S. Jomelli, V. Geirsdottir, A. Kaufman, D.S. Koch, J. McKay, N.P. Masiokas, M. Miller, G. Nesje, A. Nicolussi, K. Owen, L.A. Putnam, A.E. Wanner, H. Wiles, G. and Yang, B. 2016. Glacier fluctuations during the past 2000 years. *Quaternary Science Reviews.* **149**, 61-90.

Somos-Valenzuela, M.A. McKinney, D.C. Byers, A.C. Rounce, D.R. Portocarrero, C. and Lamsal, D. 2014a. Assessing downstream flood impacts due to a potential GLOF from Imja Lake in Nepal. *Hydrol. Earth Syst. Sci. Discuss.* **19**(3), 1401-1412.

Somos-Valenzuela, M.A. McKinney, D.C. Rounce, D.R. and Byers, A.C. 2014b. Changes in Imja Tsho in the Mount Everest region of Nepal. *The Cryosphere.* **8**(5), 1661-1671.

Steiner, J.F. Pellicciotti, F. Buri, P. Miles, E.S. Immerzeel, W.W. and Reid, T.D. 2015. Modelling ice-cliff backwasting on a debris-covered glacier in the Nepalese Himalaya. *Journal of Glaciology.* **61**(229), 889-907.

Strozzi, T. Wiesmann, A. Kääb, A. Joshi, S. and Mool, P. 2012. Glacial lake mapping with very high resolution satellite SAR data. *Natural Hazards and Earth System Sciences.* **12**(8), 2487-2498.

Stumpf, A. Malet, J.P. Allemand, P. Pierrot-Deseilligny, M. and Skupinski, G. 2015. Ground-based multi-view photogrammetry for the monitoring of landslide deformation and erosion. *Geomorphology.* **231**, 130-145.

Surendra, K.C. Khanal, S.K. Shrestha, P. and Lamsal, B. 2011. Current status of renewable energy in Nepal: Opportunities and challenges. *Renewable and Sustainable Energy Reviews.* **15**(8), 4107-4117.

Takeuchi, N. and Kohshima, S. 2000. Effect of debris cover on species composition of living organisms in supraglacial lakes on a Himalayan glacier. In: *IAHS Publ. 264 (Symposium at Seattle 2000 – Debris-Covered Glaciers), Seattle, Washington, U.S.A*. IAHS Publishing, 267-275.

Thakuri, S. Salerno, F. Bolch, T. Guyennon, N. and Tartari, G. 2016. Factors controlling the accelerated expansion of Imja Lake, Mount Everest region, Nepal. *Annals of Glaciology.* **57**(71), 245-257.

Thakuri, S. Salerno, F. Smiraglia, C. Bolch, T. D'Agata, C. Viviano, G. and Tartari, G. 2014. Tracing glacier changes since the 1960s on the south slope of Mt. Everest (central Southern Himalaya) using optical satellite imagery. *Cryosphere.* **8**(4), 1297-1315.

Thompson, S. Benn, D. Mertes, J. and Luckman, A. 2016. Stagnation and mass loss on a Himalayan debris-covered glacier: processes, patterns and rates. *Journal of Glaciology.* **62**(233), 467-485.

Thompson, S.S. Benn, D.I. Dennis, K. and Luckman, A. 2012. A rapidly growing moraine-dammed glacial lake on Ngozumpa Glacier, Nepal. *Geomorphology.* **145**, 1-11.

Vincent, C. Ramanathan, A. Wagnon, P. Dobhal, D.P. Linda, A. Berthier, E. Sharma, P. Arnaud, Y. Azam, M.F. Jose, P.G. and Gardelle, J. 2013. Balanced

conditions or slight mass gain of glaciers in the Lahaul and Spiti region (northern India, Himalaya) during the nineties preceded recent mass loss. *The Cryosphere.* **7**(2), 569-582.

Vincent, C. Wagnon, P. Shea, J.M. Immerzeel, W.W. Kraaijenbrink, P. Shrestha, D. Soruco, A. Arnaud, Y. Brun, F. Berthier, E. and Sherpa, S.F. 2016. Reduced melt on debris-covered glaciers: investigations from Changri Nup Glacier, Nepal. *The Cryosphere.* **10**(4), 1845-1858.

Vuichard, D. and Zimmermann, M. 1987. The 1985 Catastrophic Drainage of a Moraine-Dammed Lake, Khumbu Himal, Nepal: Cause and Consequences. *Mountain Research and Development.* **7**(2), 91-110.

Wagnon, P. Vincent, C. Arnaud, Y. Berthier, E. Vuillermoz, E. Gruber, S. Ménégoz, M. Gilbert, A. Dumont, M. Shea, J.M. Stumm, D. and Pokhrel, B.K. 2013. Seasonal and annual mass balances of Mera and Pokalde glaciers (Nepal Himalaya) since 2007. *The Cryosphere.* **7**(6), 1769-1786.

Watanabe, T. Ives, J.D. and Hammond, J.E. 1994. Rapid Growth of a Glacial Lake in Khumbu Himal, Himalaya: Prospects for a Catastrophic Flood. *Mountain Research and Development.* **14**(4), 329-340.

Watson, C.S. Quincey, D.J. Carrivick, J.L. and Smith, M.W. 2016. The dynamics of supraglacial ponds in the Everest region, central Himalaya. *Global and Planetary Change.* **142**, 14-27.

Watson, C.S. Quincey, D.J. Carrivick, J.L. and Smith, M.W. 2017a. Ice cliff dynamics in the Everest region of the Central Himalaya. *Geomorphology.* **278**, 238-251.

Watson, C.S. Quincey, D.J. Carrivick, J.L. Smith, M.W. Rowan, A.V. and Richardson, R. 2017b. Heterogeneous water storage and thermal regime of supraglacial ponds on debris-covered glaciers. *Earth Surface Processes and Landforms.*

Watson, C.S. Quincey, D.J. Smith, M.W. Carrivick, J.L. Rowan, A.V. and James, M. *2017c*. Quantifying ice cliff evolution with multi-temporal point clouds on the debris-covered Khumbu Glacier, Nepal. *Journal of Glaciology.*

Wessels, R.L. Kargel, J.S. and Kieffer, H.H. 2002. ASTER measurement of supraglacial lakes in the Mount Everest region of the Himalaya. *Annals of Glaciology.* **34**, 399-408.

Westoby, M.J. Brasington, J. Glasser, N.F. Hambrey, M.J. and Reynolds, J.M. 2012. 'Structure-from-Motion' photogrammetry: A low-cost, effective tool for geoscience applications. *Geomorphology.* **179**, 300-314.

Westoby, M.J. Glasser, N.F. Brasington, J. Hambrey, M.J. Quincey, D.J. and Reynolds, J.M. 2014. Modelling outburst floods from moraine-dammed glacial lakes. *Earth-Science Reviews.* **134**, 137-159.

Worni, R. Huggel, C. Clague, J.J. Schaub, Y. and Stoffel, M. 2014. Coupling glacial lake impact, dam breach, and flood processes: A modeling perspective. *Geomorphology.* **224**, 161-176.

Worni, R. Huggel, C. and Stoffel, M. 2012. Glacial lakes in the Indian Himalayas--from an area-wide glacial lake inventory to on-site and modeling based risk assessment of critical glacial lakes. *Sci Total Environ.* **468-469**, 71-84.

Xin, W. Shiyin, L. Haidong, H. Jian, W. and Qiao, L. 2012. Thermal regime of a supraglacial lake on the debris-covered Koxkar Glacier, southwest Tianshan, China. *Environmental Earth Sciences.* **67**(1), 175-183.

Yao, T. Thompson, L. Yang, W. Yu, W. Gao, Y. Guo, X. Yang, X. Duan, K. Zhao, H. Xu, B. Pu, J. Lu, A. Xiang, Y. Kattel, D.B. and Joswiak, D. 2012. Different

glacier status with atmospheric circulations in Tibetan Plateau and surroundings. *Nature Clim. Change.* **2**(9), 663-667.

Zemp, M. Frey, H. Gärtner-Roer, I. Nussbaumer, S.U. Hoelzle, M. Paul, F. Haeberli, W. Denzinger, F. Ahlstrøm, A.P. Anderson, B. Bajracharya, S. Baroni, C. Braun, L.N. Cáceres, B.E. Casassa, G. Cobos, G. Dávila, L.R. Delgado Granados, H. Demuth, M.N. Espizua, L. Fischer, A. Fujita, K. Gadek, B. Ghazanfar, A. Hagen, J.O. Holmlund, P. Karimi, N. Li, Z. Pelto, M. Pitte, P. Popovnin, V.V. Portocarrero, C.A. Prinz, R. Sangewar, C.V. Severskiy, I. Sigurðsson, O. Soruco, A. Usubaliev, R. and Vincent, C. 2015. Historically unprecedented global glacier decline in the early 21st century. *Journal of Glaciology.* **61**(228), 745-762.

Zhang, G. Yao, T. Xie, H. Wang, W. and Yang, W. 2015. An inventory of glacial lakes in the Third Pole region and their changes in response to global warming. *Global and Planetary Change.* **131**, 148-157.

Appendix A
Supplementary information

Supplementary information for Chapters 3, 4, 5 and 6 is included below.

A.1 Chapter 3. The dynamics of supraglacial ponds in the Everest region, central Himalaya

Differential GPS points were collected around the boundary of four stable supraglacial ponds during a field campaign in Oct/Nov 2015 (Supplementary Figure 3.1). Point locations were determined by boundary accessibility and were collected using a Leica GS10 sensor with sub-centimetre accuracy.

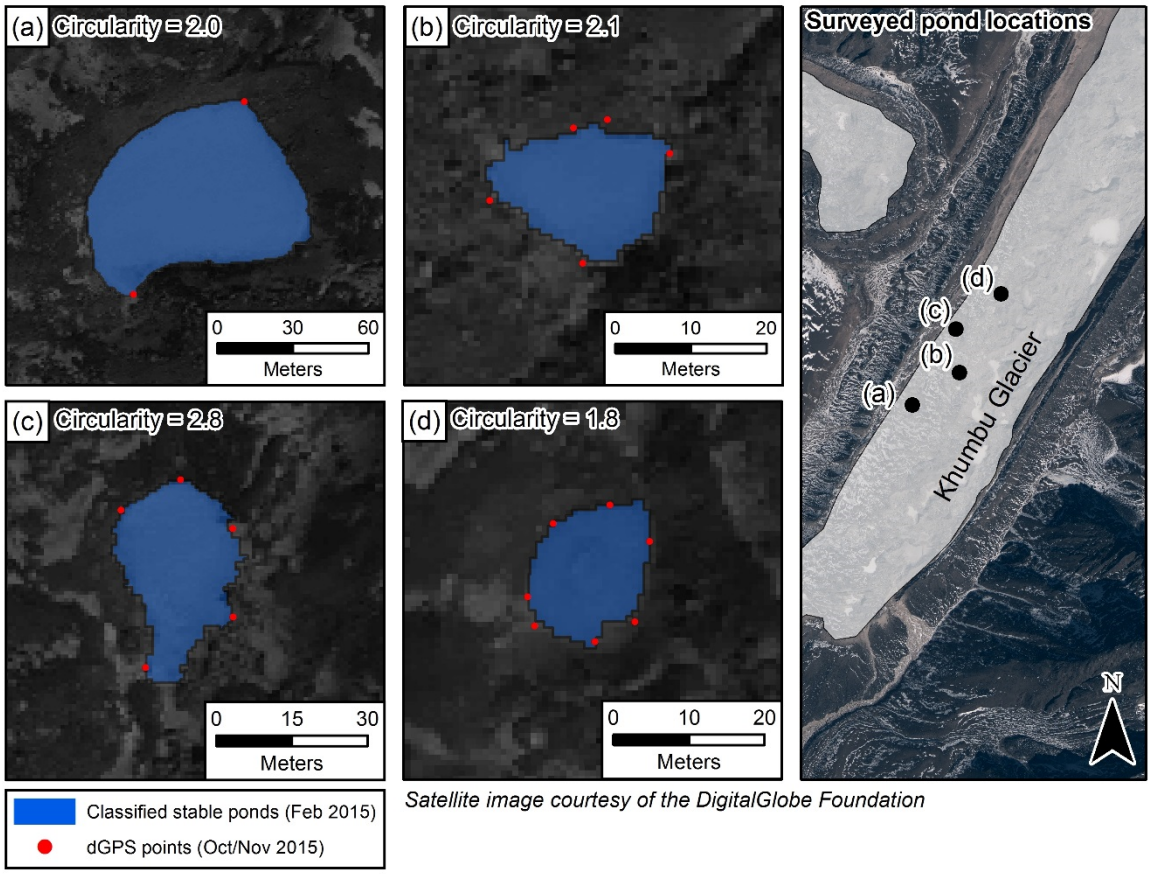

Supplementary Figure 3.1. Field validation of supraglacial pond boundaries

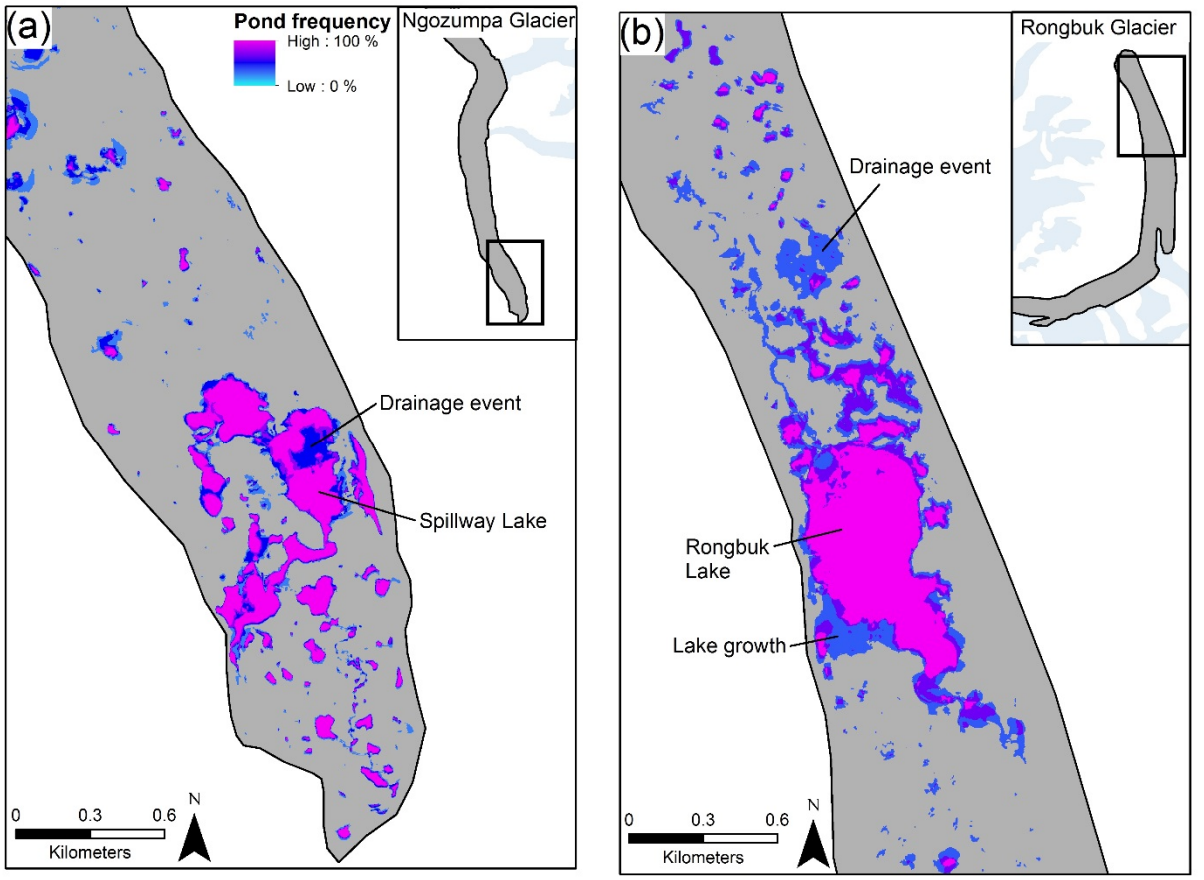

Supplementary Figure 3.2. Expansion of Spillway and Rongbuk Lakes in Figure. 3.7 showing pond frequency.

Direct pond-by-pond comparisons between Landsat and fine-resolution imagery are difficult since acquisition dates rarely align and owing to the variable user-defined thresholds used to classify ponds, which can lead to more or fewer pixels been classified a water. In this study we determined and idealised theoretical underestimation of ponded area and number of ponds (Supplementary Figure 3.3) by applying a one (900 m^2) and four pixel (3600 m^2) threshold. In reality, ponds approaching 3600 m^2 would be classified as water since water would dominate the spectral signature of the pixel, however, the specific threshold is scene- and user-dependent.

Studies may opt to implement a broad threshold to account for mixed pixels, which are majority but not exclusively water (e.g. Gardelle et al., 2011). This will generally lead to pond size overestimation (e.g. Figure 3.10). Alternatively, opting for a higher threshold of 'purer' pixels will underestimate ponded area since shoreline pixels also containing debris-cover for example, will be excluded.

Since our inventory was collected at extremely fine resolution we can effectively treat it as a ground truth and hence assess the implications of threshold choice on overall

ponded area by aggregating the ponds to coarser resolutions. This is not fully representative of a real-world Landsat analysis scenario where the true distribution and area of water pixels would not be known beforehand. It also does not consider spectral 'noise', such as surrounding debris cover, which would change the spectral signature of a pixel since the surrounding terrain was simply treated as a zero.

Method:

Pond polygons were converted to a raster grid at 2 m resolution (Supplementary Figure 3.3a) and then aggregated by summation to a 30 m raster grid (Supplementary Figure 3.3b). This creates a scale of 0–225, which is the maximum number of 2 m pixels (4 m^2) that could be contained within a new 30 m pixel (900 m^2).

For increasing percentage coverage of the original 4 m^2 pixels within the new 900 m^2 pixel, we then assessed this threshold against the true ponded area. Here, a threshold of 35% is required to account for 100 % of ponded area at a glacier scale (Supplementary Figure 3c).

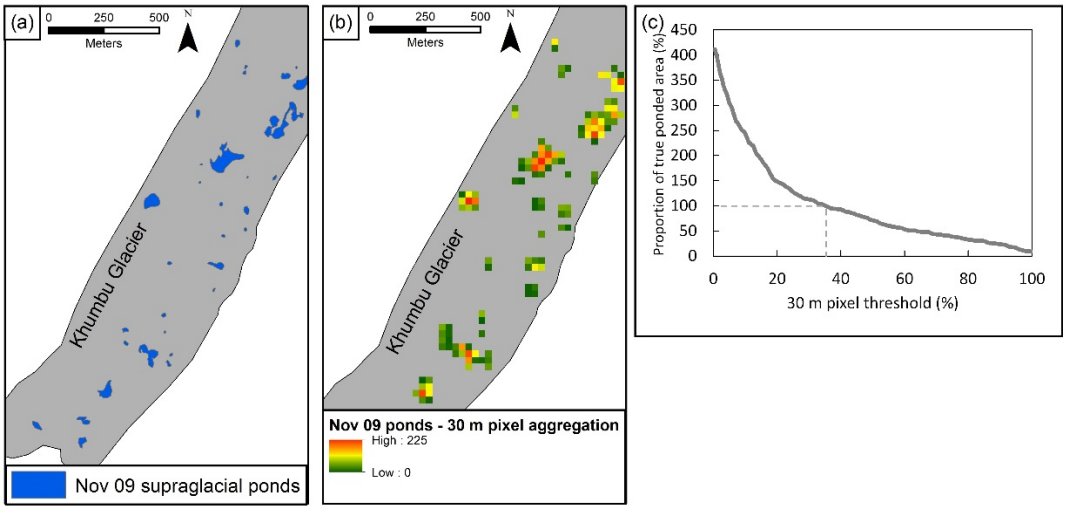

Supplementary Figure 3.3. Supraglacial ponds derived using fine-resolution imagery were rasterised to 2 m pixels (a). These 2 m pixels were then aggregated to 30 m pixels, such that the maximum number of 2 m pixels within a new 30 m pixel was 225 (b). With knowledge of the water content of each 30 m pixel derived from (b), the relationship between pixel water content and the proportion of true ponded area delineated at a glacier scale can be derived (c), and used to estimate the threshold required to delineate 100 % of the true glacier scale ponded area.

Supplementary Table 3.1. Comparing Object based and manual pond delineation

To estimate the methodological uncertainty arising from an object based pond classification vs manual classification, one operator manually digitised 50 ponds and their respective areas were compared to those derived using the objected based method. This was carried out in ArcGIS using freehand digitising and without reference

to multispectral imagery or the object based polygons (i.e. blind), and hence represents a worst case scenario. The resulting uncertainties were consistently lower than the actual uncertainty assumed in this study using a ±1 pixel buffer (Supplementary Table 1).

Pond ID	Object based area (m^2)	Manually digitised area (m^2)	Difference (%)	Assumed object based method uncertainty (%)*
1	1875.0	1737.9	7.6	16.4
2	1198.0	1101.6	8.4	19.5
3	139.9	138.0	1.4	40.7
4	1589.9	1442.0	9.8	21.4
5	4258.1	4398.3	3.2	13.2
6	363.1	311.2	15.4	34.4
7	2439.4	2391.7	2.0	10.3
8	204.2	195.1	4.5	26.9
9	5334.8	5395.3	1.1	6.3
10	510.1	460.5	10.2	25.7
11	4954.9	5071.4	2.3	8.7
12	1371.1	1454.9	5.9	16.9
13	188.2	170.0	10.1	40.0
14	863.9	946.8	9.2	24.5
15	401.7	374.6	7.0	26.0
16	199.4	219.7	9.7	35.1
17	409.0	366.5	11.0	28.2
18	1489.4	1494.3	0.3	11.0
19	1788.3	1844.7	3.1	13.3
20	108.6	104.1	4.3	39.2
21	653.7	648.4	0.8	13.2
22	1007.9	972.6	3.6	15.5
23	88.2	75.1	16.1	45.9
24	4808.4	4742.2	1.4	7.8
25	1616.8	1609.7	0.4	11.0
26	658.6	611.8	7.4	20.1
27	106.3	103.4	2.8	30.9
28	545.4	491.3	10.4	26.9

29	87.2	86.3	1.1	41.1
30	459.1	412.0	10.8	27.6
31	505.9	468.6	7.6	26.0
32	6846.5	7041.4	2.8	9.2
33	68.6	59.4	14.3	50.2
34	1278.4	1291.9	1.0	11.0
35	4840.1	4702.5	2.9	9.5
36	145.0	129.6	11.3	38.4
37	91.6	78.9	14.9	50.0
38	561.1	556.3	0.8	21.5
39	545.4	523.9	4.0	20.6
40	258.0	288.3	11.1	31.1
41	305.3	292.7	4.2	21.5
42	59.8	61.6	3.0	69.1
43	799.6	890.7	10.8	28.5
44	241.8	238.2	1.5	22.4
45	2582.4	2723.2	5.3	12.7
46	318.8	343.8	7.5	25.5
47	108.3	98.4	9.5	37.5
48	219.1	255.9	15.5	43.0
49	275.9	253.8	8.3	29.1
50	2080.0	2063.3	0.8	8.5

* Based on a ± 1 pixel buffer used in our study

A first-order estimate of supraglacial pond water storage was derived using the area-volume scaling relationship of Cook and Quincey (2015) applied to individual supraglacial ponds (Supplementary Table 3.2):

$V = 3\times10^{-7} A^{1.3315}$

Where V is the pond volume ($m^3 \times 10^6$) and A is the pond area (m^2).

The compiled data set of Cook and Quincey (2015) displayed a strong correlation between area and volume ($R^2 = 0.97$). However, data points predominantly comprise larger glacial lakes (>10,000 m^2), with only two data points below this size. Hence the uncertainty in this relationship for smaller ponds is likely to be large, highlighting the urgent requirement for supraglacial pond bathymetry data for smaller ponds.

Cook and Quincey (2015) demonstrate that expanding supraglacial ponds are not well predicted using the existing relationships, hence we expect our estimates to be an overestimate of water storage. For example, using lake area and bathymetry data Thompson et al. (2012) state the area of Spillway Lake in 2009 to be ~300,000 m^2 with a volume of at least 2.2 million m^3. Using the formula of Cook and Quincey (2015) this volume is 5.9 million m^3.

Supplementary Table 3.2. First-order estimate of ponded area volume

Glacier	Date	Total supraglacial pond area (m^2)	Total supraglacial pond volume estimated from Cook and Quincey (2015) ($m^3 \times 10^6$)
Khumbu	02/02/2015	228,391	1.06
	13/01/2014	183,723	0.82
	10/07/2013	193,562	0.83
	19/10/2011	183,980	1.03
	03/11/2009	12,502	0.57
	24/05/2009	206,590	0.93
Ngozumpa	23/12/2012	579,152*	4.82*
	17/10/2011	607,356*	6.13*
	09/06/2010	733,641*	6.80*
	03/11/2009	643,582*	6.22*
Rongbuk	02/02/2015	632,019*	9.96*
	11/10/2012	665,805*	10.91*
	19/10/2011	717,806*	12.82*
Nuptse	13/01/2014	63,788	0.24
	19/10/2011	47,080	0.20
	20/09/2002	53,332	0.24
Lhotse Nup	24/01/2015	32,392	0.09
	08/12/2013	18,812	0.04
	19/10/2011	16,760	0.05
	20/09/2002	21,271	0.07
Lhotse	24/01/2015	161,709	0.60
	08/12/2013	134,564	0.50
	19/10/2011	86,699	0.32
	20/09/2002	105,192	0.46
Lhotse Shar	24/01/2015	78,397	0.23

	08/12/2013	82,748	0.36
	19/10/2011	56,297	0.25
	20/09/2002	74,899	0.41
Imja	24/01/2015	13,767	0.13
	08/12/2013	13,585	0.08
	19/10/2011	10,186	0.05
Ama Dablam	13/01/2014	40,124	0.16
	19/10/2011	35,607	0.16
	03/11/2009	46,171	0.22
	24/05/2009	96,547	0.68
	18/12/2000	24,517	0.09

*Includes Spillway and Rongbuk Lakes respectively

A.2 Chapter 4. Heterogeneous water storage and thermal regime of supraglacial ponds on debris-covered glaciers

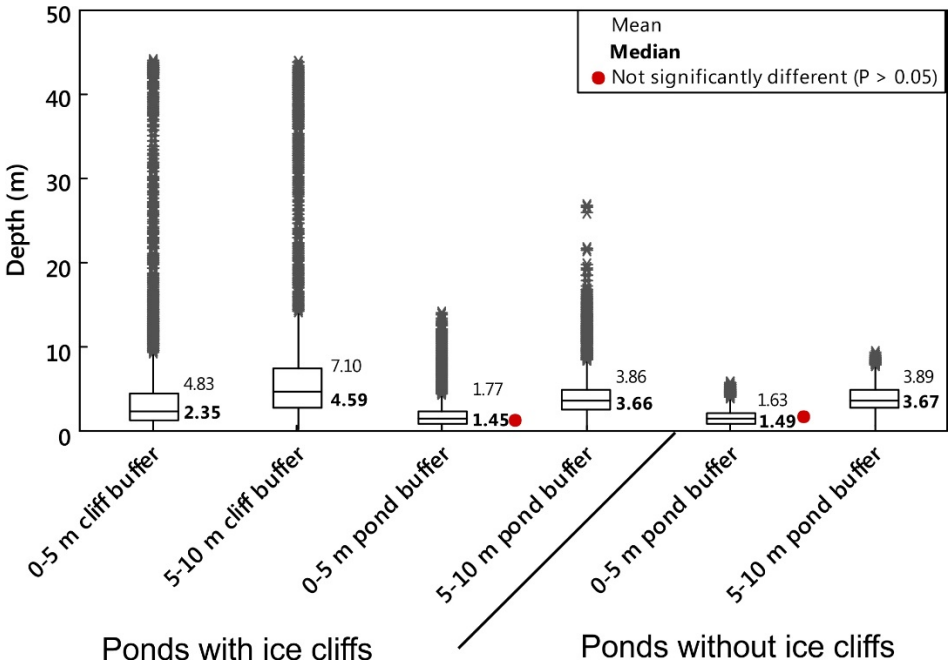

Supplementary Figure 4.1. Depth characteristics of ponds with and without cliffs using interpolated pond bathymetry. Medians were statistically significant (pair-wise Mann-Whitney U tests) at $p < 0.05$ unless indicated with a red circle.

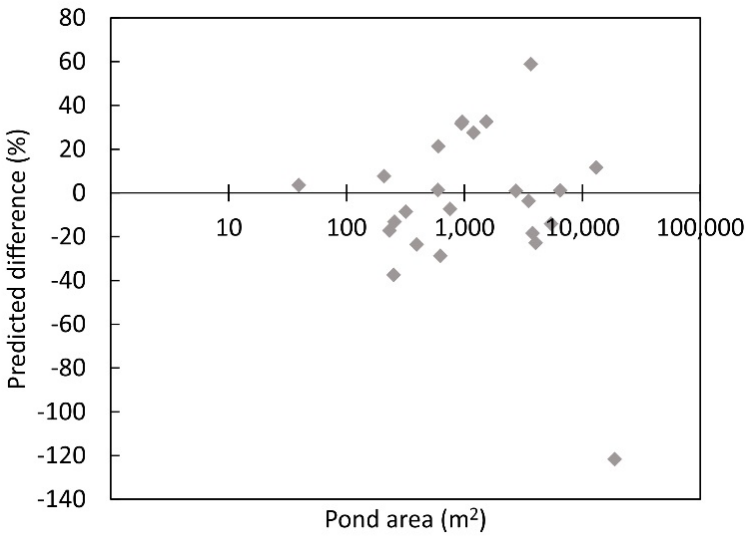

Supplementary Figure 4.2. Relationship between pond area and the percentage difference between pond volume calculated using bathymetry, and predicted pond volume using the power-law trend (Figure 4.5b) and a leave-one-out analysis.

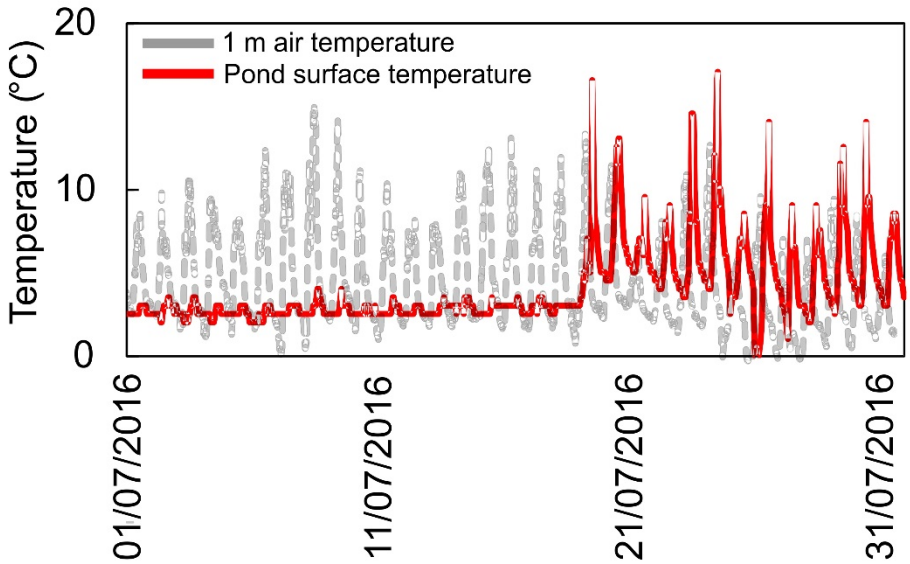

Supplementary Figure 4.3. Pond temperature at K20 alongside air temperature measured 1 m above the surface of Khumbu Glacier. It is thought the surface temperature logger became exposed on the 19th July due to pond drainage leading to a rapid temperature rise, which was coincident with the drainage of K19.

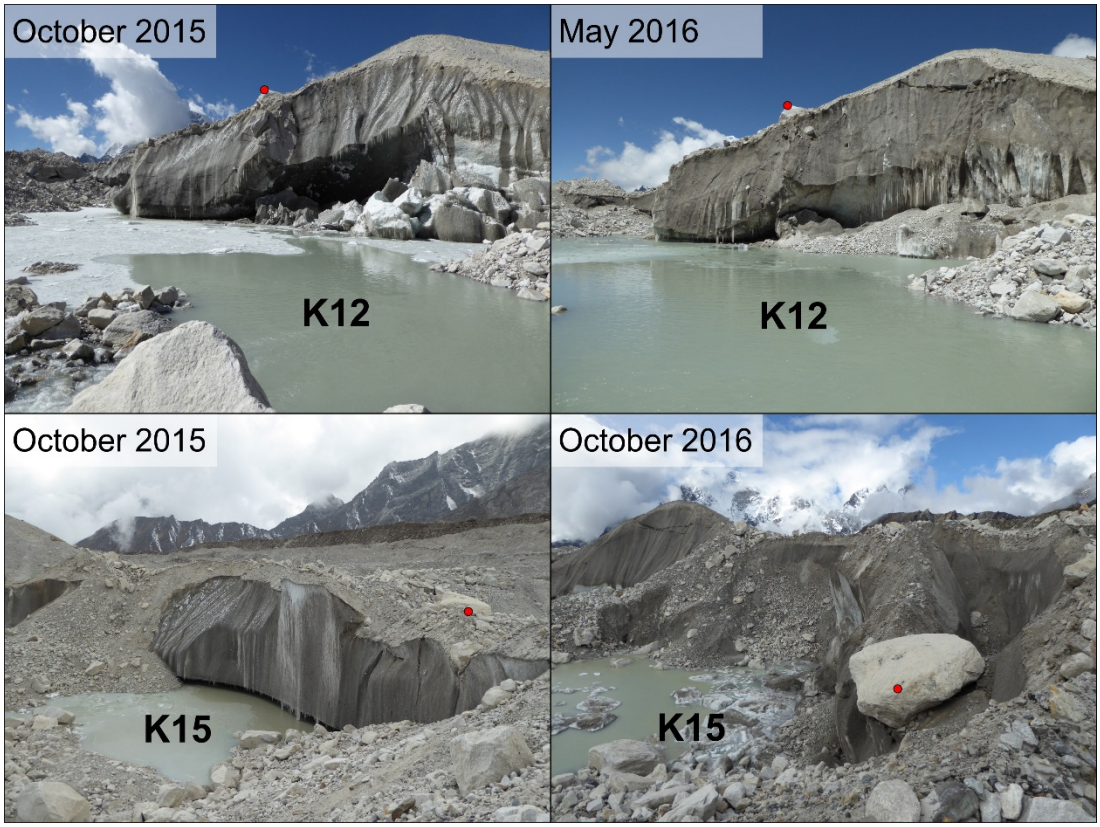

Supplementary Figure 4.4. Block and full-slab calving at K12 and K15 respectively. Red circles indicate corresponding features in each pair of images. A well-established undercut notch was present at K15 in October 2015, which facilitated the calving event.

A.3 Chapter 5. Ice cliff dynamics in the Everest region of the Central Himalaya

Supplementary Table 5.1. Ice cliff and supraglacial pond characteristics

Date	Description	Ama Dablam	Barun	Changri Nup	Changri Shar	Gaunara	Imja	Kangshung	Khumbu	Lhotse	Lhotse Nup	Lhotse Shar	Ngozumpa	Nuptse	Rongbuck
18/12/2000	No of cliffs	71													
	No of ponds	44*													
	Total cliff length (m)	5,060 ± 631													
	Total pond area (m^2)	25,128													
07/05/2003	No of cliffs									317	57			144	
	No of ponds									313	76			164	
	Total cliff length (m)									15,003 ± 1,300	2,222 ± 234			6,337 ± 590	
	Total pond area (m^2)									230,244	31,204			86,552	
24/05/2009	No of cliffs						168					459			
	No of ponds						71					260			
	Total cliff length (m)						8,422 ± 1,025					22,643 ± 2,800			
	Total pond area (m^2)						28,410					139,773			
03/11/2009	No of cliffs	75		121	125	249			436	299	59			164	582
	No of ponds	43*		101	80	162			191*	312	67			131	396
	Total cliff length (m)	6,126 ± 435		9,548 ±702	6,006 ±725	15,623 ± 1,444			23,364 ± 2,529	16,607 ± 1,734	2,698 ± 342			8,097 ± 951	40,015 ± 3,376
	Total pond area (m^2)	46,489		182,985	45,569	85,476			131,929	129,337	22,764			39,576	433,853
09/06/2010	No of cliffs												1,633		
	No of ponds												915*		
	Total cliff length (m)												72,183 ± 7,185		
	Total pond area (m^2)												742,807		
13/05/2015	No of cliffs	75	371				122	663		293	71	289		188	654
	No of ponds	63	231				58	679		335	100	200		149	567
	Total cliff length (m)	5,893 ± 398	20,008 ± 2,003				5998 ± 659	42,398 ± 3,580		17,226 ± 1,582	2,695 ± 383	15,956 ± 1,561		8,693 ± 1,015	39,711 ± 3,532
	Total pond area (m^2)	73,196	118,828				22,360	408,782		255,585	38,729	83,139		77,427	357,334
07/06/2015	No of cliffs			205	159	309			520						
	No of ponds			118	138	230			303						
	Total cliff length (m)			11,583 ±861	6,136 ± 668	17,407 ± 1,298			27,862 ± 2,184						
	Total pond area (m^2)			324755	57,174	203,502			306,571						

Data for images without complete glacier coverage are excluded
* Indicates supraglacial pond dataset from Watson et al. (2016)

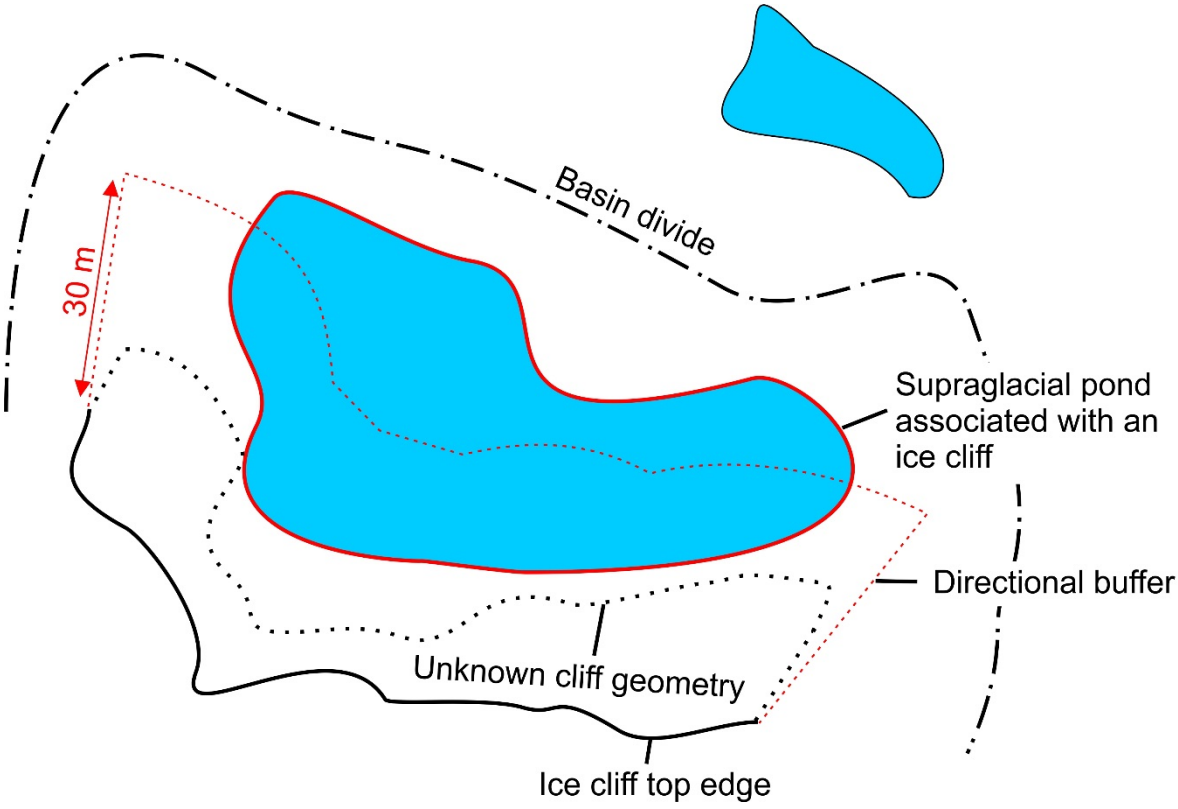

Supplementary Figure 5.1. A 30 m directional buffer is used to analyse supraglacial pond and ice cliff coincidence, accounting for an unknown cliff geometry.

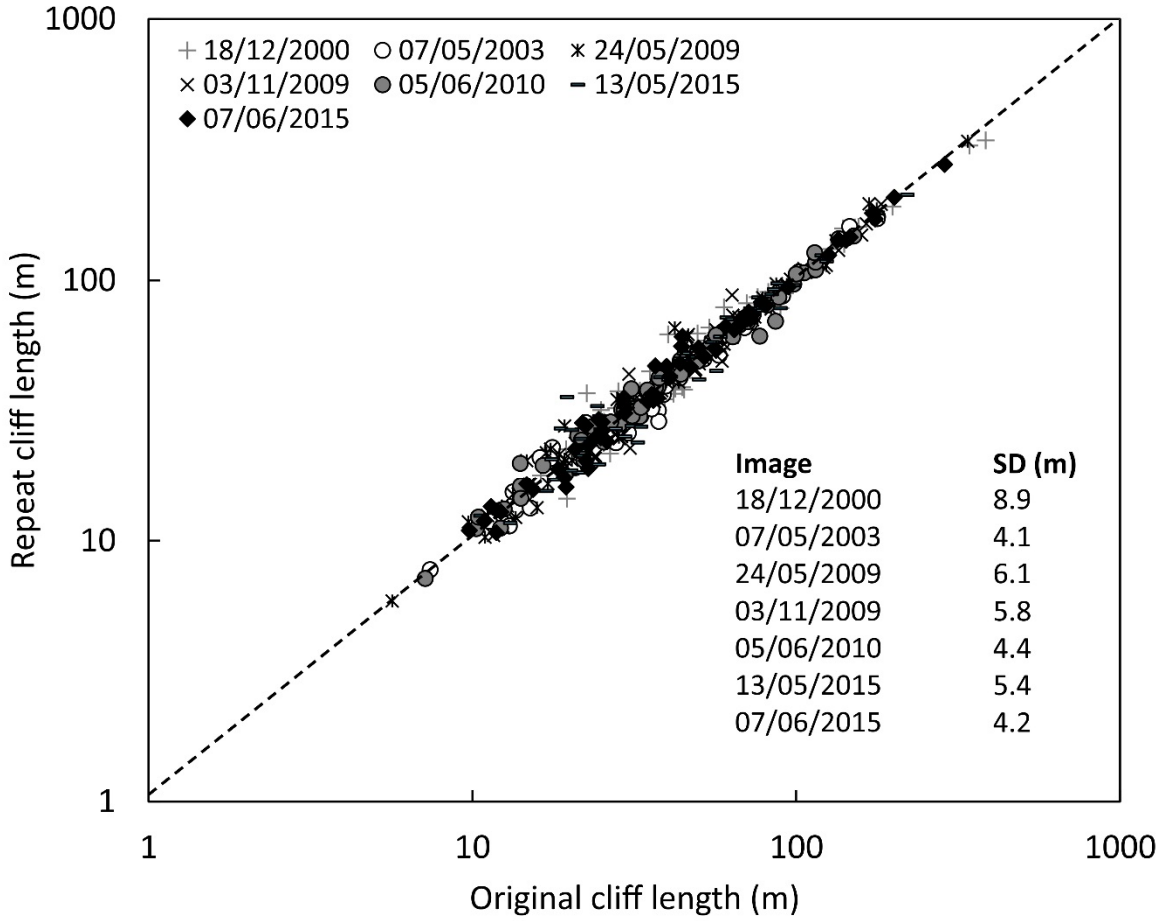

Supplementary Figure 5.2. Operator repeatability assessment from the repeat digitisation of 60 cliffs in each time period. Standard deviations are shown, which are used in Figure 5.4.

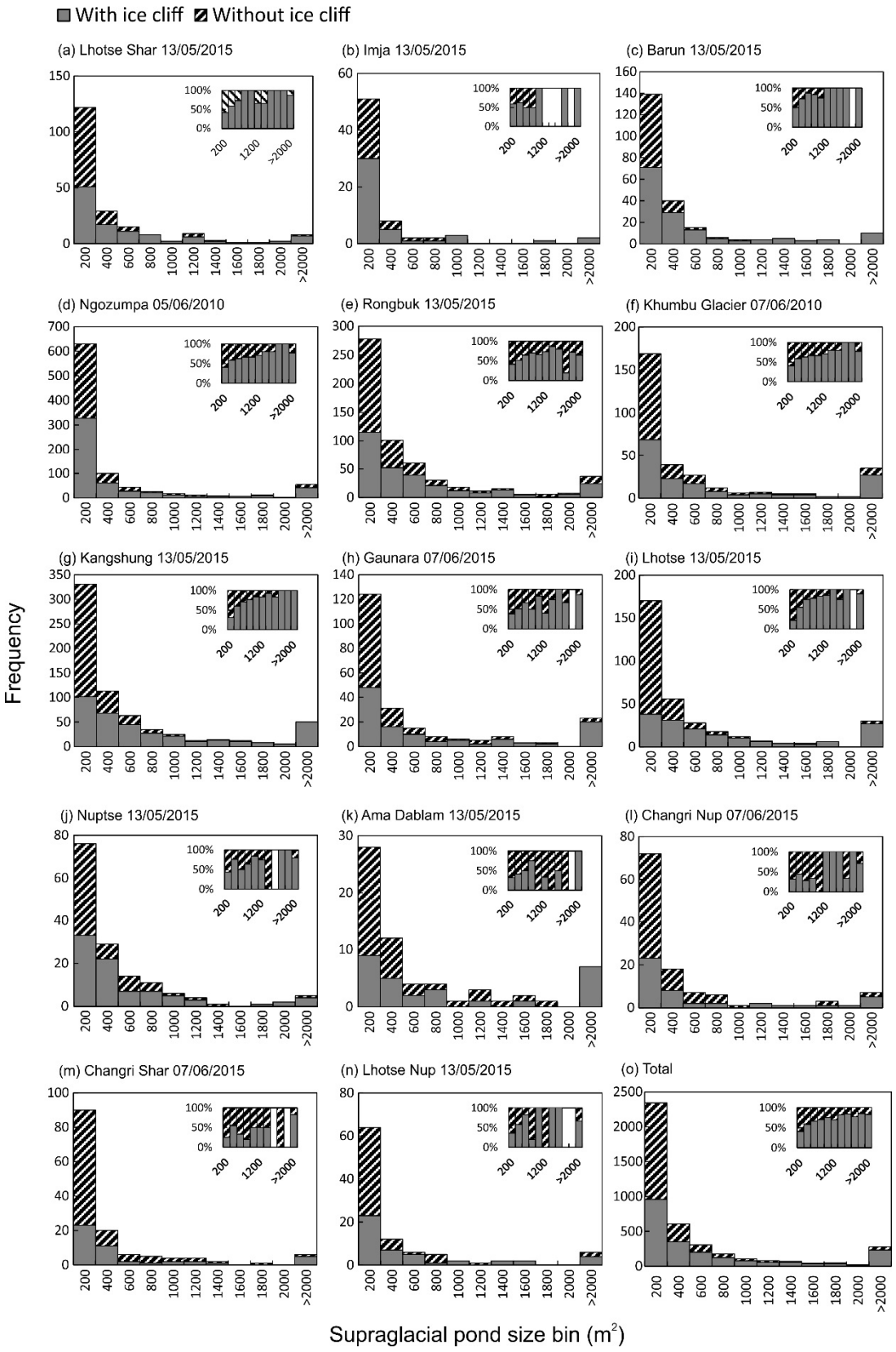

Supplementary Figure 5.3. The size distribution of supraglacial ponds and coincidence with ice cliffs, shown for the most recent time period for each glacier. Insets show the same data as a percentage distribution.

A.4 Chapter 6. Quantifying ice cliff evolution with multi-temporal point clouds on the debris-covered Khumbu Glacier, Nepal

Interactive 3D models of several ice cliffs featured in this study are available to view at:

https://sketchfab.com/rocky_glaciers

These model were processed using low density point clouds to reduce processing time, and were subsequently meshed in CloudCompare.

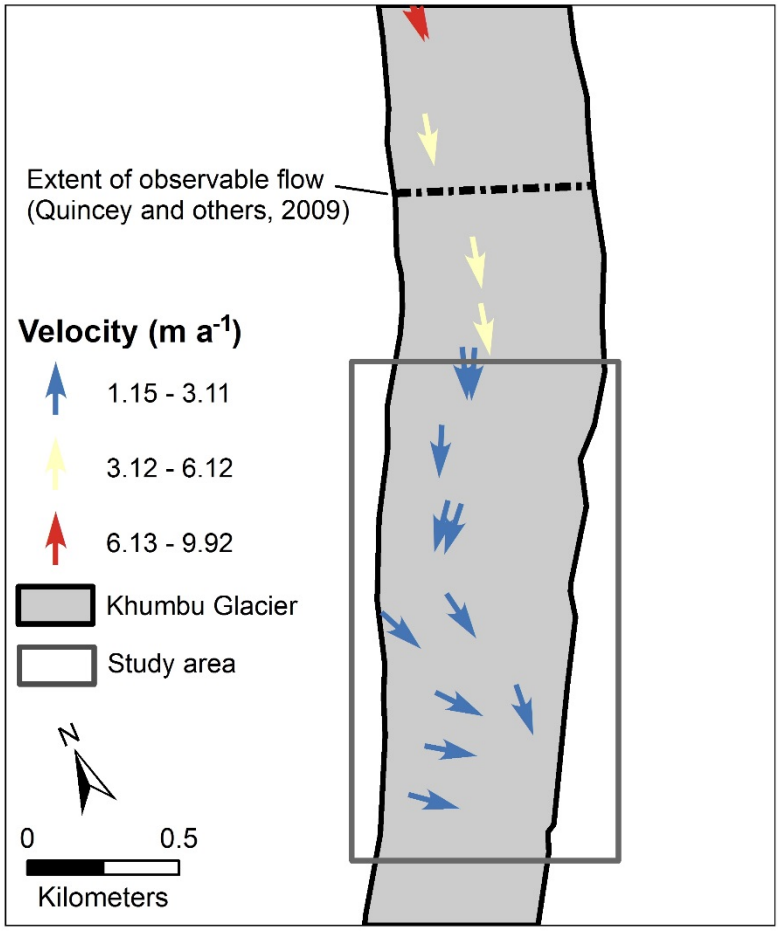

Supplementary Figure 6.1. The location of tagged boulders surveyed with a dGPS October 2015 to October 2016 at the expected transition from active to inactive ice on Khumbu Glacier.

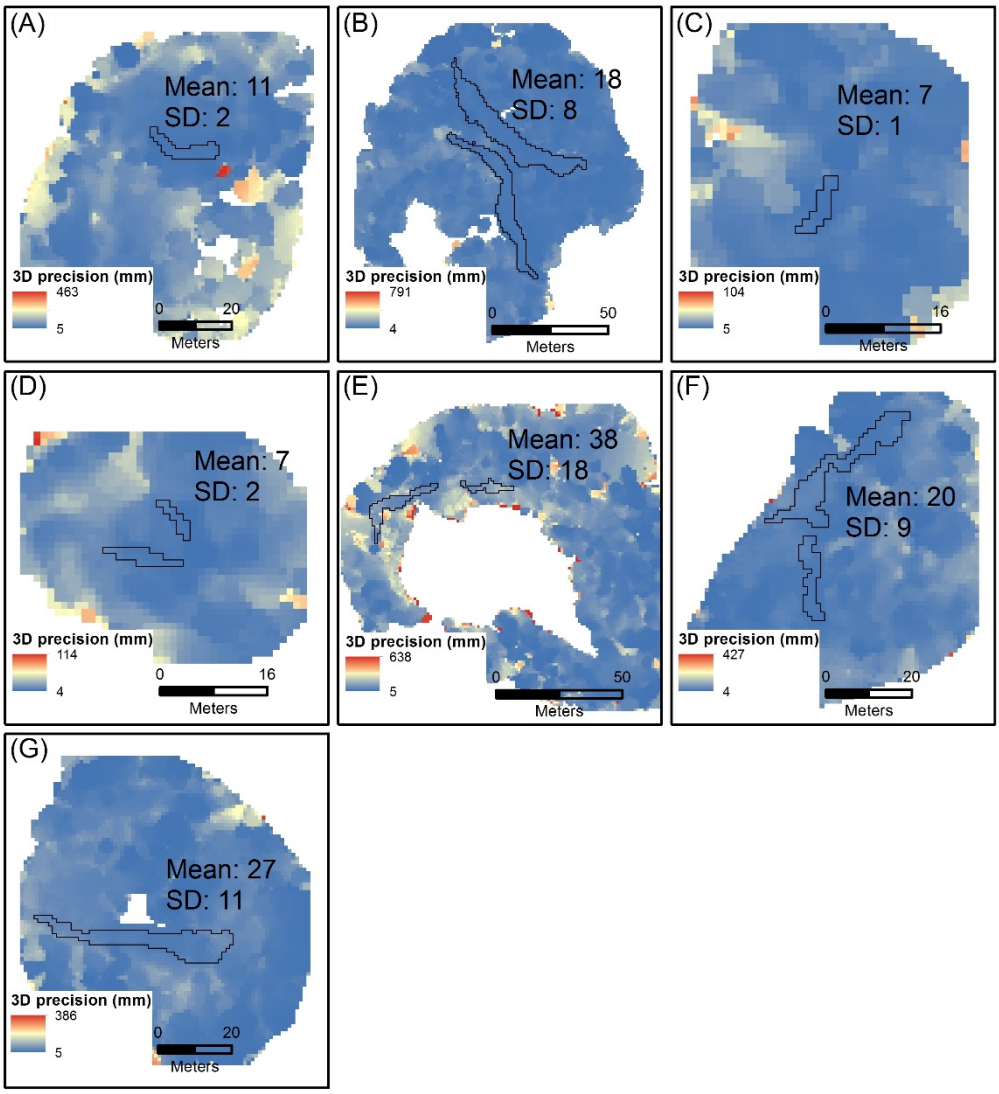

Supplementary Figure 6.2. Example precision maps derived for the May 2016 ice cliffs (black polygons). Point cloud precision estimates were interpolated onto a 1 m raster grid following James and others (2017). The mean and standard deviation of the precision estimates for each ice cliff polygon are shown in units of millimetres. Ground control point and tie point RMSE (units of pixels) used to generate the precision maps were: Cliff A 2.93 and 0.75, Cliff B 2.24 and 0.98, Cliff C 1.29 and 0.87, Cliff D 1.72 and 0.80, Cliff E 5.09 and 0.84, Cliff F 1.76 and 1.05, and Cliff G 2.41 and 0.91.

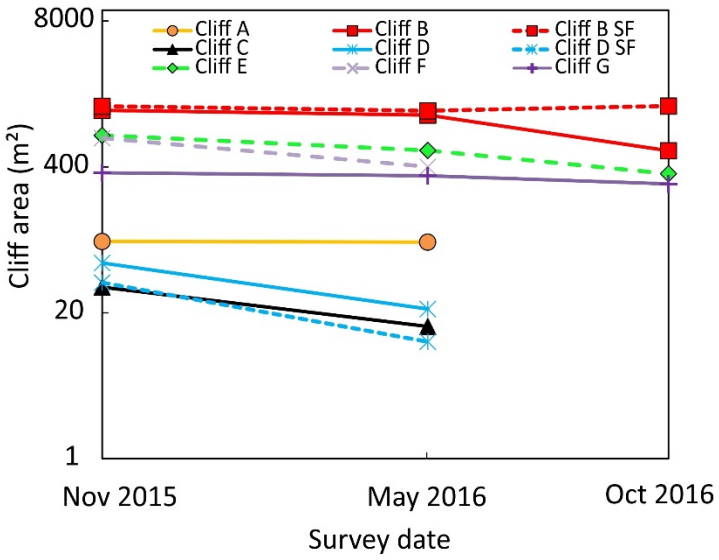

Supplementary Figure 6.3. Absolute cliff area change plotted on a logarithmic scale. Zero values are not shown for cliffs that degraded over the study period.

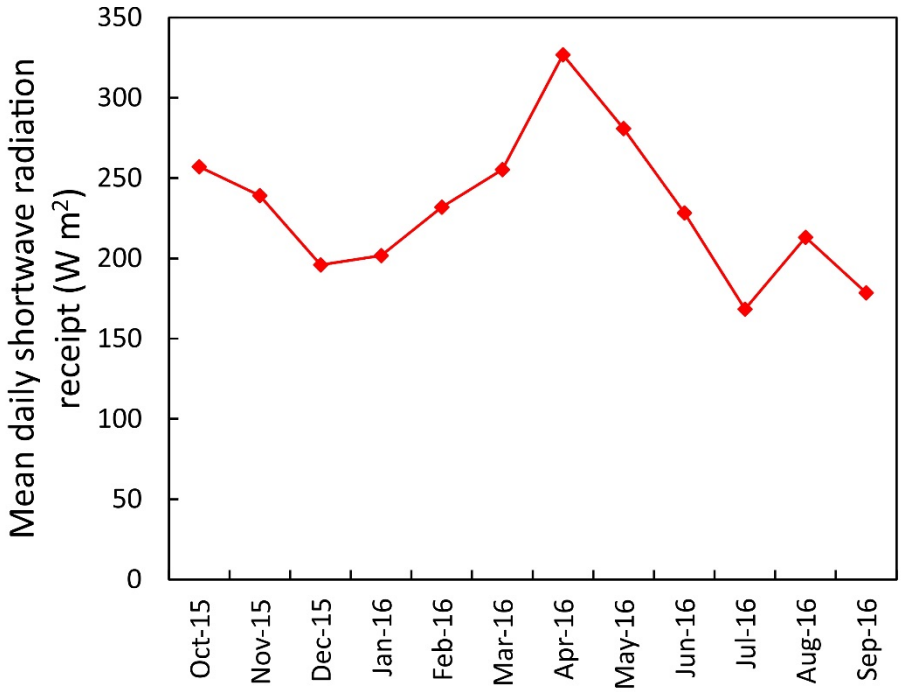

Supplementary Figure 6.4. Mean daily shortwave radiation receipt for the months October 2015 to September 2016 measured at an automatic weather station installed on Changri Nup Glacier (UTM North, Zone 45: Easting: 478293 m; Northing: 3095381 m; altitude: 5360 m), ~5.5 km from our study ice cliffs. Instrument: Kipp&Zonen CNR4 0.305<λ<2.8μm.

Supplementary Table 6.1. Percentage of ice cliff normals at time one intersecting an ice cliff at time two, from M3C2 distance calculations.

Cliff ID	Cliff-to-cliff normals (%)	
	Nov 2015 to May 2016	May 2016 to Oct 2016
A	86	0
B	45	28
B – SF	75	84
C	22	0
D	44	0
D - SF	19	0
E	54	53
F	29	0
G	86	34